

1 SEARCH FOR PRODUCTION OF A HIGGS BOSON AND A SINGLE TOP
2 QUARK IN MULTILEPTON FINAL STATES IN pp COLLISIONS AT $\sqrt{s} = 13$
3 TeV.

4 by

5 Jose Andres Monroy Montañez

6 A DISSERTATION

7 Presented to the Faculty of

8 The Graduate College at the University of Nebraska

In Partial Fulfilment of Requirements

10 For the Degree of Doctor of Philosophy

11 Major: Physics and Astronomy

12 Under the Supervision of Kenneth Bloom and Aaron Dominguez

13 Lincoln, Nebraska

14 July, 2018

15 SEARCH FOR PRODUCTION OF A HIGGS BOSON AND A SINGLE TOP
16 QUARK IN MULTILEPTON FINAL STATES IN pp COLLISIONS AT $\sqrt{s} = 13$
17 TeV.

18 Jose Andres Monroy Montañez, Ph.D.
19 University of Nebraska, 2018

20 Adviser: Kenneth Bloom and Aaron Dominguez

21 Multivariate techniques are used to discriminate the signal from the dominant back-
22 grounds. The analysis yields a 95% confidence level (C.L.) upper limit on the com-
23 bined tH + ttH production cross section times branching ratio of 0.64 pb, with an
24 expected limit of 0.32 pb, for a scenario with $k_t = \pm 1.0$ and $k_V = 1.0$. Values of k_t
25 outside the range of ± 1.25 to ± 1.60 are excluded at 95% C.L., assuming $k_V = 1.0$.

²⁶ Table of Contents

²⁷	Table of Contents	iii
²⁸	List of Figures	viii
²⁹	List of Tables	xv
³⁰	1 Theoretical approach	1
³¹	1.1 Introduction	1
³²	1.2 Standard model of particle physics	2
³³	1.2.1 Fermions	4
³⁴	1.2.1.1 Leptons	5
³⁵	1.2.1.2 Quarks	7
³⁶	1.2.2 Fundamental interactions	11
³⁷	1.2.3 Gauge invariance.	15
³⁸	1.2.4 Gauge bosons	17
³⁹	1.3 Electroweak unification and the Higgs mechanism	18
⁴⁰	1.3.1 Spontaneous symmetry breaking (SSB)	26
⁴¹	1.3.2 Higgs mechanism	30
⁴²	1.3.3 Masses of the gauge bosons	33
⁴³	1.3.4 Masses of the fermions	34

44	1.3.5	The Higgs field	35
45	1.3.6	Production of Higgs bosons at LHC	36
46	1.3.7	Higgs boson decay channels	40
47	1.4	Experimental status of the anomalous Higgs-fermion coupling	42
48	1.5	Associated production of a Higgs boson and a single top quark	44
49	1.6	CP-mixing in tH processes	49
50	2	The CMS experiment at the LHC	54
51	2.1	Introduction	54
52	2.2	The LHC	55
53	2.3	The CMS experiment	65
54	2.3.1	CMS coordinate system	68
55	2.3.2	Tracking system	70
56	2.3.3	Silicon strip tracker	73
57	2.3.4	Electromagnetic calorimeter	74
58	2.3.5	Hadronic calorimeter	76
59	2.3.6	Superconducting solenoid magnet	77
60	2.3.7	Muon system	79
61	2.3.8	CMS trigger system	80
62	2.3.9	CMS computing	81
63	3	Event generation, simulation and reconstruction	86
64	3.1	Event generation	87
65	3.2	Monte Carlo Event Generators.	90
66	3.3	CMS detector simulation.	92
67	3.4	Event reconstruction.	94
68	3.4.1	Particle-Flow Algorithm.	94

69	3.4.2 Event reconstruction examples	109
70	5 Statistical methods	112
71	5.1 Multivariate analysis	112
72	5.1.1 Decision trees	116
73	5.1.2 Boosted decision trees (BDT).	119
74	5.1.3 Overtraining	121
75	5.1.4 Variable ranking	122
76	5.1.5 BDT output example	122
77	5.2 Statistical inference	123
78	5.2.1 Nuisance parameters	124
79	5.2.2 Maximum likelihood estimation method	125
80	5.3 Upper limits	126
81	5.4 Asymptotic limits	130
82	6 Search for production of a Higgs boson and a single top quark in multilepton final states in pp collisions at $\sqrt{s} = 13$ TeV	132
84	6.1 Introduction	132
85	6.2 tHq signature	135
86	6.3 Background processes	137
87	6.4 Data and MC Samples	139
88	6.4.1 Full 2016 data set	139
89	6.4.2 Triggers	140
90	6.4.3 MC samples	142
91	6.5 Object Identification	145
92	6.5.1 Lepton reconstruction and identification	145
93	6.5.2 Lepton selection efficiency	153

94	6.5.3 Jets and b -jet tagging	155
95	6.5.4 Missing Energy MET	156
96	6.6 Event selection	157
97	6.7 Background modeling and predictions	159
98	6.7.1 $t\bar{t}V$ and diboson backgrounds	159
99	6.7.2 Non-prompt and charge mis-ID backgrounds	162
100	6.8 Pre-selection yields	166
101	6.9 Signal discrimination	168
102	6.9.1 MVA classifiers evaluation	169
103	6.9.2 Discriminating variables	169
104	6.9.3 BDTG classifiers response	174
105	6.9.4 Additional discriminating variables	175
106	6.9.5 Signal extraction procedure	178
107	6.9.6 Binning and selection optimization	180
108	6.10 Forward jet mismodeling	183
109	6.11 Signal model	185
110	6.12 Systematic uncertainties	188
111	6.13 Results	196
112	6.13.1 CL_S and cross section limits	200
113	6.13.2 Best fit	205
114	6.13.3 Effect of the nuisance parameters	206
115	6.14 CP-mixing in tHq	209
116	7 Phase 1 FPix upgrade modules	214
117	7.1 CMS pixel detector upgrade	215
118	7.2 Phase 1 FPix upgrade	217

119	7.3 FPix module structure	219
120	7.4 FPix module assembly	219
121	7.4.1 Pick and place machine setup	223
122	7.4.2 The gluing routine	248
123	7.4.3 The encapsulation routine	255
124	7.4.4 The FPix module production yields	264
125	A Datasets and triggers	265
126	B Additional plots	269
127	B.1 Pre-selection kinematic variables	269
128	B.2 BDTG input variables for $2lss$ channel	273
129	B.3 Input variables distributions from BDTG classifiers	274
130	B.4 Pulls and impacts	278
131	C Other binning strategies	280
132	D BDTG output variation with κ_V/κ_t	283
133	E $tHq-t\bar{t}H$ overlap	284
134	F Forward jet impact plots	286
135	G Cross sections and Branching ratios scalings	290
136	Bibliography	297
137	References	298

¹³⁸ List of Figures

139	1.1	Standard Model of particle physics.	3
140	1.2	Transformations between quarks	11
141	1.3	Fundamental interactions in nature.	12
142	1.4	SM interactions diagrams	13
143	1.5	Neutral current processes	19
144	1.6	Spontaneous symmetry breaking mechanism	27
145	1.7	SSB Potential form	28
146	1.8	Potential for complex scalar field	29
147	1.9	SSB mechanism for complex scalar field	30
148	1.10	Proton-Proton collision	36
149	1.11	Proton PDFs	37
150	1.12	Higgs boson production mechanism Feynman diagrams	38
151	1.13	Higgs boson production cross section and decay branching ratios	39
152	1.14	κ_t - κ_V plot of the coupling modifiers. ATLAS and CMS combination.	42
153	1.15	Higgs boson production in association with a top quark	45
154	1.16	Cross section for tHq process as a function of κ_t	48
155	1.17	Cross section for tHW process as a function of κ_{Htt}	48
156	1.18	NLO cross section for tX_0 and $t\bar{t}X_0$.	52

157	1.19 NLO cross section for $tWX_0, t\bar{t}X_0$.	53
158	2.1 CERN accelerator complex	55
159	2.2 LHC protons source. First acceleration stage.	56
160	2.3 The LINAC2 accelerating system at CERN.	57
161	2.4 LHC layout and RF cavities module.	58
162	2.5 LHC dipole magnet.	60
163	2.6 Integrated luminosity delivered by LHC and recorded by CMS during 2016	62
164	2.7 LHC interaction points	63
165	2.8 Multiple pp collision bunch crossing at CMS.	65
166	2.9 Layout of the CMS detector	66
167	2.10 CMS detector transverse slice	67
168	2.11 CMS detector coordinate system	69
169	2.12 CMS tracking system schematic view.	70
170	2.13 CMS pixel detector	71
171	2.14 SST Schematic view.	73
172	2.15 CMS ECAL schematic view	75
173	2.16 CMS HCAL schematic view	77
174	2.17 CMS solenoid magnet	78
175	2.18 CMS Muon system schematic view	79
176	2.19 CMS Level-1 trigger architecture	81
177	2.20 WLCG structure	82
178	2.21 Data flow from CMS detector through hardware Tiers	84
179	3.1 Event generation process.	87
180	3.2 Particle flow algorithm.	95
181	3.3 Stable cones identification	102

182	3.4	Jet reconstruction.	104
183	3.5	Jet energy corrections.	106
184	3.6	Secondary vertex in a b-hadron decay.	107
185	3.7	HIG-13-004 Event 1 reconstruction.	109
186	3.8	$e\mu$ event reconstruction.	110
187	3.9	Recorded event reconstruction.	111
188	5.1	Scatter plots-MVA event classification.	114
189	5.2	Scalar test statistical.	115
190	5.3	Decision tree.	116
191	5.4	Decision tree output example.	119
192	5.5	BDT output example.	122
193	5.6	t_r p.d.f. assuming each H_0 and H_1	128
194	5.7	Illustration of the CL_s limit.	129
195	5.8	Example of Brazilian flag plot	130
196	6.1	Analysis strategy workflow	135
197	6.2	tHq event signature	136
198	6.3	$t\bar{t}$ and $t\bar{t}W$ events signature	139
199	6.4	Trigger efficiency for the same-sign $\mu\mu$ category	141
200	6.5	Trigger efficiency for the $e\mu$ category	142
201	6.6	Trigger efficiency for the $3l$ category	143
202	6.7	tHq and tHW cross section in the κ_t - κ_V phase space	143
203	6.8	Tight vs loose lepton selection efficiencies in the $2lss$ channel.	153
204	6.9	Tight vs loose lepton selection efficiencies in the $3l$ channel.	154
205	6.10	Kinematic distributions in the diboson control region.	161
206	6.11	Fake rates	164

207	6.12 Elecron mis-ID probabilities.	165
208	6.13 Discriminating variables for the event pre-selection, $2lss - \mu^\pm\mu^\pm$	167
209	6.14 MVA classifiers performance.	170
210	6.15 BDTG classifier Input variables distributions.	172
211	6.16 BDT input variables. Discrimination against $t\bar{t}$ and $t\bar{t}V$ in $3l$ channel. . .	173
212	6.17 Correlation matrices for the BDT input variables.	174
213	6.18 BDTG classifier response. Default parameters.	175
214	6.19 BDTG classifier output.	176
215	6.20 Additional discriminating variables distributions.	178
216	6.21 2D BDT classifier output planes	179
217	6.22 Binning overlaid on the S/B ratio map on the plane of classifier outputs. .	180
218	6.23 Binning combination scheme.	181
219	6.24 Kinematic distributions for forward jet mismodeling study.	184
220	6.25 Most forward jets η distributions	185
221	6.26 Scaling of the tHq , tHW , and $t\bar{t}H$ production cross section with κ_t/κ_V . .	187
222	6.27 Fake rates closure test.	193
223	6.28 Fake rates closure test in the $3l$ selection.	194
224	6.29 Pre-fit BDT classifier outputs.	196
225	6.30 Pre-fit distributions in the final binning.	197
226	6.31 Post-fit distributions in the final binning.	198
227	6.32 Background-subtracted distributions in the final binning (ITC).	199
228	6.33 Background-subtracted distributions in the final binning (SM)	200
229	6.34 Asymptotic limits on the combined $tH + t\bar{t}H$ $\sigma \times \text{BR}$	202
230	6.35 Asymptotic limits on the combined $tH + t\bar{t}H$ $\sigma \times \text{BR}$, $\kappa_V = 0.5, 1.0, 1.5$. .	203
231	6.36 Observed and a priori expected significance of the fit result.	206
232	6.37 Best fit values of the combined $tH + t\bar{t}H$ $\sigma \times \text{BR}$	207

233	6.38 Post-fit pulls and impacts.	208
234	6.39 Post-fit pulls and impacts for a fit to the Asimov dataset.	209
235	6.40 BDT shape variations for five CP-mixing angles.	211
236	6.41 Asymptotic limits on the combined $tH + t\bar{t}H \sigma \times \text{BR}$ for CP mixing angle.	212
237	6.42 Best fit combined $tH + t\bar{t}H \sigma \times \text{BR}$ as a function of the CP-mixing angle.	213
238	7.1 Expected performance of the previous pixel detector in simulated $t\bar{t}$ events.	216
239	7.2 Layout of the upgraded and old pixel detectors.	217
240	7.3 FPix half disk design.	218
241	7.4 FPix module structure.	220
242	7.5 UNL module assembly work flow.	221
243	7.6 Full gluing and encapsulation setup	223
244	7.7 Bare and full chucks	224
245	7.8 BBM/HDI plate	225
246	7.9 Glue reservoir plate	225
247	7.10 Stamp and Weight tools in chucks	226
248	7.11 Stamp and Weight tools	226
249	7.12 Stamp patterns	227
250	7.13 Test of amount of glue deposited.	228
251	7.14 Glue contact area test.	229
252	7.15 Grabber tool.	230
253	7.16 Pick and place tool.	231
254	7.17 Fiducial marks on tools.	232
255	7.18 Fiducial mark recognition.	233
256	7.19 Setup used to measure the GHCO	234
257	7.20 Scratches scheme if the tool is not straight	235

258	7.21 Dispensing system components.	240
259	7.22 Webcam setup.	241
260	7.23 Webcam setup calibration.	241
261	7.24 Needle tip offset measurement.	242
262	7.25 Wire bond region.	243
263	7.26 Sylgard deposition synchronization.	245
264	7.27 Time delay measurements.	246
265	7.28 Speed function for sylgard deposition.	247
266	7.29 Time delay functions.	247
267	7.30 Gluing routine workflow.	248
268	7.31 Materials used during gluing stage	249
269	7.32 Gluing routine LabVIEW front panel	250
270	7.33 Fiducial finder LabVIEW front panel	252
271	7.34 Fiducial finder step LabVIEW front panel	253
272	7.35 Gluing and pick-and-place LabVIEW front panels	254
273	7.36 Gluing steps pictures.	255
274	7.37 Gluing session report.	256
275	7.38 ROC-HDI wirebonding.	257
276	7.39 Encapsulation workflow.	257
277	7.40 Encapsulation LabVIEW main front panel	259
278	7.41 Encapsulation region.	260
279	7.42 Encapsulation reference positions.	262
280	7.43 Encapsulation results.	264
281	B.1 Input variables to the BDT, $3l$ channel.	270
282	B.2 Input variables to the BDT, $2lss - \mu^\pm\mu^\pm$ channel	271

283	B.3	Input variables to the BDT, $2lss - e^\pm\mu^\pm$ channel	272
284	B.4	Input variables to the BDT, $2lss$ channel	273
285	B.5	BDT input variables. Discrimination against $t\bar{t}$ in $2lss$ channel.	274
286	B.6	BDT input variables. Discrimination against $t\bar{t}V$ in $2lss$ channel.	275
287	B.7	BDT input variables. Discrimination against $t\bar{t}$ in $3l$ channel.	276
288	B.8	BDT input variables. Discrimination against $t\bar{t}V$ in $3l$ channel.	277
289	B.9	Additional post-fit pulls and impacts.	278
290	B.10	Additional post-fit pulls and impacts for a fit to the Asimov dataset.	279
291	C.1	Binning by S/B regions for $2lss$ (left) and $3l$ (right).	280
292	C.2	Final bins (corresponding to S/B regions in the 2D plane)	281
293	C.3	Binning into geometric regions using a k -means algorithm.	282
294	C.4	Final bins using a k -means algorithm.	282
295	D.1	BDTG output variation with κ_V/κ_t	283
296	F.1	Post-fit pulls and impacts with p_T cut 25 GeV for the forward jet	287
297	F.2	Post-fit pulls and impacts with p_T cut 30 GeV for the forward jet	288
298	F.3	Post-fit pulls and impacts with p_T cut 25 GeV for the forward jet	289

²⁹⁹ List of Tables

300	1.1	Fermions of the SM.	4
301	1.2	Fermion masses.	5
302	1.3	Lepton properties.	7
303	1.4	Quark properties.	8
304	1.5	Fermion weak isospin and weak hypercharge multiplets.	9
305	1.6	Fundamental interactions features.	14
306	1.7	SM gauge bosons.	18
307	1.8	Higgs boson properties.	36
308	1.9	Predicted branching ratios for a SM Higgs boson with $m_H = 125 \text{ GeV}/c^2$	41
309	1.10	Predicted SM cross sections for tH production at $\sqrt{s} = 13 \text{ TeV}$	46
310	1.11	Predicted enhancement of the tHq and tHW cross sections at LHC	49
311	6.1	Trigger efficiency scale factors and associated uncertainties.	141
312	6.2	MC signal samples.	144
313	6.3	Effective areas, for electrons and muons.	149
314	6.4	Requirements on each of the three muon selections.	152
315	6.5	Criteria for each of the three electron selections.	152
316	6.6	Summary of event pre-selection.	158
317	6.7	Electron charge mis-ID probabilities.	165

318	6.8	Expected and observed yields for 35.9fb^{-1} after the pre-selection.	166
319	6.9	Signal yields split by decay channels of the Higgs boson.	168
320	6.10	BDTG input variables.	171
321	6.11	Configuration used in the final BDTG training.	175
322	6.12	Input variables ranking for BDTG classifiers	177
323	6.13	ROC-integral for all the testing cases.	177
324	6.14	Selection cuts optimization.	181
325	6.15	Limit variation as a function of bin size, $3l$ channel.	182
326	6.16	Limit variation as a function of bin size, $2lss$ channel.	182
327	6.17	Forward jet Data/MC scale factors.	186
328	6.18	κ_t/κ_V ratios.	189
329	6.19	Pre-fit size of systematic uncertainties.	195
330	6.20	Expected and observed upper limits.	201
331	6.21	Expected and observed 95% C.L. cross section upper limits.	204
332	6.22	Expected and observed CL _S limits on the signal strength.	204
333	6.23	Fit results for the ITC and SM scenarios	205
334	6.24	Best-fit signal strengths for a SM-like Higgs signal.	205
335	6.25	Cross sections for tHq , tHW and $t\bar{t}H$ as a function of $\cos(\alpha_{CP})$	210
336	6.26	Summary of expected and observed upper limits for CP-mixing angles.	213
337	7.1	Values of the needle tip height h (μm) for several combinations of parameters d and θ	244
339	A.1	Full 2016 dataset.	265
340	A.2	HLT paths	266
341	A.3	κ_V and κ_t combinations.	267
342	A.4	List of background samples used in this analysis (CMSSW 80X).	268

343	E.1 Differences in event selection $tHq-t\bar{t}H$ multilepton analysis.	284
344	E.2 Individual and shared event yields $tHq-t\bar{t}H$ multilepton selections.	285
345	G.1 Scalings of Higgs decay branching ratios vs. κ_t and $\kappa_V = 0.5$	291
346	G.2 Scalings of Higgs decay branching ratios vs. κ_t and $\kappa_V = 1.0$	292
347	G.3 Scalings of Higgs decay branching ratios vs. κ_t and $\kappa_V = 1.5$	293
348	G.4 Scalings of $\sigma \times \text{BR}$ for the signal components and $\kappa_V = 0.5$	294
349	G.5 Scalings of $\sigma \times \text{BR}$ for the signal components and $\kappa_V = 1.0$	295
350	G.6 Scalings of $\sigma \times \text{BR}$ for the signal components and $\kappa_V = 1.5$	296
351	G.7 Expected and observed upper limits for CP-mixing angles.	297

³⁵² **Chapter 1**

³⁵³ **Theoretical approach**

³⁵⁴ **1.1 Introduction**

³⁵⁵ The physical description of the universe is a challenge that physicists have faced by
³⁵⁶ making theories that refine existing principles and proposing new ones in an attempt
³⁵⁷ to embrace emerging facts and phenomena.

³⁵⁸ At the end of 1940s Julian Schwinger [1] and Richard P. Feynman [2], based on
³⁵⁹ the work of Sin-Itiro Tomonaga [3], developed an electromagnetic theory consistent
³⁶⁰ with special relativity and quantum mechanics that describes how matter and light
³⁶¹ interact; the so-called *quantum electrodynamics* (QED) was born.

³⁶² QED has become the blueprint for developing theories that describe the universe.
³⁶³ It was the first example of a quantum field theory (QFT), which is the theoretical
³⁶⁴ framework for building quantum mechanical models that describes particles and their
³⁶⁵ interactions. QFT is composed of a set of mathematical tools that combines classical
³⁶⁶ fields, special relativity and quantum mechanics, while keeping the quantum point
³⁶⁷ particles and locality ideas.

³⁶⁸ This chapter gives an overview of the standard model of particle physics, starting

369 with a description of the particles and their interactions, followed by a description of
 370 the electroweak interaction, the Higgs boson and the associated production of Higgs
 371 boson and a single top quark (tH). The description contained in this chapter is based
 372 on References [4–6].

373 1.2 Standard model of particle physics

374 The *standard model of particle physics (SM)* describes particle physics at the funda-
 375 mental level in terms of a collection of interacting particles and fields. The full picture
 376 of the SM is composed of three fields¹ whose excitations are interpreted as particles
 377 called mediators or force-carriers, a set of fields whose excitations are interpreted as
 378 elementary particles interacting through the exchange of those mediators, and a field
 379 that gives the mass to elementary particles. Figure 1.1 shows a scheme of the SM
 380 particles’ organization. In addition, for each of the particles in the scheme there exists
 381 an antiparticle with the same mass and opposite quantum numbers. The existence of
 382 antiparticles is a prediction of the relativistic quantum mechanics from the solution
 383 of the Dirac equation for which a negative energy solution is also possible. In some
 384 cases a particle is its own anti-particle, like photon or Higgs boson.

385 The mathematical formulation of the SM is based on group theory and the use of
 386 Noether’s theorem [8] which states that for a physical system modeled by a Lagrangian
 387 that is invariant under a group of transformations a conservation law is expected. For
 388 instance, a system described by a time-independent Lagrangian is invariant (symmet-
 389 ric) under time changes (transformations) with the total energy conservation law as
 390 the expected conservation law. In QED, the charge operator (Q) is the generator of

¹ The formal and complete treatment of the SM is out of the scope of this document, however a plenty of textbooks describing it at several levels are available in the literature. The treatment in References [5, 6] is quite comprehensive and detailed. Note that gravitational field is not included in the standard model formulation

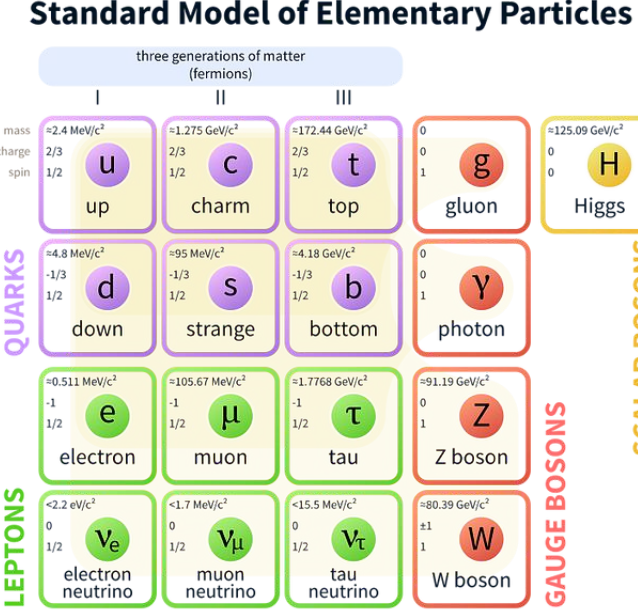


Figure 1.1: Schematic representation of the Standard Model of particle physics. The SM is a theoretical model intended to describe three of the four fundamental forces of the universe in terms of a set of particles and their interactions. [7].

391 the U(1) symmetry which according to the Noether's theorem means that there is a
 392 conserved quantity; this conserved quantity is the electric charge and thus the law
 393 conservation of electric charge is established.

394 In the SM, the symmetry group $SU(3)_C \otimes SU(2)_L \otimes U(1)_Y$ describes three of the
 395 four fundamental interactions in nature (see Section 1.2.2): strong interaction (SI),
 396 weak interaction (WI) and electromagnetic interactions (EI) in terms of symmetries
 397 associated to physical quantities:

- 398 • Strong: $SU(3)_C$ associated to color charge
 399 • Weak: $SU(2)_L$ associated to weak isospin and chirality
 400 • Electromagnetic: $U(1)_Y$ associated to weak hypercharge and electric charge
 401 It will be shown that the electromagnetic and weak interactions are combined in

402 the so-called electroweak interaction where chirality, hypercharge, weak isospin and
 403 electric charge are the central concepts.

404 **1.2.1 Fermions**

405 The basic constituents of the ordinary matter at the lowest level, which form the set
 406 of elementary particles in the SM formulation, are quarks and leptons. All of them
 407 have spin 1/2, therefore they are classified as fermions since they obey Fermi-Dirac
 408 statistics. There are six *flavors* of quarks and three of leptons organized in three
 409 generations, or families, as shown in Table 1.1.

		Generation		
Type		1st	2nd	3rd
Leptons	Charged	Electron (e)	Moun(μ)	Tau (τ)
	Neutral	Electron neutrino (ν_e)	Muon neutrino (ν_μ)	Tau neutrino (ν_τ)
Quarks	Up-type	Up (u)	Charm (c)	Top (t)
	Down-type	Down (d)	Strange (s)	Bottom (b)

Table 1.1: Fermions of the SM. There are six flavors of quarks and three of leptons, organized in three generations, or families, composed of two pairs of closely related particles. The close relationship is motivated by the fact that each pair of particles is a member of an $SU(2)_L$ doublet that has an associated invariance under isospin transformations. WI between leptons is limited to the members of the same generation; WI between quarks is not limited but greatly favored, to same generation members.

410

411 There is a mass hierarchy between generations (see Table 1.2), where the higher
 412 generation particles decays to the lower one, which can explain why the ordinary
 413 matter is made of particles from the first generation. In the SM, neutrinos are modeled
 414 as massless particles so they are not subject to this mass hierarchy; however, today it
 415 is known that neutrinos are massive so the hierarchy could be restated. The reason
 416 behind this mass hierarchy is one of the most important open questions in particle
 417 physics, and it becomes more puzzling when noticing that the mass difference between

418 first and second generation fermions is small compared to the mass difference with
 419 respect to the third generation.

Lepton	Mass (MeV/c ²)	Quark	Mass (MeV/c ²)
e	0.51	u	2.2
μ	105.65	c	1.28×10^3
τ	1776.86	t	173.1×10^3
ν_e	Unknown	d	4.7
ν_μ	Unknown	s	96
τ_μ	Unknown	b	4.18×10^3

Table 1.2: Fermion masses [9]. Generations differ by mass in a way that has been interpreted as a mass hierarchy. Approximate values with no uncertainties are used, for comparison purpose.

420

421 Usually, the second and third generation fermions are produced in high energy
 422 processes, like the ones recreated in particle accelerators.

423 1.2.1.1 Leptons

424 A lepton is an elementary particle that is not subject to the SI. As seen in Table 1.1,
 425 there are two types of leptons, the charged ones (electron, muon and tau) and the
 426 neutral ones (the three neutrinos). The electric charge (Q) is the property that gives
 427 leptons the ability to participate in the EI. From the classical point of view, Q plays
 428 a central role determining, among others, the strength of the electric field through
 429 which the electromagnetic force is exerted. It is clear that neutrinos are not affected
 430 by EI because they don't carry electric charge.

431 Another feature of the leptons that is fundamental in the mathematical description
 432 of the SM is the chirality, which is closely related to spin and helicity. Helicity
 433 defines the handedness of a particle by relating its spin and momentum such that
 434 if they are parallel then the particle is right-handed; if spin and momentum are

435 antiparallel the particle is said to be left-handed. The study of parity conservation
 436 (or violation) in β -decay has shown that only left-handed electrons/neutrinos or right-
 437 handed positrons/anti-neutrinos are created [10]; the inclusion of that feature in the
 438 theory was achieved by using projection operators for helicity, however, helicity is
 439 frame dependent for massive particles which makes it not Lorentz invariant and then
 440 another related attribute has to be used: *chirality*.

441 Chirality is a purely quantum attribute which makes it not so easy to describe in
 442 graphical terms but it defines how the wave function of a particle transforms under
 443 certain rotations. As with helicity, there are two chiral states, left-handed chiral (L)
 444 and right-handed chiral (R). In the highly relativistic limit where $E \approx p \gg m$ helicity
 445 and chirality converge, becoming exactly the same for massless particles.

446 In the following, when referring to left-handed (right-handed) it will mean left-
 447 handed chiral (right-handed chiral). The fundamental fact about chirality is that
 448 while EI and SI are not sensitive to chirality, in WI left-handed and right-handed
 449 fermions are treated asymmetrically, such that only left-handed fermions and right-
 450 handed anti-fermions are allowed to couple to WI mediators, which is a violation of
 451 parity. The way to translate this statement in a formal mathematical formulation is
 452 based on the isospin symmetry group $SU(2)_L$.

453 Each generation of leptons is seen as a weak isospin doublet.² The left-handed
 454 charged lepton and its associated left-handed neutrino are arranged in doublets of
 455 weak isospin $T=1/2$ while their right-handed partners are singlets:

$$\begin{pmatrix} \nu_l \\ l \end{pmatrix}_L, l_R := \begin{pmatrix} \nu_e \\ e \end{pmatrix}_L, \begin{pmatrix} \nu_\mu \\ \mu \end{pmatrix}_L, \begin{pmatrix} \nu_\tau \\ \tau \end{pmatrix}_L, e_R, \mu_R, \tau_R, \nu_{eR}, \nu_{\mu R}, \nu_{\tau R} \quad (1.1)$$

456 The isospin third component refers to the eigenvalues of the weak isospin operator

² The weak isospin is an analogy of the isospin symmetry in strong interaction where neutron and proton are affected equally by strong force but differ in their charge.

457 which for doublets is $T_3 = \pm 1/2$, while for singlets it is $T_3 = 0$. The physical meaning
 458 of this doublet-singlet arrangement falls in that the WI couples the two particles in
 459 the doublet by exchanging the interaction mediator while the singlet member is not
 460 involved in WI. The main properties of the leptons are summarized in Table 1.3.

461 Although all three flavor neutrinos have been observed, their masses remain un-
 462 known and only some estimations have been made [11]. The main reason is that
 463 the flavor eigenstates are not the same as the mass eigenstates which implies that
 464 when a neutrino is created its mass state is a linear combination of the three mass
 465 eigenstates and experiments can only probe the squared difference of the masses. The
 466 Pontecorvo-Maki-Nakagawa-Sakata (PMNS) mixing matrix encodes the relationship
 467 between flavor and mass eigenstates.

Lepton	$Q(e)$	T_3	L_e	L_μ	L_τ	Lifetime (s)
Electron (e)	-1	-1/2	1	0	0	Stable
Electron neutrino(ν_e)	0	1/2	1	0	0	Unknown
Muon (μ)	-1	-1/2	0	1	0	2.19×10^{-6}
Muon neutrino (ν_μ)	0	1/2	0	1	0	Unknown
Tau (τ)	-1	-1/2	0	0	1	290.3×10^{-15}
Tau neutrino (ν_τ)	0	1/2	0	0	1	Unknown

Table 1.3: Lepton properties [9]. Q: electric charge, T_3 : weak isospin. Only left-handed leptons and right-handed anti-leptons participate in the WI. Anti-particles with inverted T_3 , Q and lepton number complete the leptons set but are not listed. Right-handed leptons and left-handed anti-leptons, neither listed, form weak isospin singlets with $T_3 = 0$ and do not take part in the weak interaction.

468

469 1.2.1.2 Quarks

470 Quarks are the basic constituents of protons and neutrons. The way quarks join to
 471 form bound states, called *hadrons*, is through the SI. Quarks are affected by all the
 472 fundamental interactions which means that they carry all the four types of charges:
 473 color, electric charge, weak isospin and mass.

Flavor	$Q(e)$	I_3	T_3	B	C	S	T	B'	Y	Color
Up (u)	2/3	1/2	1/2	1/3	0	0	0	0	1/3	r,b,g
Charm (c)	2/3	0	1/2	1/3	1	0	0	0	4/3	r,b,g
Top(t)	2/3	0	1/2	1/3	0	0	1	0	4/3	r,b,g
Down(d)	-1/3	-1/2	-1/2	1/3	0	0	0	0	1/3	r,b,g
Strange(s)	-1/3	0	-1/2	1/3	0	-1	0	0	-2/3	r,b,g
Bottom(b)	-1/3	0	-1/2	1/3	0	0	0	-1	-2/3	r,b,g

Table 1.4: Quark properties [9]. Q: electric charge, I_3 : isospin, T_3 : weak isospin, B: baryon number, C: charmness, S: strangeness, T: topness, B' : bottomness, Y: hypercharge. Anti-quarks posses the same mass and spin as quarks but all charges (color, flavor numbers) have opposite sign.

474

475 Table 1.4 summarizes the features of quarks, among which the most remarkable
 476 is their fractional electric charge. Note that fractional charge is not a problem, given
 477 that quarks are not found isolated, but serves to explain how composed particles are
 478 formed out of two or more valence quarks³.

479 Color charge is responsible for the SI between quarks and is the symmetry ($SU(3)_C$)
 480 that defines the formalism to describe SI. There are three colors: red (r), blue (b)
 481 and green (g) and their corresponding three anti-colors; thus each quark carries one
 482 color unit while anti-quarks carries one anti-color unit. As explained in Section 1.2.2,
 483 quarks are not allowed to be isolated due to the color confinement effect, hence, their
 484 features have been studied indirectly by observing their bound states created when

- 485 • one quark with a color charge is attracted by an anti-quark with the correspond-
 486 ing anti-color charge forming a colorless particle called a *meson*.

 487 • three quarks (anti-quarks) with different color (anti-color) charges are attracted
 488 among them forming a colorless particle called a *baryon (anti-baryon)*.

³ Hadrons can contain an indefinite number of virtual quarks and gluons, known as the quark and gluon sea, but only the valence quarks determine hadrons' quantum numbers.

489 In practice, when a quark is left alone isolated a process called *hadronization* occurs
 490 where the quark emits gluons (see Section 1.2.4) which eventually will generate new
 491 quark-antiquark pairs and so on; those quarks will recombine to form hadrons that
 492 will decay into leptons. This proliferation of particles looks like a *jet* coming from
 493 the isolated quark. More details about the hadronization process and jet structure
 494 will be given in chapter3.

495 In the first version of the quark model (1964), M. Gell-Mann [12] and G. Zweig
 496 [13, 14] developed a consistent way to classify hadrons according to their properties.
 497 Only three quarks (u, d, s) were involved in a scheme in which all baryons have baryon
 498 number $B=1$ and therefore quarks have $B=1/3$; non-baryons have $B=0$. Baryon
 499 number is conserved in SI and EI which means that single quarks cannot be created
 500 but in pairs $q - \bar{q}$.

501 The scheme organizes baryons in a two-dimensional space (I_3 - Y); Y (hyper-
 502 charge) and I_3 (isospin) are quantum numbers related by the Gell-Mann-Nishijima
 503 formula [15, 16]:

$$Q = I_3 + \frac{Y}{2} \quad (1.2)$$

504 where $Y = B + S + C + T + B'$ are the quantum numbers listed in Table 1.4.

505 There are six quark flavors organized in three generations (see Table 1.1) fol-
 506 lowing a mass hierarchy which, again, implies that higher generations decay to first
 507 generation quarks.

	Quarks			T_3	Y_W	Leptons			T_3	Y_W
Doublets	$(\frac{u}{d'})_L$	$(\frac{c}{s'})_L$	$(\frac{t}{b'})_L$	$(\frac{1/2}{-1/2})$	$1/3$	$(\nu_e)_L$	$(\nu_\mu)_L$	$(\nu_\tau)_L$	$(\frac{1/2}{-1/2})$	-1
Singlets	u_R	c_R	t_R	0	$4/3$	ν_{eR}	$\nu_{\mu R}$	$\nu_{\tau R}$	0	-2

Table 1.5: Fermion weak isospin and weak hypercharge multiplets. Weak hypercharge is calculated through the Gell-Mann-Nishijima formula 1.2 but using the weak isospin and charge for quarks.

508

509 Isospin doublets of quarks are also defined (see Table 1.5), and same as for neutrinos,
 510 the WI eigenstates are not the same as the mass eigenstates which means that
 511 members of different quark generations are connected by the WI mediator; thus, up-
 512 type quarks are coupled not to down-type quarks (the mass eigenstates) directly but
 513 to a superposition of down-type quarks (q'_d ; *the weak eigenstates*) via WI according
 514 to:

$$515 \quad q'_d = V_{CKM} q_d$$

$$\begin{pmatrix} d' \\ s' \\ b' \end{pmatrix} = \begin{pmatrix} V_{ud} & V_{us} & V_{ub} \\ V_{cd} & V_{cs} & V_{cb} \\ V_{td} & V_{ts} & V_{tb} \end{pmatrix} \begin{pmatrix} d \\ s \\ b \end{pmatrix} \quad (1.3)$$

516 where V_{CKM} is known as Cabibbo-Kobayashi-Maskawa (CKM) mixing matrix [17,18]
 517 given by

$$\begin{pmatrix} |V_{ud}| & |V_{us}| & |V_{ub}| \\ |V_{cd}| & |V_{cs}| & |V_{cb}| \\ |V_{td}| & |V_{ts}| & |V_{tb}| \end{pmatrix} = \begin{pmatrix} 0.97427 \pm 0.00015 & 0.22534 \pm 0.00065 & 0.00351^{+0.00015}_{-0.00014} \\ 0.22520 \pm 0.00065 & 0.97344 \pm 0.00016 & 0.0412^{+0.0011}_{-0.0005} \\ 0.00867^{+0.00029}_{-0.00031} & 0.0404^{+0.0011}_{-0.0005} & 0.999146^{+0.000021}_{-0.000046} \end{pmatrix}. \quad (1.4)$$

518 The weak decays of quarks are represented in the diagram of Figure 1.2; again
 519 the CKM matrix plays a central role since it contains the probabilities for the differ-
 520 ent quark decay channels, in particular, note that quark decays are greatly favored
 521 between generation members.

522 CKM matrix is a 3×3 unitary matrix parametrized by three mixing angles and
 523 the *CP-mixing phase*; the latter is the parameter responsible for the Charge-Parity

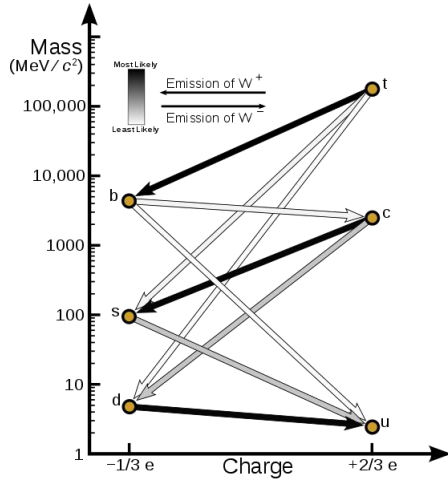


Figure 1.2: Transformations between quarks through the exchange of a WI. Higher generations quarks decay to first generation quarks by emitting a W boson. The arrow color indicates the likelihood of the transition according to the grey scale in the top left side which represent the CKM matrix parameters [19].

524 symmetry violation (CP-violation) in the SM. The fact that the top quark decays
 525 almost all the time to a bottom quark is exploited in this thesis when making the
 526 selection of the signal events by requiring the presence of a jet tagged as a jet coming
 527 from a b quark in the final state.

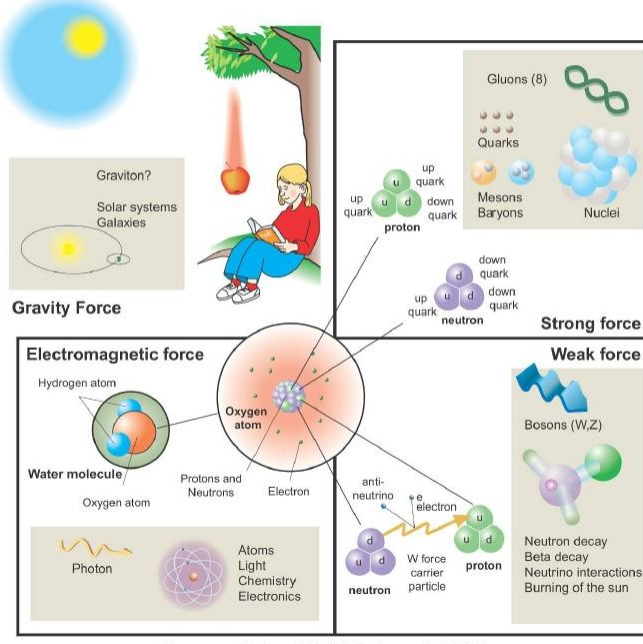
528 1.2.2 Fundamental interactions

529 Even though there are many manifestations of force in nature, like the ones repre-
 530 sented in Figure 1.3, we can classify all of them in four fundamental interactions:

- 531 • *Electromagnetic interaction (EI)* affects particles that are *electrically charged*,
 532 like electrons and protons. Figure 1.4a. shows a graphical representation, known
 533 as *Feynman diagram*, of electron-electron scattering.
- 534 • *Strong interaction (SI)* described by Quantum Chromodynamics (QCD). Hadrons
 535 like the proton and the neutron have internal structure given that they are com-

Fundamental interactions.

Illustration: Typoform



Summer School KPI 15 August 2009

Figure 1.3: Fundamental interactions in nature. Despite the many manifestations of forces in nature, we can track all of them back to one of the fundamental interactions. The most common forces are gravity and electromagnetic given that all of us are subject and experience them in everyday life.

posed of two or more valence quarks⁴. Quarks have fractional electric charge which means that they are subject to electromagnetic interaction and in the case of the proton they should break apart due to electrostatic repulsion; however, quarks are held together inside the hadrons against their electrostatic repulsion by the *Strong Force* through the exchange of *gluons*. The analog to the electric charge is the *color charge*. Electrons and photons are elementary particles as quarks but they don't carry color charge, therefore they are not subject to SI. A Feynman diagram for gluon exchange between quarks is shown in Figure 1.4b.

- *Weak interaction (WI)* described by the weak theory (WT), is responsible, for instance, for the radioactive decay in atoms and the deuterium production

⁴ Particles made of four and five quarks are exotic states not so common.

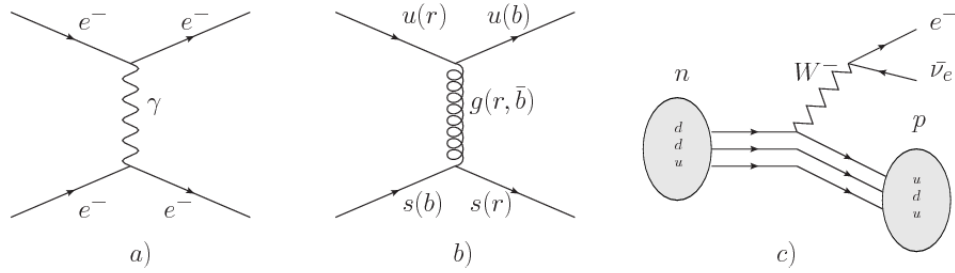


Figure 1.4: Feynman diagrams representing the interactions in SM; a) EI: e - e scattering; b) SI: gluon exchange between quarks ; c) WI: β -decay

within the sun. Quarks and leptons are the particles affected by the weak interaction; they possess a property called *flavor charge* (see 1.2.1) which can be changed by emitting or absorbing one weak force mediator. There are three mediators of the *weak force* known as Z boson in the case of electrically neutral flavor changes and W^\pm bosons in the case of electrically charged flavor changes. The *weak isospin* is the WI analog to electric charge in EI, and color charge in SI, and defines how quarks and leptons are affected by the weak force. Figure 1.4c. shows the Feynman diagram of β -decay where a neutron (n) is transformed in a proton (p) by emitting a W^- particle.

- *Gravitational interaction (GI)* described by General Theory of Relativity (GR). It is responsible for the structure of galaxies and black holes as well as the expansion of the universe. As a classical theory, in the sense that it can be formulated without even appeal to the concept of quantization, it implies that the space-time is a continuum and predictions can be made without limitation to the precision of the measurement tools. The latter represents a direct contradiction of the quantum mechanics principles. Gravity is deterministic while quantum mechanics is probabilistic; despite that, efforts to develop a quantum theory of gravity have predicted the *graviton* as mediator of the gravitational

564 force⁵.

Interaction	Acts on	Relative strength	Range (m)	Mediators
Electromagnetic (QED)	Electrically charged particles	10^{-2}	Infinite	Photon
Strong (QCD)	Quarks and gluons	1	10^{-15}	Gluon
Weak (WI)	Leptons and quarks	10^{-6}	10^{-18}	W^\pm, Z
Gravitational (GI)	Massive particles	10^{-39}	Infinite	Graviton

Table 1.6: Fundamental interactions features [20].

565

566 Table 1.6 summarizes the main features of the fundamental interactions. The
 567 strength of the interactions is represented by the coupling constants which depend
 568 on the energy scale at which the interaction is evaluated, therefore, it is the relative
 569 strength of the fundamental forces that reveals the meaning of strong and weak; in
 570 a context where the relative strength of the SI is 1, the EI is about hundred times
 571 weaker and WI is about million times weaker than the SI. A good description on how
 572 the relative strength and range of the fundamental interactions are calculated can
 573 be found in References [20, 21]. In the everyday life, only EI and GI are explicitly
 574 experienced due to the range of these interactions; i.e., at the human scale distances
 575 only EI and GI have appreciable effects, in contrast to SI which at distances greater
 576 than 10^{-15} m become negligible. Is it important to clarify that the weakness of the
 577 WI is attributed to the fact that its mediators are highly massive which affects the
 578 propagators of the interaction, as a result, the effect of the coupling constant is
 579 reduced.

⁵ Actually a wide variety of theories have been developed in an attempt to describe gravity; some famous examples are string theory and supergravity.

580 **1.2.3 Gauge invariance.**

581 QED was built successfully on the basis of the classical electrodynamics theory (CED)
 582 of Maxwell and Lorentz, following theoretical and experimental requirements imposed
 583 by

- 584 • Lorentz invariance: independence on the reference frame.
- 585 • Locality: interacting fields are evaluated at the same space-time point to avoid
 586 action at a distance.
- 587 • Renormalizability: physical predictions are finite and well defined.
- 588 • Particle spectrum, symmetries and conservation laws already known must emerge
 589 from the theory.
- 590 • Local gauge invariance.

591 The gauge invariance requirement reflects the fact that the fundamental fields
 592 cannot be directly measured but associated fields which are the observables. Electric
 593 (E) and magnetic (B) fields in CED are associated with the electric scalar potential
 594 V and the vector potential \mathbf{A} . In particular, \mathbf{E} can be obtained by measuring the
 595 change in the space of the scalar potential (ΔV); however, two scalar potentials
 596 differing by a constant f correspond to the same electric field. The same happens
 597 in the case of the vector potential \mathbf{A} ; thus, different configurations of the associated
 598 fields result in the same set of values of the observables. The freedom in choosing one
 599 particular configuration is known as *gauge freedom*; the transformation law connecting
 600 two configurations is known as *gauge transformation* and the fact that the observables
 601 are not affected by a gauge transformation is called *gauge invariance*.

602 When the gauge transformation:

$$\begin{aligned} \mathbf{A} &\rightarrow \mathbf{A} - \Delta f \\ V &\rightarrow V - \frac{\partial f}{\partial t} \end{aligned} \tag{1.5}$$

603 is applied to Maxwell equations, they are still satisfied and the fields remain invariant.
 604 Thus, CED is invariant under gauge transformations and is called a *gauge theory*.
 605 The set of all gauge transformations form the *symmetry group* of the theory, which
 606 according to the group theory, has a set of *group generators*. The number of group
 607 generators determine the number of *gauge fields* of the theory.

608 As mentioned in the first lines of Section 1.2, QED has one symmetry group ($U(1)$)
 609 with one group generator (the Q operator) and one gauge field (the electromagnetic
 610 field A^μ). In CED there is not a clear definition, beyond the historical convention,
 611 of which fields are the fundamental and which are the associated, but in QED the
 612 fundamental field is A^μ . When a gauge theory is quantized, the gauge fields are
 613 quantized and their quanta are called *gauge bosons*. The word boson characterizes
 614 particles with integer spin which obey Bose-Einstein statistics.

615 As will be detailed in Section 1.3, interactions between particles in a system can
 616 be obtained by considering first the Lagrangian density of free particles in the sys-
 617 tem, which of course is incomplete because the interaction terms have been left out,
 618 and demanding global phase transformation invariance. Global phase transforma-
 619 tion means that a gauge transformation is performed identically to every point
 620 in the space⁶ and the Lagrangian remains invariant. Then, the global transforma-
 621 tion is promoted to a local phase transformation (this time the gauge transforma-
 622 tion depends on the position in space) and again invariance is required.

⁶ Here space corresponds to the 4-dimensional space i.e. space-time.

623 Due to the space dependence of the local transformation, the Lagrangian density is
 624 not invariant anymore. In order to reinstate the gauge invariance, the gauge covariant
 625 derivative is introduced in the Lagrangian and with it the gauge field responsible for
 626 the interaction between particles in the system. The new Lagrangian density is gauge
 627 invariant, includes the interaction terms needed to account for the interactions and
 628 provides a way to explain the interaction between particles through the exchange of
 629 the gauge boson.

630 This recipe was used to build QED and the theories that aim to explain the
 631 fundamental interactions.

632 1.2.4 Gauge bosons

633 The importance of the gauge bosons comes from the fact that they are the force
 634 mediators or force carriers. The features of the gauge bosons reflect those of the fields
 635 they represent and they are extracted from the Lagrangian density used to describe
 636 the interactions. In Section 1.3, it will be shown how the gauge bosons of the EI and
 637 WI emerge from the electroweak Lagrangian. The SI gauge bosons features are also
 638 extracted from the SI Lagrangian but it is not detailed in this document. The main
 639 features of the SM gauge bosons will be briefly presented below and summarized in
 640 Table 1.7.

- 641 • **Photon.** EI occurs when the photon couples to (is exchanged between) parti-
 642 cles carrying electric charge; however, The photon itself does not carry electric
 643 charge, therefore, there is no coupling between photons. Given that the photon
 644 is massless the EI is of infinite range, i.e., electrically charged particles interact
 645 even if they are located far away one from each other; this also implies that
 646 photons always move with the speed of light.

- 647 • **Gluon.** SI is mediated by gluons which just as photons are massless. They
 648 carry one unit of color charge and one unit of anticolor charge, hence, gluons
 649 can couple to other gluons. As a result, the range of the SI is not infinite
 650 but very short due to the attraction between gluons, giving rise to the *color*
 651 *confinement* which explains why color charged particles cannot be isolated but
 652 live within composite particles, like quarks inside protons.
- 653 • **W, Z.** W^\pm and Z, are massive which explains their short-range. Given that
 654 the WI is the only interaction that can change the flavor of the interacting
 655 particles, the W boson is the responsible for the nuclear transmutation where
 656 a neutron is converted into a proton or vice versa with the involvement of an
 657 electron and a neutrino (see Figure 1.4c). The Z boson is the responsible for the
 658 neutral weak processes like neutrino elastic scattering where no electric charge
 659 but momentum transference is involved. WI gauge bosons carry isospin charge
 660 which makes interaction between them possible.

Interaction	Mediator	Electric charge (e)	Color charge	Weak Isospin	mass (GeV/c ²)
Electromagnetic	Photon (γ)	0	No	0	0
Strong	Gluon (g)	0	Yes -octet	No	0
Weak	W^\pm	± 1	No	± 1	80.385 ± 0.015
	Z	0	No	0	91.188 ± 0.002

Table 1.7: SM gauge bosons main features [9].

661

662 **1.3 Electroweak unification and the Higgs 663 mechanism**

664 Physicists dream of building a theory that contains all the interactions in one single
 665 interaction, i.e., showing that at some scale in energy all the four fundamental inter-

666 actions are unified and only one interaction emerges in a *Theory of everything*. The
 667 first sign of the feasibility of such unification came from success in the construction
 668 of the CED. Einstein spent years trying to reach that full unification, which by 1920
 669 only involved electromagnetism and gravity, with no success; however, a new par-
 670 tial unification was achieved in the 1960's, when S.Glashow [22], A.Salam [23] and
 671 S.Weinberg [24] independently proposed that electromagnetic and weak interactions
 672 are two manifestations of a more general interaction called *electroweak interaction*
 673 (*EWI*). EWI was developed by following the useful prescription provided by QED
 674 and the gauge invariance principles.

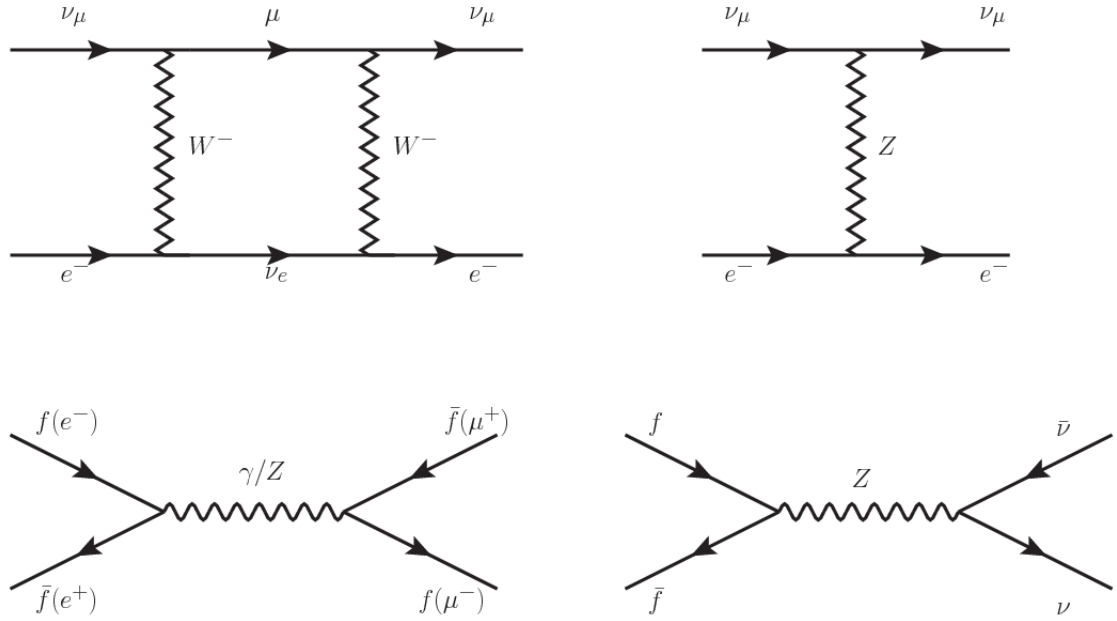


Figure 1.5: Top: $\nu_\mu - e^-$ scattering going through charged currents (left) and neutral currents (right). Bottom: neutral current processes for charged fermions (left) and involving neutrinos (right). While neutral current processes involving only charged fermions can proceed through EI or WI, those involving neutrinos can only proceed via WI.

675 The *classic* weak theory developed by Fermi, did not have the concept of the W
 676 boson but instead it was treated as a point interaction with the dimensionful constant
 677 G_F associated with it. It works really well at low energies very far off the W mass

678 shell. When going up in energy, the theory of weak interactions involving the W
 679 boson is capable of explaining the β -decay and in general the processes mediated by
 680 W^\pm bosons. However, there were some processes like the $\nu_\mu - e$ scattering which
 681 would require the exchange of two W bosons (see Figure 1.5 top diagrams) giving
 682 rise to divergent loop integrals and then non-finite predictions. The EWI theory, by
 683 including neutral currents involving fermions via the exchange of a neutral bosons Z,
 684 overcomes those divergences and the predictions become realistic.

685 Neutral weak interaction vertices conserve flavor in the same way as the electro-
 686 magnetic vertices do, but additionally, the Z boson can couple to neutrinos which
 687 implies that processes involving charged fermions can proceed through EI or WI but
 688 processes involving neutrinos can proceed only through WI.

689 The prescription to build a gauge theory of the WI consists of proposing a free
 690 field Lagrangian density that includes the particles involved; next, by requesting
 691 invariance under global phase transformations first and generalizing to local phase
 692 transformations invariance later, the conserved currents are identified and interactions
 693 are generated by introducing gauge fields. Given that the goal is to include the EI
 694 and WI in a single theory, the group symmetry considered should be a combination of
 695 $SU(2)_L$ and $U(1)_{em}$, however the latter cannot be used directly because the EI treats
 696 left and right-handed particles indistinctly in contrast to the former. Fortunately, the
 697 weak hypercharge, which is a combination of the weak isospin and the electric charge
 698 (Eqn. 1.2) is suitable to be used since it is conserved by the EI and WI. Thus, the
 699 symmetry group to be considered is

$$G \equiv SU(2)_L \otimes U(1)_Y \quad (1.6)$$

700 The following treatment applies to any of the fermion generations, but for sim-

701 plicity the first generation of leptons will be considered [5, 6, 25, 26].

702 Given the first generation of leptons

$$\psi_1 = \begin{pmatrix} \nu_e \\ e^- \end{pmatrix}_L, \quad \psi_2 = \nu_{eR}, \quad \psi_3 = e_R^- \quad (1.7)$$

703 the charged fermionic currents are given by

$$J_\mu \equiv J_\mu^+ = \bar{\nu}_{eL} \gamma_\mu e_L, \quad J_\mu^\dagger \equiv J_\mu^- = \bar{e}_L \gamma_\mu \nu_{eL} \quad (1.8)$$

704 and the free Lagrangian is given by

$$\mathcal{L}_0 = \sum_{j=1}^3 i\bar{\psi}_j(x) \gamma^\mu \partial_\mu \psi_j(x). \quad (1.9)$$

705 Mass terms are included directly in the QED free Lagrangians since they preserve
 706 the invariance under the symmetry transformations involved which treat left and right
 707 handed particles similarly, however mass terms of the form

$$m_W^2 W_\mu^\dagger(x) W^\mu(x) + \frac{1}{2} m_Z^2 Z_\mu(x) Z^\mu(x) - m_e \bar{\psi}_e(x) \psi_e(x) \quad (1.10)$$

708 which represent the mass of W^\pm , Z and electrons, are not invariant under G trans-
 709 formations, therefore the gauge fields described by the EWI are in principle massless.

710 Experiments have shown that the EWI gauge fields are not massless [27–30];
 711 however, they have to acquire mass through a mechanism compatible with the gauge
 712 invariance; that mechanism is known as the *Higgs mechanism* and will be considered
 713 later in this Section. The global transformations in the combined symmetry group G
 714 can be written as

$$\begin{aligned}
\psi_1(x) &\xrightarrow{G} \psi'_1(x) \equiv U_Y U_L \psi_1(x), \\
\psi_2(x) &\xrightarrow{G} \psi'_2(x) \equiv U_Y \psi_2(x), \\
\psi_3(x) &\xrightarrow{G} \psi'_3(x) \equiv U_Y \psi_3(x)
\end{aligned} \tag{1.11}$$

715 where U_L represent the $SU(2)_L$ transformation acting only on the weak isospin dou-
 716 blet and U_Y represent the $U(1)_Y$ transformation acting on all the weak isospin mul-
 717 tiplets. Explicitly

$$U_L \equiv \exp\left(i \frac{\sigma_i}{2} \alpha^i\right), \quad U_Y \equiv \exp(i y_i \beta) \quad (i = 1, 2, 3) \tag{1.12}$$

718 with σ_i the Pauli matrices and y_i the weak hypercharges. In order to promote the
 719 transformations from global to local while keeping the invariance, it is required that
 720 $\alpha^i = \alpha^i(x)$, $\beta = \beta(x)$ and the replacement of the ordinary derivatives by the covariant
 721 derivatives

$$\begin{aligned}
D_\mu \psi_1(x) &\equiv \left[\partial_\mu + ig\sigma_i W_\mu^i(x)/2 + ig'y_1 B_\mu(x) \right] \psi_1(x) \\
D_\mu \psi_2(x) &\equiv \left[\partial_\mu + ig'y_2 B_\mu(x) \right] \psi_2(x) \\
D_\mu \psi_3(x) &\equiv \left[\partial_\mu + ig'y_3 B_\mu(x) \right] \psi_3(x)
\end{aligned} \tag{1.13}$$

722 introducing in this way four gauge fields, $W_\mu^i(x)$ and $B_\mu(x)$, in the process. The
 723 covariant derivatives (Eqn. 1.13) are required to transform in the same way as fermion
 724 fields $\psi_i(x)$ themselves, therefore, the gauge fields transform as:

$$\begin{aligned} B_\mu(x) &\xrightarrow{G} B'_\mu(x) \equiv B_\mu(x) - \frac{1}{g'} \partial_\mu \beta(x) \\ W_\mu^i(x) &\xrightarrow{G} W_\mu^{i\prime}(x) \equiv W_\mu^i(x) - \frac{i}{g} \partial_\mu \alpha_i(x) - \varepsilon_{ijk} \alpha_i(x) W_\mu^j(x). \end{aligned} \quad (1.14)$$

725 The G invariant version of the Lagrangian density 1.9 can be written as

$$\mathcal{L}_0 = \sum_{j=1}^3 i \bar{\psi}_j(x) \gamma^\mu D_\mu \psi_j(x) \quad (1.15)$$

726 where free massless fermion and gauge fields and fermion-gauge boson interactions
 727 are included. The EWI Lagrangian density must additionally include kinetic terms
 728 for the gauge fields (\mathcal{L}_G) which are built from the field strengths, according to

$$B_{\mu\nu}(x) \equiv \partial_\mu B_\nu - \partial_\nu B_\mu \quad (1.16)$$

$$W_{\mu\nu}^i(x) \equiv \partial_\mu W_\nu^i(x) - \partial_\nu W_\mu^i(x) - g \varepsilon^{ijk} W_\mu^j W_\nu^k \quad (1.17)$$

729 the last term in Eqn. 1.17 is added in order to hold the gauge invariance; therefore,

$$\mathcal{L}_G = -\frac{1}{4} B_{\mu\nu}(x) B^{\mu\nu}(x) - \frac{1}{4} W_{\mu\nu}^i(x) W_i^{\mu\nu}(x) \quad (1.18)$$

730 which contains not only the free gauge fields contributions, but also the gauge fields
 731 self-interactions and interactions among them.

732 The three weak isospin conserved currents resulting from the $SU(2)_L$ symmetry
 733 are given by

$$J_\mu^i(x) = \frac{1}{2} \bar{\psi}_1(x) \gamma_\mu \sigma^i \psi_1(x) \quad (1.19)$$

734 while the weak hypercharge conserved current resulting from the $U(1)_Y$ symmetry is
 735 given by

$$J_\mu^Y = \sum_{j=1}^3 \bar{\psi}_j(x) \gamma_\mu y_j \psi_j(x) \quad (1.20)$$

736 In order to evaluate the electroweak interactions modeled by an isos triplet field
 737 W_μ^i that couples to isospin currents J_μ^i with strength g and additionally the singlet
 738 field B_μ which couples to the weak hypercharge current J_μ^Y with strength $g'/2$. The
 739 interaction Lagrangian density to be considered is

$$\mathcal{L}_I = -g J^{i\mu}(x) W_\mu^i(x) - \frac{g'}{2} J^{Y\mu}(x) B_\mu(x) \quad (1.21)$$

740 Note that the weak isospin currents are not the same as the charged fermionic cur-
 741 rents that were used to describe the WI (Eqn. 1.8), since the weak isospin eigenstates
 742 are not the same as the mass eigenstates, but they are closely related

$$J_\mu = \frac{1}{2}(J_\mu^1 + iJ_\mu^2), \quad J_\mu^\dagger = \frac{1}{2}(J_\mu^1 - iJ_\mu^2). \quad (1.22)$$

743 The same happens with the gauge fields W_μ^i which are related to the mass eigen-
 744 states W^\pm by

$$W_\mu^+ = \frac{1}{\sqrt{2}}(W_\mu^1 - iW_\mu^2), \quad W_\mu^- = \frac{1}{\sqrt{2}}(W_\mu^1 + iW_\mu^2). \quad (1.23)$$

745 The fact that there are three weak isospin conserved currents is an indication that
 746 in addition to the charged fermionic currents, which couple charged to neutral leptons,
 747 there should be a neutral fermionic current that does not involve electric charge
 748 exchange; therefore, it couples neutral fermions or fermions of the same electric charge.
 749 The third weak isospin current contains a term that is similar to the electromagnetic

750 current (j_μ^{em}), indicating that there is a relation between them and resembling the
 751 Gell-Mann-Nishijima formula 1.2 adapted to electroweak interactions

$$Q = T_3 + \frac{Y_W}{2}. \quad (1.24)$$

752 Just as Q generates the $U(1)_{em}$ symmetry, the weak hypercharge generates the
 753 $U(1)_Y$ symmetry as said before. It is possible to write the relationship in terms of
 754 the currents as

$$j_\mu^{em} = J_\mu^3 + \frac{1}{2} J_\mu^Y. \quad (1.25)$$

755 The neutral gauge fields W_μ^3 and B_μ cannot be directly identified with the Z
 756 and the photon fields since the photon interacts similarly with left and right-handed
 757 fermions; however, they are related through a linear combination given by

$$\begin{aligned} A_\mu &= B_\mu \cos \theta_W + W_\mu^3 \sin \theta_W \\ Z_\mu &= -B_\mu \sin \theta_W + W_\mu^3 \cos \theta_W \end{aligned} \quad (1.26)$$

where θ_W is known as the *Weinberg angle*. The interaction Lagrangian is now given by

$$\begin{aligned} \mathcal{L}_I = -\frac{g}{\sqrt{2}}(J^\mu W_\mu^+ + J^{\mu\dagger} W_\mu^-) - &\left(g \sin \theta_W J_\mu^3 + g' \cos \theta_W \frac{J_\mu^Y}{2}\right) A^\mu \\ &- \left(g \cos \theta_W J_\mu^3 - g' \sin \theta_W \frac{J_\mu^Y}{2}\right) Z^\mu \end{aligned} \quad (1.27)$$

758 the first term is the weak charged current interaction, while the second term is the

759 electromagnetic interaction under the condition

$$g \sin \theta_W = g' \cos \theta_W = e, \quad \frac{g'}{g} = \tan \theta_W \quad (1.28)$$

760 contained in the Eqn.1.25; the third term is the neutral weak current.

761

762 Note that the neutral fields transformation given by the Eqn. 1.26 can be written
 763 in terms of the coupling constants g and g' as:

$$A_\mu = \frac{g' W_\mu^3 + g B_\mu}{\sqrt{g^2 + g'^2}}, \quad Z_\mu = \frac{g W_\mu^3 - g' B_\mu}{\sqrt{g^2 + g'^2}}. \quad (1.29)$$

764 So far, the Lagrangian density describing the non-massive EWI is:

$$\mathcal{L}_{nmEWI} = \mathcal{L}_0 + \mathcal{L}_G \quad (1.30)$$

765 where fermion and gauge fields have been considered massless because their regular
 766 mass terms are manifestly non invariant under G transformations; therefore, masses
 767 have to be generated in a gauge invariant way. The mechanism by which this goal is
 768 achieved is known as the *Higgs mechanism* and is closely connected to the concept of
 769 *spontaneous symmetry breaking*.

770 1.3.1 Spontaneous symmetry breaking (SSB)

771 Figure 1.6 left shows a steel nail (top) which is subject to an external force; the form
 772 of the potential energy is also shown (bottom).

773 Before reaching the critical force value, the system has rotational symmetry with
 774 respect to the nail axis; however, after the critical force value is reached the nail buck-

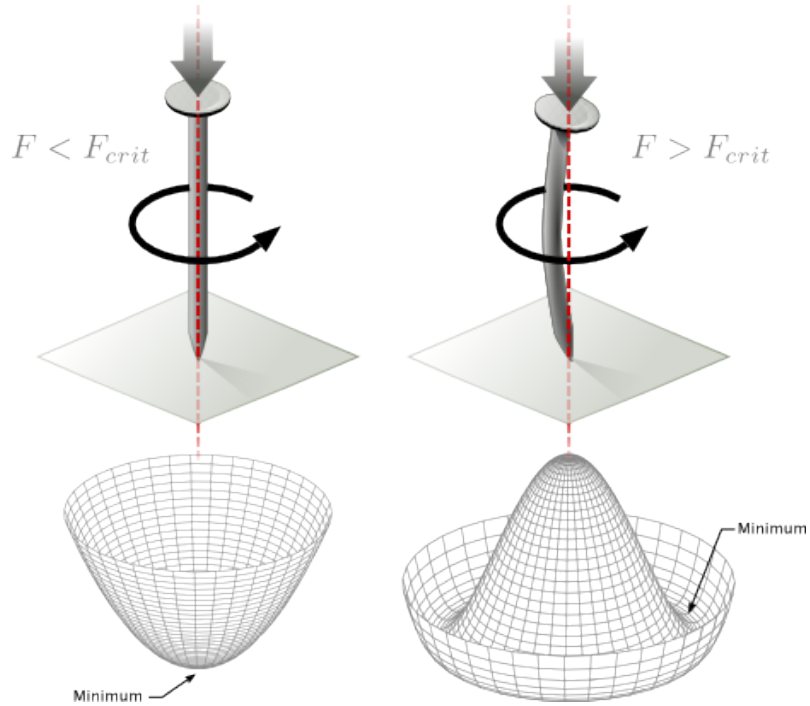


Figure 1.6: Spontaneous symmetry breaking mechanism. The steel nail, subject to an external force (top left), has rotational symmetry with respect to its axis. When the external force overcomes a critical value the nail buckles (top right) choosing a minimal energy state (ground state) and thus *breaking spontaneously the rotational symmetry*. The potential energy (bottom) changes but holds the rotational symmetry; however, an infinite number of asymmetric ground states are generated and circularly distributed in the bottom of the potential [31].

775 les (top right). The form of the potential energy (bottom right) changes appearing a
 776 set of infinity minima but preserving its rotational symmetry. Right before the nail
 777 buckles there is no indication of the direction the nail will bend because any of the
 778 directions are equivalent, but once the nail bends, choosing a direction, an arbitrary
 779 minimal energy state (ground state) is selected and it does not share the system's
 780 rotational symmetry. This mechanism for reaching an asymmetric ground state is
 781 known as *spontaneous symmetry breaking*.

782 The lesson from this analysis is that the way to introduce the SSB mechanism
 783 into a system is by adding the appropriate potential to it.

784 Figure 1.7 shows a plot of the potential $V(\phi)$ in the case of a scalar field ϕ

$$V(\phi) = \mu^2 \phi^\dagger \phi + \lambda (\phi^\dagger \phi)^2 \quad (1.31)$$

If $\mu^2 > 0$ the potential has only one minimum at $\phi = 0$ and describes a scalar field with mass μ . If $\mu^2 < 0$ the potential has a local maximum at $\phi = 0$ and two minima at $\phi = \pm\sqrt{-\mu^2/\lambda}$ which enables the SSB mechanism to work.

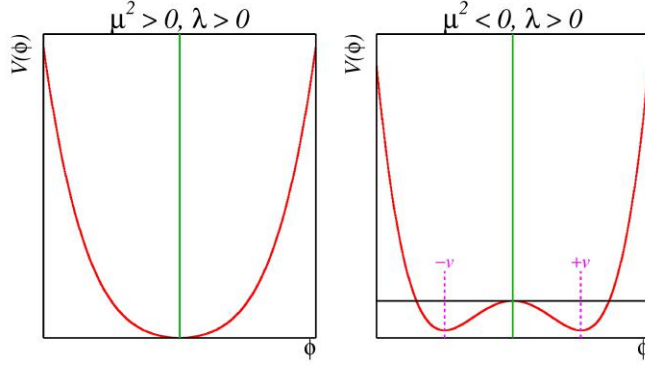


Figure 1.7: Shape of the potential $V(\phi)$ for $\lambda > 0$ and: $\mu^2 > 0$ (left) and $\mu^2 < 0$ (right). The case $\mu^2 < 0$ corresponds to the potential suitable for introducing the SSB mechanism by choosing one of the two ground states which are connected via reflection symmetry. [31].

In the case of a complex scalar field $\phi(x)$

$$\phi(x) = \frac{1}{\sqrt{2}}(\phi_1 + i\phi_2) \quad (1.32)$$

the Lagrangian (invariant under global $U(1)$ transformations) is given by

$$\mathcal{L} = (\partial_\mu \phi)^\dagger (\partial^\mu \phi) - V(\phi), \quad V(\phi) = \mu^2 \phi^\dagger \phi + \lambda (\phi^\dagger \phi)^2 \quad (1.33)$$

where an appropriate potential has been added in order to introduce the SSB.

As seen in Figure 1.8, the potential has now an infinite number of minima circularly distributed along the ξ -direction which makes possible the occurrence of the SSB by choosing an arbitrary ground state; for instance, $\xi = 0$, i.e. $\phi_1 = v, \phi_2 = 0$

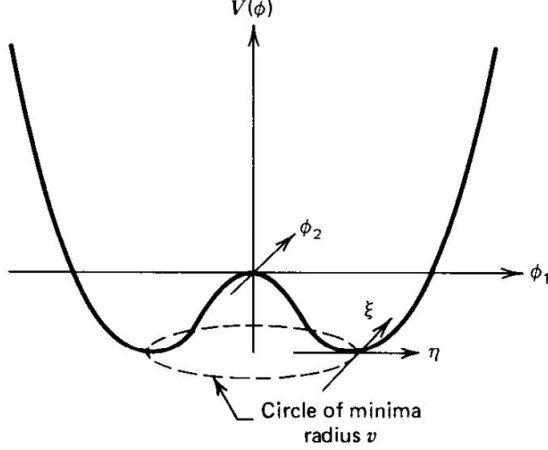


Figure 1.8: Potential for complex scalar field. There is a circle of minima of radius v along the ξ -direction [6].

$$\phi_0 = \frac{v}{\sqrt{2}} \exp(i\xi) \quad \xrightarrow{\text{SSB}} \quad \phi_0 = \frac{v}{\sqrt{2}} \quad (1.34)$$

794 As usual, excitations over the ground state are studied by making an expansion
795 about it; thus, the excitations can be parametrized as:

$$\phi(x) = \frac{1}{\sqrt{2}}(v + \eta(x) + i\xi(x)) \quad (1.35)$$

796 which when substituted into Eqn. 1.33 produces a Lagrangian in terms of the new
797 fields η and ξ

$$\mathcal{L}' = \frac{1}{2}(\partial_\mu \xi)^2 + \frac{1}{2}(\partial_\mu \eta)^2 + \mu^2 \eta^2 - V(\phi_0) - \lambda v \eta (\eta^2 + \xi^2) - \frac{\lambda}{4}(\eta^2 + \xi^2)^2 \quad (1.36)$$

798 where the last two terms represent the interactions and self-interaction between the
799 two fields η and ξ . The particular feature of the SSB mechanism is revealed when
800 looking to the first three terms of \mathcal{L}' . Before the SSB, only the massless ϕ field is

801 present in the system; after the SSB there are two fields of which the η -field has
 802 acquired mass $m_\eta = \sqrt{-2\mu^2}$ while the ξ -field is still massless (see Figure 1.9).

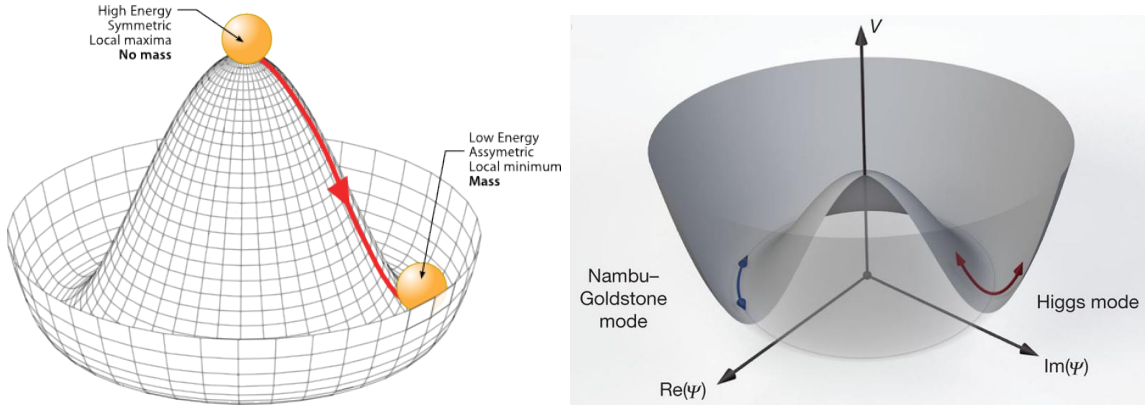


Figure 1.9: SSB mechanism for a complex scalar field [31, 32].

803 Thus, *the SSB mechanism serves as a method to generate mass but as a side ef-
 804 fect a massless field is introduced in the system.* This fact is known as the Goldstone
 805 theorem and states that a massless scalar field appears in the system for each con-
 806 tinuous symmetry spontaneously broken. Another version of the Goldstone theorem
 807 states that “*if a Lagrangian is invariant under a continuous symmetry group G, but*
 808 *the vacuum is only invariant under a subgroup H ⊂ G, then there must exist as many*
 809 *massless spin-0 particles (Nambu-Goldstone bosons) as broken generators.*” [26] The
 810 Nambu-Goldstone boson can be understood considering that the potential in the ξ -
 811 direction is flat so excitations in that direction are not energy consuming and thus
 812 represent a massless state.

813 1.3.2 Higgs mechanism

814 When the SSB mechanism is introduced in the formulation of the EWI in an attempt
 815 to generate the mass of the so far massless gauge bosons and fermions, an interesting
 816 effect is revealed. In order to keep the G symmetry group invariance and generate

817 the mass of the EW gauge bosons, a G invariant Lagrangian density (\mathcal{L}_S) has to be
 818 added to the non massive EWI Lagrangian (Eqn. 1.30)

$$\mathcal{L}_S = (D_\mu \phi)^\dagger (D^\mu \phi) - \mu^2 \phi^\dagger \phi - \lambda (\phi^\dagger \phi)^2, \quad \lambda > 0, \mu^2 < 0 \quad (1.37)$$

$$D_\mu \phi = \left(i\partial_\mu - g \frac{\sigma_i}{2} W_\mu^i - g' \frac{Y}{2} B_\mu \right) \phi \quad (1.38)$$

819 ϕ has to be an isospin doublet of complex scalar fields so it preserves the G invariance;
 820 thus ϕ can be defined as:

$$\phi = \begin{pmatrix} \phi^+ \\ \phi^0 \end{pmatrix} \equiv \frac{1}{\sqrt{2}} \begin{pmatrix} \phi_1 + i\phi_2 \\ \phi_3 + i\phi_4 \end{pmatrix}. \quad (1.39)$$

821 The minima of the potential are defined by

$$\phi^\dagger \phi = \frac{1}{2} (\phi_1^2 + \phi_2^2 + \phi_3^2 + \phi_4^2) = -\frac{\mu^2}{2\lambda}. \quad (1.40)$$

822 The choice of the ground state is critical. By choosing a ground state, invariant
 823 under $U(1)_{em}$ gauge symmetry, the photon will remain massless and the W^\pm and Z
 824 bosons masses will be generated which is exactly what is needed. In that sense, the
 825 best choice corresponds to a weak isospin doublet with $T_3 = -1/2$, $Y_W = 1$ and $Q = 0$
 826 which defines a ground state with $\phi_1 = \phi_2 = \phi_4$ and $\phi_3 = v$:

$$\phi_0 \equiv \frac{1}{\sqrt{2}} \begin{pmatrix} 0 \\ v \end{pmatrix}, \quad v^2 \equiv -\frac{\mu^2}{\lambda}. \quad (1.41)$$

827 where the vacuum expectation value v is fixed by the Fermi coupling G_F according
 828 to $v = (\sqrt{2}G_F)^{1/2} \approx 246$ GeV.

829 The G symmetry has been broken and three Nambu-Goldstone bosons will appear.

830 The next step is to expand ϕ about the chosen ground state as:

$$\phi(x) = \frac{1}{\sqrt{2}} \exp\left(\frac{i}{v} \sigma_i \theta^i(x)\right) \begin{pmatrix} 0 \\ v + H(x) \end{pmatrix} \approx \frac{1}{\sqrt{2}} \begin{pmatrix} \theta_1(x) + i\theta_2(x) \\ v + H(x) - i\theta_3(x) \end{pmatrix} \quad (1.42)$$

831 to describe fluctuations from the ground state ϕ_0 . The fields $\theta_i(x)$ represent the
 832 Nambu-Goldstone bosons while $H(x)$ is known as *Higgs field*. The fundamental fea-
 833 ture of the parametrization used is that the dependence on the $\theta_i(x)$ fields is factored
 834 out in a global phase that can be eliminated by taking the physical *unitary gauge*
 835 $\theta_i(x) = 0$. Therefore the expansion about the ground state is given by:

$$\phi(x) \frac{1}{\sqrt{2}} \begin{pmatrix} 0 \\ v + H(x) \end{pmatrix} \quad (1.43)$$

836 which when substituted into \mathcal{L}_S (Eqn. 1.37) results in a Lagrangian containing the
 837 now massive three gauge bosons W^\pm, Z , one massless gauge boson (photon) and
 838 the new Higgs field (H). The three degrees of freedom corresponding to the Nambu-
 839 Goldstone bosons are now integrated into the massive gauge bosons as their lon-
 840 gitudinal polarizations which were not available when they were massless particles.
 841 The effect by which vector boson fields acquire mass after an spontaneous symmetry
 842 breaking, but without an explicit gauge invariance breaking is known as the *Higgs*
 843 *mechanism*.

844 The mechanism was proposed by three independent groups: F.Englert and R.Brout
 845 in August 1964 [33], P.Higgs in October 1964 [34] and G.Guralnik, C.Hagen and
 846 T.Kibble in November 1964 [35]; however, its importance was not realized until
 847 S.Glashow [22], A.Salam [23] and S.Weinberg [24], independently, proposed that elec-
 848 tromagnetic and weak interactions are two manifestations of a more general interac-
 849 tion called *electroweak interaction* in 1967.

850 **1.3.3 Masses of the gauge bosons**

851 The masses of the gauge bosons are extracted by evaluating the kinetic part of La-
 852 grangian \mathcal{L}_S in the ground state (known also as the vacuum expectation value), i.e.,

$$\left| \left(\partial_\mu - ig \frac{\sigma_i}{2} W_\mu^i - i \frac{g'}{2} B_\mu \right) \phi_0 \right|^2 = \left(\frac{1}{2} v g \right)^2 W_\mu^+ W^{-\mu} + \frac{1}{8} v^2 (W_\mu^3, B_\mu) \begin{pmatrix} g^2 & -gg' \\ -gg' & g'^2 \end{pmatrix} \begin{pmatrix} W^{3\mu} \\ B^\mu \end{pmatrix} \quad (1.44)$$

853 comparing with the typical mass term for a charged boson $M_W^2 W^+ W^-$

$$M_W = \frac{1}{2} v g. \quad (1.45)$$

The second term in the right side of the Eqn.1.44 comprises the masses of the neutral bosons, but it needs to be written in terms of the gauge fields Z_μ and A_μ in order to be compared to the typical mass terms for neutral bosons, therefore using Eqn. 1.29

$$\begin{aligned} \frac{1}{8} v^2 [g^2 (W_\mu^3)^2 - 2gg' W_\mu^3 B^\mu + g'^2 B_\mu^2] &= \frac{1}{8} v^2 [g W_\mu^3 - g' B_\mu]^2 + 0[g' W_\mu^3 + g B_\mu]^2 \quad (1.46) \\ &= \frac{1}{8} v^2 [\sqrt{g^2 + g'^2} Z_\mu]^2 + 0[\sqrt{g^2 + g'^2} A_\mu]^2 \end{aligned}$$

854 and then

$$M_Z = \frac{1}{2} v \sqrt{g^2 + g'^2}, \quad M_A = 0 \quad (1.47)$$

855 **1.3.4 Masses of the fermions**

856 The lepton mass terms can be generated by introducing a gauge invariant Lagrangian
 857 term describing the Yukawa coupling between the lepton field and the Higgs field

$$\mathcal{L}_{Yl} = -G_l \left[(\bar{\nu}_l, \bar{l})_L \begin{pmatrix} \phi^+ \\ \phi^0 \end{pmatrix} l_R + \bar{l}_R (\phi^-, \bar{\phi}^0) \begin{pmatrix} \nu_l \\ l \end{pmatrix} \right], \quad l = e, \mu, \tau. \quad (1.48)$$

858 After the SSB and replacing the usual field expansion about the ground state
 859 (Eqn.1.41) into \mathcal{L}_{Yl} , the mass term arises

$$\mathcal{L}_{Yl} = -m_l (\bar{l}_L l_R + \bar{l}_R l_L) - \frac{m_l}{v} (\bar{l}_L l_R + \bar{l}_R l_L) H = -m_l \bar{l} \left(1 + \frac{H}{v} \right) \quad (1.49)$$

860

$$m_l = \frac{G_l}{\sqrt{2}} v \quad (1.50)$$

861 where the additional term represents the lepton-Higgs interaction. The quark masses
 862 are generated in a similar way as lepton masses but for the upper member of the
 863 quark doublet a different Higgs doublet is needed:

$$\phi_c = -i\sigma_2 \phi^* = \begin{pmatrix} -\bar{\phi}^0 \\ \phi^- \end{pmatrix}. \quad (1.51)$$

864 Additionally, given that the quark isospin doublets are not constructed in terms
 865 of the mass eigenstates but in terms of the flavor eigenstates, as shown in Table 1.5,
 866 the coupling parameters will be related to the CKM matrix elements; thus, the quark
 867 Lagrangian is given by:

$$\mathcal{L}_{Yq} = -G_d^{i,j} (\bar{u}_i, \bar{d}'_i)_L \begin{pmatrix} \phi^+ \\ \phi^0 \end{pmatrix} d_{jR} - G_u^{i,j} (\bar{u}_i, \bar{d}'_i)_L \begin{pmatrix} -\bar{\phi}^0 \\ \phi^- \end{pmatrix} u_{jR} + h.c. \quad (1.52)$$

868 with $i, j = 1, 2, 3$. After SSB and expansion about the ground state, the diagonal form

869 of \mathcal{L}_{Yq} is:

$$\mathcal{L}_{Yq} = -m_d^i \bar{d}_i d_i \left(1 + \frac{H}{v}\right) - m_u^i \bar{u}_i u_i \left(1 + \frac{H}{v}\right) \quad (1.53)$$

870 Fermion masses depend on arbitrary couplings G_l and $G_{u,d}$ and are not predicted
871 by the theory.

872 1.3.5 The Higgs field

873 After the characterization of the fermions and gauge bosons as well as their interac-
874 tions, it is necessary to characterize the Higgs field itself. The Lagrangian \mathcal{L}_S in Eqn.
875 1.37 written in terms of the gauge bosons is given by

$$\mathcal{L}_S = \frac{1}{4} \lambda v^4 + \mathcal{L}_H + \mathcal{L}_{HV} \quad (1.54)$$

876

$$\mathcal{L}_H = \frac{1}{2} \partial_\mu H \partial^\mu H - \frac{1}{2} m_H^2 H^2 - \frac{1}{2v} m_H^2 H^3 - \frac{1}{8v^2} m_H^2 H^4 \quad (1.55)$$

877

$$\mathcal{L}_{HV} = m_H^2 W_\mu^+ W^{\mu-} \left(1 + \frac{2}{v} H + \frac{2}{v^2} H^2\right) + \frac{1}{2} m_Z^2 Z_\mu Z^\mu \left(1 + \frac{2}{v} H + \frac{2}{v^2} H^2\right) \quad (1.56)$$

878 The mass of the Higgs boson is deduced as usual from the mass term in the Lagrangian
879 resulting in:

$$m_H = \sqrt{-2\mu^2} = \sqrt{2\lambda}v \quad (1.57)$$

880 however, it is not predicted by the theory either. The experimental measurement of
881 the Higgs boson mass have been performed by the *Compact Muon Solenoid (CMS)*
882 experiment and the *A Toroidal LHC Appartus (ATLAS)* experiments at the *Large
883 Hadron Collider (LHC)*, [36–38], and is presented in Table 1.8.

884

Property	Value
Electric charge	0
Color charge	0
Spin	0
Weak isospin	-1/2
Weak hypercharge	1
Parity	1
Mass (GeV/c ²)	125.09±0.21 (stat.)±0.11 (syst.)

Table 1.8: Higgs boson properties. Higgs mass is not predicted by the theory and the value here corresponds to the experimental measurement.

1.3.6 Production of Higgs bosons at LHC

886 At the LHC, Higgs bosons are produced as a result of the collision of two counter-
887 rotating protons beams. A detailed description of the LHC machine will be presented
in chapter 2.

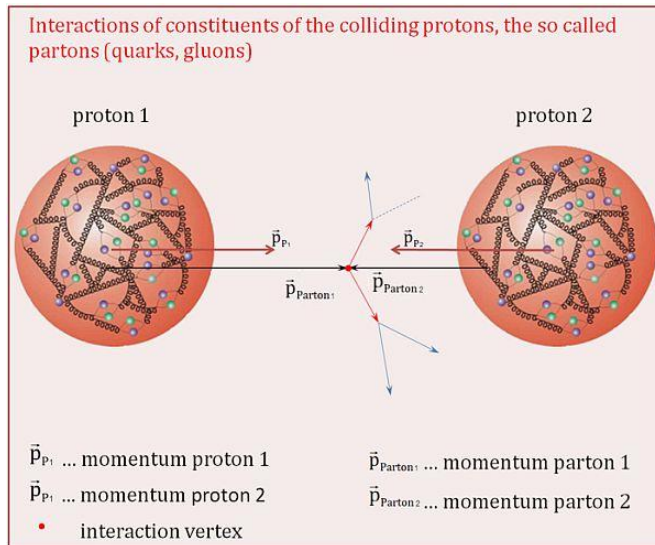


Figure 1.10: Proton-proton collision. Protons are composed of 3 valence quarks, a sea of quarks and gluons; therefore in a proton-proton collision, quarks and gluons are those who collide. [39].

888

889 Protons are composed of quarks and these quarks are bound by gluons; however,
890 what is commonly called the quark content of the proton makes reference to the
891 valence quarks. In fact, a proton is not just a rigid entity with three balls in it all
892 tied up with springs, but the gluons exchanged by the valence quarks tend to split

893 spontaneously into quark-antiquark pairs or more gluons, creating *sea of quarks and*
 894 *gluons* as represented in Figure 1.10.

895 In a proton-proton (pp) collision, the proton's constituents, quarks and gluons, are
 896 those that collide. The pp cross section depends on the momentum of the colliding
 897 particles, reason for which it is needed to know how the momentum is distributed
 898 inside the proton. Quarks and gluons are known as partons, hence, the functions
 899 that describe how the proton momentum is distributed among partons inside it are
 900 called *parton distribution functions (PDFs)*; PDFs are determined from experimental
 901 data obtained in experiments where the internal structure of hadrons is tested, and
 902 depend on the momentum transfer Q and the fraction of momentum x carried by an
 903 specific parton. Figure 1.11 shows the proton PDFs ($xf(x, Q^2)$) for two values of Q .

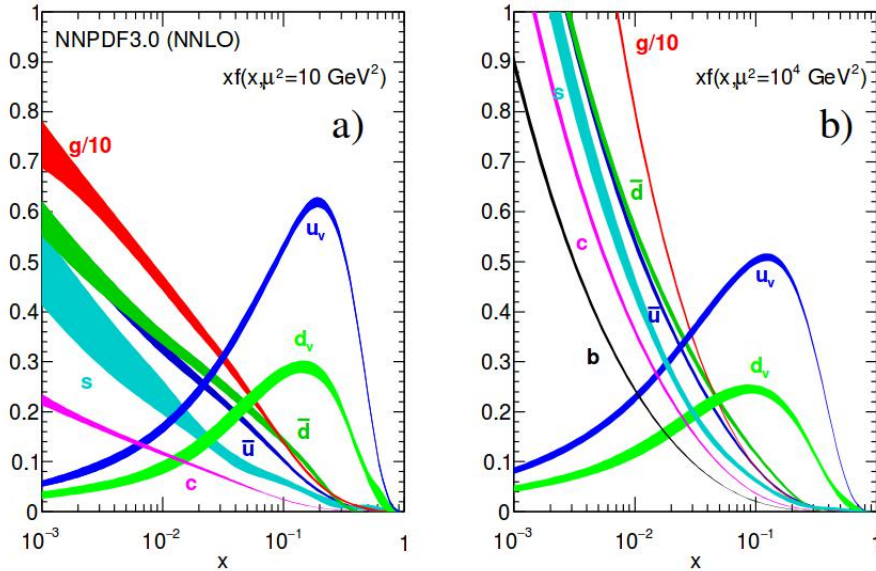


Figure 1.11: Proton PDFs for two values of Q^2 : left. $\mu^2 = Q^2 = 10 \text{ GeV}^2$, right. $\mu^2 = Q^2 = 10^4 \text{ GeV}^2$. u_v and d_v correspond to the u and d valence quarks, $s, c, b, \bar{u}, \bar{d}$ correspond to sea quarks, and g corresponds to gluons. Note that gluons carry a high fraction of the proton's momentum. [9]

904 In physics, a common approach to study complex systems consists of starting
 905 with a simpler version of them, for which a well known description is available, and

adding an additional *perturbation* which represents a small deviation from the known behavior. If the perturbation is small enough, the physical quantities associated with the perturbed system are expressed as a series of corrections to those of the simpler system. The perturbation series corresponds to an expansion in power series of a small parameter, therefore, the more terms are considered in the series (the higher order in the perturbation series), the more precise is the description of the complex system. If the perturbation does not get progressively smaller, the strategy cannot be applied and new methods have to be employed.

High energy systems, like the Higgs production at LHC explored in this thesis, usually can be treated perturbatively with the expansion made in terms of the coupling constants. The overview presented here will be oriented specifically to the Higgs boson production mechanisms in pp collisions at LHC.

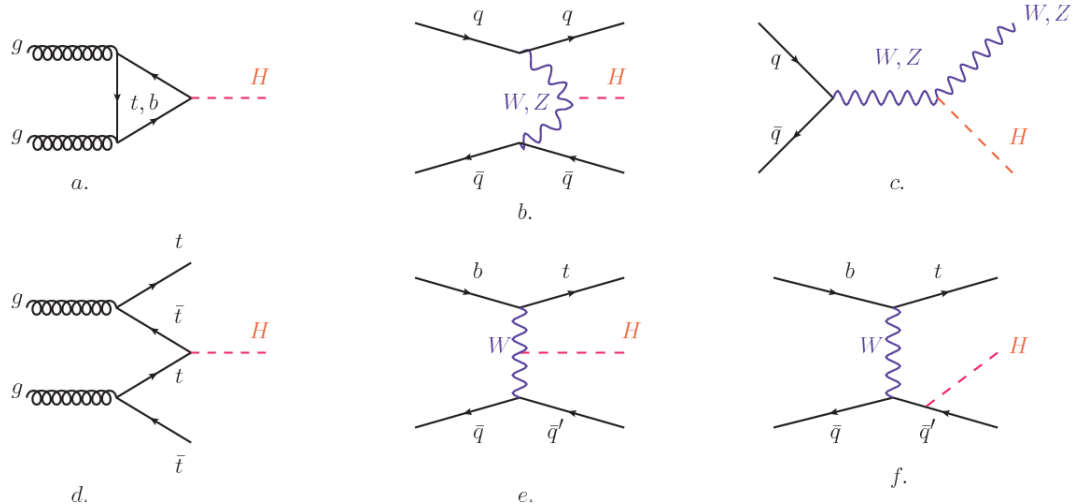


Figure 1.12: Main Higgs boson production mechanism Feynman diagrams. a. gluon-gluon fusion, b. vector boson fusion (VBF), c. Higgs-strahlung, d. Associated production with a top or bottom quark pair, e-f. associated production with a single top quark.

Figure 1.12 shows the Feynman diagrams for the leading order (first order) Higgs production processes at LHC; note that in these diagrams the incoming particles are not the protons themselves but the partons from the protons that actually participate

in the interaction, hence, theorists typically calculate the cross section for the parton interaction, and then convolute that cross section with the information from the PDFs to get a production cross section that is actually measured in experiments. The cross section for Higgs production as a function of the center of mass-energy (\sqrt{s}) for pp collisions is showed in Figure 1.13 left. The tags NLO (next to leading order), NNLO (next to next to leading order) and N3LO (next to next to next to leading order) make reference to the order at which the perturbation series have been considered while the tags QCD and EW correspond to the strong and electroweak coupling constants respectively.

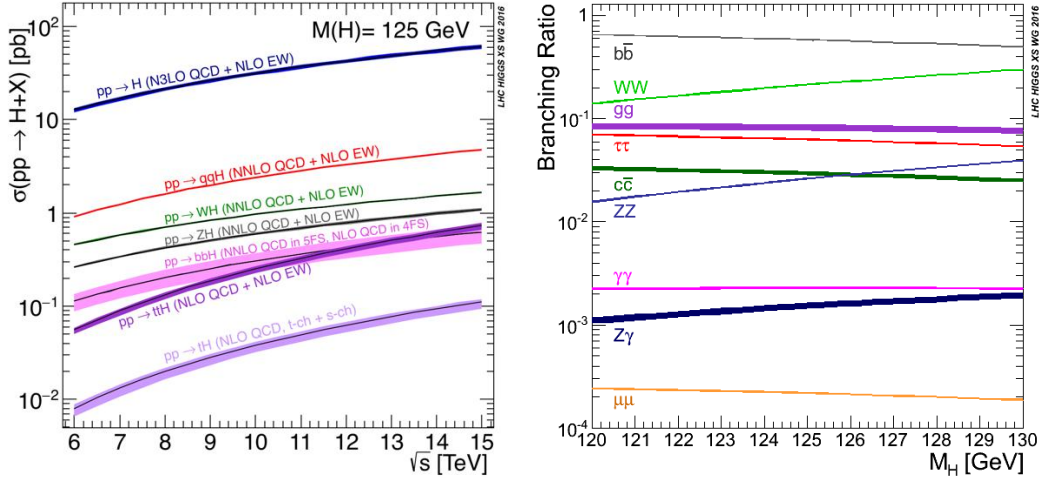


Figure 1.13: Higgs boson production cross sections (left) and decay branching ratios (right) for the main mechanisms. The VBF is indicated as qqH [40].

The main production mechanism is the gluon fusion (Figure 1.12a and $pp \rightarrow H$ in Figure 1.13) given that gluons carry the highest fraction of momentum of the protons in pp colliders (as shown in Figure ??). Since the Higgs boson does not couple to gluons, the mechanism proceeds through the exchange of a virtual top-quark loop. Note that in this process the Higgs boson is produced alone, turning out to be problematic for some Higgs decays, because such absence of anything produced in

936 association with the Higgs represent a trouble for triggering, however, this mechanism
 937 is experimentally clean when combined with the two-photon or the four-lepton decay
 938 channels (see Section 1.3.7).

939 Vector boson fusion (Figure 1.12b and $pp \rightarrow qqH$ in Figure 1.13) has the second
 940 largest production cross section. The scattering of two fermions is mediated by a weak
 941 gauge boson which later emits a Higgs boson. In the final state, the two fermions tend
 942 to be located in the central region of the detector; this kind of features are generally
 943 used as a signature when analyzing the datasets provided by the experiments⁷.

944 In the Higgs-strahlung mechanism (Figure 1.12c and $pp \rightarrow WH, pp \rightarrow ZH$ in
 945 Figure 1.13) two fermions annihilate to form a weak gauge boson. If the initial
 946 fermions have enough energy, the emergent boson might emit a Higgs boson.

947 The associated production with a top or bottom quark pair and the associated
 948 production with a single top quark (Figure 1.12d-f and $pp \rightarrow bbH, pp \rightarrow t\bar{t}H, pp \rightarrow tH$
 949 in Figure 1.13) have a smaller cross section than the main three mechanisms above,
 950 but they provide a good opportunity to test the Higgs-top coupling. The analysis
 951 reported in this thesis is developed using these production mechanisms. A detailed
 952 description of the tH mechanism will be given in Section 1.5.

953 1.3.7 Higgs boson decay channels

954 When a particle can decay through several modes, also known as channels, the prob-
 955 ability of decaying through a given channel is quantified by the *branching ratio (BR)*
 956 of the decay channel; thus, the BR is defined as the ratio of number of decays go-
 957 ing through that given channel to the total number of decays. In regard to the
 958 Higgs boson decay, the BR can be predicted with accuracy once the Higgs mass is
 959 known [41, 42]. In Figure 1.13 right, a plot of the BR as a function of the Higgs mass

⁷ More details about how to identify events of interest in this analysis will be given in chapter 6.

960 is presented; the largest predicted BR corresponds to the $b\bar{b}$ pair decay channel (see
 961 Table 1.9) given that it is the heaviest particle pair whose on-shell⁸ production is
 962 kinematically allowed in the decay.

Decay channel	Branching ratio	Rel. uncertainty
$H \rightarrow b\bar{b}$	5.84×10^{-1}	+3.2% – 3.3%
$H \rightarrow W^+W^-$	2.14×10^{-1}	+4.3% – 4.2%
$H \rightarrow \tau^+\tau^-$	6.27×10^{-2}	+5.7% – 5.7%
$H \rightarrow ZZ$	2.62×10^{-2}	+4.3% – 4.1%
$H \rightarrow \gamma\gamma$	2.27×10^{-3}	+5.0% – 4.9%
$H \rightarrow Z\gamma$	1.53×10^{-3}	+9.0% – 8.9%
$H \rightarrow \mu^+\mu^-$	2.18×10^{-4}	+6.0% – 5.9%

Table 1.9: Predicted branching ratios and the relative uncertainty for some decay channels of a SM Higgs boson with $m_H = 125\text{GeV}/c^2$ [9]; the uncertainties are driven by theoretical uncertainties for the different Higgs boson partial widths and by parametric uncertainties associated to the strong coupling and the masses of the quarks which are the input parameters. Further details on these calculations can be found in Reference [43]

963

964 Decays to other lepton and quark pairs, like electron, strange, up, and down
 965 quark pairs not listed in the table, are also possible but their likelihood is too small
 966 to measure since they are very lightweight, hence, their interaction with the Higgs
 967 boson is very weak. On other hand, the decay to top quark pairs is heavily suppressed
 968 due to the top quark mass ($\approx 173\text{ GeV}/c^2$).

969 Decays to gluons proceed indirectly through a virtual top quark loop while the
 970 decays to photons proceed through a virtual W boson loop, therefore, their branching
 971 ratio is smaller compared to direct interaction decays. Same is true for the decay to
 972 a photon and a Z boson.

⁸ In general, on-shell or real particles are those which satisfy the energy-momentum relation ($E^2 - |\vec{p}|^2 c^2 = m^2 c^4$); off-shell or virtual particles does not satisfy it which is possible under the uncertainty principle of quantum mechanics. Usually, virtual particles correspond to internal propagators in Feynman diagrams.

973 In the case of decays to pairs of W and Z bosons, the decay proceed with one of
 974 the bosons being on-shell and the other being off-shell. The likelihood of the process
 975 diminish depending on how far off-shell are the virtual particles involved, hence, the
 976 branching ratio for W boson pairs is bigger than for Z boson pairs since Z boson mass
 977 is bigger than W boson mass.

978 Note that the decay to a pair of virtual top quarks is possible, but the probability
 979 is way too small.

980 **1.4 Experimental status of the anomalous
 981 Higgs-fermion coupling**

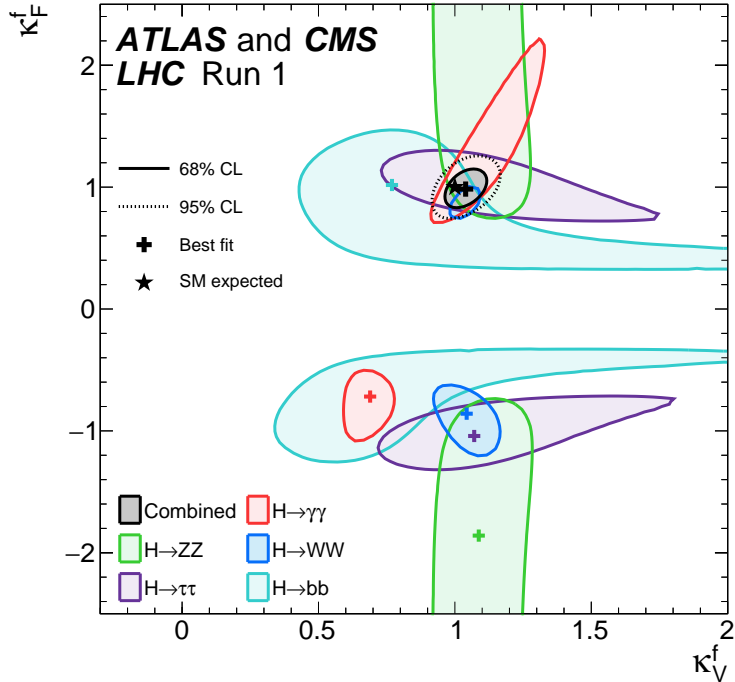


Figure 1.14: Combination of the ATLAS and CMS fits for coupling modifiers $\kappa_t - \kappa_V$; also shown the individual decay channels combination and their global combination. No assumptions have been made on the sign of the coupling modifiers [44].

982 ATLAS and CMS have performed analyses of the anomalous Higgs-fermion cou-
 983 pling by making likelihood scans for the two coupling modifiers, κ_f and κ_V , under
 984 the assumption that $\kappa_Z = \kappa_W \equiv \kappa_V$ and $\kappa_t = \kappa_\tau = \kappa_b \equiv \kappa_f$. Figure 1.14 shows the
 985 result of the combination of ATLAS and CMS fits; also the individual decay channels
 986 combination and the global combination results are shown. Note that from this plot
 987 there is limited information on the sign of the coupling since the only information
 988 available about the sign of the coupling comes from decays rather than production.

989 While all the channels are compatible for positive values of the modifiers, for
 990 negative values of κ_f there is no compatibility. The best fit for individual channels
 991 is compatible with negative values of κ_f except for the $H \rightarrow bb$ channel. The best
 992 fit for the combination yields $\kappa_f \geq 0$, in contrast to the yields from the individual
 993 channels; the reason of this yield resides in the $H \rightarrow \gamma\gamma$ coupling. $H \rightarrow \gamma\gamma$ decay
 994 proceeds through a loop of either top quarks or W bosons, hence, this channel is
 995 sensitive to κ_t thanks to the interference of these two amplitude contributions; under
 996 the assumption that no beyond SM particles take part in the loops, a flipped sign
 997 of κ_t will increase the $H \rightarrow \gamma\gamma$ branching fraction by a factor of ~ 2.4 which is not
 998 supported by measurements; thus, this large asymmetry between the positive and
 999 negative coupling ratios in the $H \rightarrow \gamma\gamma$ channel drives the yield of the global fit and
 1000 means that the anomalous H-t coupling is excluded as stated in Reference [44],
 1001 but there is a caveat, this exclusion holds only if no new particles contribute to the
 1002 loop in the main diagram for that decay.

1003 Although the $H \rightarrow bb$ channel is expected to be the most sensitive channel and
 1004 its best fit value of κ_t is positive, and then the global fit yield is still supported,
 1005 the contributions from all the other decay channels, small compared to the $H \rightarrow bb$,
 1006 indicate that the anomalous H-t coupling cannot be excluded completely, motivating
 1007 to look at tH processes which can help with both, the limited information on the sign

1008 of the H-t coupling and the access to information from the Higgs boson production
 1009 rather than from its decays.

1010 It will be shown in Section 1.5 that the same interference effect enhance the tH
 1011 production rate and could reveal evidence of direct production of heavy new particles
 1012 as predicted in composite and little Higgs models [45], or new physics related to
 1013 Higgs boson mediated flavor changing neutral currents [46] as well as probes the
 1014 CP-violating phase of the H-t coupling [47, 48].

1015 **1.5 Associated production of a Higgs boson and a 1016 single top quark**

1017 The production of Higgs boson in association with a top quark has been extensively
 1018 studied [47, 49–52]. While measurements of the main Higgs production mechanisms
 1019 rates are sensitive to the strength of the Higgs coupling to W boson or top quark,
 1020 they are not sensitive to the relative sign between the two couplings. In this thesis,
 1021 the Higgs boson production mechanism explored is the associated production with a
 1022 single top quark (tH) which offers sensitivity to the relative sign of the Higgs couplings
 1023 to W boson and to top quark. The description given here is based on Reference [51]

A process where two incoming particles interact and produce a final state with two particles can proceed in three called channels (see, for instance, Figure 1.15 omitting the red line). The t-channel represents processes where an intermediate particle is emitted by one of the incoming particles and absorbed by the other. The s-channel represents processes where the two incoming particles merge into an intermediate particle which eventually will split into the particles in the final state. The third channel, u-channel, is similar to the t-channel but the two outgoing particles interchange their

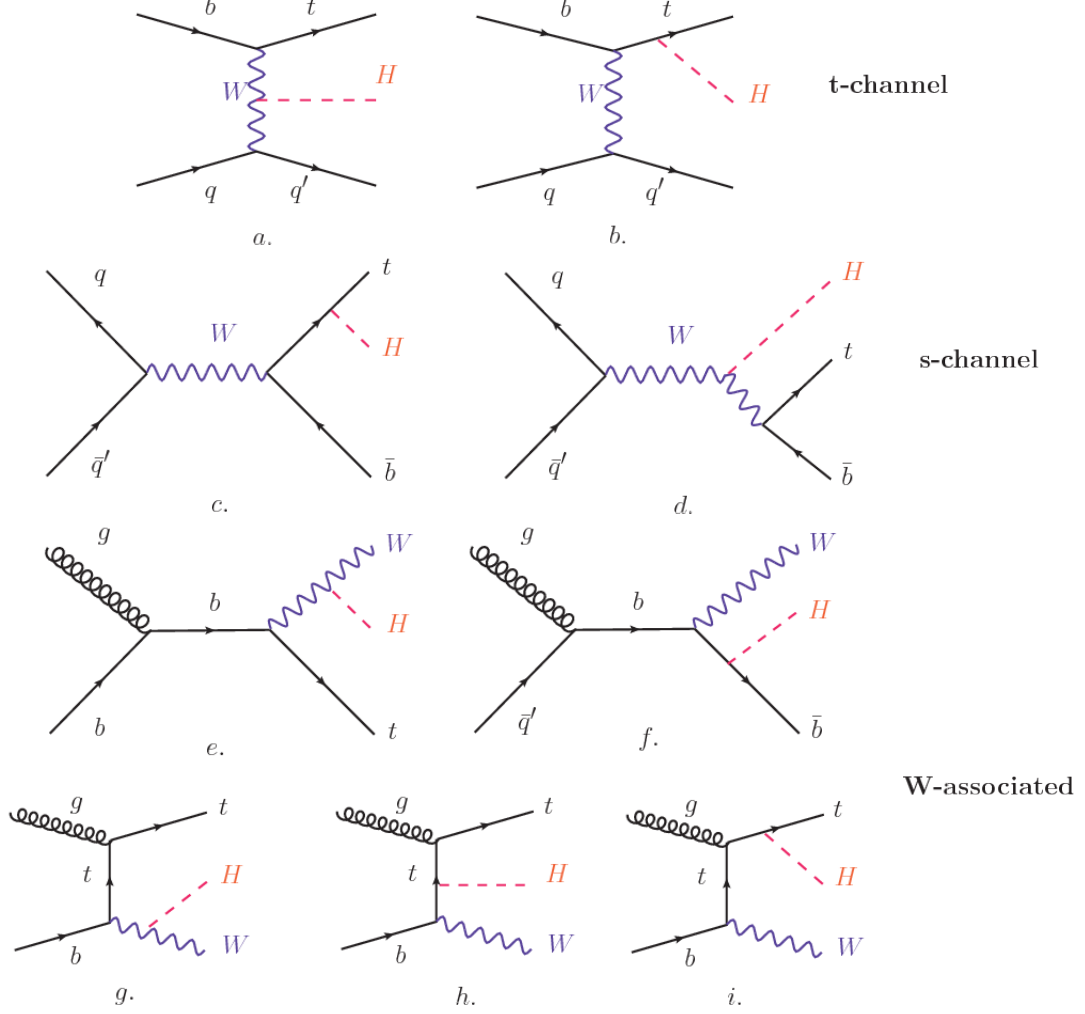


Figure 1.15: Associated Higgs boson production with a top quark mechanism Feynman diagrams. a.,b. t-channel (tHq), c.,d. s-channel (tHb), e-i. W-associated.

roles. These three channels are connected to the so-called Mandelstam variables

$$s = (p_1 + p_2)^2 = (p'_1 + p'_2)^2 \rightarrow \text{square of the center mass-energy.} \quad (1.58)$$

$$t = (p_1 - p'_1)^2 = (p'_2 - p_2)^2 \rightarrow \text{square of the four-momentum transfer.} \quad (1.59)$$

$$u = (p_1 - p'_2)^2 = (p'_1 - p_2)^2 \rightarrow \text{square of the crossed four-momentum transfer.} \quad (1.60)$$

$$s + t + u = m_1^2 + m_2^2 + m'_1^2 + m'_2^2 \quad (1.61)$$

which relate the momentum, energy and the angles of the incoming and outgoing particles in an scattering process of two particles to two particles. The importance of the Mandelstam variables reside in that they form a minimum set of variables needed to describe the kinematics of this scattering process; they are Lorentz invariant which makes them very useful when doing calculations.

The tH production, where Higgs boson can be radiated either from the top quark or from the W boson, is represented by the leading order Feynman diagrams in Figure 1.15. The cross section for the tH process is calculated, as usual, summing over the contributions from the different Feynman diagrams; therefore it depends on the interference between the contributions. In the SM, the interference for t-channel (tHq process) and W-associated (tHW process) production is destructive [49] resulting in the small cross sections presented in Table 1.10.

tH production channel	Cross section (fb)
t-channel ($pp \rightarrow tHq$)	$70.79^{+2.99}_{-4.80}$
W-associated ($pp \rightarrow tHW$)	$15.61^{+0.83}_{-1.04}$
s-channel($pp \rightarrow tHb$)	$2.87^{+0.09}_{-0.08}$

Table 1.10: Predicted SM cross sections for tH production at $\sqrt{s} = 13$ TeV [53, 54].

1036

The s-channel contribution can be neglected. It will be shown that a deviation from the SM destructive interference would result in an enhancement of the tH cross section compared to that in SM, which could be used to get information about the sign of the Higgs-top coupling [51, 52]. In order to describe tH production processes, Feynman diagram 1.15b will be considered; there, the W boson is radiated by a quark in the proton and eventually it will interact with the b quark. In the high energy regime, the effective W approximation [55] is used to describe the process as the

1044 emission of an approximately on-shell W and its hard scattering with the b quark;
 1045 i.e. $Wb \rightarrow th$. The scattering amplitude for the process is given by

$$\mathcal{A} = \frac{g}{\sqrt{2}} \left[(\kappa_t - \kappa_V) \frac{m_t \sqrt{s}}{m_W v} A \left(\frac{t}{s}, \varphi; \xi_t, \xi_b \right) + \left(\kappa_V \frac{2m_W s}{v t} + (2\kappa_t - \kappa_V) \frac{m_t^2}{m_W v} \right) B \left(\frac{t}{s}, \varphi; \xi_t, \xi_b \right) \right], \quad (1.62)$$

1046 where $\kappa_V \equiv g_{HVV}/g_{HVV}^{SM}$ and $\kappa_t \equiv g_{Ht}/g_{Ht}^{SM} = y_t/y_t^{SM}$ are scaling factors that quantify
 1047 possible deviations of the couplings from the SM values, Higgs-Vector boson (H-
 1048 W) and Higgs-top (H-t) respectively, from the SM couplings; $s = (p_W + p_b)^2$, $t =$
 1049 $(p_W - p_H)^2$, φ is the Higgs azimuthal angle around the z axis taken parallel to the
 1050 direction of motion of the incoming W; A and B are functions describing the weak
 1051 interaction in terms of the chiral states (ξ_t, ξ_b) of the quarks b and t . Terms that
 1052 vanish in the high energy limit have been neglected as well as the Higgs and b quark
 1053 masses⁹.

1054 The scattering amplitude grows with energy like \sqrt{s} for $\kappa_V \neq \kappa_t$, in contrast to
 1055 the SM ($\kappa_t = \kappa_V = 1$), where the first term in 1.62 cancels out and the amplitude
 1056 is constant for large s ; therefore, a deviation from the SM predictions represents an
 1057 enhancement in the tHq cross section. In particular, for a SM H-W coupling and a
 1058 H-t coupling of inverted sign with respect to the SM ($\kappa_V = -\kappa_t = 1$) the tHq cross
 1059 section is enhanced by a factor greater 10 as seen in the Figure 1.16 taken from
 1060 Reference [51]; Reference [56] has reported similar enhancement results.

1061 A similar analysis is valid for the W-associated channel but, in that case, the in-
 1062 terference is more complicated since there are more than two contributions and an ad-
 1063 ditional interference with the production of Higgs boson and a top pair process($t\bar{t}H$).
 1064 The calculations are made using the so-called Diagram Removal (DR) technique where

⁹ A detailed explanation of the structure and approximations used to derive \mathcal{A} can be found in Reference [51]

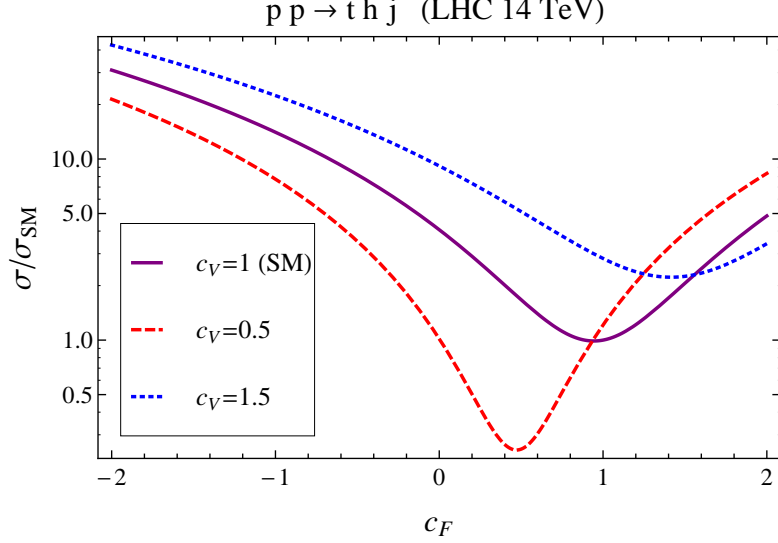


Figure 1.16: Cross section for tHq process as a function of κ_t , normalized to the SM, for three values of κ_V . In the plot c_f refers to the Higgs-fermion coupling which is dominated by the H-t coupling and represented here by κ_t . Solid, dashed and dotted lines correspond to $c_V \rightarrow \kappa_V = 1, 0.5, 1.5$ respectively. Note that for the SM ($\kappa_V = \kappa_t = 1$), the destructive effect of the interference is maximal.

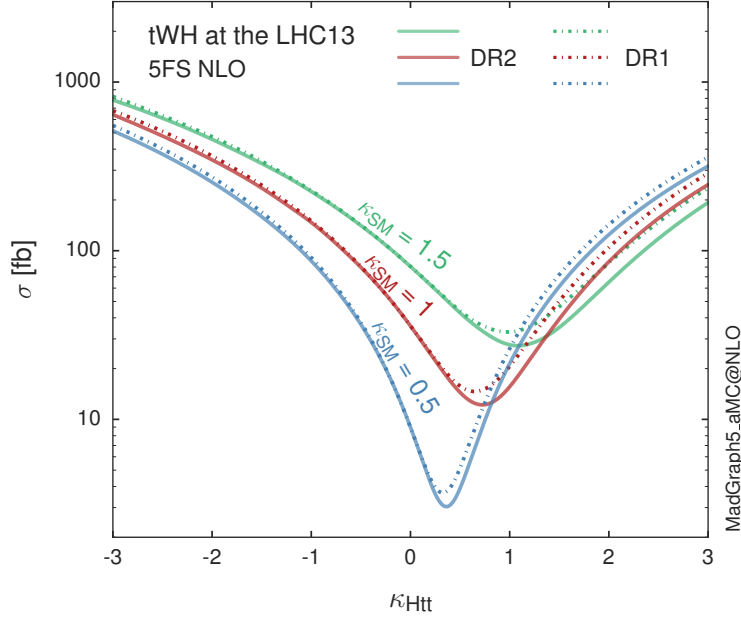


Figure 1.17: Cross section for tHW process as a function of κ_{Htt} , for three values of κ_{SM} at $\sqrt{s} = 13$ TeV. $\kappa_{Htt}^2 = \sigma_{Htt}/\sigma_{Htt}^{SM}$ is a simple re-scaling of the SM Higgs interactions.

interfering diagrams are removed (or added) from the calculations in order to evaluate the impact of the removed contributions. DR1 was defined to neglect $t\bar{t}H$ interference while DR2 was defined to take $t\bar{t}H$ interference into account [48]. As shown in Figure 1.17, the tHW cross section is enhanced from about 15 fb (SM: $\kappa_{Htt} = 1$) to about 150 fb ($\kappa_{Htt} = -1$). Differences between curves for DR1 and DR2 help to gauge the impact of the interference with $t\bar{t}H$. Results of the calculations of the tHq and tHW cross sections at $\sqrt{s} = 13$ TeV can be found in Reference [57] and a summary of the results is presented in Table 1.11.

	\sqrt{s} TeV	$\kappa_t = 1$	$\kappa_t = -1$
$\sigma^{LO}(tHq)(fb)$ [51]	8	≈ 17.4	≈ 252.7
	14	≈ 80.4	≈ 1042
$\sigma^{NLO}(tHq)(fb)$ [51]	8	$18.28^{+0.42}_{-0.38}$	$233.8^{+4.6}_{-0.0}$
	14	$88.2^{+1.7}_{-0.0}$	$982.8^{+28}_{-0.0}$
$\sigma^{LO}(tHq)(fb)$ [56]	14	≈ 71.8	≈ 893
$\sigma^{LO}(tHW)(fb)$ [56]	14	≈ 16.0	≈ 139
$\sigma^{NLO}(tHq)(fb)$ [57]	8	$18.69^{+8.62\%}_{-17.13\%}$	-
	13	$74.25^{+7.48\%}_{-15.35\%}$	$848^{+7.37\%}_{-13.70\%}$
	14	$90.10^{+7.34\%}_{-15.13\%}$	$1011^{+7.24\%}_{-13.39\%}$
$\sigma^{LO}(tHW)(fb)$ [48]	13	$15.77^{+15.91\%}_{-15.76\%}$	-
$\sigma^{NLO}DR1(tHW)(fb)$ [48]	13	$21.72^{+6.52\%}_{-5.24\%}$	≈ 150
$\sigma^{NLO}DR2(tHW)(fb)$ [48]	13	$16.28^{+7.34\%}_{-15.13\%}$	≈ 150

Table 1.11: Predicted enhancement of the tHq and tHW cross sections at LHC for $\kappa_V = 1$ and $\kappa_t = \pm 1$ at LO and NLO; the cross section enhancement of more than a factor of 10 is due to the flipping in the sign of the H-t coupling with respect to the SM one.

1073

1.6 CP-mixing in tH processes

In addition to the sensitivity to sign of the H-t coupling, the tHq and tHW processes have been proposed as a tool to investigate the possibility of a H-t coupling that does

1077 not conserve CP [47, 48, 58].

1078 In this thesis, the sensitivity of tH processes to CP-mixing is also studied on the
 1079 basis of References [47, 48] using the effective field theory framework where a generic
 1080 particle (X_0) of spin-0 and a general CP violating interaction with the top quark
 1081 (Htt coupling), can couple to scalar and pseudo-scalar fermionic densities. The H-W
 1082 interaction is assumed to be SM-like. The Lagrangian modeling the H-t interaction
 1083 is given by

$$\mathcal{L}_0^t = -\bar{\psi}_t (c_\alpha \kappa_{Htt} g_{Htt} + i s_\alpha \kappa_{Att} g_{Att} \gamma_5) \psi_t X_0, \quad (1.63)$$

1084 where α is the CP-mixing phase, $c_\alpha \equiv \cos \alpha$ and $s_\alpha \equiv \sin \alpha$, κ_{Htt} and κ_{Att} are real
 1085 dimensionless re-scaling parameters¹⁰ used to parametrize the magnitude of the CP-
 1086 violating and CP-conserving parts of the amplitude. The model defines $g_{Htt} =$
 1087 $g_{Att} = m_t/v = y_t/\sqrt{2}$ with $v \sim 246$ GeV the Higgs vacuum expectation value. In
 1088 this parametrization, three special cases can be recovered

1089 • CP-even coupling $\rightarrow \alpha = 0^\circ$

1090 • CP-odd coupling $\rightarrow \alpha = 90^\circ$

1091 • SM coupling $\rightarrow \alpha = 0^\circ$ and $\kappa_{Htt} = 1$

1092 The loop induced X_0 coupling to gluons can also be described in terms of the
 1093 parametrization above, according to

$$\mathcal{L}_0^g = -\frac{1}{4} (c_\alpha \kappa_{Hgg} g_{Hgg} G_{\mu\nu}^a G^{a,\mu\nu} + s_\alpha \kappa_{Agg} g_{Agg} G_{\mu\nu}^a \tilde{G}^{a,\mu\nu}) X_0. \quad (1.64)$$

1094 where $g_{Hgg} = -\alpha_s/3\pi v$ and $g_{Agg} = \alpha_s/2\pi v$ and $G_{\mu\nu}$ is the gluon field strength tensors.

1095 Under the assumption that the top quark dominates the gluon-fusion process at LHC

¹⁰ analog to κ_t and κ_V

1096 energies, $\kappa_{Hgg} \rightarrow \kappa_{Htt}$ and $\kappa_{Agg} \rightarrow \kappa_{Att}$, so that the ratio between the gluon-gluon
 1097 fusion cross section for X_0 and for the SM Higgs prediction can be written as

$$\frac{\sigma_{NLO}^{gg \rightarrow X_0}}{\sigma_{NLO,SM}^{gg \rightarrow H}} = c_\alpha^2 \kappa_{Htt}^2 + s_\alpha^2 \left(\kappa_{Att} \frac{g_{Agg}}{g_{Hgg}} \right)^2. \quad (1.65)$$

1098 If the re-scaling parameters are set to

$$\kappa_{Htt} = 1, \quad \kappa_{Att} = \left| \frac{g_{Hgg}}{g_{Agg}} \right| = \frac{2}{3}. \quad (1.66)$$

1099 the gluon-fusion SM cross section is reproduced for every value of the CP-mixing
 1100 angle α ; therefore, by imposing that condition to the Lagrangian density 1.63, the
 1101 CP-mixing angle is not constrained by current data. Figure 1.18 shows the NLO cross
 1102 sections for t-channel tX_0 (blue) and $t\bar{t}X_0$ (red) associated production processes as a
 1103 function of the CP-mixing angle α . X_0 is a generic spin-0 particle with top quark
 1104 CP-violating coupling. Re-scaling factors κ_{Htt} and κ_{Att} have been set to reproduce
 1105 the SM gluon-fusion cross sections.

1106 It is interesting to notice that the tX_0 cross section is enhanced, by a factor of
 1107 about 10, when a continuous rotation in the scalar-pseudoscalar plane is applied; this
 1108 enhancement is similar to the enhancement produced when the H-t coupling is flipped
 1109 in sign with respect to the SM ($y_t = -y_{t,SM}$ in the plot), as showed in Section 1.5. In
 1110 contrast, the degeneracy in the $t\bar{t}X_0$ cross section is still present given that it depends
 1111 quadratically on the H-t coupling, but more interesting is to notice that $t\bar{t}X_0$ cross
 1112 section is exceeded by tX_0 cross section after $\alpha \sim 60^\circ$.

1113 A similar parametrization can be used to investigate the tHW process sensitivity
 1114 to CP-violating H-t coupling. As said in 1.5, the interference in the W-associated
 1115 channel is more complicated because there are more than two contributions and also
 1116 there is interference with the $t\bar{t}H$ production process.

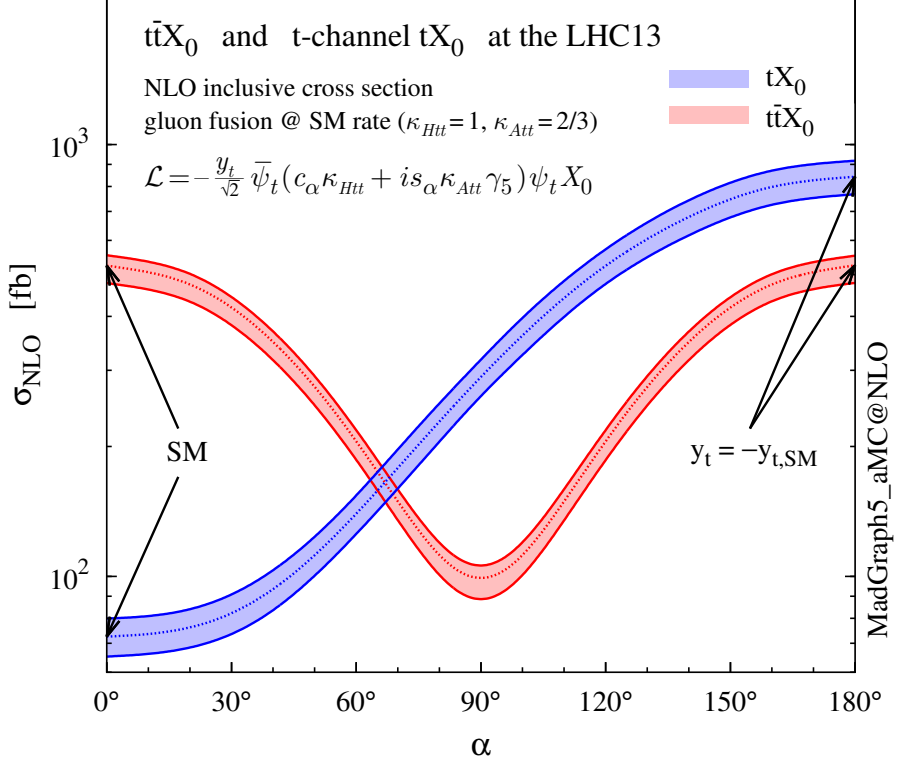


Figure 1.18: NLO cross sections for t-channel tX_0 (blue) and $t\bar{t}X_0$ (red) associated production processes as a function of the CP-mixing angle α . X_0 is a generic spin-0 particle with top quark CP-violating coupling [47].

1117 Figure 1.19 shows the NLO cross sections for t-channel tX_0 (blue), $t\bar{t}X_0$ (red)
 1118 associated production and for the combined $tWX_0+t\bar{t}X_0+interference$ (orange) as
 1119 a function of the CP-mixing angle. It is clear that the effect of the interference in the
 1120 combined case is the lifting of the degeneracy present in the $t\bar{t}X_0$ production. The
 1121 constructive interference enhances the cross section from about 500 fb at SM ($\alpha = 0$)
 1122 to about 600 fb ($\alpha = 180^\circ \rightarrow y_t = -y_{t,SM}$).

1123 An analysis combining tHq and tHW processes will be made in this thesis taking
 1124 advantage of the sensitivity improvement.

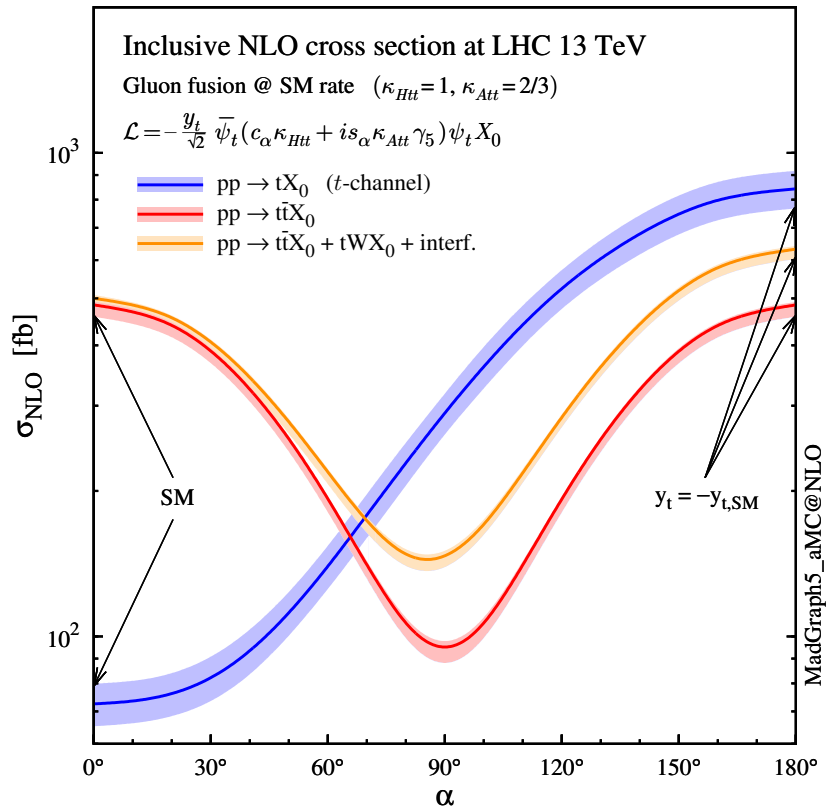


Figure 1.19: NLO cross sections for t-channel tX_0 (blue), $t\bar{t}X_0$ (red) associated production processes and combined $tWX_0 + t\bar{t}X_0$ (including interference) production as a function of the CP-mixing angle α [47].

₁₁₂₅ **Chapter 2**

₁₁₂₆ **The CMS experiment at the LHC**

₁₁₂₇ **2.1 Introduction**

₁₁₂₈ Located on the Swiss-French border, the European Council for Nuclear Research
₁₁₂₉ (CERN) is the largest scientific organization leading particle physics research. About
₁₁₃₀ 13000 people in a broad range of roles including users, students, scientists, engineers,
₁₁₃₁ among others, contribute to the data taking and analysis, with the goal of unveiling
₁₁₃₂ the secrets of nature and revealing the fundamental structure of the universe. CERN
₁₁₃₃ is also the home of the Large Hadron Collider (LHC), the largest particle accelerator
₁₁₃₄ around the world, where protons (or heavy ions) traveling close to the speed of light,
₁₁₃₅ are made to collide. These collisions open a window to investigate how particles (and
₁₁₃₆ their constituents if they are composite) interact with each other, providing clues
₁₁₃₇ about the laws of nature. This chapter presents an overview of the LHC structure
₁₁₃₈ and operation. A detailed description of the CMS detector is offered, given that the
₁₁₃₉ data used in this thesis have been taken with this detector.

1140 2.2 The LHC

1141 With 27 km of circumference, the LHC is currently the most powerful circular acceler-
 1142 ator in the world. It is installed in the same tunnel where the Large Electron-Positron
 1143 (LEP) collider was located, taking advantage of the existing infrastructure. The LHC
 1144 is part of the CERN's accelerator complex composed of several successive accelerat-
 1145 ing stages before the particles are injected into the LHC ring where they reach their
 1146 maximum energy (see Figure 2.1).

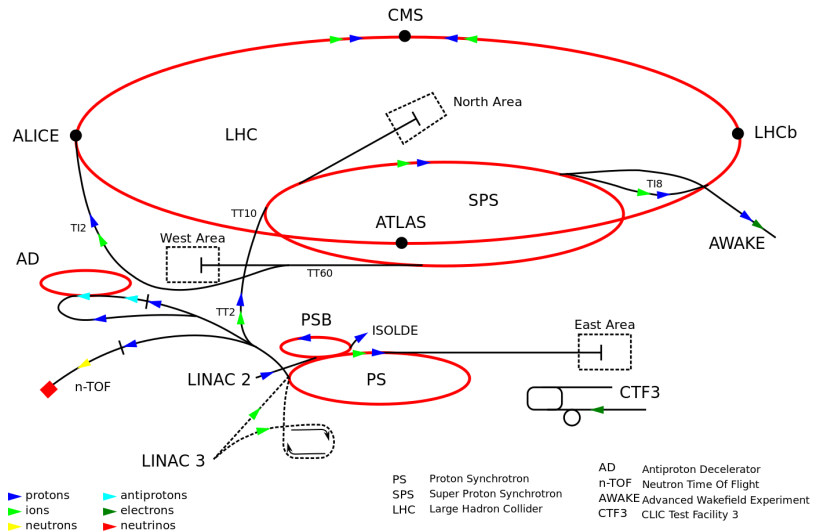


Figure 2.1: CERN accelerator complex. Blue arrows show the path followed by protons along the acceleration process [61].

1147 The LHC runs in three collision modes depending on the particles being acceler-
 1148 ated

1149 • Proton-Proton collisions (pp) for multiple physics experiments.

1150 • Lead-Lead collisions ($Pb-Pb$) for heavy ion experiments.

1151 • Proton-Lead collisions ($p-Pb$) for quark-gluon plasma experiments.

1152 In this thesis only pp collisions will be considered.

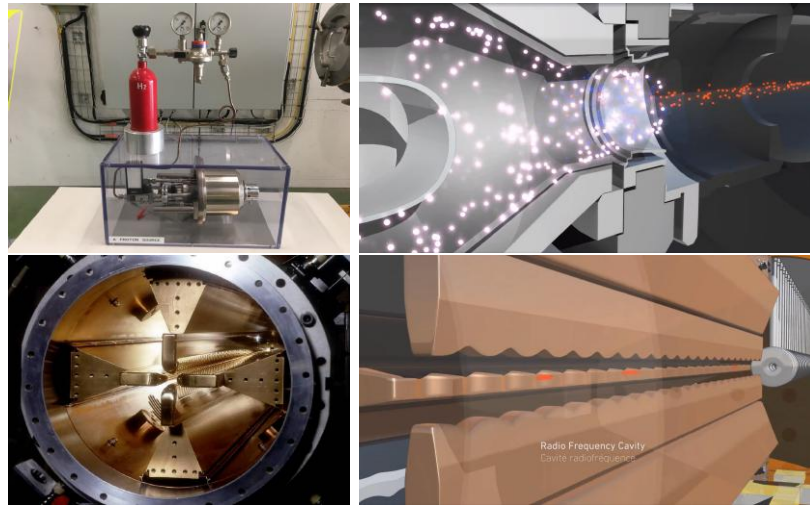


Figure 2.2: LHC protons source and the first acceleration stage. Top: the bottle contains hydrogen gas which is injected into the metal cylinder (white dots) to be broken down into electrons (blue dots) and protons (red dots); Bottom: the obtained protons are directed towards the radio frequency quadrupole which perform the first acceleration, focus the beam and create the bunches of protons. Left images are real pictures while right images are drawings [65, 66].

1153 Collection of protons starts with hydrogen atoms taken from a bottle, containing
 1154 hydrogen gas, and injecting them in a metal cylinder; hydrogen atoms are broken
 1155 down into electrons and protons by an intense electric field (see Figure 2.2 top).
 1156 The resulting protons leave the metal cylinder towards a radio frequency quadrupole
 1157 (RFQ) that focus the beam, accelerates the protons and creates the packets of protons
 1158 called bunches. In the RFQ, an electric field is generated by a RF wave at a frequency
 1159 that matches the resonance frequency of the cavity where the electrodes are contained.
 1160 The beam of protons traveling on the RFQ axis experiences an alternating electric
 1161 field gradient that generates the focusing forces.

1162 In order to accelerate the protons, a longitudinal time-varying electric field com-
 1163 ponent is added to the system; it is done by giving the electrodes a sine-like profile as
 1164 shown in Figure 2.2 bottom. By matching the speed and phase of the protons with
 1165 the longitudinal electric field the bunching is performed; protons synchronized with

1166 the RFQ (synchronous protons) do not feel an accelerating force, but those protons in
 1167 the beam that have more (or less) energy than the synchronous proton (asynchronous
 1168 protons) will feel a decelerating (accelerating) force; therefore, asynchronous protons
 1169 will oscillate around the synchronous ones forming bunches of protons [63]. From the
 1170 RFQ protons emerge with energy 750 keV in bunches of about 1.15×10^{11} protons [64].

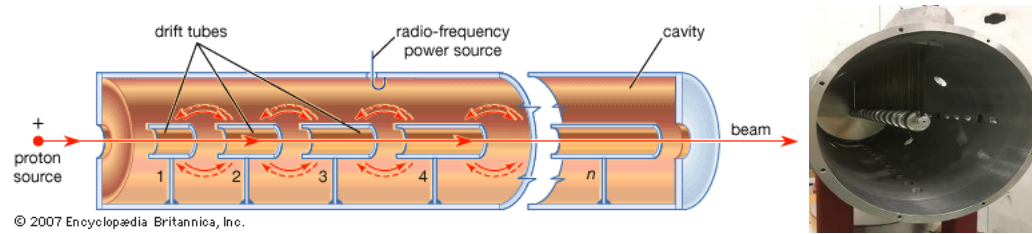


Figure 2.3: Left: drawing of the LINAC2 accelerating system at CERN. Electric fields generated by radio frequency (RF) create acceleration and deceleration zones inside the cavity; deceleration zones are blocked by drift tubes where quadrupole magnets focus the proton beam. Right: picture of a real RF cavity [67].

1171 Proton bunches coming from the RFQ go to the linear accelerator 2 (LINAC2)
 1172 where they are accelerated to reach 50 MeV energy. In the LINAC2 stage, acceleration
 1173 is performed using electric fields generated by radio frequency which create zones
 1174 of acceleration and deceleration as shown in Figure 2.3. In the deceleration zones,
 1175 the electric field is blocked using drift tubes where protons are free to drift while
 1176 quadrupole magnets focus the beam.

1177 The beam coming from LINAC2 is injected into the proton synchrotron booster
 1178 (PSB) to reach 1.4 GeV in energy. The next acceleration is provided at the proton
 1179 synchrotron (PS) up to 26 GeV, followed by the injection into the super proton
 1180 synchrotron (SPS) where protons are accelerated to 450 GeV. Finally, protons are
 1181 injected into the LHC where they are accelerated to the target energy of 6.5 TeV.

1182 PSB, PS, SPS and LHC accelerate protons using the same RF acceleration tech-
 1183 nique described before.

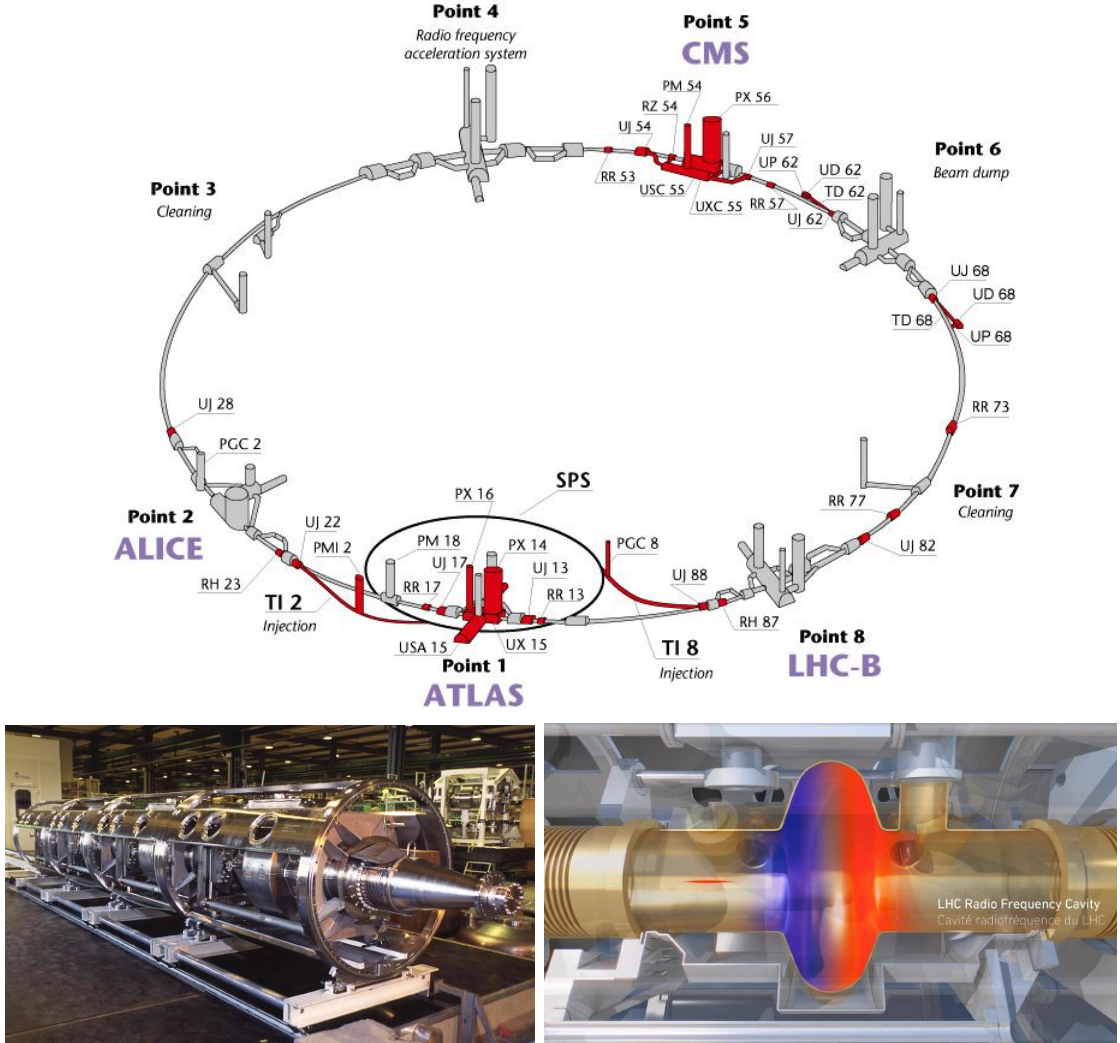


Figure 2.4: Top: LHC layout. The red zones indicate the infrastructure additions to the LEP installations, built to accommodate the ATLAS and CMS experiments which exceed the size of the former experiments located there [62]. Bottom: LHC RF cavities. A module (left picture) accommodates 4 cavities, each like the one in the right drawing, that accelerate protons and preserve the bunch structure of the beam. The color gradient pattern represents the strength of the electric field inside the cavity; red zone corresponds to the maximum of the oscillation electric field while the blue zone corresponds to the minimum. [66, 68]

1184 The LHC has a system of 16 RF cavities located in the so-called point 4, as
 1185 shown in Figure 2.4 top, tuned at a frequency of 400 MHz. The bottom side of
 1186 Figure 2.4 shows a picture of a RF module composed of 4 RF cavities working in a
 1187 superconducting state at 4.5 K; also, a representation of the accelerating electric field

1188 that accelerates the protons in the bunch is shown. The maximum of the oscillating
 1189 electric field (red region) picks the proton bunches at the entrance of the cavity
 1190 and keeps accelerating them through the whole cavity. The protons are carefully
 1191 timed so that in addition to the acceleration effect the bunch structure of the beam
 1192 is preserved.

1193 While protons are accelerated in one section of the LHC ring, where the RF cavities
 1194 are located, in the rest of their path they have to be kept in the curved trajectory
 1195 defined by the LHC ring. Technically, LHC is not a perfect circle; RF, injection, beam
 1196 dumping, beam cleaning and sections before and after the experimental points where
 1197 protons collide are all straight sections. In total, there are 8 arcs 2.45 km long each
 1198 and 8 straight sections 545 m long each. In order to curve the proton's trajectory in
 1199 the arc sections, superconducting dipole magnets are used.

1200 Inside the LHC ring, there are two proton beams traveling in opposite directions
 1201 in two separated beam pipes; the beam pipes are kept at ultra-high vacuum ($\sim 10^{-9}$
 1202 Pa) to ensure that there are no particles that interact with the proton beams. The
 1203 superconducting dipole magnets used in LHC are made of a NbTi alloy, capable of
 1204 transporting currents of about 12000 A when cooled at a temperature below 2K using
 1205 liquid helium (see Figure 2.5).

1206 Protons in the arc sections of LHC feel a centripetal force exerted by the dipole
 1207 magnets; the magnitude of magnetic field needed to keep the protons in the LHC
 1208 curved trayectomy can be found assuming that protons travel at $v \approx c$, using the
 1209 standard values for proton mass and charge and the LHC radius, as

$$F_m = \frac{mv^2}{r} = qBv \rightarrow B = 8.33T \quad (2.1)$$

1210 which is about 100000 times the Earth's magnetic field. A representation of the

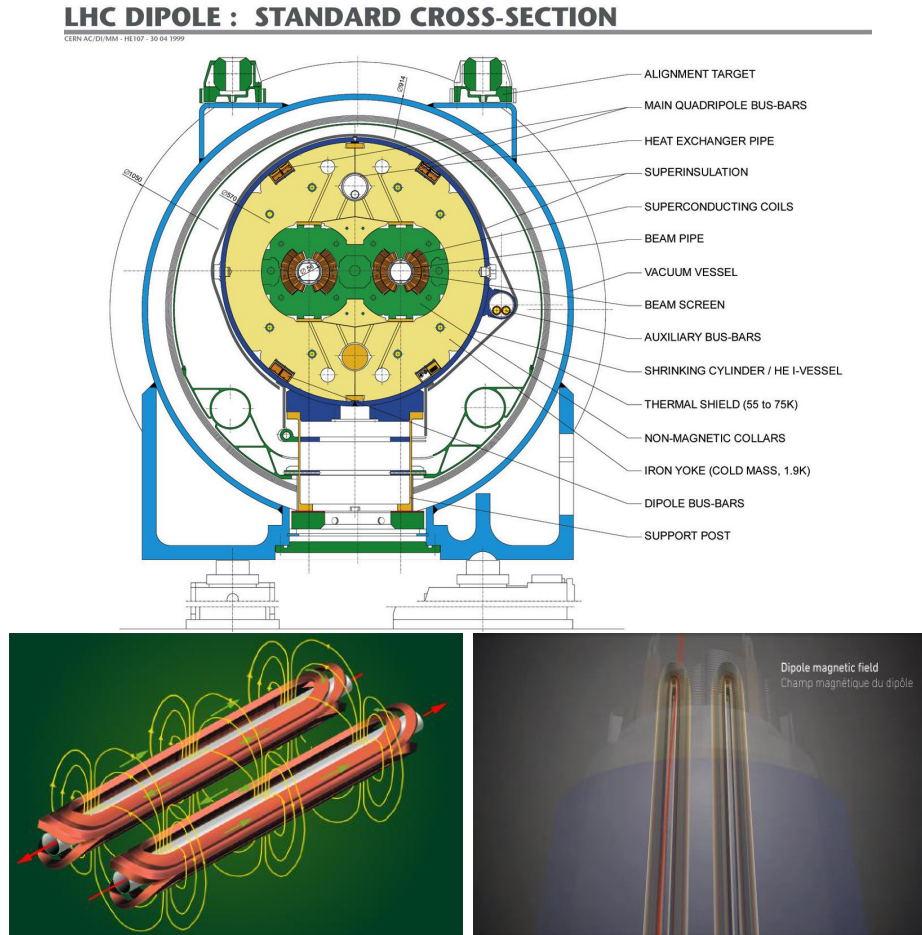


Figure 2.5: Top: LHC dipole magnet transverse view; cooling, shielding and mechanical support are indicated. Bottom left: Magnetic field generated by the dipole magnets; note that the direction of the field inside one beam pipe is opposite with respect to the other beam pipe which guarantee that both proton beams are curved in the same direction towards the center of the ring. The effect of the dipole magnetic field on the proton beam is represented on the bottom right side [66, 69, 70].

1211 magnetic field generated by the dipole magnets is shown on the bottom left side of
 1212 Figure 2.5. The bending effect of the magnetic field on the proton beam is shown on
 1213 the bottom right side of Figure 2.5. Note that the dipole magnets are not curved;
 1214 the arc section of the LHC ring is composed of straight dipole magnets of about 15
 1215 m. In total there are 1232 dipole magnets along the LHC ring.
 1216 In addition to the bending of the beam trajectory, the beam has to be focused. The

focusing is performed by quadrupole magnets installed in a different straight section; in total 858 quadrupole magnets are installed along the LHC ring. Other effects like electromagnetic interaction among bunches, interaction with electron clouds from the beam pipe, the gravitational force on the protons, differences in energy among protons in the same bunch, among others, are corrected using sextupole and other magnetic multipoles.

The two proton beams inside the LHC ring are made of bunches with a cylindrical shape of about 7.5 cm long and about 1 mm in diameter; when bunches are close to the interaction point (IP), the beam is focused up to a diameter of about 16 μm in order to maximize the probability of collisions between protons. The number of collisions per second is proportional to the cross section of the bunches with the *luminosity* (L) as the proportionality factor, thus, the luminosity can be calculated using

$$L = fn \frac{N_1 N_2}{4\pi\sigma_x\sigma_y} \quad (2.2)$$

where f is the revolution frequency, n is the number of bunches per beam, N_1 and N_2 are the numbers of protons per bunch, σ_x and σ_y are the gaussian transverse sizes of the bunches. With the expected parameters, the LHC expected luminosity is about

$$f = \frac{v}{2\pi r_{LHC}} \approx \frac{3 \times 10^8 \text{m/s}}{27 \text{km}} \approx 11.1 \text{kHz},$$

$$n = 2808$$

$$N_1 = N_2 \sim 1.5 \times 10^{11}$$

$$\sigma_x = \sigma_y = 16 \mu\text{m}$$

1232

$$L = 1.28 \times 10^{34} \text{cm}^{-2}\text{s}^{-1} = 1.28 \times 10^{-5} \text{fb}^{-1}\text{s}^{-1} \quad (2.3)$$

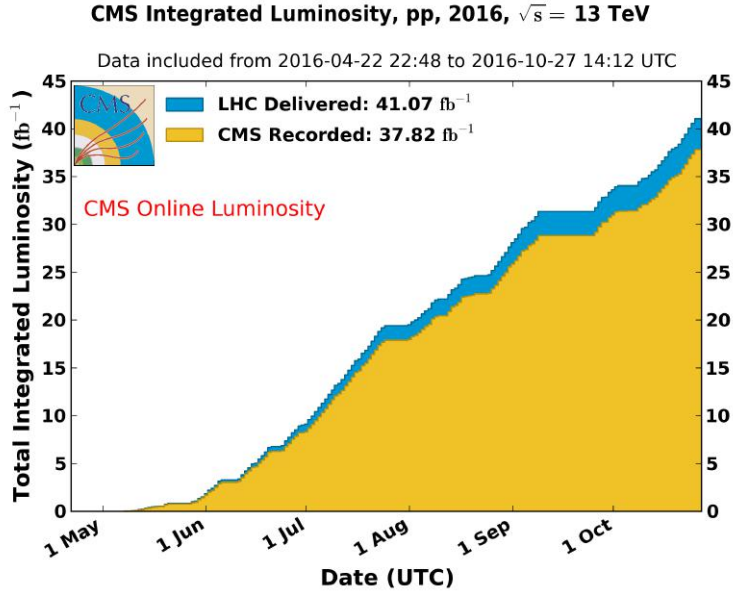


Figure 2.6: Integrated luminosity delivered by LHC and recorded by CMS during 2016. The difference between the delivered and the recorded luminosity is due to fails and issues occurred during the data taking in the CMS experiment [71].

1233 Luminosity is a fundamental aspect of LHC given that the bigger luminosity the
 1234 bigger number of collisions, which means that for processes with a very small cross
 1235 section the number of expected occurrences is increased and so the chances of being
 1236 detected. The integrated luminosity, collected by the CMS experiment during 2016
 1237 is shown in Figure 2.6; the data analyzed in this thesis corresponds to an integrated
 1238 luminosity of 35.9 fb^{-1} at a center of mass-energy $\sqrt{s} = 13 \text{ TeV}$.

1239 One way to increase L is increasing the number of bunches in the beam. Cur-
 1240 rently, the separation between two consecutive bunches in the beam is 7.5 m which
 1241 corresponds to a time separation of 25 ns. In the full LHC ring the allowed number
 1242 of bunches is $n = 27\text{km}/7.5\text{m} = 3600$; however, there are some gaps in the bunch pat-
 1243 tern intended for preparing the dumping and injection of the beam, thus, the proton
 1244 beams are composed of 2808 bunches.

1245 Once the proton beams reach the desired energy, they are brought to cross each

1246 other producing pp collisions. The bunch crossing happens in precise places where
 1247 the four LHC experiments are located, as seen in the top of Figure 2.7. In 2008 pp
 1248 collisions of $\sqrt{s} = 7$ TeV were performed; the energy was increased to 8 TeV in 2012
 1249 and to 13 TeV in 2015.

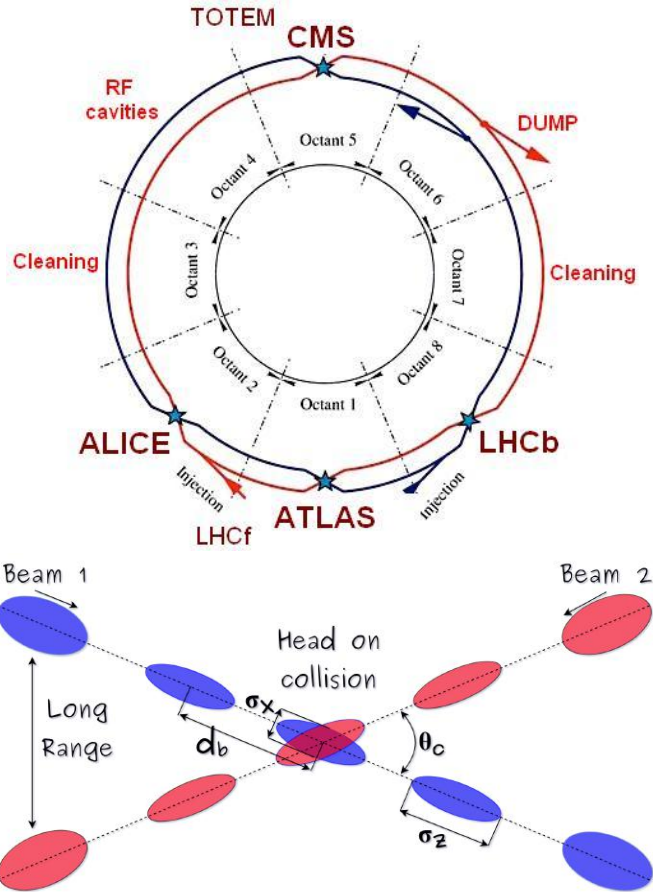


Figure 2.7: Top: LHC interaction points. Bunch crossing occurs where the LHC experiments are located [72]. Sections indicated as cleaning are dedicated to collimate the beam in order to protect the LHC ring from collisions with protons in very spreaded bunches. Bottom: bunch crossing scheme. Since the bunch crossing is not perfectly head-on, the luminosity is reduced in a factor of 17%; adapted from Reference [86].

1250 The CMS and ATLAS experiments are multi-purpose experiments, hence, they
 1251 are enabled to explore physics in any of the LHC collision modes. LHCb experiment
 1252 is optimized to explore bottom quark physics, while ALICE is optimized for heavy

1253 ion collisions searches; TOTEM and LHCf are dedicated to forward physics studies;
 1254 MoEDAL (not indicated in the Figure) is intended for monopole or massive pseudo
 1255 stable particles searches.

1256 At the IP there are two interesting details that need to be addressed. The first
 1257 one is that the bunch crossing does not occur head-on but at a small crossing angle θ_c
 1258 (280 μ rad in CMS and ATLAS) as shown in the bottom side of Figure 2.7, affecting
 1259 the overlapping between bunches; the consequence is a reduction of about 17% in
 1260 the luminosity (represented by a factor not included in eqn. 2.2). The second one
 1261 is the occurrence of multiple pp collisions in the same bunch crossing; this effect is
 1262 called *pileup* (PU). A fairly simple estimation of the PU follows from estimating the
 1263 probability of collision between two protons, one from each of the bunches in the
 1264 course of collision; it depends roughly on the ratio of proton size and the cross section
 1265 of the bunch in the IP, i.e.,

$$P(pp\text{-}collision) \sim \frac{d_{proton}^2}{\sigma_x \sigma_y} = \frac{(1\text{fm})^2}{(16\mu\text{m})^2} \sim 4 \times 10^{-21} \quad (2.4)$$

1266 however, there are $N = 1.15 \times 10^{11}$ protons in a bunch, thus the estimated number of
 1267 collisions in a bunch crossing is

$$PU = N^2 * P(pp\text{-}collision) \sim 50pp \text{ collision per bunch crossing}, \quad (2.5)$$

1268 about 20 of which are inelastic. A multiple pp collision event in a bunch crossing at
 1269 CMS is shown in Figure 2.8.

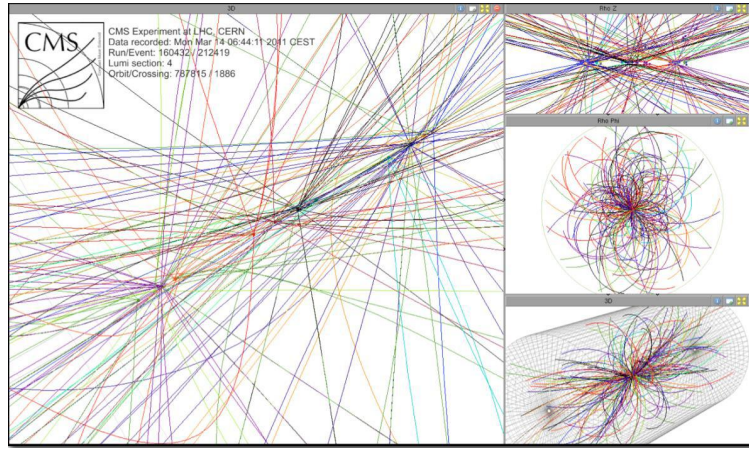


Figure 2.8: Multiple pp collision bunch crossing at CMS. [73].

1270 2.3 The CMS experiment

1271 CMS is a general-purpose detector designed to conduct research in a wide range
 1272 of physics from the standard model to new physics like extra dimensions and dark
 1273 matter. Located at Point 5 in the LHC layout as shown in Figure 2.4, CMS is
 1274 composed of several detection systems distributed in a cylindrical structure; in total,
 1275 CMS weights about 12500 tons in a very compact 21.6 m long and 14.6 m diameter
 1276 cylinder. It was built in 15 separate sections at the ground level and lowered to the
 1277 cavern individually to be assembled. A complete and detailed description of the CMS
 1278 detector and its components is given in Reference [74] on which this section is based.
 1279 Figure 2.9 shows the layout of the CMS detector. The detection system is composed
 1280 of (from the innermost to the outermost)

- 1281 • Pixel detector.
- 1282 • Silicon strip tracker.
- 1283 • Preshower detector.
- 1284 • Electromagnetic calorimeter.

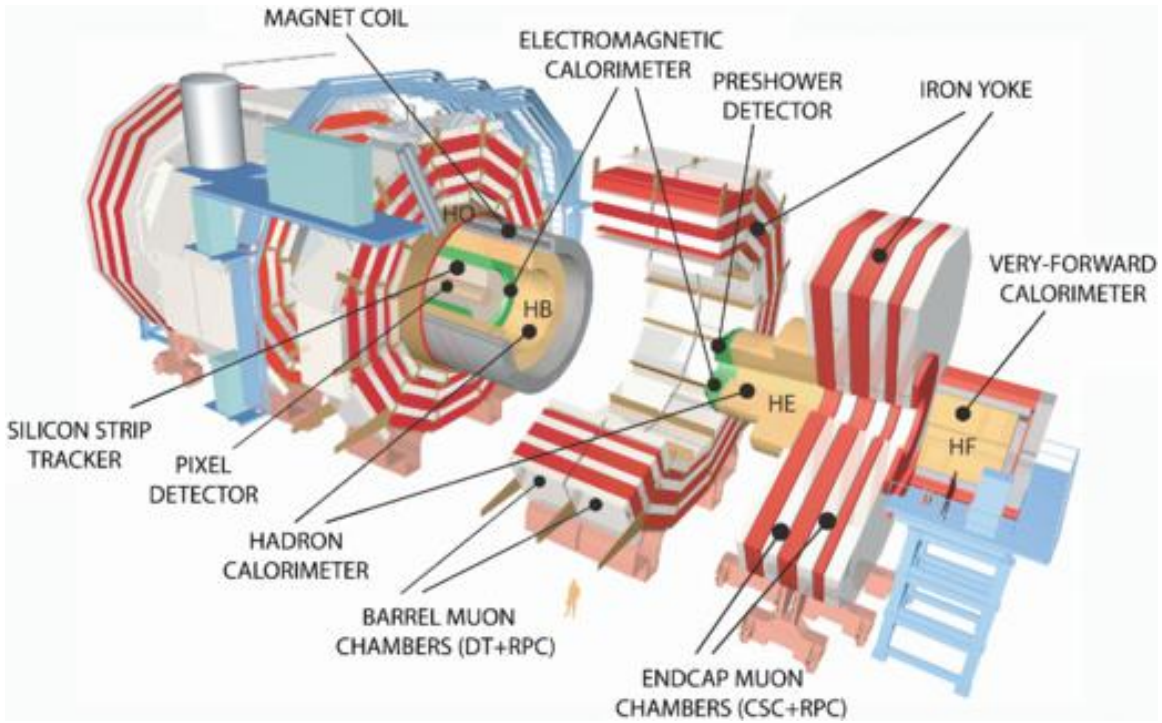


Figure 2.9: Layout of the CMS detector. The several subdetectors are indicated. The central region of the detector is referred as the barrel section while the endcaps are referred as the forward sections. [75].

1285 • Hadronic calorimeter.

1286 • Muon chambers (barrel and endcap)

1287 The central region of the detector is commonly referred as the barrel section while
1288 the endcaps are referred as the forward sections of the detector; thus, each subdetector
1289 is composed of a barrel section and a forward section.

1290 When a pp collision happens inside the CMS detector, many different particles are
1291 produced, but only some of them live long enough to be detected; they are electrons,
1292 photons, pions, kaons, protons, neutrons and muons; neutrinos are not detected by
1293 the CMS detector. Thus, the CMS detector was designed to detect those particles and
1294 measure their properties. Figure 2.10 shows a transverse slice of the CMS detector.
1295 The silicon tracker (pixel detector + strip tracker) is capable to register the track of

1296 the charged particles traversing it, while calorimeters (electromagnetic and hadronic)
 1297 measure the energy of the particles that are absorbed by their materials. Considering
 1298 the detectable particles, mentioned above, emerging from the IP, a basic description
 1299 of the detection process is as follows.

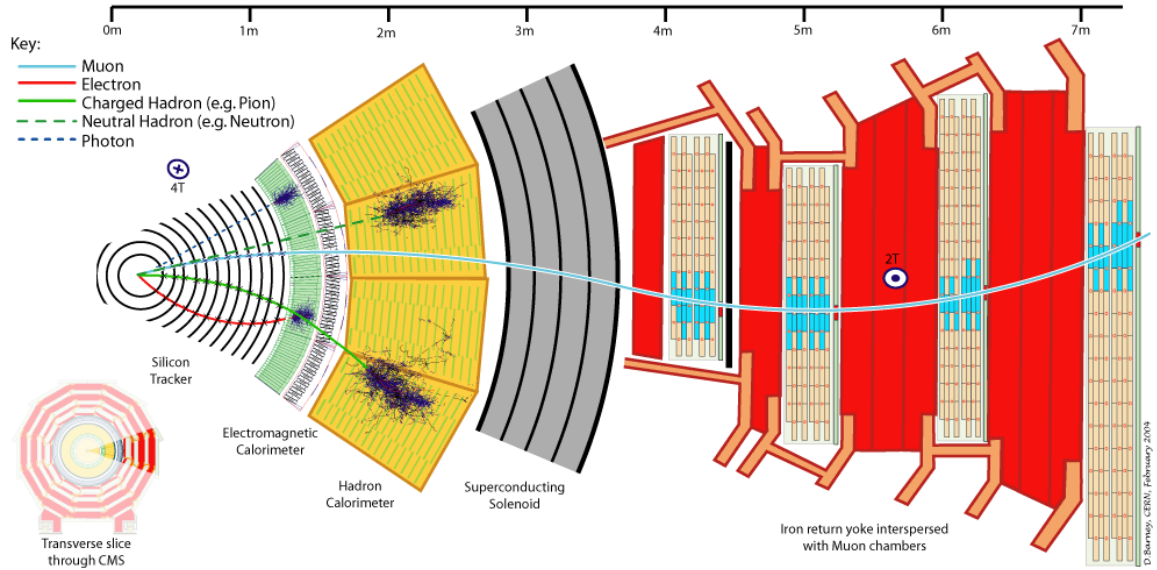


Figure 2.10: CMS detector transverse slice [76].

1300 A muon emerging from the IP, will create a track on the silicon tracker and on
 1301 the muon chambers. The design of the CMS detector is driven by the requirements
 1302 on the identification, momentum resolution and unambiguous charge determination
 1303 of the muons; therefore, a large bending power is provided by the solenoid magnet
 1304 made of superconducting cable capable of generating a 3.8 T magnetic field. The
 1305 muon track is bent twice since the magnetic field inside the solenoid is directed along
 1306 the z -direction but outside its direction is reversed. Muons interact very weakly with
 1307 the calorimeters, therefore, it is not absorbed but escape away from the detector.

1308 An electron emerging from the IP will create a track along the tracker which will
 1309 be bent due to the presence of the magnetic field, later, it will be absorbed in the
 1310 electromagnetic calorimeter where its energy is measured.

1311 A photon will not leave a track because it is neutral, but it will be absorbed in
 1312 the electromagnetic calorimeter.

1313 A neutral hadron, like the neutron, will not leave a track either but it will lose a
 1314 small amount of its energy during its passage through the electromagnetic calorimeter
 1315 and then it will be absorbed in the hadron calorimeter depositing the rest of its energy.

1316 A charged hadron, like the proton or π^\pm , will leave a curved track on the silicon
 1317 tracker, some of its energy in the electromagnetic calorimeter and finally will be
 1318 absorbed in the hadronic calorimeter.

1319 A more detailed description of each detection system will be presented in the
 1320 following sections.

1321 2.3.1 CMS coordinate system

1322 The coordinate system used by CMS is centered on the geometrical center of the
 1323 detector which is the nominal IP as shown in Figure 2.11¹. The z -axis is parallel
 1324 to the beam direction, while the Y -axis pointing vertically upward, and the X -axis
 1325 pointing radially inward toward the center of the LHC.

1326 In addition to the common cartesian and cylindrical coordinate systems, two co-
 1327 ordinates are of particular utility in particle physics: rapidity (y) and pseudorapidity
 1328 (η), defined in connection to the polar angle θ , energy and longitudinal momentum
 1329 component (momentum along the z -axis) according to

$$y = \frac{1}{2} \ln \frac{E + p_z}{E - p_z} \quad \eta = -\ln \left(\tan \frac{\theta}{2} \right) \quad (2.6)$$

1330 Rapidity is related to the angle between the XY -plane and the direction in which
 1331 the products of a collision are emitted; it has the nice property that the difference

¹ Not all the pp interaction occur at the nominal IP because of the bunch lenght, therefore, each pp collision has its own IP location

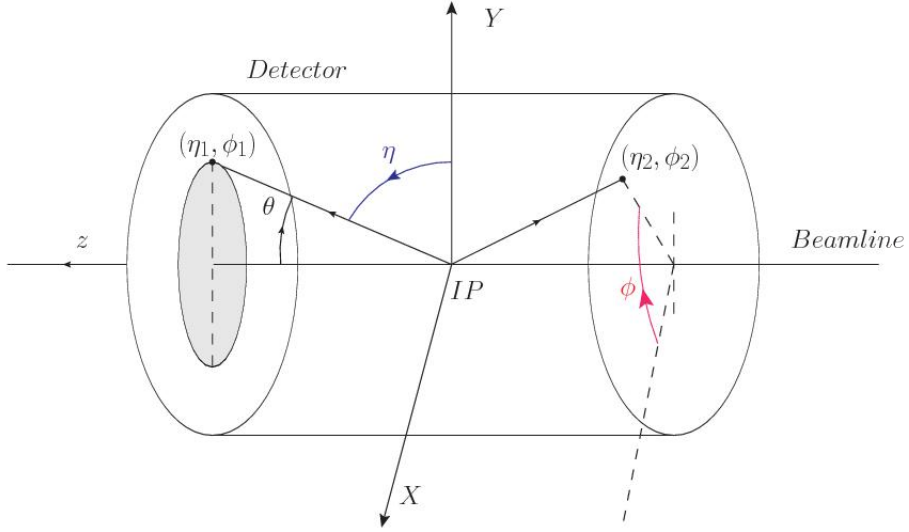


Figure 2.11: CMS detector coordinate system.

1332 between the rapidities of two particles is invariant with respect to Lorentz boosts
 1333 along the z -axis, hence, data analysis becomes more simple when based on rapid-
 1334 ity; however, it is not simple to measure the rapidity of highly relativistic particles,
 1335 as those produced after pp collisions. Under the highly relativistic motion approxi-
 1336 mation, y can be rewritten in terms of the polar angle, concluding that rapidity is
 1337 approximately equal to the pseudorapidity defined above, i.e., $y \approx \eta$. Note that η
 1338 is easier to measure than y given the direct relationship between the former and the
 1339 polar angle.

1340 The angular distance between two objects in the detector (ΔR) is commonly used
 1341 to judge the isolation of those object; it is defined in terms of their coordinates (η_1, ϕ_1) ,
 1342 (η_2, ϕ_2) as

$$\Delta R = \sqrt{(\Delta\eta)^2 - (\Delta\phi)^2} \quad (2.7)$$

1343 2.3.2 Tracking system

1344 The CMS tracking system is designed to provide a precise measurement of the trajectories (*track*) followed by the charged particles created after the pp collisions; also, the
 1345 precise reconstruction of the primary and secondary origins of the tracks (*vertices*) is
 1346 expected in an environment where, each 25 ns, the bunch crossing produces about 20
 1347 inelastic collisions and about 1000 particles.
 1348

1349 Physics requirements guiding the tracking system performance include the precise characterization of events involving gauge bosons, W and Z, and their leptonic
 1350 decays for which an efficient isolated lepton and photon reconstruction is of capital
 1351 importance, given that isolation is required to suppress background events to a level
 1352 that allows observations of interesting processes like Higgs boson decays or beyond
 1353 SM events.

1355 The ability to identify and reconstruct b -jets and B-hadrons within these jets is also
 1356 a fundamental requirement, achieved through the ability to reconstruct accurately
 1357 displaced vertices, given that b -jets are part of the signature of top quark physics, like
 1358 the one treated in this thesis.

1359 An schematic view of the CMS tracking system is shown in Figure 2.12

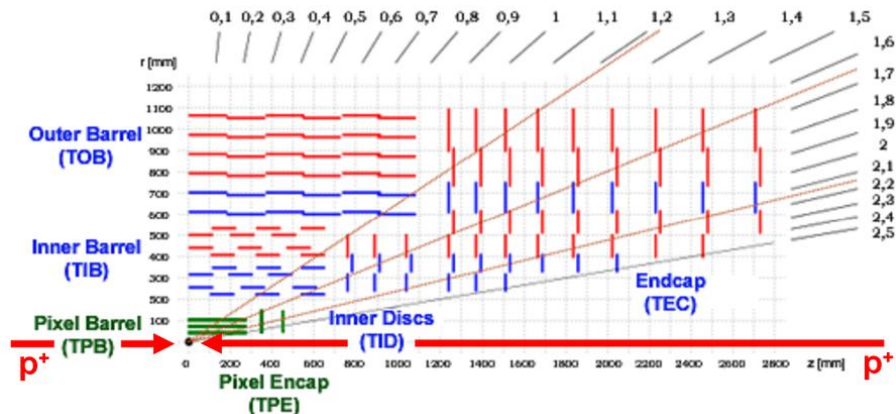


Figure 2.12: CMS tracking system schematic view [78].

1360 In order to satisfy these performance requirements, the tracking system uses two
 1361 different detector subsystems arranged in concentric cylindrical volumes, the pixel
 1362 detector and the silicon strip tracker; the pixel detector is located in the high particle
 1363 density region ($r < 20\text{cm}$) while the silicon strip tracker is located in the medium and
 1364 lower particle density regions $20\text{cm} < r < 116\text{cm}$.

1365 **Pixel detector**

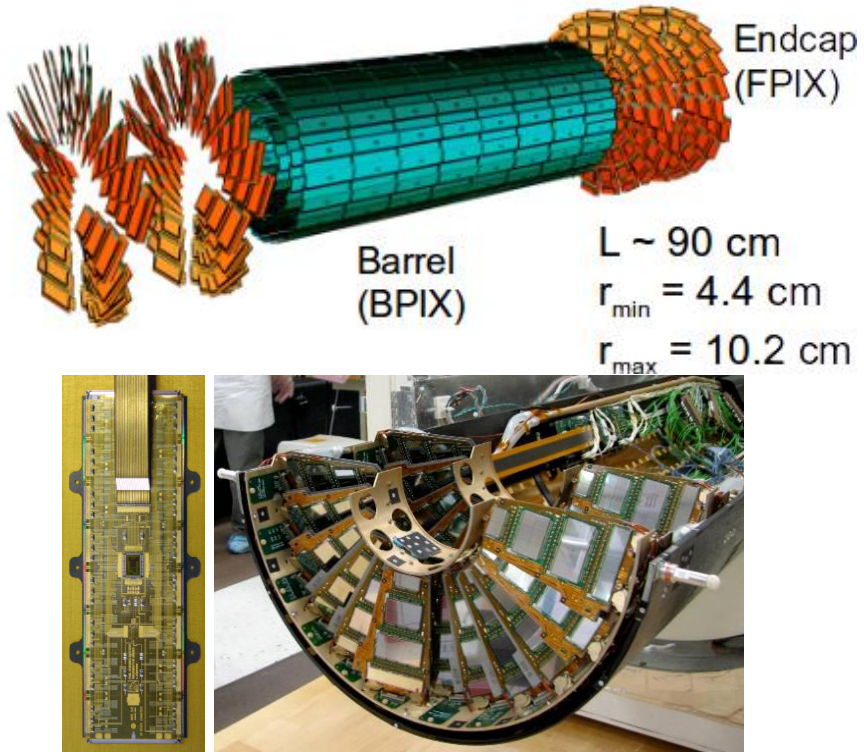


Figure 2.13: CMS pixel detector. Top: schematic view; Bottom: pictures of a barrel(BPIX) module(left) and forward modules(right) [74].

1366 The pixel detector was replaced during the 2016-2017 extended year-end technical
 1367 stop, due to the increasingly challenging operating conditions like the higher particle
 1368 flux and more radiation harsh environment, among others. The new one is responding
 1369 as expected, reinforcing its crucial role in the successful way to fulfill the new LHC

physics objectives after the discovery of the Higgs boson. Since the data sets used in this thesis were produced using the previous version of the pixel detector, it will be the subject of the description in this section. The last chapter of this thesis is dedicated to describe my contribution to the *Forward Pixel Phase 1 upgrade*.

The pixel detector was composed of 1440 silicon pixel detector modules organized in three-barrel layers in the central region (BPix) and two disks in the forward region (FPix) as shown in the top side of Figure 2.13; it was designed to record efficiently and with high precision, up to $20\mu\text{m}$ in the XY -plane and $20\mu\text{m}$ in the z -direction, the first three space-points (*hits*) nearest to the IP region in the range $|\eta| \leq 2.5$. The first barrel layer was located at a radius of 44 mm from the beamline, while the third layer was located at a radius of 102 mm, closer to the strip tracker inner barrel layer (see Section 2.3.3) in order to reduce the rate of fake tracks. The high granularity of the detector is represented in its about 66 Mpixels, each of size $100 \times 150\mu\text{m}^2$. The transverse momentum resolution of tracks can be measured with a resolution of 1-2% for muons of $p_T = 100$ GeV.

A charged particle passing through the pixel sensors produce ionization in them, giving energy for electrons to be removed from the silicon atoms, hence, creating electron-hole pairs. The collection of charges in the pixels generates an electrical signal that is read out by an electronic readout chip (ROC); each pixel has its own electronics which amplifies the signal. Combining the signal from the pixels activated by a traversing particle in the several layers of the detector allows one to reconstruct the particle's trajectory in 3D.

Commonly, the charge produced by traversing of a particle is collected by and shared among several pixels; by interpolating between pixels, the spatial resolution is improved. In the barrel section the charge sharing in the $r\phi$ -plane is due to the Lorentz effect. In the forward pixels the charge sharing is enhanced by arranging the

1396 blades in the turbine-like layout as shown in Figure 2.13 bottom left.

1397 2.3.3 Silicon strip tracker

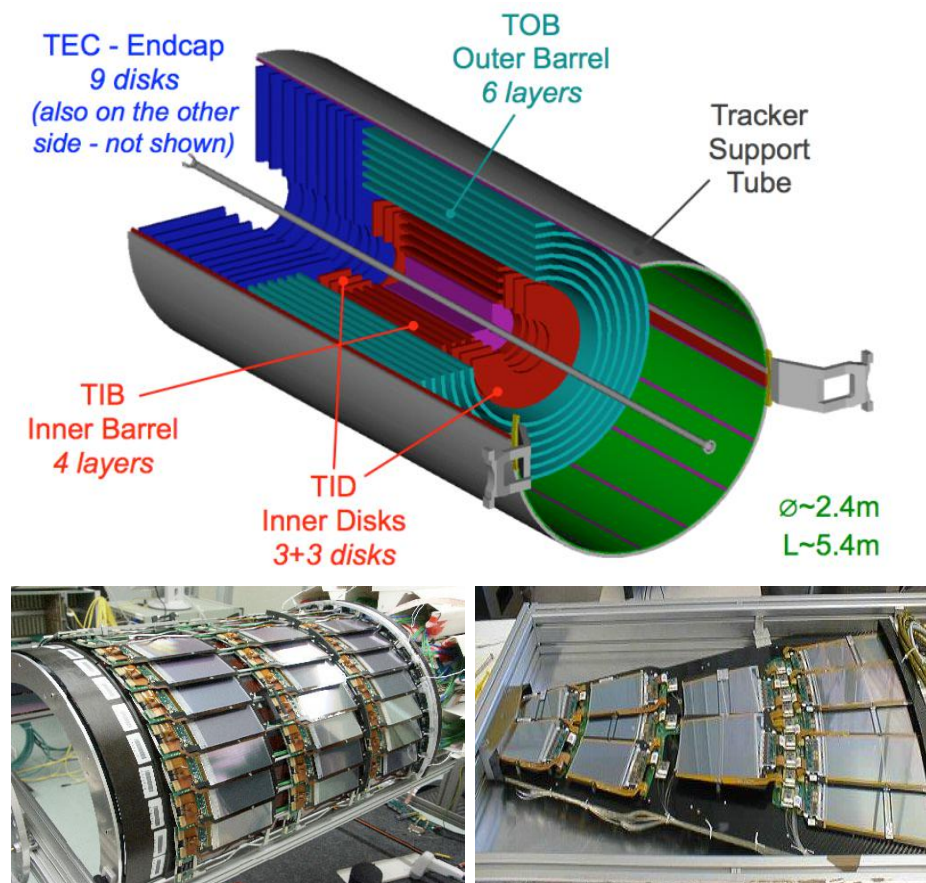


Figure 2.14: Top: CMS Silicon Strip Tracker (SST) schematic view. The SST is composed of the tracker inner barrel (TIB), the tracker inner disks (TID), the tracker outer barrel (TOB) and the tracker endcaps (TEC). Each part is made of silicon strip modules; the modules in blue represent two modules mounted back-to-back and rotated in the plane of the module by a stereo angle of 120 mrad in order to provide a 3-D reconstruction of the hit positions. Bottom: pictures of the TIB (left) and TEC (right) modules [80–82].

1398 The silicon strip tracker (SST) is the second stage in the CMS tracking system.

1399 The top side of Figure 2.14 shows a schematic of the SST. The inner tracker region is

1400 composed of the tracker inner barrel (TIB) and the tracker inner disks (TID) covering

1401 the region $r < 55$ cm and $|z| < 118$ cm. The TIB is composed of 4 layers while the TID

1402 is composed of 3 disks at each end. The silicon sensors in the inner tracker are 320
 1403 μm thick, providing a resolution of about 13-38 μm in the $r\phi$ position measurement.

1404 The modules indicated in blue in the schematic view of Figure 2.14 are two mod-
 1405 ules mounted back-to-back and rotated in the plane of the module by a *stereo* angle
 1406 of 100 mrad; the hits from these two modules, known as *stereo hits*, are combined to
 1407 provide a measurement of the second coordinate (z in the barrel and r on the disks)
 1408 allowing the reconstruction of hit positions in 3-D.

1409 The outer tracker region is composed of the tracker outer barrel (TOB) and the
 1410 tracker endcaps (TEC). The six layers of the TOB offer coverage in the region $r > 55$
 1411 cm and $|z| < 118$ cm, while the 9 disks of the TEC cover the region $124 < |z| < 282$
 1412 cm. The resolution offered by the outer tracker is about 13-38 μm in the $r\phi$ position
 1413 measurement. The inner four TEC disks use silicon sensors 320 μm thick; those in
 1414 the TOB and the outer three TEC disks use silicon sensors of 500 μm thickness. The
 1415 silicon strips run parallel to the z -axis and the distance between strips varies from 80
 1416 μm in the inner TIB layers to 183 μm in the inner TOB layers; in the endcaps the
 1417 wedge-shaped sensors with radial strips, whose pitch range between 81 μm at small
 1418 radii and 205 μm at large radii.

1419 The whole SST has 15148 silicon modules, 9.3 million silicon strips and cover a
 1420 total active area of about 198 m^2 .

1421 2.3.4 Electromagnetic calorimeter

1422 The CMS electromagnetic calorimeter (ECAL) is designed to measure the energy of
 1423 electrons and photons. It is composed of 75848 lead tungstate crystals which have a
 1424 short radiation length (0.89 cm) and fast response, since 80% of the light is emitted
 1425 within 25 ns; however, they are combined with Avalanche photodiodes (APDs) as

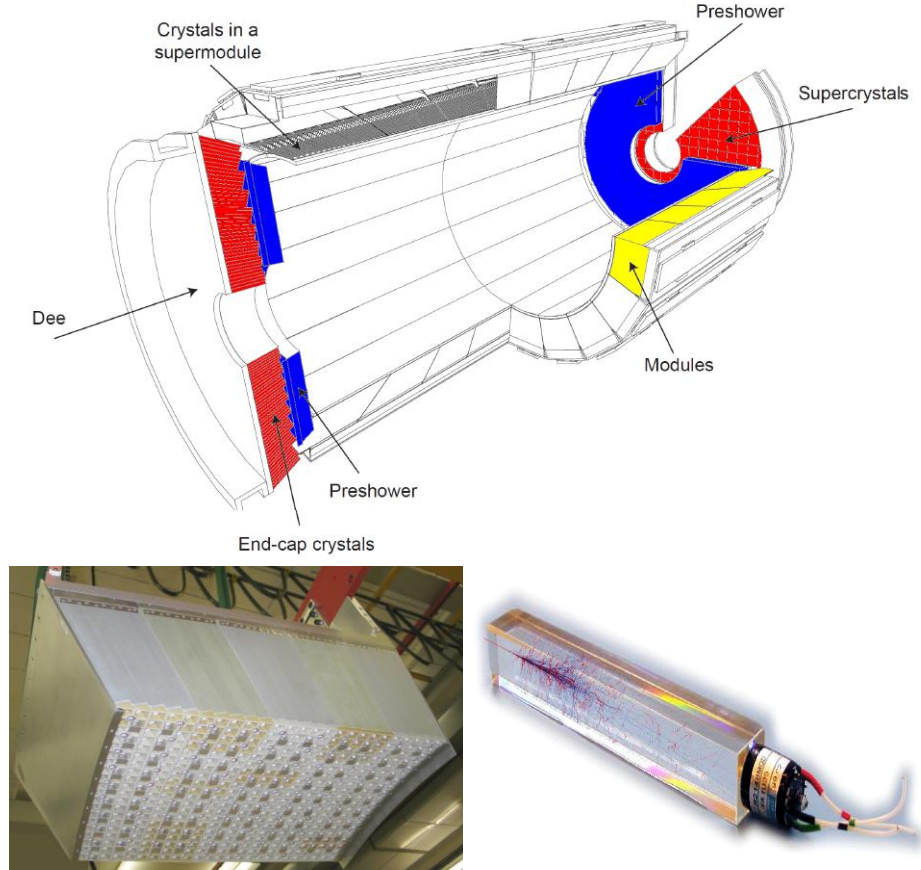


Figure 2.15: Top: CMS ECAL schematic view. Bottom: Module equipped with the crystals (left); ECAL crystal(right) with an artistic representation of an electromagnetic shower [74].

1426 photodetectors given that crystals themselves have a low light yield ($30\gamma/\text{MeV}$). A
 1427 schematic view of the ECAL is shown in Figure 2.15.

1428 Energy is measured when electrons and photons are absorbed by the crystals
 1429 which generates an electromagnetic *shower*, as seen in bottom right picture of the
 1430 Figure 2.15; the shower is seen as a *cluster* of energy which depending on the amount
 1431 of energy deposited can involve several crystals. The ECAL barrel (EB) covers the
 1432 region $|\eta| < 1.479$, using crystals of depth of 23 cm and $2.2 \times 2.2 \text{ cm}^2$ transverse
 1433 section; the ECAL endcap (EE) covers the region $1.479 < |\eta| < 3.0$ using crystals of
 1434 depth 22 cm and transverse section of $2.86 \times 2.86 \text{ cm}^2$; the photodetectors used are

1435 vacuum phototriodes (VPTs). Each EE is divided in two structures called *Dees*.

1436 The preshower detector (ES) is installed in front of the EE and covers the region
 1437 $1.653 < |\eta| < 2.6$. The ES provides a precise measurement of the position of electro-
 1438 magnetic showers, which allows to distinguish electrons and photon signals from π^0
 1439 decay signals. The ES is composed of a layer of lead radiators followed by a layer of
 1440 silicon strip sensors. The lead radiators initiate electromagnetic showers when reached
 1441 by photons and electrons, then, the strip sensors measure the deposited energy and
 1442 the transverse shower profiles. The full ES thickness is 20 cm.

1443 2.3.5 Hadronic calorimeter

1444 Hadrons are not absorbed by the ECAL² but by the hadron calorimeter (HCAL),
 1445 which is made of a combination of alternating brass absorber layers and silicon photo-
 1446 multiplier(SiPM) layers; therefore, particles passing through the scintillator material
 1447 produce showers, as in the ECAL, as a result of the inelastic scattering of the hadrons
 1448 with the detector material. Since the particles are not absorbed in the scintillator,
 1449 their energy is sampled; therefore the total energy is not measured but estimated from
 1450 the energy clusters, which reduces the resolution of the detector. Brass was chosen
 1451 as the absorber material due to its short interaction length ($\lambda_I = 16.42\text{cm}$) and its
 1452 non-magnetivity. Figure 2.16 shows a schematic view of the CMS HCAL.

1453 The HCAL is divided into four sections; the Hadron Barrel (HB), the Hadron
 1454 Outer (HO), the Hadron Endcap (HE) and the Hadron Forward (HF) sections. The
 1455 HB covers the region $0 < |\eta| < 1.4$, while the HE covers the region $1.3 < |\eta| < 3.0$.
 1456 The HF, made of quartz fiber scintillator and steel as absorption material, covers the
 1457 forward region $3.0 < |\eta| < 5.2$. Both the HB and HF are located inside the solenoid.
 1458 The HO is placed outside the magnet as an additional layer of scintillators with the

² Most hadrons are not absorbed, but few low-energy ones might be.

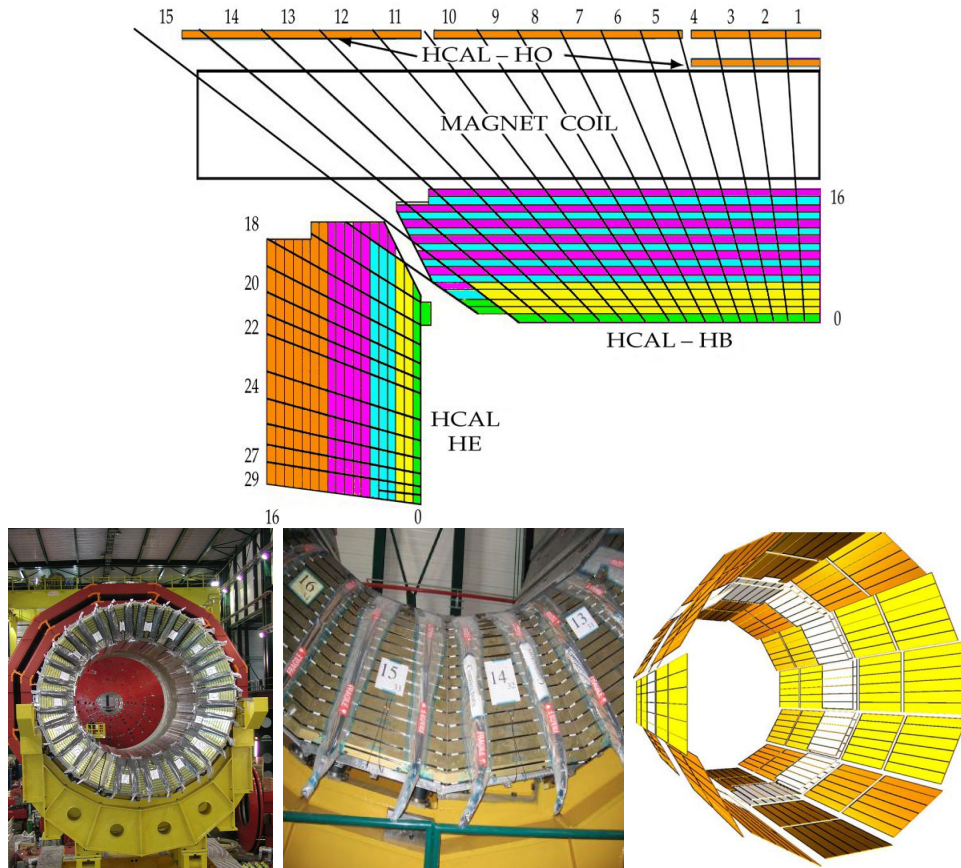


Figure 2.16: Top: CMS HCAL schematic view, the colors indicate the layers that are grouped into the same readout channels. Bottom: picture of a section of the HB; the absorber material is the golden region and scintillators are placed in between the absorber material (left and center). Schematic view of the HO (right). [83,84]

1459 purpose of measure the energy tails of particles passing through the HB and the
 1460 magnet (see Figure 2.16 top and bottom right).

1461 **2.3.6 Superconducting solenoid magnet**

1462 The superconducting magnet installed in the CMS detector is designed to provide
 1463 an intense and highly uniform magnetic field in the central part of the detector.
 1464 In fact, the tracking system takes advantage of the bending power of the magnetic
 1465 field to measure with precision the momentum of the particles that traverse it; the

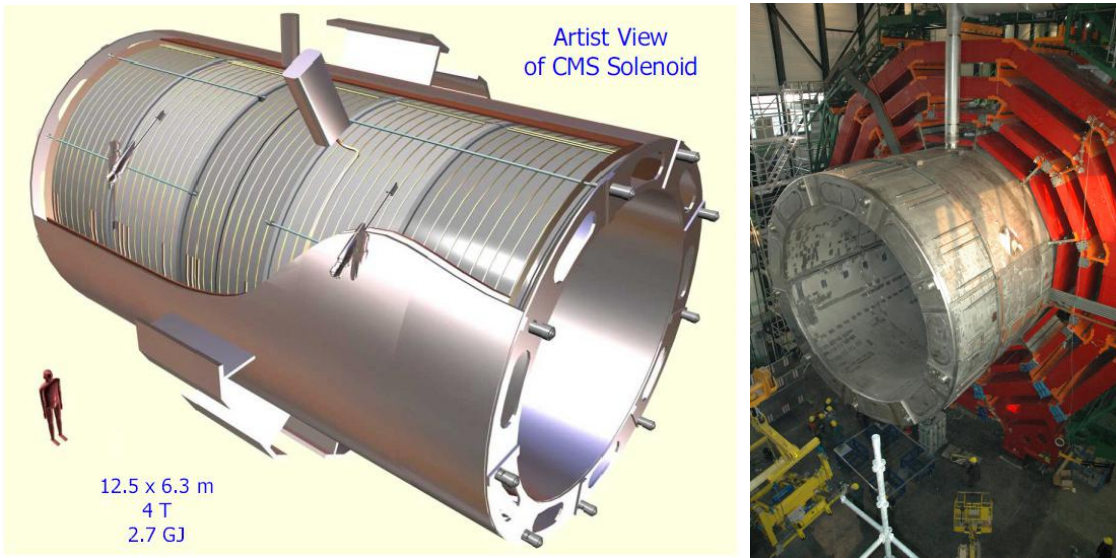


Figure 2.17: Artistic representation of the CMS solenoid magnet(left). The magnet is supported on an iron yoke (right) which also serves as the house of the muon detector and as mechanical support for the whole CMS detector [77].

1466 unambiguous determination of the sign for high momentum muons was a driving
 1467 principle during the design of the magnet. The magnet has a diameter of 6.3 m, a
 1468 length of 12.5 m and a cold mass of 220 t; the generated magnetic field reaches a
 1469 strength of 3.8T. Since it is made of Ni-Tb superconducting cable it has to operate at
 1470 a temperature of 4.7 K by using a helium cryogenic system; the current circulating in
 1471 the cables reaches 18800 A under normal running conditions. The left side of Figure
 1472 2.17 shows an artistic view of the CMS magnet, while the right side shows a transverse
 1473 view of the cold mass where the winding structure is visible.

1474 The yoke (see Figure 2.17), composed of 5 barrel wheels and 6 endcap disks made
 1475 of iron, serves not only as the media for magnetic flux return but also provides housing
 1476 for the muon detector system and structural stability to the full detector.

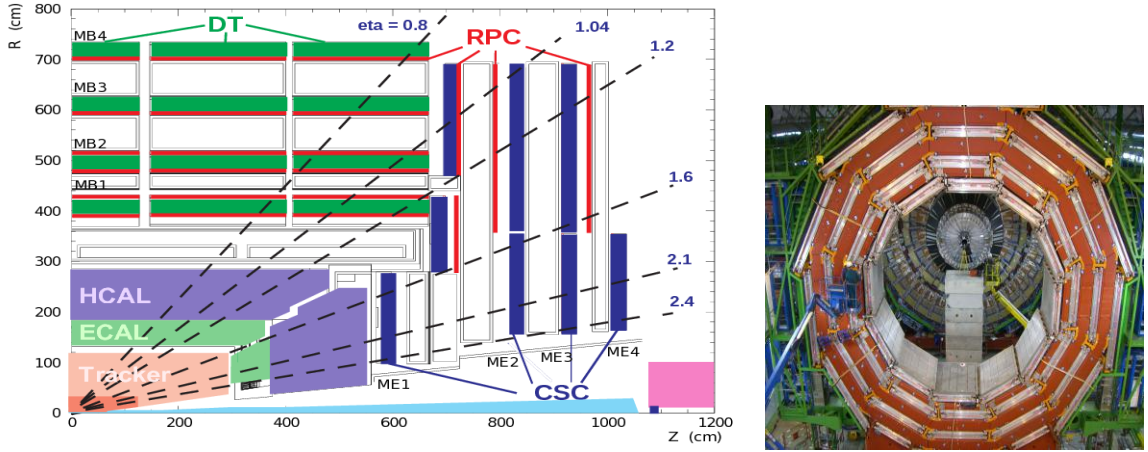


Figure 2.18: Left: CMS muon system schematic view; Right: one of the yoke rings with the muon DTs and RPCs installed; in the back it is possible to see the muon endcap [85].

1477 2.3.7 Muon system

1478 Muons are the only charged particles able to pass through all the CMS detector due
 1479 to their low ionization energy loss; thus, muons can be separated easily from the
 1480 high amount of particles produced in a pp collision. Also, muons are expected to be
 1481 produced in the decay of several new particles; therefore, good detection of muons
 1482 was one of the leading principles when designing the CMS detector.

1483 The CMS muon detection system (muon spectrometer) is embedded in the return
 1484 yoke as seen in Figure 2.18. It is composed of three different detector types, the drift
 1485 tube chambers (DT), cathode strip chambers (CSC), and resistive plate chambers
 1486 (RPC); DT are located in the central region $\eta < 1.2$ arranged in four layers of drift
 1487 chambers filled with an Ar/CO₂ gas mixture.

1488 The muon endcaps are made of CSCs covering the region $\eta < 2.4$ and filled with
 1489 a mixture of Ar/CO₂/CF₄. The reason behind using a different detector type lies on
 1490 the different conditions in the forward region like the higher muon rate and higher
 1491 residual magnetic field compared to the central region.

1492 The third type of detector used in the muon system is a set of four disks of RPCs

1493 working in avalanche mode. The RPCs provide good spatial and time resolutions. The
 1494 track of high- p_T muon candidates is built combining information from the tracking
 1495 system and the signal from up to six RPCs and four DT chambers.

1496 The muon tracks are reconstructed from the hits in the several layers of the muon
 1497 system.

1498 2.3.8 CMS trigger system

1499 CMS expects pp collisions every 25 ns, i.e., an interaction rate of 40 MHz for which
 1500 it is not possible to store the recorded data in full. In order to handle this high event
 1501 rate data, an online event selection, known as triggering, is performed; triggering
 1502 reduces the event rate to 100 Hz for storage and further offline analysis.

1503 The trigger system starts with a reduction of the event rate to 100 kHz in the
 1504 so-called *the level 1 trigger* (L1). L1 is based on dedicated programmable hardware
 1505 like Field Programmable Gate Arrays (FPGAs) and Application Specific Integrated
 1506 Circuits (ASICs), partly located in the detector itself; another portion is located in
 1507 the CMS underground cavern. Hit pattern information from the muon chambers
 1508 and the energy deposits in the calorimeter are used to decide if an event is accepted
 1509 or rejected, according to selection requirements previously defined, which reflect the
 1510 interesting physics processes. Figure 2.19 shows the L1 trigger architecture.

1511 The second stage in the trigger system is called *the high-level trigger* (HLT); events
 1512 accepted by L1 are passed to HLT in order to make an initial reconstruction of them.
 1513 HLT is software based and runs on a dedicated server farm, using selection algorithms
 1514 and high-level object definitions; the event rate at HLT is reduced to 100 Hz. The
 1515 first HLT stage takes information from the muon detectors and the calorimeters to
 1516 make the initial object reconstruction; in the next HLT stage, information from the

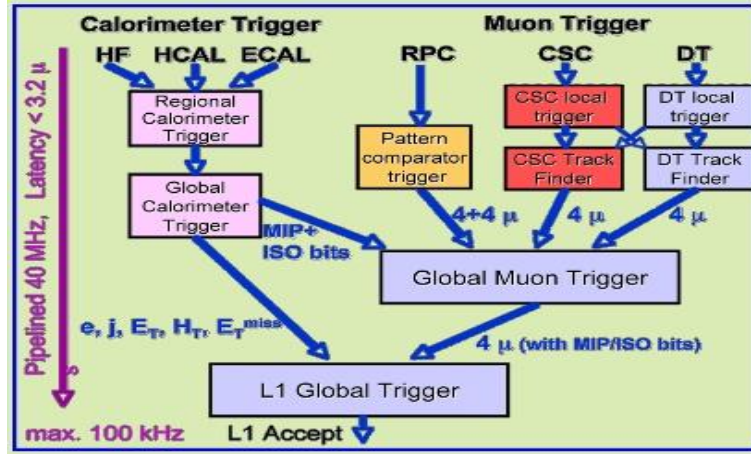


Figure 2.19: CMS Level-1 trigger architecture [86].

pixel and strip detectors is used to do first fast tracking and then full tracking online.
This initial object reconstruction is used in further steps of the trigger system.

Events and preliminary reconstructed physics objects from HLT are sent to be fully reconstructed at the CERN computing center known also as Tier-0 facility. Again, the pixel detector information provides high-quality seeds for the track reconstruction algorithm offline, primary vertex reconstruction, electron and photon identification, muon reconstruction, τ identification, and b-tagging. After full reconstruction, data sets are made available for offline analyses.

2.3.9 CMS computing

Data coming from the experiment have to be stored and made available for further analysis; in order to cope with all the tasks implied in the offline data processing, like transfer, simulation, reconstruction and reprocessing, among others, a large computing power is required. The CMS computing system is based on the distributed architecture concept, where users of the system and physical computer centers are distributed worldwide and interconnected by high-speed networks.

The worldwide LHC computing grid (WLCG) is the mechanism used to provide

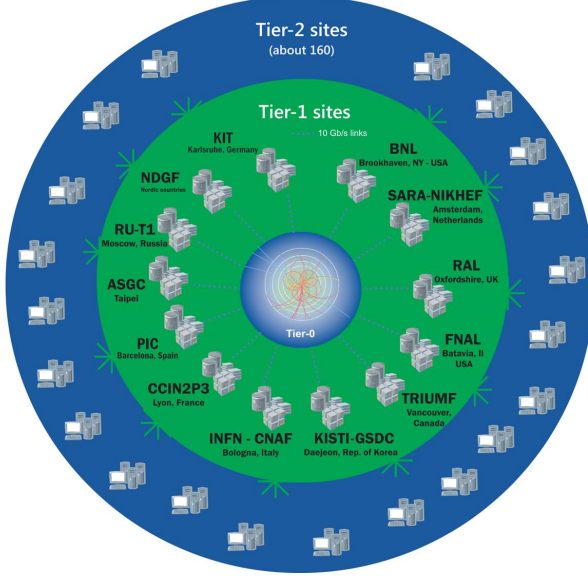


Figure 2.20: WLCG structure. The primary computer centers (Tier-0) are located at CERN (data center) and at the Wigner datacenter in Budapest. Tier-1 is composed of 13 centers and Tier-2 is composed of about 160 centers. [87].

1533 that distributed environment. WLCG is a tiered structure connecting computing
 1534 centers around the world, which provides the necessary storage and computing facil-
 1535 ities. The primary computing centers of the WLCG are located at the CERN and
 1536 the Wigner datacenter in Budapest and are known as Tier-0 as shown in Figure 2.20.
 1537 The main responsibilities for each tier level are [87]

- 1538 • **Tier-0:** initial reconstruction of recorded events and storage of the resulting
 1539 datasets, the distribution of raw data to the Tier-1 centers.
- 1540 • **Tier-1:** provide storage capacity, support for the Grid, safe-keeping of a pro-
 1541 portional share of raw and reconstructed data, large-scale reprocessing and safe-
 1542 keeping of corresponding output, generation of simulated events, distribution
 1543 of data to Tier 2s, safe-keeping of a share of simulated data produced at these
 1544 Tier 2s.
- 1545 • **Tier-2:** store sufficient data and provide adequate computing power for spe-

1546 cific analysis tasks and proportional share of simulated event production and
1547 reconstruction.

1548 Aside from the general computing strategy to manage the huge amount of data
1549 produced by experiments, CMS uses a software framework to perform a variety of
1550 processing, selection and analysis tasks. The central concept of the CMS data model
1551 referred to as *event data model* (EDM) is the *Event*; therefore, an event is the unit
1552 that contains the information from a single bunch crossing, any data derived from
1553 that information like the reconstructed objects, and the details of the derivation.

1554 Events are passed as the input to the *physics modules* that obtain information
1555 from them and create new information; for instance, *event data producers* add new
1556 data into the events, *analyzers* produce an information summary from an event set,
1557 *filters* perform selection and triggering.

1558 CMS uses several event formats with different levels of detail and precision

1559 • **Raw format:** events in this format contain the full recorded information from
1560 the detector as well as trigger decision and other metadata. An extended version
1561 of raw data is used to store information from the CMS Monte Carlo simulation
1562 tools (see Chapter 3). Raw data are stored permanently, occupying about
1563 2MB/event

1564 • **RECO format:** events in this format correspond to raw data that have been
1565 submitted to reconstruction algorithms like primary and secondary vertex re-
1566 construction, particle ID, and track finding. RECO events contain physics ob-
1567 jects and all the information used to reconstruct them; average size is about 0.5
1568 MB/event.

- 1569 • **AOD format:** Analysis Object Data (AOD) is the data format used in the
 1570 physics analyses given that it contains the parameters describing the high-level
 1571 physics objects in addition to enough information to allow a kinematic refitting if
 1572 needed. AOD events are filtered versions of the RECO events to which skimming
 1573 or other filtering have been applied, hence AOD events are subsets of RECO
 1574 events. Requires about 100 kB/event.
- 1575 • **Non-event data** are data needed to interpret and reconstruct events. Some
 1576 of the non-event data used by CMS contains information about the detector
 1577 contraction and condition data like calibrations, alignment, and detector status.

1578 Figure 2.21 shows the data flow scheme between CMS detector and tiers.

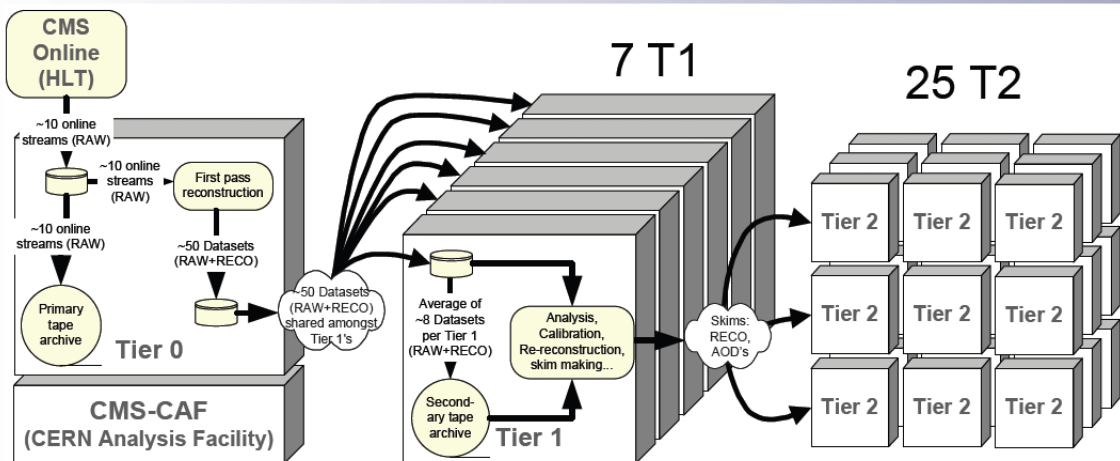


Figure 2.21: Data flow from CMS detector through tiers.

1579 The whole collection of software built as a framework is referred to as *CMSSW*. This
 1580 framework provides the services needed by the simulation, calibration and alignment,
 1581 and reconstruction modules that process event data, so that physicists can perform
 1582 analysis. The CMSSW event processing model is composed of one executable, called
 1583 `cmsRun`, and several plug-in modules which contains all the tools (calibration, recon-

1584 struction algorithms) needed to process an event. The same executable is used for
1585 both detector data and Monte Carlo simulations [88].

1586 **Chapter 3**

1587 **Event generation, simulation and
1588 reconstruction**

1589 The process of analyzing data recorded by the CMS experiment involves several stages
1590 where the data are processed in order to interpret the information provided by all
1591 the detection systems; in those stages, the particles produced after the pp collision
1592 are identified by reconstructing their trajectories and measuring their features. In
1593 addition, the SM provides a set of predictions that have to be compared with the
1594 experimental results; however, in most of the cases, theoretical predictions are not
1595 directly comparable to experimental results due to the diverse source of uncertainties
1596 introduced by the experimental setup and theoretical approximations, among others.

1597 The strategy to face these conditions consists in using statistical methods imple-
1598 mented in computational algorithms to produce numerical results that can be con-
1599 trasted with the experimental results. These computational algorithms are commonly
1600 known as Monte Carlo (MC) methods and, in the case of particle physics, they are
1601 designed to apply the SM rules and produce predictions about the physical observ-
1602 ables measured in the experiments. Since particle physics is governed by quantum

mechanics principles, predictions are not allowed from single events; therefore, a high number of events are *generated* and predictions are produced in the form of statistical distributions for the observables. Effects of the detector presence are included in the predictions by introducing simulations of the detector itself.

This chapter presents a description of the event generation strategy and the tools used to perform the detector simulation and physics objects reconstruction. A comprehensive review of event generators for LHC physics can be found in Reference [89] on which this chapter is based.

3.1 Event generation

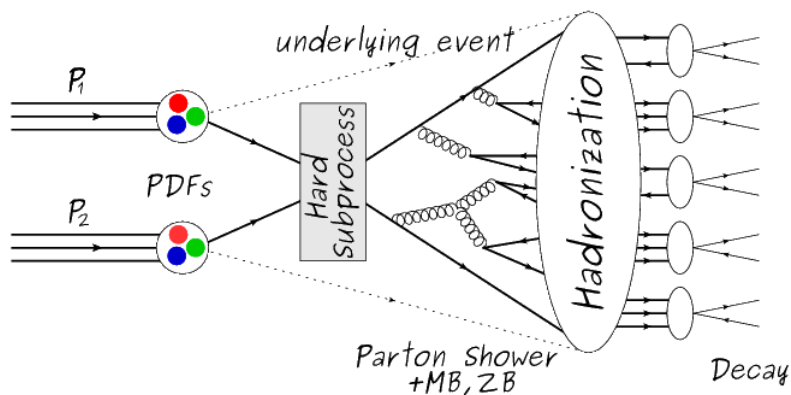


Figure 3.1: Event generation process. The actual interaction is generated in the hard subprocess. The parton shower describes the evolution of the partons from the hard subprocess. Modified from Reference [90].

The event generation is intended to create events that mimic the behavior of actual events produced in collisions; they obey a sequence of steps from the particles collision hard process to the decay process into the final state. Figure 3.1 shows a schematic view of the event generation process; the fact that the full process can be treated as several independent steps is motivated by the QCD factorization theorem.

1617 Generation starts by taking into account the PDFs of the incoming particles.
 1618 Event generators offer the option to chose from several PDF sets depending on the
 1619 particular process under simulation¹; in the following, pp collisions will be consid-
 1620 ered. The *hard subprocess* describes the actual interaction between partons from the
 1621 incoming protons; it is represented by the matrix element connecting the initial and
 1622 final states of the interaction. Normally, the matrix element can be written as a
 1623 sum over Feynman diagrams and consider interferences between terms in the sum-
 1624 mation. During the generation of the hard subprocess, the production cross section
 1625 is calculated.

1626 The order to which the cross section is calculated depends on the order of the Feyn-
 1627 man diagrams involved in the calculation; therefore, radiative corrections are included
 1628 by considering a higher order Feynman diagrams where QCD radiation dominates.
 1629 Currently, cross sections calculated to LO do not offer a satisfactory description of the
 1630 processes, i.e., the results are only reliable for the shape of distributions; therefore,
 1631 NLO calculations have to be performed with the implication that the computing time
 1632 needed is highly increased.

1633 The final parton content of the hard subprocess is subjected to the *parton shower*
 1634 which generates the gluon radiation. Parton shower evolves the partons, i.e., glouns
 1635 split into quark-antiquark pairs and quarks with enough energy radiate gluons giv-
 1636 ing rise to further parton multiplication, following the DGLAP (Dokshitzer-Gribov-
 1637 Lipatov-Altarelli-Parisi) equations. Showering continues until the energy scale is low
 1638 enough to reach the non-perturbative limit.

1639 In the simulation of LHC processes that involve b quarks, like the single top quark
 1640 or Higgs associated production, it is needed to consider that the b quark is heavier
 1641 than the proton; hence, the QCD interaction description is made in two different

¹ Tool in Reference [91] allows to plot different PDF sets under customizable conditions.

1642 schemes [95]

- 1643 • four-flavor (4F) scheme. b quarks appear only in the final state because they
 1644 are heavier than the proton and therefore they can be produced only from the
 1645 splitting of a gluon into pairs or singly in association with a t quark in high
 1646 energy-scale interactions; furthermore, during the simulation, the b -PDFs are set
 1647 to zero. Calculations in this scheme are more complicated due to the presence
 1648 of the second b quark but the full kinematics is considered already at LO and
 1649 therefore the accuracy of the description is better.

- 1650 • five-flavor (5F) scheme. b quarks are considered massless, therefore they can
 1651 appear in both initial and final states since they can now be part of the proton;
 1652 thus, during the simulation b -PDFs are not set to zero. In this scheme, calcu-
 1653 lations are simpler than in the 4F scheme and possible logarithmic divergences
 1654 are absorbed by the PDFs through the DGLAP evolution.

1655 In this thesis, the tHq events are generated using the 4F scheme in order to reduce
 1656 uncertainties, while the tHW events are generated using the 5F scheme to eliminate
 1657 LO interference with $t\bar{t}H$ process [48].

1658 Partons involved in the pp collision are the focus of the simulation, however, the
 1659 rest of the partons inside the incoming protons are also affected because the remnants
 1660 are colored objects; also, multiple parton interactions can occur. The hadronization
 1661 of the remnants and multiple parton interactions are known as *underlying event* and
 1662 it has to be included in the simulation. In addition, multiple pp collisions in the same
 1663 bunch crossing (pile-up mentioned in 2.2) occurs, actually in two forms

- 1664 • *in-time PU* which refers to multiple pp collision in the bunch crossing but that
 1665 are not considered as primary vertices.

1666 • *Out-of-time PU* which refers to overlapping pp collisions from consecutive bunch
 1667 crossings; this can occur due to the time-delays in the detection systems where
 1668 information from one bunch crossing is assigned to the next or previous one.

1669 While the underlying event effects are included in generation using generator-
 1670 specific tools, PU effects are added to the generation by overlaying Minimum-bias (MB)
 1671 and Zero-bias (ZB) events to the generated events. MB events are inelastic events
 1672 selected by using a loose trigger with as little bias as possible, therefore accepting a
 1673 large fraction of the overall inelastic event; ZB events correspond to random events
 1674 recorded by the detector when collisions are likely. MB models in-time PU and ZB
 1675 models out-of-time PU.

1676 The next step in the generation process is called *hadronization*. Since particles
 1677 with a net color charge are not allowed to exits isolated, they have to recombine
 1678 to form bound states. This is precisely the process by which the partons resulting
 1679 from the parton shower arrange themselves as color singlets to form hadrons. At
 1680 this step, the energy-scale is low and the strong coupling constant is large, therefore
 1681 hadronization process is non-perturbative and the evolution of the partons is described
 1682 using phenomenological models. Most of the baryons and mesons produced in the
 1683 hadronization are unstable and hence they will decay in the detector.

1684 The last step in the generation process corresponds to the decay of the unstable
 1685 particles generated during hadronization; it is also simulated in the hadronization
 1686 step, based on the known branching ratios.

1687 **3.2 Monte Carlo Event Generators.**

1688 The event generation described in the previous section has been implemented in
 1689 several software packages for which a brief description is given.

- 1690 • **PYTHIA 8.** It is a program designed to perform the generation of high energy
 1691 physics events which describes the collisions between particles such as electrons
 1692 and protons. Several theories and models are implemented in it, in order to
 1693 describe physical aspects like hard and soft interaction, parton distributions,
 1694 initial and final-state parton showers, multiple parton interactions, beam rem-
 1695 nants, hadronization² and particle decay. Thanks to extensive testing, several
 1696 optimized parametrizations, known as *tunings*, have been defined in order to
 1697 improve the description of actual collisions to a high degree of precision; for
 1698 analysis at $\sqrt{s} = 13$ TeV, the underline event CUETP8M1 tune is employed [97].
 1699 The calculation of the matrix element is performed at LO which is not enough
 1700 for the current required level of precision; therefore, pythia is often used for
 1701 parton shower, hadronization and decays, while other event generators are used
 1702 to generate the matrix element at NLO.
- 1703 • **MadGraph5_aMC@NLO.** MadGraph is a matrix element generator which
 1704 calculates the amplitudes for all contributing Feynman diagrams of a given
 1705 process but does not provide a parton shower while MC@NLO incorporates
 1706 NLO QCD matrix elements consistently into a parton shower framework; thus,
 1707 MadGraph5_aMC@NLO, as a merger of the two event generators MadGraph5
 1708 and aMC@NLO, is an event generator capable to calculate tree-level and NLO
 1709 cross sections and perform the matching of those with the parton shower. It is
 1710 one of the most frequently used matrix element generators; however, it has the
 1711 particular feature of the presence of negative event weights which reduce the
 1712 number of events used to reproduce the properties of the objects generated [98].
- 1713 • **POWHEG.** It is an NLO matrix element generator where the hardest emis-

² based in the Lund string model [96]

1714 sion of color charged particles is generated in such a way that the negative event
 1715 weights issue of MadGraph5_aMC@NLO is overcome; however, the method re-
 1716 quires an interface with p_T -ordered parton shower or a parton shower generator
 1717 where this highest emission can be vetoed in order to avoid double counting of
 1718 this highest-energetic emission. PYTHIA is a commonly matched to POWHEG
 1719 event generator [100].

1720 Events resulting from the whole generation process are known as MC events.

1721 **3.3 CMS detector simulation.**

1722 After generation, MC events contain the physics of the collisions but they are not
 1723 ready to be compared to the events recorded by the experiment since these recorded
 1724 events correspond to the response of the detection systems to the interaction with
 1725 the particles traversing them. The simulation of the CMS detector has to be applied
 1726 on top of the event generation; it is simulated with a MC toolkit for the simulation
 1727 of particles passing through matter called Geant4 which is also able to simulate the
 1728 electronic signals that would be measured by all detectors inside CMS.

1729 The simulation takes the generated particles contained in the MC events as input,
 1730 makes them pass through the simulated geometry, and models physics processes that
 1731 particles experience during their passage through matter. The full set of results from
 1732 particle-matter interactions corresponds to the simulated hit which contains informa-
 1733 tion about the energy loss, momentum and position. Particles of the input event are
 1734 called *primary*, while the particles originating from GEANT4-modeled interactions of
 1735 a primary particle with matter are called a *secondary*. Simulated hits are the input
 1736 of subsequent modules that emulate the response of the detector readout system and

1737 triggers. The output from the emulated detection systems and triggers is known as
 1738 digitization [101, 102].

1739 The modeling of the CMS detector corresponds to the accurate modeling of the
 1740 interaction among particles, the detector material, and the magnetic field. This
 1741 simulation procedure includes the following standard steps

1742 • Modeling of the Interaction Region.

1743 • Modeling of the particle passage through the hierarchy of volumes that compose
 1744 CMS detector and of the accompanying physics processes.

1745 • Modeling of the effect of multiple interactions per beam crossing and/or the
 1746 effect of events overlay (Pile-Up simulation).

1747 • Modeling of the detector's electronics response, signal shape, noise, calibration
 1748 constants (digitization).

1749 In addition to the full simulation, i.e., a detailed detector simulation, a faster
 1750 simulation (FastSim) have been developed, that may be used where much larger
 1751 statistics are required. In FastSim, detector material effects are parametrized and
 1752 included in the hits; those hits are used as input of the same higher-level algorithms³
 1753 used to analyze the recorded events. In this way, comparisons between fast and full
 1754 simulations can be performed [104].

1755 After the full detector simulation, the output events can be directly compared
 1756 to events actually recorded in the CMS detector. The collection of MC events that
 1757 reproduces the expected physics for a given process is known as MC sample.

³ track fitting, calorimeter clustering, b tagging, electron identification, jet reconstruction and calibration, trigger algorithms which will be considered in the next sections

1758 **3.4 Event reconstruction.**

1759 The CMS experiment use the *particle-flow event reconstruction algorithm (PF)* to do
 1760 the reconstruction of particles produced in pp collisions. Next sections will present
 1761 a basic description of the *Elements* used by PF (tracker tracks, energy clusters, and
 1762 muon tracks), based in the References [105, 106] where more detailed descriptions can
 1763 be found.

1764 **3.4.1 Particle-Flow Algorithm.**

1765 Each of the several sub detection systems of the CMS detector is dedicated to identify
 1766 an specific type of particles, i.e., photons and electrons are absorbed by the ECAL
 1767 and their reconstruction is based on ECAL information; hadrons are reconstructed
 1768 from clusters in the HCAL while muons are reconstructed from hits in the muon
 1769 chambers. PF is designed to correlate signals from all the detector layers (tracks and
 1770 energy clusters) in order to reconstruct and identify each final state particle and its
 1771 properties as sketched in Figure 3.2.

1772 For instance, a charged hadron is identified by a geometrical connection, known
 1773 as *link*, between one or more calorimeter clusters and a track in the tracker, provided
 1774 there are no hits in the muon system; combining several measurements allows a better
 1775 determination of the energy and charge sign of the charged hadron.

1776 **Charged-particle track reconstruction.**

1777 The strategy used by PF in order to reconstruct tracks is called *Iterative Tracking*
 1778 which occurs in four steps

- 1779 • Seed generation where initial track candidates are found by looking for a combi-
 1780 nation of hits in the pixel detector, strip tracker, and muon chambers. In total

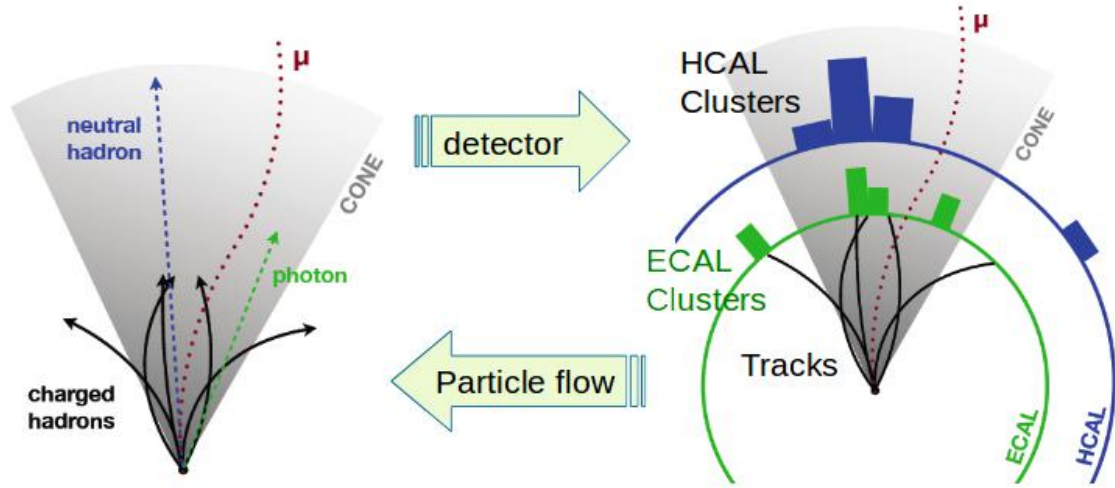


Figure 3.2: Particle flow algorithm. Information from the several CMS detection systems is provided as input to the algorithm which then combines it to identify and reconstruct all the particles in the final state and their properties. Reconstruction of simulated events is also performed by providing information from MC samples, detector and trigger simulation [107].

1781 ten iterations are performed, each one with a different seeding requirement.
 1782 Seeds are used to estimate the trajectory parameters and uncertainties at the
 1783 time of the full track reconstruction. Seeds are also considered track candidates.

- 1784 • Track finding using a tracking software known as Combinatorial Track Finder
 1785 (CTF) [108]. The seed trajectories are extrapolated along the expected flight
 1786 path of a charged particle, in agreement to the trajectory parameters obtained
 1787 in the first step, in an attempt to find additional hits that can be assigned to
 1788 the track candidates.
- 1789 • Track-fitting where the found tracks are passed as input to a module which
 1790 provides the best estimate of the parameters of each trajectory.
- 1791 • Track selection where track candidates are submitted to a selection which dis-
 1792 cards those that fail a set of defined quality criteria.

1793 Iterations differ in the seeding configuration and the final track selection as elab-

1794 orated in References [105, 106]. In the first iteration, high p_T tracks and tracks pro-
 1795 duced near to the interaction region are identified and those hits are masked thereby
 1796 reducing the combinatorial complexity. Next, iterations search for more complicated
 1797 tracks, like low p_T tracks and tracks from b hadron decays, which tend to be displaced
 1798 from the interaction region.

1799 **Vertex reconstruction.**

1800 During the track reconstruction, an extrapolation toward to the calorimeters is per-
 1801 formed in order to match energy deposits; that extrapolation is performed also toward
 1802 the beamline in order to find the origin of the track known as *vertex*. The vertex re-
 1803 construction is performed by selecting from the available reconstructed tracks, those
 1804 that are consistent with being originated in the interaction region where pp collisions
 1805 are produced. The selection involves a requirement on the number of tracker (pixel
 1806 and strip) hits and the goodness of the track fit.

1807 Selected tracks are clustered using a *deterministic annealing algorithm* (DA)⁴. A
 1808 set of candidate vertices and their associated tracks, resulting from the DA, are then
 1809 fitted with an *adaptive vertex fitter* (AVF) to produce the best estimate of the vertices
 1810 locations.

1811 The p_T of the tracks associated to a reconstructed vertex is added, squared and
 1812 used to organize the vertices; the vertex with the highest squared sum is designated
 1813 as the *primary vertex* (PV) while the rest are designated as PU vertices.

1814 **Calorimeter clustering.**

1815 After traversing the CMS tracker system, electrons, photons and hadrons deposit their
 1816 energy in the ECAL and HCAL cells. The PF clustering algorithm aims to provide

⁴ DA algorithm and AVF are described in detail in References [110, 111]

1817 a high detection efficiency even for low-energy particles and an efficient distinction
 1818 between close energy deposits. The clustering runs independently in the ECAL barrel
 1819 and endcaps, HCAL barrel and endcaps, and the two preshower layers, following two
 1820 steps

- 1821 • cells with an energy larger than a given seed threshold and larger than the energy
 1822 of the neighboring cells are identified as cluster seeds. The neighbor cells are
 1823 those that either share a side with the cluster seed candidate, or the eight closest
 1824 cells including cells that only share a corner with the seed candidate.
- 1825 • cells with at least a corner in common with a cell already in the cluster seed
 1826 and with an energy above a cell threshold are grouped into topological clusters.

1827 Clusters formed in this way are known as *particle-flow clusters*. With this cluster-
 1828 ing strategy, it is possible to detect and measure the energy and direction of photons
 1829 and neutral hadrons as well as differentiate these neutral particles from the charged
 1830 hadron energy deposits. In cases involving charged hadrons for which the track pa-
 1831 rameters are not determined accurately, for instance, low-quality and high- p_T tracks,
 1832 clustering helps in the energy measurements.

1833 **Electron track reconstruction.**

1834 Although the charged-particle track reconstruction described above works for elec-
 1835 trons, they lose a significant fraction of their energy via bremsstrahlung photon radi-
 1836 ation before reaching the ECAL; thus, the reconstruction performance depends on the
 1837 ability to measure also the radiated energy. The reconstruction strategy, in this case,
 1838 requires information from the tracking system and from the ECAL. Bremsstrahlung
 1839 photons are emitted at similar η values to that of the electron but at different values
 1840 of ϕ ; therefore, the radiated energy can be recovered by grouping ECAL clusters in a

1841 η window over a range of ϕ around the electron direction. The group is called ECAL
 1842 supercluster.

1843 Electron candidates from the track-seeding and ECAL super clustering are merged
 1844 into a single collection which is submitted to a full electron tracking fit with a
 1845 Gaussian-sum filter (GSF) [109]. The electron track and its associated ECAL su-
 1846 percluster form a *particle-flow electron*.

1847 **Muon track reconstruction.**

1848 Given that the CMS detector is equipped with a muon spectrometer capable to iden-
 1849 tify and measure the momentum of the muons traversing it, the muon reconstruction
 1850 is not specific to PF; therefore, three different muon types are defined

- 1851 • *Standalone muon.* A clustering on the DTs or CSCs hits is performed to form
 1852 track segments; those segments are used as seeds for the reconstruction in the
 1853 muon spectrometer. All DTs, CSCs, and RPCs hits along the muon trajectory
 1854 are combined and fitted to form the full track. The fitting output is called a
 1855 *standalone-muon track*.
- 1856 • *Tracker muon.* Each track in the inner tracker with p_T larger than 0.5 GeV and
 1857 a total momentum p larger than 2.5 GeV is extrapolated to the muon system.
 1858 A *tracker muon track* corresponds to a extrapolated track that matches at least
 1859 one muon segment.
- 1860 • *Global muon.* When tracks in the inner tracker (inner tracks) and standalone-
 1861 muon tracks are matched and turn out being compatibles, their hits are com-
 1862 bined and fitted to form a *global-muon track*.

1863 Global muons sharing the same inner track with tracker muons are merged into
 1864 a single candidate. PF muon identification uses the muon energy deposits in ECAL,
 1865 HCAL, and HO associated with the muon track to improve the muon identification.

1866 **Particle identification and reconstruction.**

1867 PF elements are connected by a linker algorithm that tests the connection between any
 1868 pair of elements; if they are found to be linked, a geometrical distance that quantifies
 1869 the quality of the link is assigned. Two elements may be linked indirectly through
 1870 common elements. Linked elements form *PF blocks* and each PF block may contain
 1871 elements originating in one or more particles. Links can be established between
 1872 tracks, between calorimeter clusters, and between tracks and calorimeter clusters.
 1873 The identification and reconstruction start with a PF block and proceed as follows

1874 • Muons. An *isolated global muon* is identified by evaluating the presence of
 1875 inner track and energy deposits close to the global muon track in the (η, ϕ)
 1876 plane, i.e., in a particular point of the global muon track, inner tracks and
 1877 energy deposits are sought within a radius of $\Delta R = 0.3$ (see eqn. 2.7) from the
 1878 muon track; if they exist and the p_T of the found track added to the E_T of the
 1879 found energy deposit does not exceed 10% of the muon p_T then the global muon
 1880 is an isolated global muon. This isolation condition is stringent enough to reject
 1881 hadrons misidentified as muons.

1882 *Non-isolated global muons* are identified using additional selection requirements
 1883 on the number of track segments in the muon system and energy deposits along
 1884 the muon track. Muons inside jets are identified with more stringent criteria
 1885 in isolation and momentum as described in Reference [112]. The PF elements
 1886 associated with an identified muon are masked from the PF block.

- 1887 ● Electrons are identified and reconstructed as described above plus some addi-
 1888 tional requirements on fourteen variables like the amount of energy radiated,
 1889 the distance between the extrapolated track position at the ECAL and the po-
 1890 sition of the associated ECAL supercluster, among others, which are combined
 1891 in an specialized multivariate analysis strategy that improves the electron iden-
 1892 tification. Tracks and clusters used to identify and reconstruct electrons are
 1893 masked in the PF block.
- 1894 ● Isolated photons are identified from ECAL superclusters with E_T larger than 10
 1895 GeV, for which the energy deposited at a distance of 0.15, from the supercluster
 1896 position on the (η, ϕ) plane, does not exceed 10% of the supercluster energy;
 1897 note that this is an isolation requirement. In addition, there must not be links
 1898 to tracks. Clusters involved in the identification and reconstruction are masked
 1899 in the PF block.
- 1900 ● Bremsstrahlung photons and prompt photons tend to convert to electron-positron
 1901 pairs inside the tracker, therefore, a dedicated finder algorithm is used to link
 1902 tracks that seem to originate from a photon conversion; in case those two tracks
 1903 are compatible with the direction of a bremsstrahlung photon, they are also
 1904 linked to the original electron track. Photon conversion tracks are also masked
 1905 in the PF block.
- 1906 ● The remaining elements in the PF block are used to identify hadrons. In the
 1907 region $|\eta| \leq 2.5$, neutral hadrons are identified with HCAL clusters not linked
 1908 to any track while photons from neutral pion decays are identified with ECAL
 1909 clusters without links to tracks. In the region $|\eta| > 2.5$ ECAL clusters linked to
 1910 HCAL clusters are identified with a charged or neutral hadron shower; ECAL
 1911 clusters with no links are identified with photons. HCAL clusters not used yet,

1912 are linked to one or more unlinked tracks and to an unlinked ECAL in order to
 1913 reconstruct charged-hadrons or a combination of photons and neutral hadrons
 1914 according to certain conditions on the calibrated calorimetric energy.

- 1915 • Charged-particle tracks may be liked together when they converge to a *sec-*
 1916 *ondary vertex (SV)* displaced from the IP where the PV and PU vertices are
 1917 reconstructed; at least three tracks are needed in that case, of which at most
 1918 one has to be an incoming track with hits in tracker region between a PV and
 1919 the SV.

1920 The linker algorithm, as well as the whole PF algorithm, has been validated and
 1921 commissioned; results from that validation are presented in the Reference [105].

1922 **Jet reconstruction.**

1923 Quarks and gluons may be produced in the pp collisions, therefore, their hadronization
 1924 will be seen in the detector as a shower of hadrons and their decay products in the
 1925 form of a *jet*. Two classes of clustering algorithms have been developed based in
 1926 their jet definition [113]:

- 1927 • Iterative cone algorithms (IC). Jets are defined in terms of circles of fixed radius
 1928 R in the $\eta\text{-}\phi$ plane, known as *stable cones*, for which the sum of the momenta
 1929 of all the particles within the cone points in the same direction as the center
 1930 of the circle. The seed of the iteration is the hardest non-isolated particle in
 1931 the event, then, the resulting momentum direction is assigned as the new cone
 1932 direction and a new iteration starts; iteration process stops when the cone if
 1933 found to be stable.

- 1934 • Sequential recombination algorithms. The distance between non-isolated par-
 1935 ticles is calculated; if that distance is below a threshold, these particles are
 1936 recombined into a new object. The sequence is repeated until the separation
 1937 between the recombined object and any other particle is above certain thresh-
 1938 old; the recombined object is called a jet and the algorithm starts again with
 1939 the remaining particles.

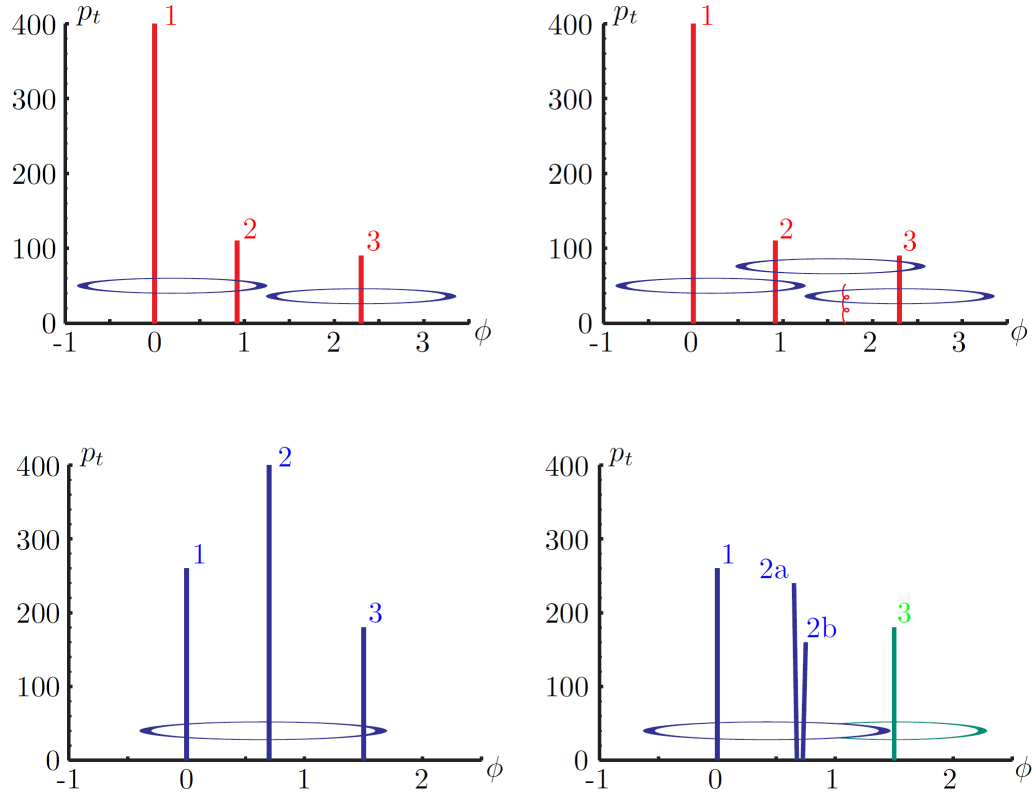


Figure 3.3: Stable cones identification using IC algorithms [113].

- 1940 Two conditions are of particular importance for the clustering algorithms, *infrared*
 1941 and *collinear (IRC) safety*. In order to explain the concept of infrared (IR) safety,
 1942 consider an event with three hard particles as shown in the top left side of Figure 3.3,
 1943 two stable cones are found and then two jets are identified; if a soft gluon is added, as
 1944 shown in the top right side of Figure 3.3, three stable cones are found and the three

1945 hard particles are now clustered into a single jet. If the addition of soft particles
 1946 change the outcome of the clustering, then it is said that the algorithm is IR unsafe.
 1947 Soft radiation is highly likely in perturbative QCD, which dominates the physics of
 1948 the jets, and then IR unsafe effect leads to divergences [113].

1949 The concept of collinear safety can also be explained considering a three hard
 1950 particles event, as shown in the bottom left side of Figure 3.3, where one stable cone
 1951 containing all three particles is found and one jet is identified; if the hardest particle
 1952 is split into two collinear particles (2a and 2b) in the bottom right side of Figure 3.3,
 1953 then the clustering results in a different jet identification and the algorithm is said
 1954 to be collinear unsafe. The collinear unsafe effect leads to divergences in jet cross
 1955 section calculations [114].

1956 It has been determined that IC algorithms are IRC unsafe, and therefore, they
 1957 have to be replaced by algorithms that not only provide the finite perturbative results
 1958 from theoretical computations, but also that are not highly dependent on underlying
 1959 event and pileup effects which leads to significant corrections [113].

1960 The sequential recombination algorithms arise as the IRC safe alternative used by
 1961 the CMS experiment; in particular the anti- k_t algorithm which is a generalization of
 1962 the previously existing k_t [115] and Cambridge/Aachen [116] jet clustering algorithms.

1963 The anti- k_t algorithm is used to perform the jet reconstruction by clustering those
 1964 PF particles within a cone (see Figure 3.4); previously, isolated electrons, isolated
 1965 muons, and charged particles associated with other interaction vertices are excluded
 1966 from the clustering.

1967 The anti- k_t algorithm proceeds in a sequential recombination of PF particles; the
 1968 distance between particles i and j (d_{ij}) and the distance between particles and the
 1969 beam are defined as

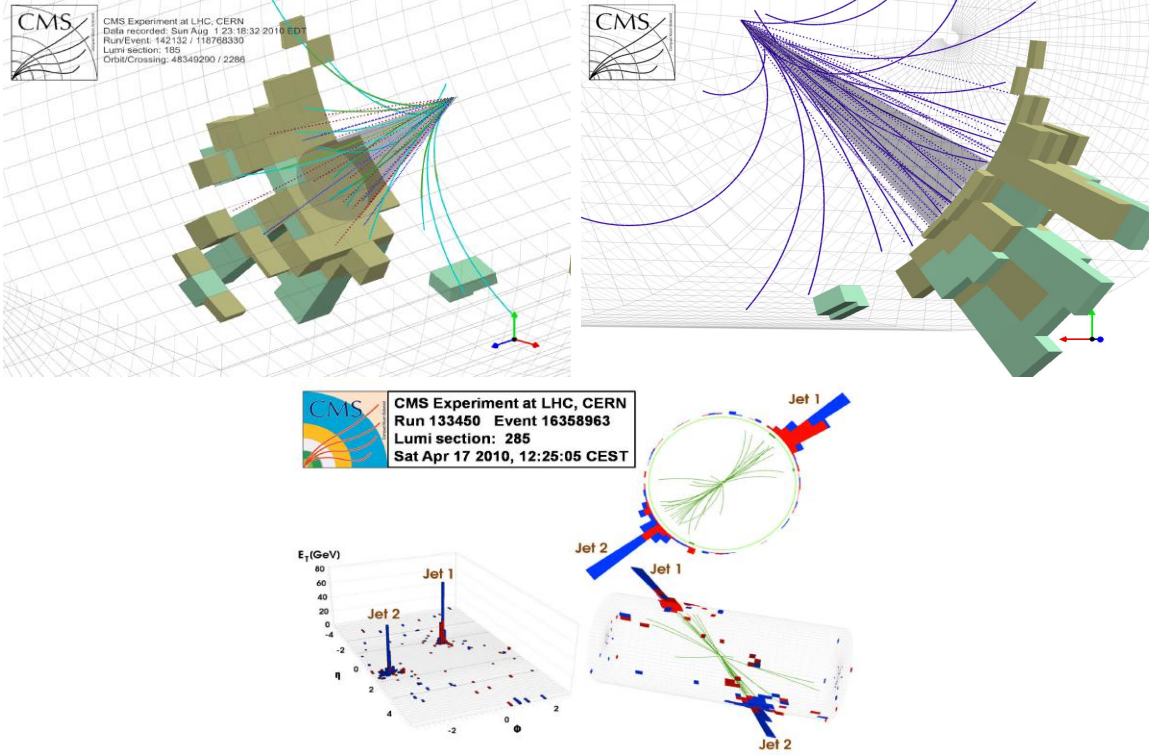


Figure 3.4: Jet reconstruction performed by the anti- k_t algorithm. Top: Two different views of a CMS recorded event are presented. Continuous lines correspond to tracks left by charged particles in the tracker while dotted lines are the imaginary paths followed by neutral particles. The green cubes represent the ECAL cells while the blue ones represent the HCAL cells; in both cases, the height of the cube represent the amount of energy deposited in the cells [117]. Bottom: Reconstruction of a recorded event with two jets [118].

$$d_{ij} = \min\left(\frac{1}{k_{ti}^2}, \frac{1}{k_{tj}^2}\right) \frac{\Delta_{ij}^2}{R^2}$$

$$d_{iB} = \frac{1}{k_{ti}^2} \quad (3.1)$$

1970 where $\Delta_{ij}^2 = (y_i - y_j)^2 + (\phi_i - \phi_j)^2$, k_{ti} , y_i and ϕ_i are the transverse momentum, ra-
1971 pidity and azimuth of particle i respectively and R is the called jet radius. For all
1972 the remaining PF particles, after removing the isolated ones, d_{ij} and d_{iB} are calcu-

1973 lated⁵ and the smallest is identified; if it is a d_{ij} , particles i and j are replaced with
 1974 a new object whose momentum is the vectorial sum of the combined particles. If the
 1975 smallest distance is a d_{iB} the clustering process ends, the object i (which at this stage
 1976 should be a combination of several PF particles) is declared as a *Particle-flow-jet* (PF
 1977 jet) and all the associated PF particles are removed from the detector. The clustering
 1978 process is repeated until no PF particles remain. R is a free parameter that can be
 1979 adjusted according to the specific analysis conditions; usually, two values are used,
 1980 $R=0.4$ and $R=0.5$, giving the name to the so-called AK4-jet and AK5-jet respectively.

1981 An advantage of the anti- k_t algorithm over other clustering algorithms is the reg-
 1982 ularity of the boundaries of the resulting jets. For all known IRC safe algorithms,
 1983 soft radiation can introduce irregularities in the boundaries of the final jets; however,
 1984 anti- k_t algorithm is soft-resilient, meaning that jets shape is not affected by soft radi-
 1985 ation, which is a valuable property considering that knowing the typical shape of jets
 1986 makes experimental calibration of jets more simple. In addition, that soft-resilience
 1987 is expected to simplify certain theoretical calculations and reduce the momentum-
 1988 resolution loss caused by underlying-event (UE) and pileup contamination [114].

1989 The effect of the UE and pileup contamination over a jet identification, can be
 1990 seen as if soft events are added to the jet; for instance, if a soft event representing UE
 1991 or pileup is added to an event for which a set of jets J have been identified, and the
 1992 clustering is rerun on that new extended event, the outcome will be different in two
 1993 aspects: jets will contain some additional soft energy and the distribution of particles
 1994 in jets may have change; that effect is called *back-reaction*. The back-reaction effect in
 1995 the anti- k_t algorithm is suppressed not by the amount of momentum added to the jet
 1996 but by the jet transverse momentum $p_{T,J}$, which means that this strong suppression
 1997 leads to a smaller correction due to EU and pileup effect [114].

⁵ Notice that this is a combinatorial calculation.

1998 **Jet energy Corrections**

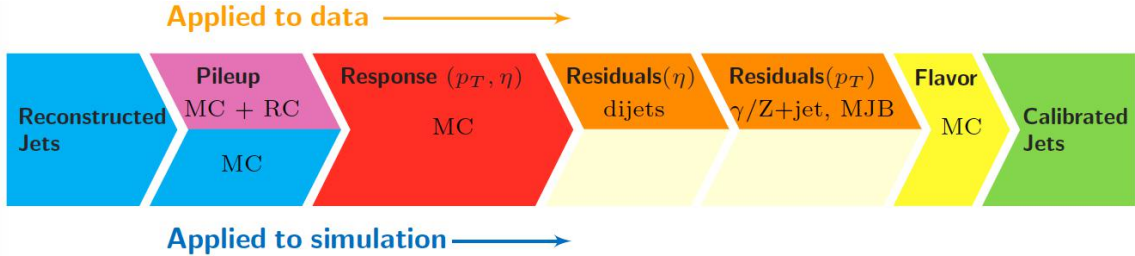


Figure 3.5: Jet energy correction diagram. Correction levels are applied sequentially in the indicated fixed order [120].

1999 Even though jets can be reconstructed efficiently, there are some effects that are
 2000 not included in the reconstruction and that lead to discrepancies between the re-
 2001 constructed results and the predicted results; in order to overcome these discrep-
 2002 ancies, a factorized model has been designed in the form of jet energy corrections
 2003 (JEC) [119, 120] applied sequentially as shown in the diagram of Figure 3.5.

2004 At each level, the jet four-momentum is multiplied by a scaling factor based on
 2005 jet properties, i.e., η , flavor, etc.

- 2006 • Level 1 correction removes the energy coming from pile-up. The scale factor is
 2007 determined using a MC sample of QCD dijet (2 jets) events with and without
 2008 pileup overlay; it is parametrized in terms of the offset energy density ρ , jet
 2009 area A , jet η and jet p_T . Different corrections are applied to data and MC due
 2010 to the detector simulation.
- 2011 • MC-truth correction accounts for differences between the reconstructed jet en-
 2012 ergy and the MC particle-level energy. The correction is determined on a QCD
 2013 dijet MC sample and is parametrized in terms of the jet p_T and η .
- 2014 • Residuals correct remaining small differences within jet response in data and
 2015 MC. The Residuals η -dependent correction compares jets of similar p_T in the

2016 barrel reference region. The Residuals p_T -dependent correct the jet absolute
 2017 scale (JES vs p_T).

2018 • Jet-flavor corrections are derived in the same way as MC-truth corrections but
 2019 using QCD pure flavor samples.

2020 ***b*-tagging of jets.**

2021 A particular feature of the hadrons containing bottom quarks (*b*-hadrons) is that
 2022 their lifetime is long enough to travel some distance before decaying, but it is not as
 2023 long as those of light quark hadrons; therefore, when looking at the hadrons produced
 2024 in pp collisions, *b*-hadrons decay typically inside the tracker rather than reaching the
 2025 calorimeters as some light-hadrons do. As a result, a *b*-hadron decay gives rise to a
 2026 displaced vertex (secondary vertex) with respect to the primary vertex as shown in
 2027 Figure 3.6; the SV displacement is in the order of a few millimeters. A jet resulting
 2028 from the decay of a *b*-hadron is called *b* jet; other jets are called light jets.

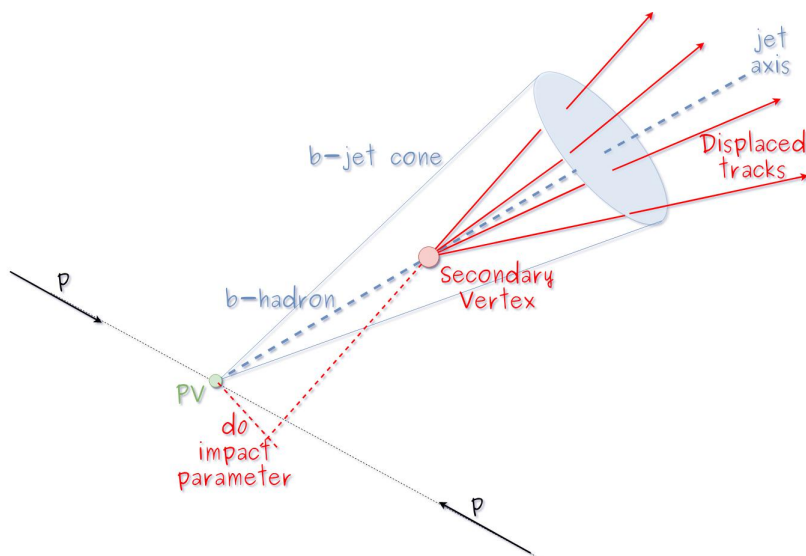


Figure 3.6: Secondary vertex in a *b*-hadron decay.

2029 Several methods to identify *b*-jets (*b*-tagging) have been developed; the method

2030 used in this thesis is known as *Combined Secondary Vertex* algorithm in its second
 2031 version (CSVv2) [121]. By using information of the impact parameter, the recon-
 2032 structed secondary vertices, and the jet kinematics as input in a multivariate analysis
 2033 that combines the discrimination power of each variable in one global discrimina-
 2034 tor variable, three working points (references): loose, medium and tight, are defined
 2035 which quantify the probabilities of mistag jets from light quarks as jets from b quarks;
 2036 10, 1 and 0.1 % respectively. Although the mistagging probability decreases with the
 2037 working point strength, the efficiency to correctly tag b -jets also decreases as 83, 69
 2038 and 49 % for the respective working point; therefore, a balance needs to be achieved
 2039 according to the specific requirements of the analysis.

2040 **Missing transverse energy.**

2041 The fact that proton bunches carry momentum along the z -axis implies that for
 2042 each event it is expected that the momentum in the transverse plane is balanced.
 2043 Imbalances are quantified by the missing transverse energy (MET) and are attributed
 2044 to several sources including particles escaping undetected through the beam pipe,
 2045 neutrinos produced in weak interactions processes which do not interact with the
 2046 detector and thus escaping without leaving a sign, or even undiscovered particles
 2047 predicted by models beyond the SM.

2048 The PF algorithm assigns the negative sum of the momenta of all reconstructed
 2049 PF particles to the *particle-flow MET* according to

$$\vec{E}_T = - \sum_i \vec{p}_{T,i} \quad (3.2)$$

2050 JEC are propagated to the calculation of the \vec{E}_T as described in the Reference [122].

2051 **3.4.2 Event reconstruction examples**

2052 Figures 3.7-3.9 show the results of the reconstruction performed on 3 recorded events.

2053 Descriptions are taken directly from the source.

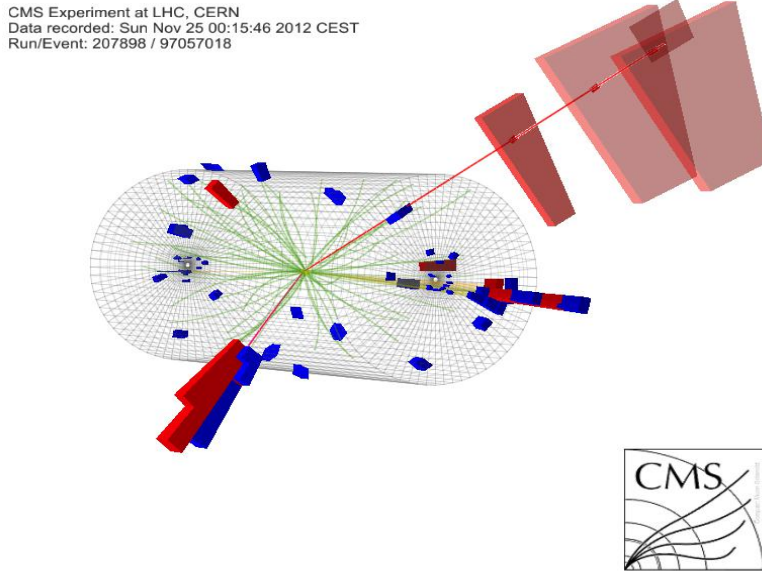


Figure 3.7: HIG-13-004 Event 1 reconstruction results; “HIG-13-004 Event 1: Event recorded with the CMS detector in 2012 at a proton-proton center-of-mass energy of 8 TeV. The event shows characteristics expected from the decay of the SM Higgs boson to a pair of τ leptons. Such an event is characterized by the production of two forward-going jets, seen here in opposite endcaps. One of the τ decays to a muon (red lines on the right) and neutrinos, while the other τ decays into a charged hadron and a neutrino.” [123].

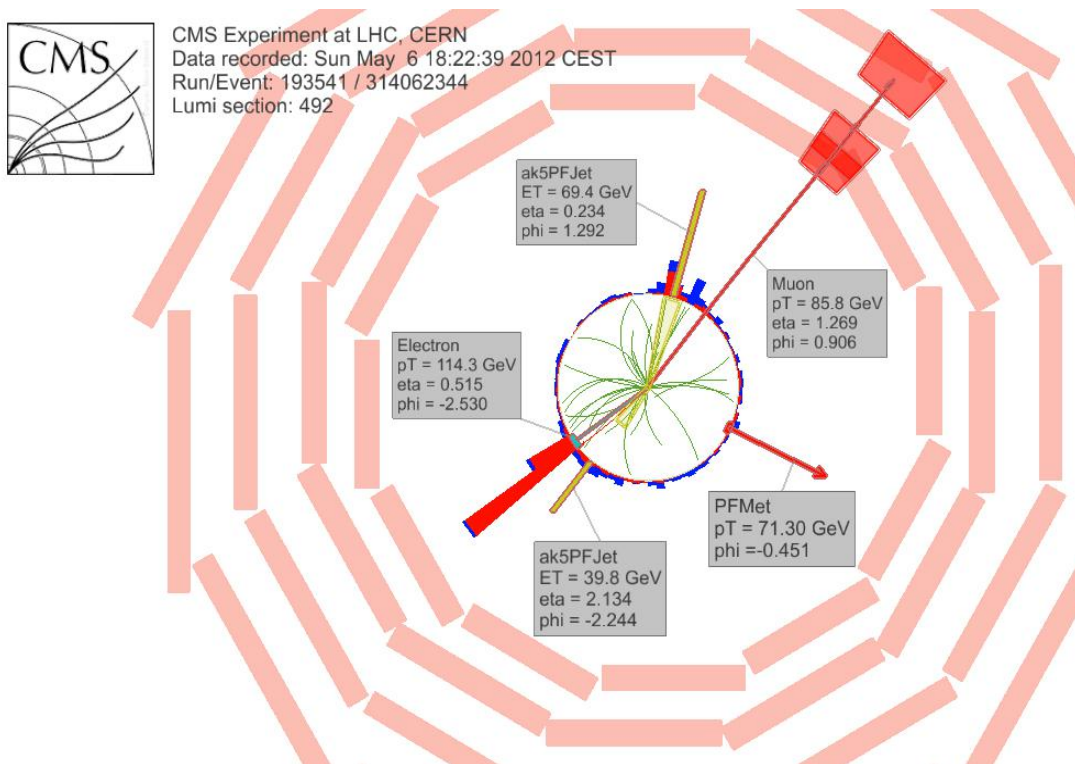


Figure 3.8: $e\mu$ event reconstruction results; “An $e\mu$ event candidate selected in 8 TeV data, as seen from the direction of the proton beams. The kinematics of the main objects used in the event selection are highlighted: two isolated leptons and two particle-flow jets. The reconstructed missing transverse energy is also displayed for reference” [124].

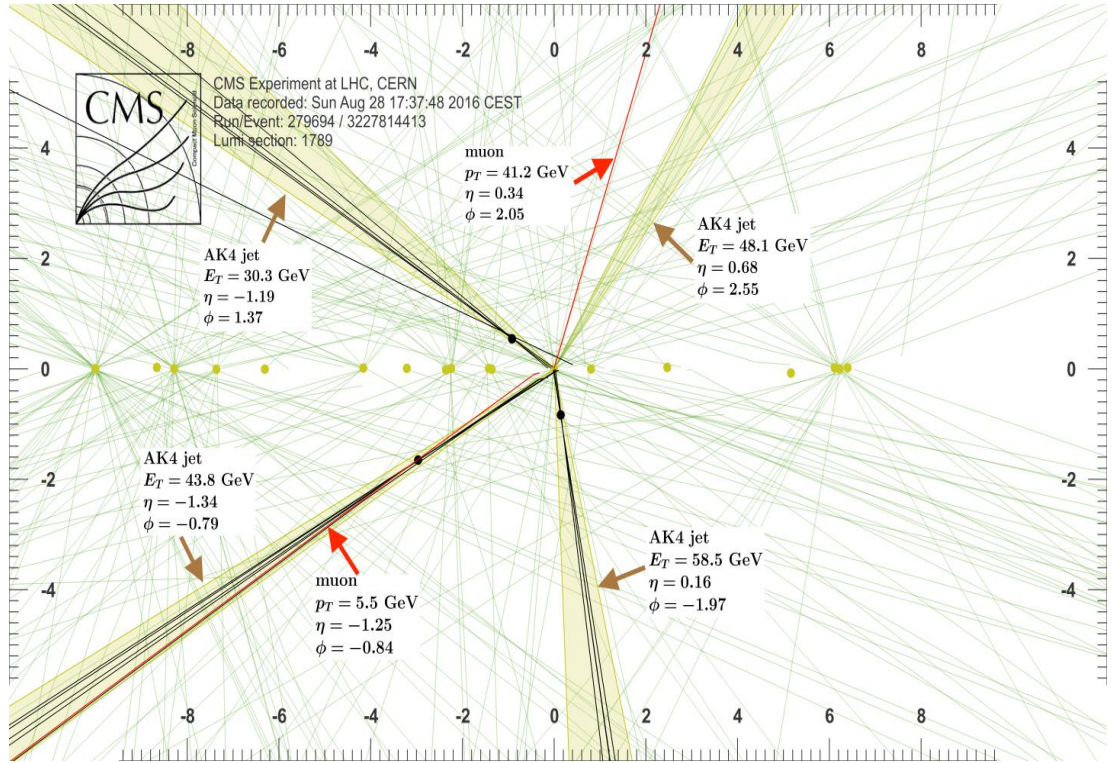


Figure 3.9: Recorded event reconstruction results; “Recorded event (ρ - z projection) with three jets with $p_T > 30$ GeV with one displaced muon track in 2016 data collected at 13 TeV. Each of the three jets has a displaced reconstructed vertex. The jet with $p_T(j) = 43.8$ GeV, $\eta(j) = -1.34$, $\phi(j) = -0.79$ contains muon with $p_T(\mu) = 5.5$ GeV, $\eta(\mu) = -1.25$, $\phi(\mu) = -0.84$. Event contains reconstructed isolated muon with $p_T(\mu) = 41.2$ GeV, $\eta(\mu) = 0.34$, $\phi(\mu) = 2.05$ and MET with $p_T = 72.5$ GeV, $\phi = -0.32$. Jet candidates for a b -jet from top quark leptonic and hadronic decays are tagged by CSVv2T algorithm. One of the other two jets is tagged by CharmT algorithm. Tracks with $p_T > 0.5$ GeV are shown. The number of reconstructed primary vertices is 18. Reconstructed $m_T(W)$ is 101.8 GeV. Beam spot position correction is applied. Reconstructed primary vertices are shown in yellow color, while reconstructed displaced vertices and associated tracks are presented in black color. Dimensions are given in cm” [125].

2054 **Chapter 5**

2055 **Statistical methods**

2056 In the course of analyzing the data sets provided by the CMS experiment and used in
2057 this thesis, several statistical tools have been employed; in this chapter, a description
2058 of these tools will be presented, starting with the general statement of the multivariate
2059 analysis methods, followed by the particularities of the Boosted Decision Trees (BDT)
2060 method and its application to the classification problem. Statistical inference methods
2061 used will also be presented. This chapter is based mainly on References [126–128].

2062 **5.1 Multivariate analysis**

2063 Multivariate data analysis (MVA) makes use of the statistical techniques developed to
2064 analyze more than one variable at once, taking into account all the correlations among
2065 variables. MVA is employed in a variety of fields like consumer and market research,
2066 quality control and process optimization. Using MVA it is possible to identify the
2067 dominant patterns in a data sample, like groups, outliers and trends, and determine
2068 to which group a set of values belong; in the particle physics context, MVA methods
2069 are used to perform the selection of certain type of events from a large data set.

2070 Processes with small cross section, such as the tHq process ($\sigma_{SM}(\sqrt{s} = 13\text{TeV}) =$
 2071 70.96 fb), are hard to detect in the presence of the processes with larger cross sections,
 2072 $\sigma_{SM}^{t\bar{t}}(\sqrt{s} = 13\text{TeV}) = 823.44 \text{ fb}$ for instance; therefore, only a small fraction of the data
 2073 contains events of interest (signal), the major part is signal-like events, which mimic
 2074 signal characteristics but belong to different processes, so they are a background to
 2075 the process of interest. This implies that it is not possible to say with certainty
 2076 that a given event is a signal or a background and statistical methods should be
 2077 involved. In that sense, the challenge can be formulated as one where a set of events
 2078 have to be classified according to certain special features; these features correspond
 2079 to the measurements of several parameters like energy or momentum, organized in a
 2080 set of *input variables*. The measurements for each event can be written in a vector
 2081 $\mathbf{x} = (x_1, \dots, x_n)$ for which

- 2082 • $f(\mathbf{x}|s)$ is the probability density (*likelihood function*) that \mathbf{x} is the set of mea-
 2083 sured values given that the event is a signal event (signal hypothesis).
- 2084 • $f(\mathbf{x}|b)$ is the probability density (*likelihood function*) that \mathbf{x} is the set of mea-
 2085 sured values given that the event is a background event (background hypothe-
 2086 sis).

2087 Figure 5.1 shows three ways to perform a classification of events for which mea-
 2088 surements of two properties, i.e., two input variables x_1 and x_2 , have been performed;
 2089 blue circles represent signal events while red triangles represent background events.
 2090 The classification on the left is *cut-based* requiring $x_1 < c_1$ and $x_2 < c_2$; usually the
 2091 cut values (c_1 and c_2) are chosen according to some knowledge about the event pro-
 2092 cess. In the middle plot, the classification is performed using a linear function of
 2093 the input variables, hence the boundary is a straight line, while in the right plot the

2094 the relationship between input variables is not linear thus the boundary is not linear
 2095 either.

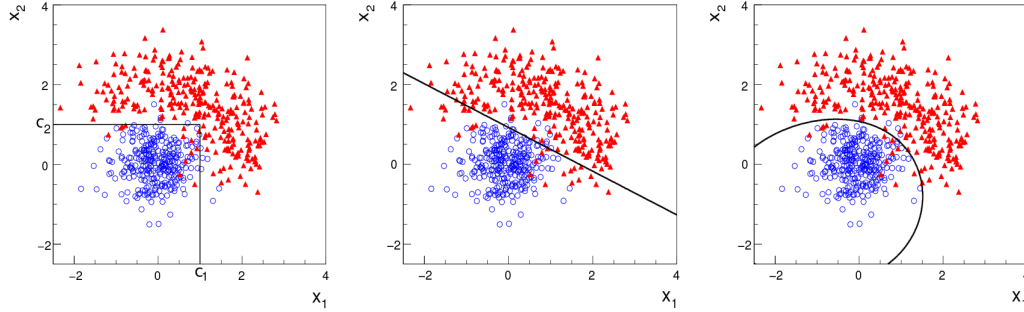


Figure 5.1: Scatter plots-MVA event classification. Distribution of two input variables x_1 and x_2 measured for a set of events; blue circles represent signal events and red triangles represent background events. The classification is based on cuts (left), linear boundary (center), and nonlinear boundary (right) [126]

2096 In general, the boundary can be parametrized in terms of the input variables such
 2097 that the cut is set on the parametrization instead of on the variables, i.e., $y(\mathbf{x}) = y_{cut}$
 2098 with y_{cut} being a constant; thus, the acceptance or rejection of an event is based on
 2099 which side of the boundary the event is located. If $y(\mathbf{x})$, usually called *test statistic*,
 2100 has functional form, it can be used to determine the probability distribution functions
 2101 $p(y|s)$ and $p(y|b)$ and then perform a test statistic with a single cut on the scalar
 2102 variable y .

2103 Figure 5.2 shows an example of what would be the probability distribution func-
 2104 tions under the signal and background hypotheses for a scalar test statistic with a cut
 2105 on the classifier y . Note that the tails of the distributions indicate that some signal
 2106 events fall in the rejection region and some background events fall on the acceptance
 2107 region; therefore, it is convenient to define the *efficiency* with which events of a given
 2108 type are accepted. The signal and background efficiencies are given by

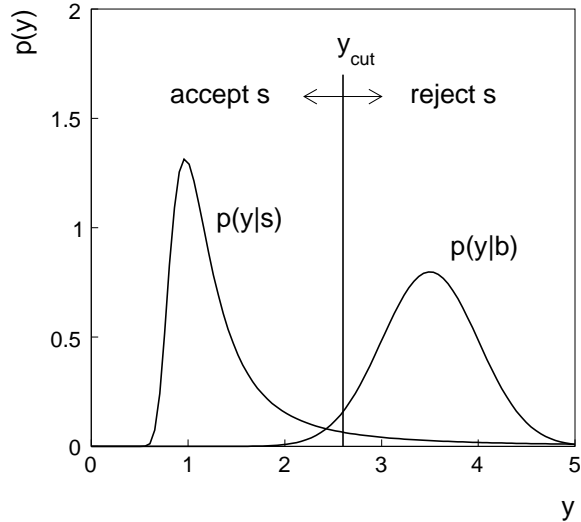


Figure 5.2: Distributions of the scalar test statistic $y(\mathbf{x})$ under the signal and background hypotheses. [126]

$$\varepsilon_s = P(\text{accept event}|s) = \int_A f(\mathbf{x}|s) d\mathbf{x} = \int_{-\infty}^{y_{cut}} p(y|s) dy , \quad (5.1)$$

$$\varepsilon_b = P(\text{accept event}|b) = \int_A f(\mathbf{x}|b) d\mathbf{x} = \int_{-\infty}^{y_{cut}} p(y|b) dy , \quad (5.2)$$

where A is the acceptance region. If the background hypothesis is the *null hypothesis* (H_0), the signal hypothesis would be *alternative hypothesis* (H_1); in this context, the background efficiency corresponds to the significance level of the test (α) and describes the misidentification probability, while the signal efficiency corresponds to the power of the test ($1-\beta$)¹ and describes the probability of rejecting the background hypothesis if the signal hypothesis is true. What is sought in an analysis is to maximize the power of the test relative to the significance level, i.e., set a selection with the largest possible selection efficiency and the smallest possible misidentification probability.

¹ β is the fraction of signal events that fall out of the acceptance region

2117 **5.1.1 Decision trees**

2118 For this thesis, the implementation of the MVA strategy, described above, is per-
 2119 formed through decision trees by using the TMVA software package [127] included
 2120 in the ROOT analysis framework [129]. In a simple picture, a decision tree classifies
 2121 events according to their input variables values by setting a cut on each input variable
 2122 and checking which events are on which side of the cut, just as proposed in the MVA
 2123 strategy, but in addition, as a machine learning algorithm, decision trees offer the
 2124 possibility to be trained and then perform the classification efficiently.

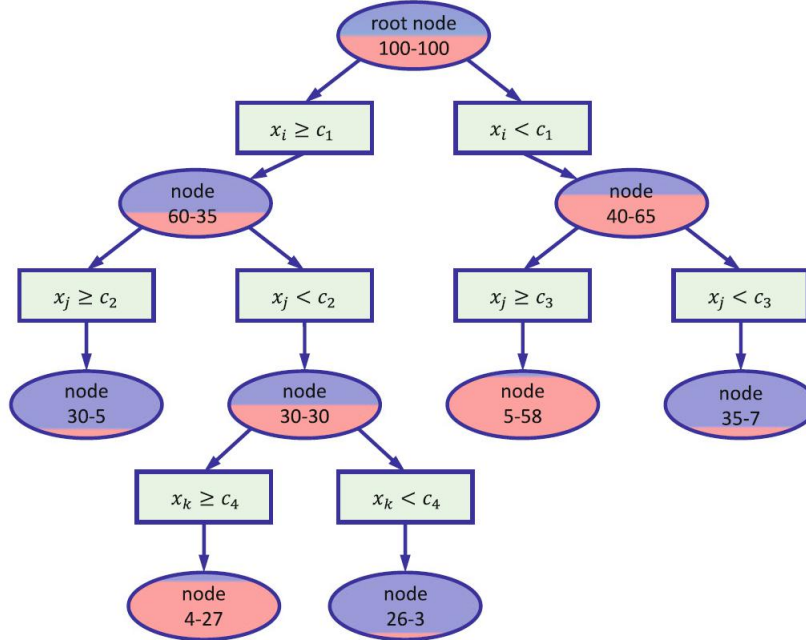


Figure 5.3: Example of a decision tree. Each node is fed with a MC sample mixing signal and background events (left-right numbers); nodes colors represent the relative number of signal/background events [128].

2125 The training or growing of a decision tree is the process where the rules for clas-
 2126 sifying events are defined; this process is represented in Figure 5.3 and consists of
 2127 several steps:

- 2128 • take MC samples of signal and background events and split them into two parts

2129 each; the first parts will be used in the decision tree training, while the second
 2130 parts will be used for testing the final classifier obtained from the training.
 2131 Each event has associated a set of input variables $\mathbf{x} = (x_1, \dots, x_n)$ which serve
 2132 to distinguish between signal and background events. The training sample is
 2133 taken in at the *root node*.

- 2134 • Pick one variable, say x_i .
- 2135 • Pick one value of x_i , each event has its own value of x_i , and split the training
 2136 sample into two subsamples B_1 and B_2 ; B_1 contains events for which $x_i < c_1$
 2137 while B_2 contains the rest of the training events;
- 2138 • scan all possible values of x_i and find the splitting value that provides the *best*
 2139 classification², i.e., B_1 is mostly made of signal events while B_2 is mostly made
 2140 of background events.
- 2141 • It is possible that variables other than the picked one produce a better classi-
 2142 fication, hence, all the variables have to be evaluated. Pick the next variable,
 2143 say x_j , and repeat the scan over its possible values.
- 2144 • At the end, all the variables and their values will have been scanned, the *best*
 2145 variable and splitting value will have been identified, say x_1, c_1 , and there will
 2146 be two nodes fed with the subsamples B_1 and B_2 .

2147 Nodes are further split by repeating the decision process until a given number of
 2148 final nodes is obtained, nodes are largely dominated by either signal or background
 2149 events, or nodes have too few events to continue. Final nodes are called *leaves* and
 2150 they are classified as signal or background leaves according to the class of the majority
 2151 of events in them. Each *branch* in the tree corresponds to a sequence of cuts.

² Quality of the classification will be treated in the next paragraph.

2152 The quality of the classification at each node is evaluated through a separation
 2153 criteria; there are several of them but the *Gini Index* (G) is the one used in the
 2154 decision trees trained for the analysis in this thesis. G is written in terms of the
 2155 purity (P), i.e., the fraction of signal events in the samples after the separation is
 2156 made; it is given by

$$G = P(1 - P) \quad (5.3)$$

2157 note that $P=0.5$ at the root node while $G=0$ for pure leaves. For a node A split into
 2158 two nodes B_1 and B_2 the G gain is

$$\Delta G = G(A) - G(B_1) - G(B_2). \quad (5.4)$$

2159 The *best* classification corresponds to that for which the gain of G is maximized;
 2160 hence, the scanning over all the variables in an event and their values is of great
 2161 importance.

2162 In order to provide a numerical output for the classification, events in a sig-
 2163 nal(background) leaf are assigned an score of 1(-1) each, defining in this way the
 2164 decision tree *classifier/weak learner* as

$$f(\mathbf{x}) = \begin{cases} 1 & \mathbf{x} \text{ in signal region,} \\ -1 & \mathbf{x} \text{ in background region.} \end{cases}$$

2165 Figure 5.4 shows an example of the classification of a sample of events, containing
 2166 two variables, performed by a decision tree.

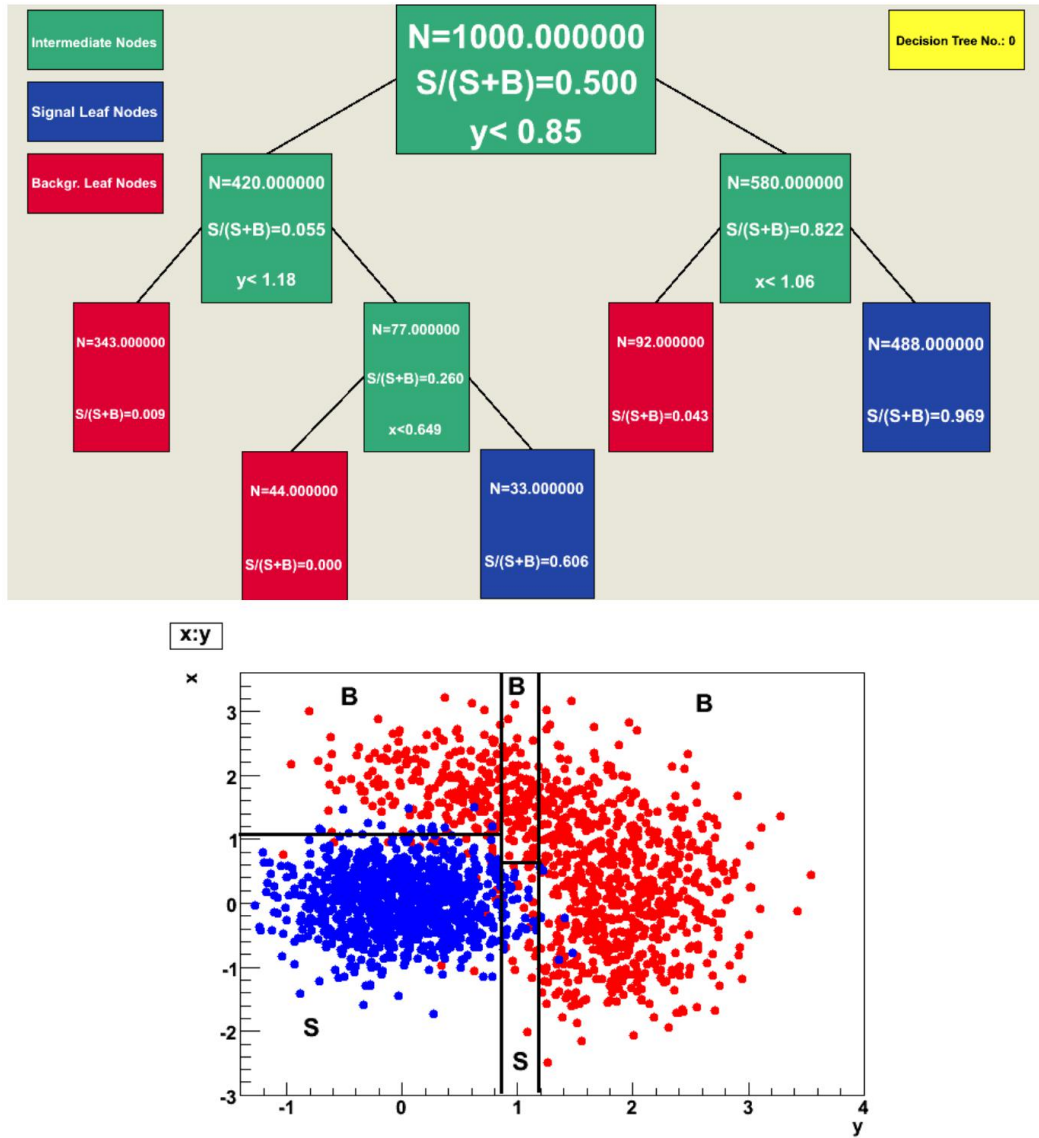


Figure 5.4: Example of a decision tree output. Each leaf, blue for signal events and red for background events, is represented by a region in the variables phase space [130].

2167 5.1.2 Boosted decision trees (BDT).

2168 Event misclassification occurs when a training event ends up in the wrong leaf, i.e., a
 2169 signal event ends up in a background leaf or a background event ends up in a signal
 2170 leaf. A way to correct it is to assign a weight to the misclassified events and train
 2171 a second tree using the reweighted events; the event reweighting is performed by a

2172 boosting algorithm in such a way that when used in the training of a new decision
 2173 tree the *boosted events* get correctly classified. The process is repeated iteratively
 2174 adding a new tree to the forest and creating a set of classifiers, which are combined
 2175 to create the next classifier; the final classifier offers more stability³ and has a smaller
 2176 misclassification rate than any individual ones. The resulting tree collection is known
 2177 as a *boosted decision tree (BDT)*.

2178 Thus, purity of the sample is generalized to

$$P = \frac{\sum_s w_s}{\sum_s w_s + \sum_b w_b} \quad (5.5)$$

2179 where w_s and w_b are the weights of the signal and background events respectively;
 2180 the Gini index is also generalized

$$G = \left(\sum_i^n w_i \right) P(1 - P) \quad (5.6)$$

2181 with n the number of events in the node. The final score of an event, after pass-
 2182 ing through the forest, is calculated as the renormalized sum of all the individual
 2183 (possibly weighted) scores; thus, high(low) score implies that the event is most likely
 2184 signal(background).

2185 The boosting procedure, implemented in the *Gradient boosting* algorithm used in
 2186 this thesis, produces a classifier $F(\mathbf{x})$ which is the weighted sum of the individual
 2187 classifiers obtained after each iteration, i.e.,

$$F(\mathbf{x}) = \sum_{m=1}^M \beta_m f(\mathbf{x}; a_m) \quad (5.7)$$

2188 where M is the number of trees in the forest. The *loss function* $L(F, y)$ represents the

³ Decision trees suffer from sensitivity to statistical fluctuations in the training sample which may lead to very different results with a small change in the training samples.

2189 deviation between the classifier $F(\mathbf{x})$ response and the true value y obtained from the
 2190 training sample (1 for signal events and -1 for background event), according to

$$L(F, y) = \ln(1 + e^{-2F(\mathbf{x})y}) \quad (5.8)$$

2191 thus, the reweighting is employed to ensure the minimization of the loss function; a
 2192 more detailed description of the minimization procedure can be found in Reference
 2193 [131]. The final classifier output is later used as a final discrimination variable, labeled
 2194 as *BDT output/response*.

2195 5.1.3 Overtraining

2196 Decision trees offer the possibility to have as many nodes as desired in order to
 2197 reduce the misclassification to zero (in theory); however, when a classifier is too much
 2198 adjusted to a particular training sample, the classifier's response to a slightly different
 2199 sample may leads to a completely different classification results; this effect is known
 2200 as *overtraining*.

2201 An alternative to reduce the overtraining in BDTs consists in pruning the tree
 2202 by removing statistically insignificant nodes after the tree growing is completed but
 2203 this option is not available for BDTs with gradient boosting in the TMVA-toolkit,
 2204 therefore, the overtraining has to be reduced by tuning the algorithm, number of
 2205 nodes, minimum number of events in the leaves, etc. The overtraining can be evaluated
 2206 by comparing the responses of the classifier when running over the training and
 2207 test samples.

2208 5.1.4 Variable ranking

2209 BDTs have a couple of particular advantages related to the input variables; they are
 2210 relatively insensitive to the number of input variables used in the vector \mathbf{x} . The
 2211 ranking of the BDT input variables is determined by counting the number of times a
 2212 variable is used to split decision tree nodes; in addition, the separation gain-squared
 2213 achieved in the splitting and the number of events in the node are accounted by
 2214 applying a weighting to that number. Thus, those variables with small or no power
 2215 to separate signal and background events are rarely chosen to split the nodes, i.e., are
 2216 effectively ignored.

2217 In addition, variables correlations play an important role for some MVA methods
 2218 like the Fisher discriminant algorithm in which the first step consist of performing a
 2219 linear transformation to a phase space where the correlations between variables are
 2220 removed; in the case of BDT algorithm, correlations do not affect the performance.

2221 5.1.5 BDT output example

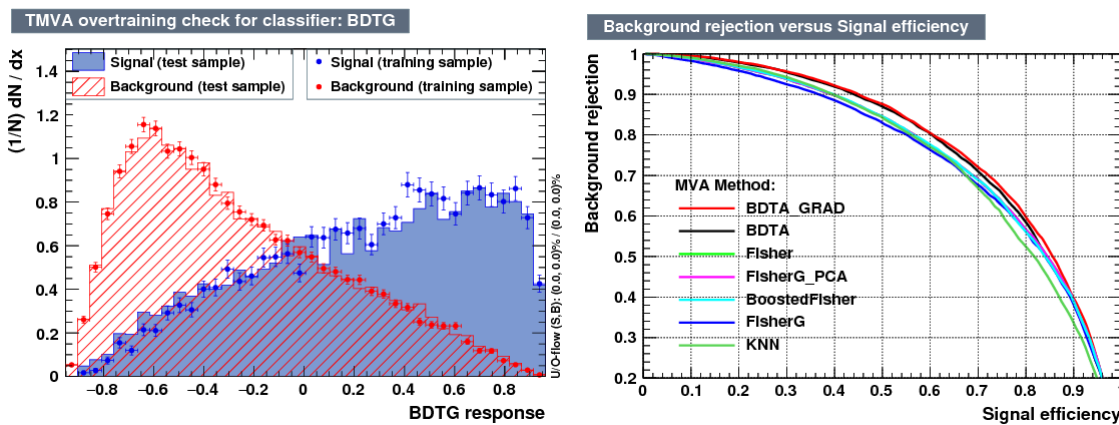


Figure 5.5: Left: Output distributions for the gradient boosted decision tree (BDTG) classifier using a sample of signal ($pp \rightarrow tHq$) and background ($pp \rightarrow tt$) events. Right: Background rejection vs signal efficiency (ROC curves) for various MVA classifiers running over the same sample used to produce the plot on the left.

2222 The left side of figure 5.5 shows the BDT output distributions for signal ($pp \rightarrow$
 2223 tHq) and background ($pp \rightarrow t\bar{t}$) events; this plot is the equivalent to the one showed
 2224 in Figure 5.2. A forest with 800 trees, maximum depth per tree = 3, and gradient
 2225 boosting have been used as training parameters. The BDTG classifier offers a good
 2226 separation power. There is a small overtraining in the signal distribution, while the
 2227 background distribution is very well predicted which might indicate that the sample
 2228 is composed of more background than signal events.

2229 The right side of figure 5.5 shows the background rejection vs signal efficiency
 2230 curves for several combinations of MVA classifiers-boosting algorithms running over
 2231 the same MC sample; these curves are known as ROC curves and give an indication
 2232 of the performance of the classifier. In this particular example, the best performance
 2233 is achieved with the BDTG classifier (BDTA_GRAD), which motivate its use in this
 2234 thesis.

2235 **5.2 Statistical inference**

2236 Once events are classified, the next step consists of finding the parameters that define
 2237 the likelihood functions $f(\mathbf{x}|s)$, $f(\mathbf{x}|b)$ for signal and background events respectively.
 2238 In general, likelihood functions depend not only on the measurements but also on
 2239 parameters (θ_m) that define their shapes; the process of estimating these *unknown*
 2240 *parameters* and their uncertainties from the experimental data is called *inference*.

2241 The statistical inference tools used in this analysis are implemented in the RooFit
 2242 toolkit [132] and COMBINE package [133] included in the CMSSW software frame-
 2243 work.

2244 **5.2.1 Nuisance parameters**

2245 The unknown parameter vector θ is made of two types of parameters: those pa-
 2246 rameters that provide information about the physical observables of interest for the
 2247 experiment or *parameters of interest*, and the *nuisance parameters* that are not of
 2248 a direct interest for the experiment but that need to be included in the analysis in
 2249 order to achieve a satisfactory description of the data; they represent effects of the
 2250 detector response like the finite resolutions of the detection systems, miscalibrations,
 2251 and in general any source of uncertainty introduced in the analysis.

2252 Nuisance parameters can be estimated from experimental data; for instance, data
 2253 samples from a test beam are usually employed for calibration purposes. In cases
 2254 where experimental samples are not availables, the estimation of nuisance parameters
 2255 makes use of dedicated simulation programs to provide the required samples.

2256 The estimation of the unknown parameters involves certain deviations from their
 2257 true values, hence, the measurement of the nuisance parameter is written in terms
 2258 of an estimated value, also called central value, $\hat{\theta}$ and its uncertainty $\delta\theta$ using the
 2259 notation

$$\theta = \hat{\theta} \pm \delta\theta \quad (5.9)$$

2260 where the interval $[\hat{\theta} - \delta\theta, \hat{\theta} + \delta\theta]$ is called *confidence interval*; it is usually interpreted,
 2261 in the limit of infinite number of experiments, as the interval where the true value
 2262 of the unknown parameter θ is contained with a probability of 0.6827 (if no other
 2263 convention is stated); this interval represents the area under a Gaussian distribution
 2264 in the interval $\pm 1\sigma$.

2265 Conventionally, uncertainties are split into two classes: *systematic*, associated with
 2266 the systematic effects, and *statistical*, related only to fluctuations in data and having

2267 statistical nature.

2268 5.2.2 Maximum likelihood estimation method

2269 The estimation of the unknown parameters that are in best agreement with the ob-
 2270 served data is performed through a function of the data sample that returns the
 2271 estimate of those parameters; that function is called an *estimator*. Estimators are
 2272 usually constructed using mathematical expressions encoded in computer programs.

2273 In this thesis, the estimator used is the likelihood function $f(\mathbf{x}|\boldsymbol{\theta})$ ⁴ which depends
 2274 on a set of measured variables \mathbf{x} and a set of unknown parameters $\boldsymbol{\theta}$. The likelihood
 2275 function for N events in a sample is the combination of all the individual likelihood
 2276 functions, i.e.,

$$L(\boldsymbol{\theta}) = \prod_{i=1}^N f(\mathbf{x}^i|\boldsymbol{\theta}) = \prod_{i=1}^N f(x_1^i, \dots, x_n^i; \theta_1, \dots, \theta_m) \quad (5.10)$$

2277 and the estimation method used is the *Maximum Likelihood Estimation* method
 2278 (MLE); it is based on the combined likelihood function defined by eqn. 5.10 and
 2279 the procedure seeks for the parameter set that corresponds to the maximum value of
 2280 the combined likelihood function, i.e., the *maximum likelihood estimator* of the un-
 2281 known parameter vector $\boldsymbol{\theta}$ is the function that produces the vector of *best estimators*
 2282 $\hat{\boldsymbol{\theta}}$ for which the likelihood function $L(\boldsymbol{\theta})$ evaluated at the measured \mathbf{x} is maximum.

2283 Usually, the logarithm of the likelihood function is used in numerical algorithm
 2284 implementations in order to avoid underflow the numerical precision of the computers
 2285 due to the product of small likelihoods. In addition, it is common to minimize the
 2286 negative logarithm of the likelihood function, therefore, the negative log-likelihood

⁴ analogue to the likelihood functions described in previous sections

2287 function is

$$F(\boldsymbol{\theta}) = -\ln L(\boldsymbol{\theta}) = -\sum_{i=1}^N f(\mathbf{x}^i | \boldsymbol{\theta}). \quad (5.11)$$

2288 The minimization process is performed by the software MINUIT [134] implemented in the ROOT analysis framework. In case of data samples with large number 2289 of measurements, the computational resources necessary to calculate the likelihood 2290 function are too big; therefore, the parameter estimation is performed using binned 2291 distributions of the variables of interest for which the *binned likelihood function* is 2292 given by

$$L(\mathbf{x}|r, \boldsymbol{\theta}) = \prod_{i=1} \frac{(r \cdot s_i(\boldsymbol{\theta}) + b_i(\boldsymbol{\theta}))^{n_i}}{n_i!} e^{-r \cdot s_i(\boldsymbol{\theta}) - b_i(\boldsymbol{\theta})} \prod_{j=1} \frac{1}{\sqrt{2\pi}\sigma_{\theta_j}^2} e^{-(\theta_j - \theta_{0,j})^2/2\sigma_{\theta_j}^2}, \quad (5.12)$$

2294 with s_i and b_i the expected number of signal and background yields for the bin i , n_i is 2295 the observed number of events in the bin i and $r = \sigma/\sigma_{SM}$ is the signal strength. Note 2296 that the number of entries per bin follows a Poisson distribution. The effect of the 2297 nuisance parameters have been included in the likelihood function through Gaussian 2298 distributions that models the nuisance. The three parameters, r , s_i and b_i are jointly 2299 fitted to estimate the value of r .

2300 5.3 Upper limits

2301 In this analysis, two hypotheses are considered; the background only hypothesis 2302 ($H_0(b)$) and the signal plus background hypothesis ($H_1(s+b)$), i.e., the sample of 2303 events is composed of background only events ($r=0$) or it is a mixture of signal plus 2304 background events ($r=1$). The exclusion of one hypothesis against the other means 2305 that the observed data sample better agrees with H_0 or rather with H_1 . In order 2306 to discriminate these hypotheses, a test statistic is constructed on the basis of the

2307 likelihood function evaluated for each of the hypothesis.

2308 The *Neyman-Pearson* lemma [135] states that the test statistic that provides the
 2309 maximum power for H_1 for a given significance level (background misidentification
 2310 probability α), is given by the ratio of the likelihood functions $L(\mathbf{x}|H_1)$ and $L(\mathbf{x}|H_0)$;
 2311 however, in order to use that definition it is necessary to know the true likelihood
 2312 functions, which in practice is not always possible. Approximate functions obtained
 2313 by numerical methods, like the BDT method described above, have to be used, so
 2314 that the *profile likelihood* test statistic is defined by

$$\lambda(\mathbf{r}) = \frac{L(\mathbf{x}|r, \hat{\boldsymbol{\theta}}(r))}{L(\mathbf{x}|\hat{r}, \hat{\boldsymbol{\theta}})}, \quad (5.13)$$

2315 where, \hat{r} and $\hat{\boldsymbol{\theta}}$ maximize the likelihood function, and $\hat{\boldsymbol{\theta}}$ maximizes the likelihood
 2316 function for a given value of the signal strength modifier r . In practice, the test
 2317 statistic t_r

$$t_r = -2\ln\lambda(r) \quad (5.14)$$

2318 is used to evaluate the presence of signal in the sample, since the minimum of t_r at
 2319 $r = \hat{r}$ suggests the presence of signal with signal strength \hat{r} . The uncertainty interval
 2320 for r is determined by the values of r for which $t_r = +1$.

2321 The expected probability density function (p.d.f) $f(t_r|r, \boldsymbol{\theta})$ of the test statistic t_r
 2322 can be obtained numerically by generating MC samples where one hypothesis, $H_0(b)$
 2323 or $H_1(s+b)$, is assumed; thus, MC samples contain the possible values of t_r obtained
 2324 from *pseudo-experiments* as shown in Figure 5.6. The probability that t_r takes a value
 2325 equal or greater than the observed value ($t_{r,obs}$) when a signal with a signal modifier
 2326 r is present in the data sample, is called the *p-value* of the observation; it can be
 2327 calculated using

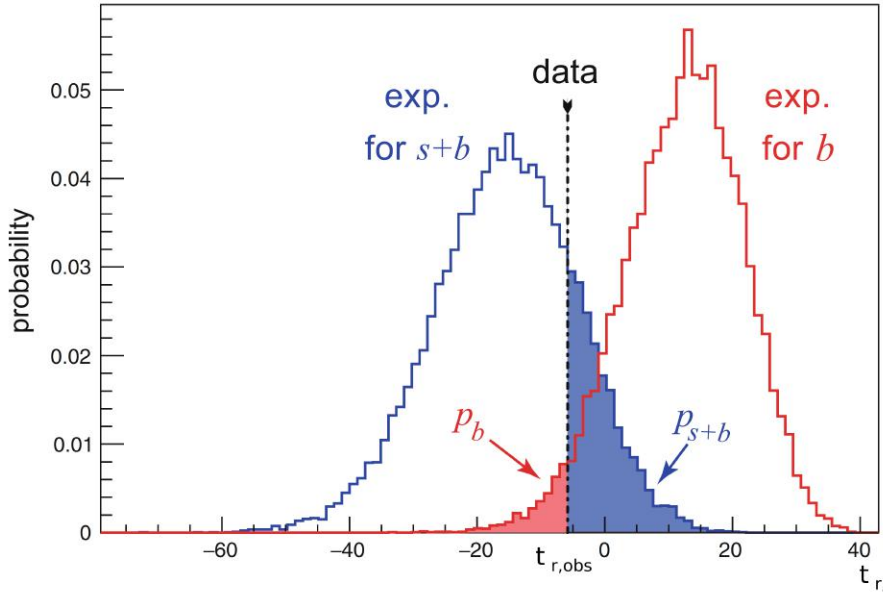


Figure 5.6: t_r p.d.f. from MC pseudo experiments assuming H_0 (red) and H_1 (blue). The black dashed line shows the value of the test statistic as measured from data. Adapted from Reference [128].

$$p_r = \int_{t_{r,obs}}^{\infty} f(t'_r | r, \boldsymbol{\theta}) dt'_r, \quad (5.15)$$

thus, $p_r < 0.05$ means that, for that particular value of r , H_1 could be excluded at 95% Confidence Level (CL). The corresponding background-only p-value is given by

$$1 - p_b = \int_{t_{r,obs}}^{\infty} f(t'_r | 0, \boldsymbol{\theta}) dt'_r, \quad (5.16)$$

If the t_r p.d.f.s for both hypotheses are well separated, as shown in the top side of Figure 5.7, the experiment is sensitive to the presence of signal in the sample. If the signal presence is small, both p.d.f.s will be largely overlapped (bottom of Figure ??) and either the signal hypothesis could be rejected with not enough justification because the experiment is not sensitive to the signal or a fluctuation of the background could be misinterpreted as presence of signal with the corresponding rejection of the

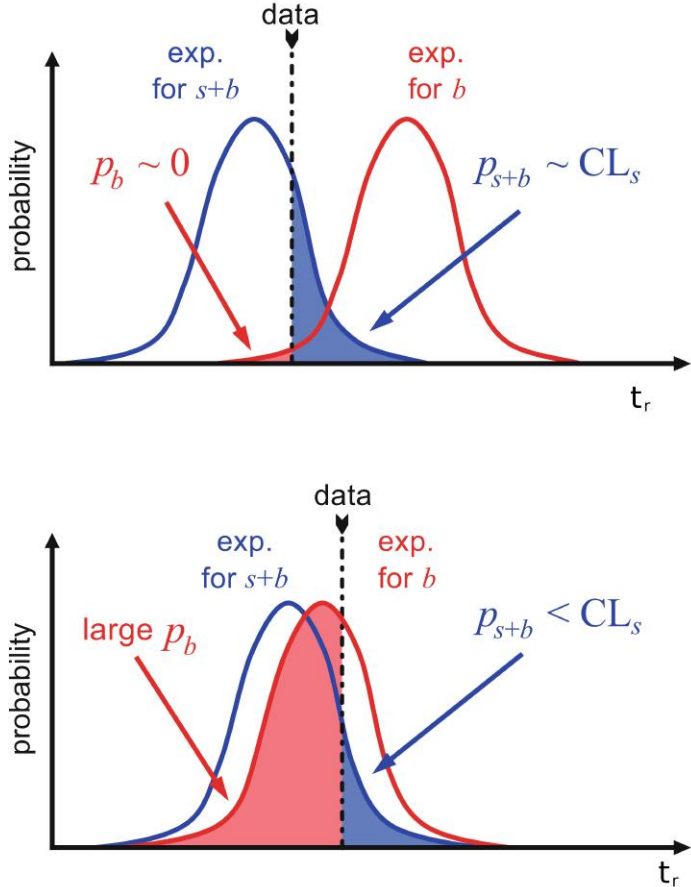


Figure 5.7: CL_s limit illustration. When the test statistic p.d.f. for the two hypotheses H_0 and H_1 are well separated (top) and when they are largely overlapped (bottom). Adapted from Reference [128].

2336 background-only hypothesis. These issues are corrected by using the modified p-
2337 value [136]

$$p'_r = \frac{p_r}{1 - p_b} \equiv CL_s. \quad (5.17)$$

2338 If H_1 is true, then p_b is small, $CL_s \simeq p_r$ and H_0 is rejected; if there is large
2339 overlap and a statistical fluctuation causes that p_b is large, then both numerator and
2340 denominator in Eqn. 5.17 become small but CL_s would allow the rejection of H_1
2341 even if there is poor sensitivity to signal.

2342 The upper limit of the parameter of interest r^{up} is determined by excluding the
 2343 range of values of r for which $CL_s(r, \theta)$ is lower than the confidence level desired,
 2344 normally 90% or 95%, e.g, scanning over r and finding the value for which $p_r'^{up} =$
 2345 0.05. The expected upper limit can be calculated using pseudo-experiments based on
 2346 the background-only hypothesis and obtaining a distribution for r_{ps}^{up} ; the median of
 2347 that distribution corresponds to the expected upper limit, while the $\pm 1\sigma$ and $\pm 2\sigma$
 2348 deviations correspond to the values of the distribution that defines the 68% and 95%
 2349 of the area under the distribution centered in the median. It is usual to present all
 2350 the information about the expected and observed limits in the so-called *Brazilian-flag*
 2351 *plot* as the one showed in Figure 5.8. The solid line represent the observed CL_s

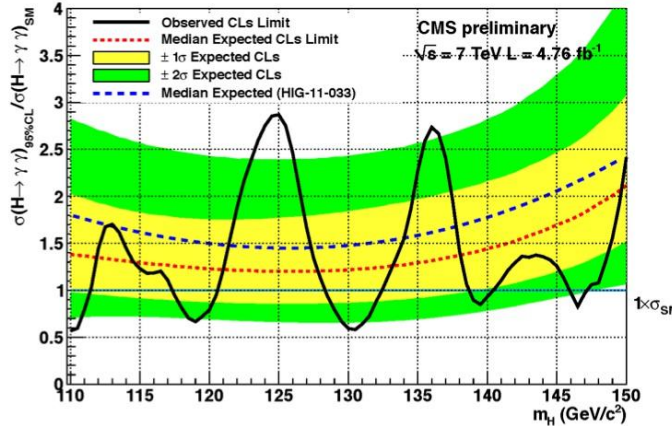


Figure 5.8: Brazilian flag plot of CMS experiment limits for Higgs boson decaying to photons [137].

2352 5.4 Asymptotic limits

2353 As said before, the complexity of the likelihood functions, the construction of test
 2354 statistics, and the calculation of the limits and their uncertainties is not always man-
 2355 ageable and requires extensive computational resources; in order to overcome those
 2356 issues, asymptotic approximations for likelihood-based test statistics, like the ones

described in previous sections, have been developed [138, 139] using Wilks' theorem.
Asymptotic approximations replace the construction of the test statistics p.d.f.s using
MC pseudo-experiments, with the approximate calculation of the test statistics p.d.f.s
by employing the so-called *Asimov dataset*.

The Asimov dataset is defined as the dataset that produce the true values of the
nuisance parameters when it is used to evaluate the estimators for all the parameters;
it is obtained by setting the values of the variables in the dataset to their expected
values [139].

Limits calculated by using the asymptotic approximation and the Asimov dataset
are know as *asymptotic limits*.

²³⁶⁷ **Chapter 6**

²³⁶⁸ **Search for production of a Higgs**

²³⁶⁹ **boson and a single top quark in**

²³⁷⁰ **multilepton final states in pp**

²³⁷¹ **collisions at $\sqrt{s} = 13$ TeV**

²³⁷² **6.1 Introduction**

²³⁷³ The Higgs boson discovery, supported on experimental observations and theoretical
²³⁷⁴ predictions made about the SM, gives the clue of the way in that elementary parti-
²³⁷⁵ cles acquire mass through the Higgs mechanism; therefore, knowing the Higgs mass,
²³⁷⁶ the Higgs-vector boson and Higgs-fermion couplings can be tested. In order to test
²³⁷⁷ the Higgs-top coupling, several measurements have been performed, as stated in the
²³⁷⁸ chapter 1, but they are limited in sensitivity to measure the square of the coupling.
²³⁷⁹ The production of a Higgs boson in association with a single top quark (tH) not
²³⁸⁰ only offers access to the sign of the coupling, but also, to the CP phase of the Higgs

2381 couplings.

2382 This chapter presents the search for the associated production of a Higgs boson
 2383 and a single top quark (tHq) events, focusing on leptonic signatures provided by the
 2384 Higgs decay modes to WW , ZZ , and $\tau\tau$; the 13 TeV dataset produced in 2016, with
 2385 an integrated luminosity of 35.9fb^{-1} , is used.

2386 As shown in Section 1.5, the SM cross section of tHq process is affected by a
 2387 destructive interference between two contributions (see Figure 1.15), where the Higgs
 2388 couples to either the W boson or the top quark; however, if the sign of the Higgs-
 2389 top coupling is flipped with respect to the SM prediction, a large enhancement of
 2390 the cross section occurs, making this analysis sensitive to such deviation. A second
 2391 process, where the Higgs boson and top quark are accompanied by a W boson (tHW)
 2392 has similar behavior, albeit with a weaker interference pattern and lower contribution
 2393 to the cross section, therefore, a combination of both processes would increase the
 2394 sensitivity to the sign of the coupling; in this analysis both contributions are combined
 2395 and referred to as tH channel. A third contribution comes from $t\bar{t}H$ process. The
 2396 purpose of this analysis is to investigate the exclusion of the presence of the $tH +$
 2397 $t\bar{t}H$ processes in the SM under the assumption of the anomalous Higgs-top coupling
 2398 modifier ($\kappa_t = -1$). The analysis exploits signatures with two leptons of the same sign
 2399 ($2lss$) channel and three leptons ($3l$) channel in the final state.

2400 Constraints on the sign of the Higgs-top coupling (y_t) have been derived from the
 2401 decay rate of Higgs boson to photon pairs [50] and from the cross section for associated
 2402 production of Higgs and Z bosons via gluon fusion [141], with recent results disfavoring
 2403 negative signs of the coupling [44, 59, 142], although the negative sign coupling have
 2404 not been completely excluded.

2405 The analysis presented here, expands previous analyses performed at 8 TeV [143,
 2406 144] and searches for associated production of $t\bar{t}$ pair and a Higgs boson in the mul-

2407 tilepton final state channel [145]; it also complements searches in $H \rightarrow b\bar{b}$ [146].

2408 The first sections present the characteristic tHq signature as well as the expected
 2409 backgrounds. The MC samples, data sets, and the physics object definitions are then
 2410 described; after, the background predictions, the signal extraction, the statistical
 2411 treatment of the selected events and the discussion of the systematic uncertainties
 2412 are described. The final section presents the results for the exclusion limits as a
 2413 function of the ratio of κ_t and the dimensionless modifier of the Higgs-vector boson
 2414 coupling κ_V .

2415 The analysis is designed to efficiently identify and select prompt leptons from on-
 2416 shell W and Z boson decays and to reject non-prompt leptons from b quark decays
 2417 and spurious lepton signatures from hadronic jets. Events are then selected in the
 2418 $2lss$ and $3l$ channels, and are required to contain hadronic jets, some of which must
 2419 be consistent with b quark hadronization. Finally, the signal yield is extracted by
 2420 simultaneously fitting the output of two dedicated multivariate discriminants, trained
 2421 to separate the tHq signal from the two dominant backgrounds, in all categories. The
 2422 fit result is then used to set an upper limit on the combined $t\bar{t}H + tH$ production
 2423 cross section, as a function of the relative coupling strengths of Higgs-top quark and
 2424 Higgs-Vector boson. Figure 6.1 shows an schematic overview of the analysis strategy
 2425 workflow.

2426 With respect to the 8 TeV analysis, the object selections have been adjusted for
 2427 the updated LHC running conditions at 13 TeV, the lepton identification has been
 2428 improved, and more powerful multivariate analysis techniques are used for the signal
 2429 extraction.

2430 The analysis has been made public by CMS as a Physics Analysis Summary [147]
 2431 combining the result for the three lepton and two lepton same-sign channels; the
 2432 content present in this chapter is based on that document and on References [145,149]

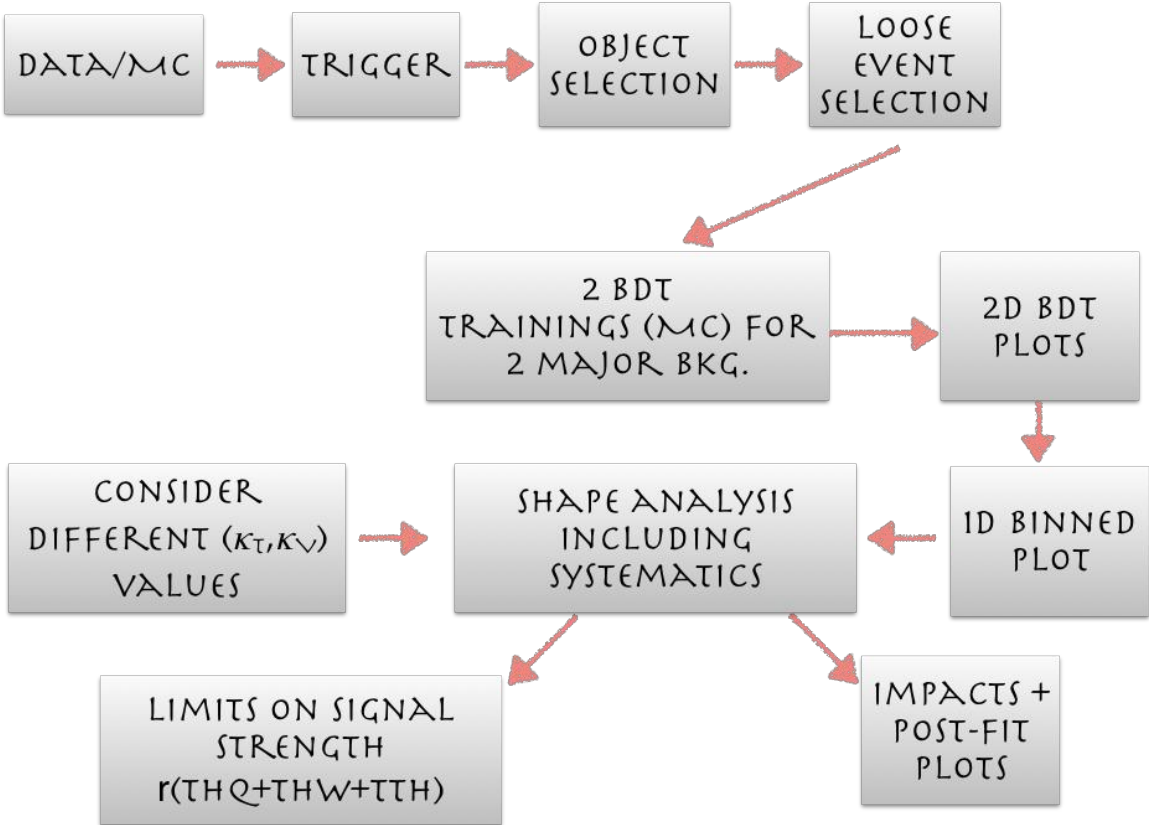


Figure 6.1: A schematic overview of the analysis workflow. Based on sets of optimized physics object definitions and selection criteria, signal and background events in a data sample are discriminated. The discrimination is performed by a BDT, previously trained using MC samples of the dominant backgrounds, using discriminant variables based on the b -jet multiplicity, the activity in the forward region of the detector, and the kinematic properties of leptons. The CL_s limits on the combined $t\bar{t}H + tH$ production cross section, as a function of the relative coupling strengths are calculated.

unless other Reference is stated. Currently, an effort to turn the analysis into a paper combining the multilepton and $H \rightarrow b\bar{b}$ is ongoing.

6.2 tHq signature

In order to select events of tHq process, its features are translated into a set of selection rules; Figure 6.2 shows the Feynman diagram and a schematic view of the

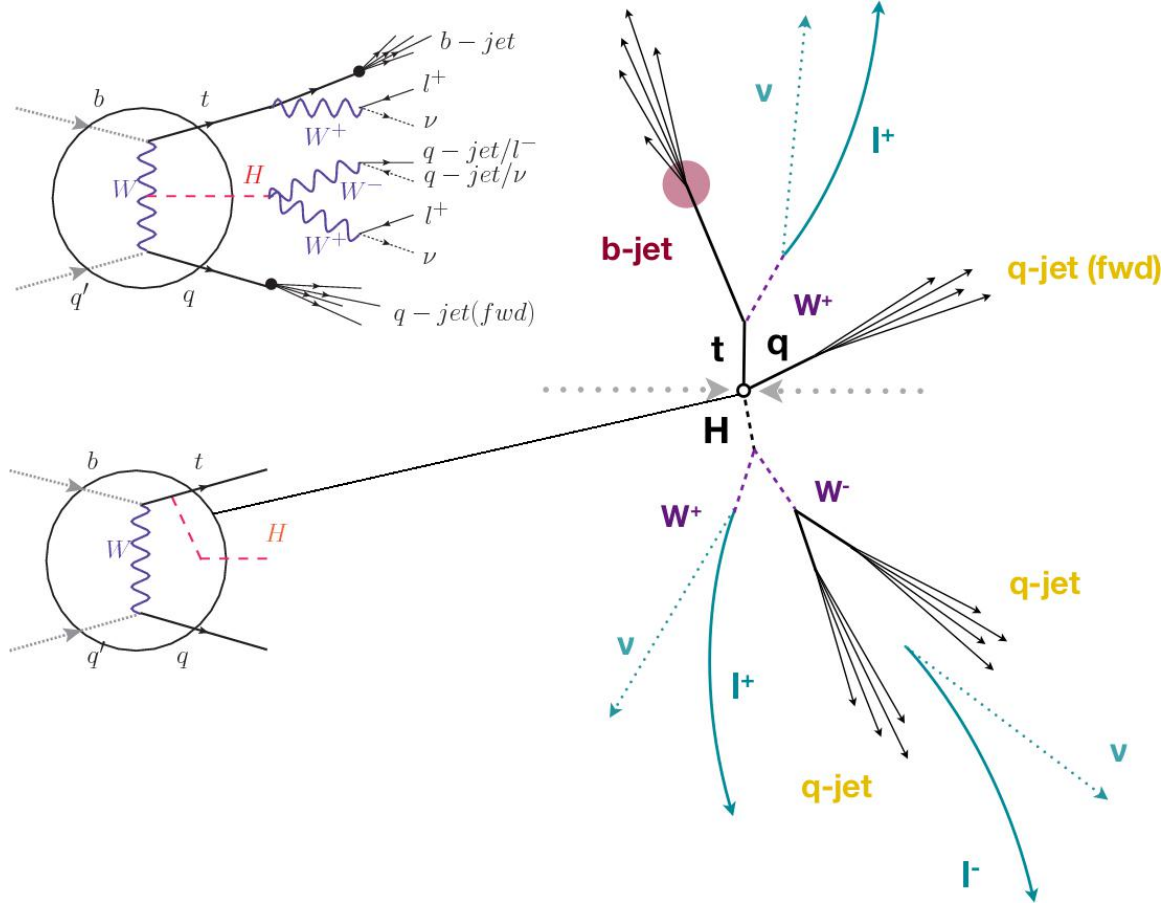


Figure 6.2: tHq event signature. Left: Feynman diagram including the whole evolution up to the final state for the case of the Higgs boson emitted by the W boson (top); Feynman diagram for the case where the Higgs boson is emitted by the top quark. Right: Schematic view as it would be seen in the detector; the circle in the Feynman diagrams on the left corresponds to the circle in the center of the schematic view as indicated by the line connecting them. In the $2lss$ channel, one of the W bosons from the Higgs boson decays to two light-quark jets while in the $3l$ channel both W bosons decay to leptons.

2438 tHq process from the pp collision to the final state configuration. A single top quark
 2439 is produced accompanied by a light quark, denoted as q ; this light quark is produced
 2440 predominantly in the forward region of the detector. The Higgs boson can be either
 2441 emitted by the exchanged W boson or directly by the singly produced top quark.

2442 Due to their high masses/short lifetimes, top quark and Higgs boson decay after
 2443 their production within the detector. The Higgs boson is required to decay into a W

2444 boson pair¹. The top quark almost always decays into a bottom quark and a W boson,
 2445 as encoded in the CMK matrix. The W bosons are required to decay leptonically
 2446 either all the three in the $3l$ channel or the pair with equal electrical charge in the
 2447 $2lss$ channel case; τ leptons are not reconstructed separately and only their leptonic
 2448 decays into either electrons or muons are considered in this analysis.

2449 In summary, the signal process is characterized by a the final state with

- 2450 • one light-flavored forward jet,
 - 2451 • one central b-jet,
 - 2452 • $2lss$ channel → two leptons of the same sign, two neutrinos and two light (often
 2453 soft) jets,
 - 2454 • $3l$ channel → three leptons, three neutrinos and no central light-flavored jets,
- 2455 The presence of neutrinos is inferred from the presence of MET.

2456 6.3 Background processes

2457 The background processes are those that can mimic the signal signature or at least
 2458 can be reconstructed as signal as a result of certain circumstances. The backgrounds
 2459 can be classified as

- 2460 • irreducible backgrounds: where genuine prompt leptons are produced in on-
 2461 shell W and Z boson decays; they can be reliably estimated directly from MC
 2462 simulated events, using higher-order cross sections or data control regions for
 2463 the overall normalization.

¹ ZZ and $\tau\tau$ decays are also include in the analysis but they are not separately reconstructed

2464 • reducible backgrounds: where at least one of the leptons is *non-prompt*, i.e.,
 2465 produced within a hadronic jet; genuine leptons from heavy flavor decays and
 2466 misreconstructed jets, also known as *mis-ID leptons* are considered non-prompt
 2467 leptons or or *fake leptons* as well as electrons from photon conversions. These
 2468 non-prompt leptons leave tracks and hits in the detection systems as would a
 2469 prompt lepton, but evaluation the correlation of those hits with nearby jets
 2470 could be a way of removing them. The misassignment of electron charge in
 2471 processes like $t\bar{t}$ or Drell-Yan, represents an additional source of background,
 2472 but it is relevant only for the $2lss$ channel. Reducible backgrounds are not well
 2473 predicted by simulation, hence, they are estimated using data-driven methods.

2474 The main sources of background events for tHq process are $t\bar{t}$ process and $t\bar{t}V(V =$
 2475 W, Z, γ) processes. Figure 6.3 shows the signature for $t\bar{t}$ and $t\bar{t}W$ processes.

2476 The largest contribution to irreducible backgrounds comes from $t\bar{t}W$ and $t\bar{t}Z$
 2477 processes for which the number of ($b-$)jets (($b-$)jet multiplicity) is higher than that
 2478 of the signal events, while for other contributing background events, WZ , ZZ , and
 2479 rare SM processes like $W^\pm W^\pm qq$, $t\bar{t}t\bar{t}$, tZq , tZW , WWW , WWZ , WZZ , ZZZ ,
 2480 the ($b-$)jet multiplicity is lower compared to that of the signal events. None of the
 2481 irreducible backgrounds present activity in the forward region of the detector.

2482 On the side of the reducible backgrounds, the largest contribution comes from the
 2483 $t\bar{t}$ events which have a very similar signature to the signal events but does no present
 2484 activity in the forward region of the detector either; A particular feature of the $t\bar{t}$
 2485 events is their charge-symmetry, which is different from the characteristics of signal
 2486 events.

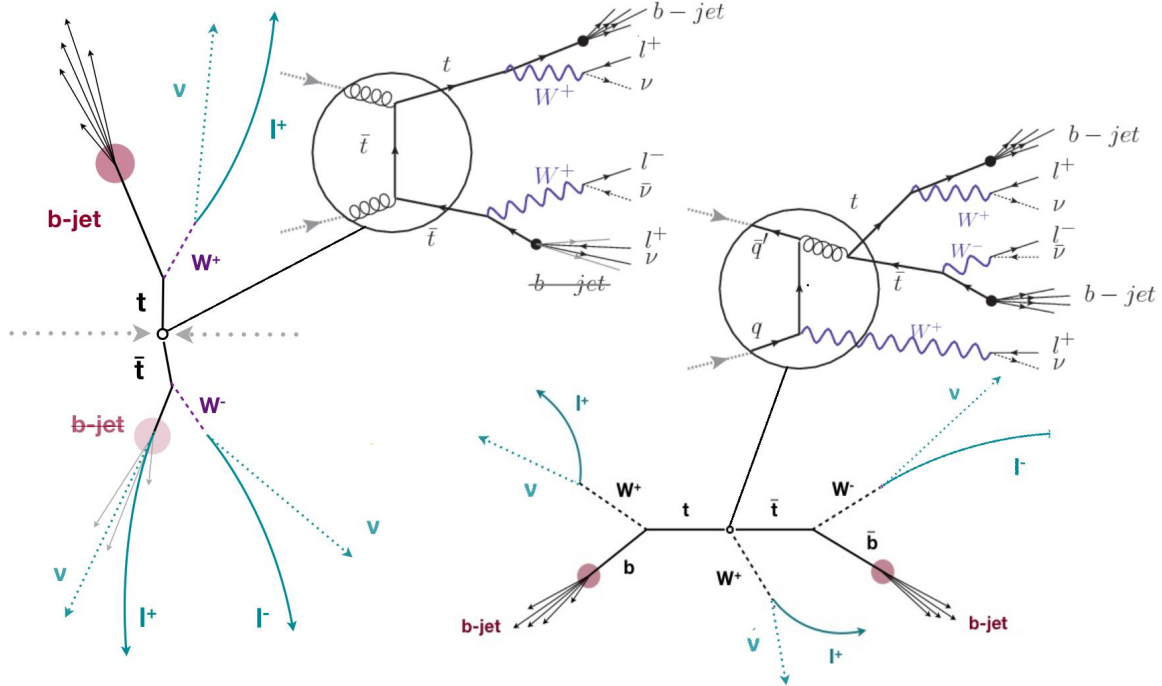


Figure 6.3: $t\bar{t}$ (left) and $t\bar{t}W$ (right) events signature as they would be seen in the detector; the Feynman diagrams including the whole evolution up to the final state are also showed. The $t\bar{t}$ process signature is very similar to that of the signal process with one fake lepton and no forward activity. The $t\bar{t}W$ process presents a higher b -jet multiplicity compared to the signal process, a prompt lepton and no forward activity.

2487 6.4 Data and MC Samples

2488 6.4.1 Full 2016 data set

2489 The data set used in this analysis was collected by the CMS experiment during 2016,
 2490 while running at $\sqrt{s} = 13$ TeV, and corresponds to a total integrated luminosity
 2491 of 35.9 fb^{-1} . Only periods when the CMS magnet was on were considered when
 2492 selecting the data samples; that corresponds to the 23Sep2016 (Run B to G) and
 2493 PromptReco (Run H) versions of the datasets.

2494 Multilepton final states with either two same-sign leptons or three leptons tar-
 2495 get the case where the Higgs boson decays to a pair of W bosons, τ leptons, or Z
 2496 bosons, and where the top quark decays leptonically, hence, the SingleElectron,

2497 SingleMuon, DoubleEG, MuonEG, DoubleMuon dataset (see Table A.1) compose the
2498 full dataset. The certified luminosity sections are selected using the golden JSON file
2499 defined by the CMS experiment [148].

2500 **6.4.2 Triggers**

2501 The events considered are those online-reconstructed events triggered by one, two, or
2502 three leptons. Single-lepton triggers are included in order to boost the acceptance
2503 of events where the p_T of the sub-leading lepton falls below the threshold of the
2504 double-lepton triggers. The trigger efficiency is increased by including double-lepton
2505 triggers in the $3l$ category, and single-lepton triggers in all categories; it is possible
2506 given the logical “or” of the trigger decisions of all the individual triggers in a given
2507 category. Table A.2 shows the lowest-threshold non-prescaled triggers present in the
2508 High-Level Trigger (HLT) menus for both Monte-Carlo and data in 2016.

2509 **Trigger efficiency scale factors**

2510 Trigger efficiency describes the ability of events to pass the trigger requirements. It
2511 is measured in simulated events using generator information given that there is no
2512 trigger bias with the MC sample. Measuring the trigger efficiency in data requires a
2513 more elaborated procedure; first, select a set of events collected by a trigger that is
2514 uncorrelated with the lepton triggers such that the selected events form an unbiased
2515 sample. In this analysis, that uncorrelated trigger is a MET trigger. Second step
2516 is looking for candidate events with exactly two good leptons (exactly three good
2517 leptons for the $3l$ channel). Finally, measure the efficiency for the candidate events to
2518 pass the logical “or” of triggers being considered in a given event category as defined
2519 in Table A.2.

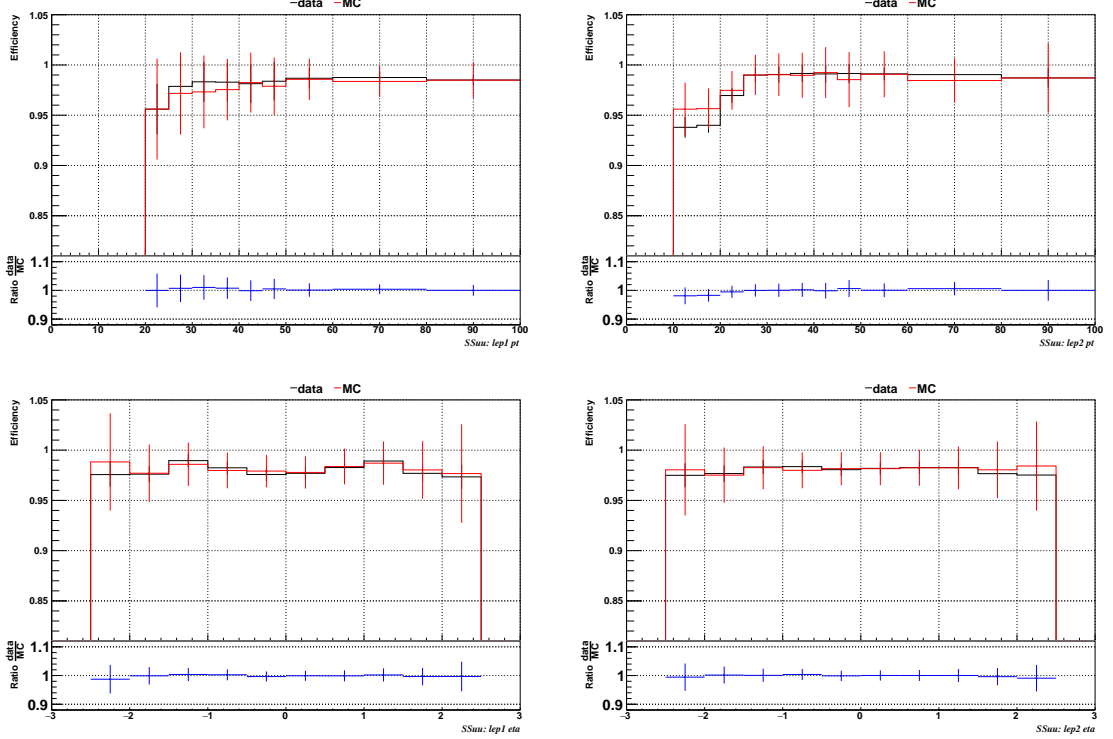


Figure 6.4: Comparison between data and MC trigger efficiencies in the same-sign $\mu\mu$ category, as a function of the p_T (top) and η (bottom) of the leading lepton (left) and the sub-leading lepton (right) [149].

Category	Scale Factor
ee	1.01 ± 0.02
e μ	1.01 ± 0.01
$\mu\mu$	1.00 ± 0.01
3l	1.00 ± 0.03

Table 6.1: Trigger efficiency scale factors and associated uncertainties, shown here rounded to the nearest percent.

2520 Comparisons between the data and MC efficiencies for each category, showed in
 2521 Figures 6.4, 6.5, and 6.6, reveal that they are in good agreement; the difference is
 2522 corrected by applying scale factors derived from the ratio between both efficiencies.
 2523 Applied flat scale factors in each category are shown in Table 6.1; they have been
 2524 inherited from Reference [149].

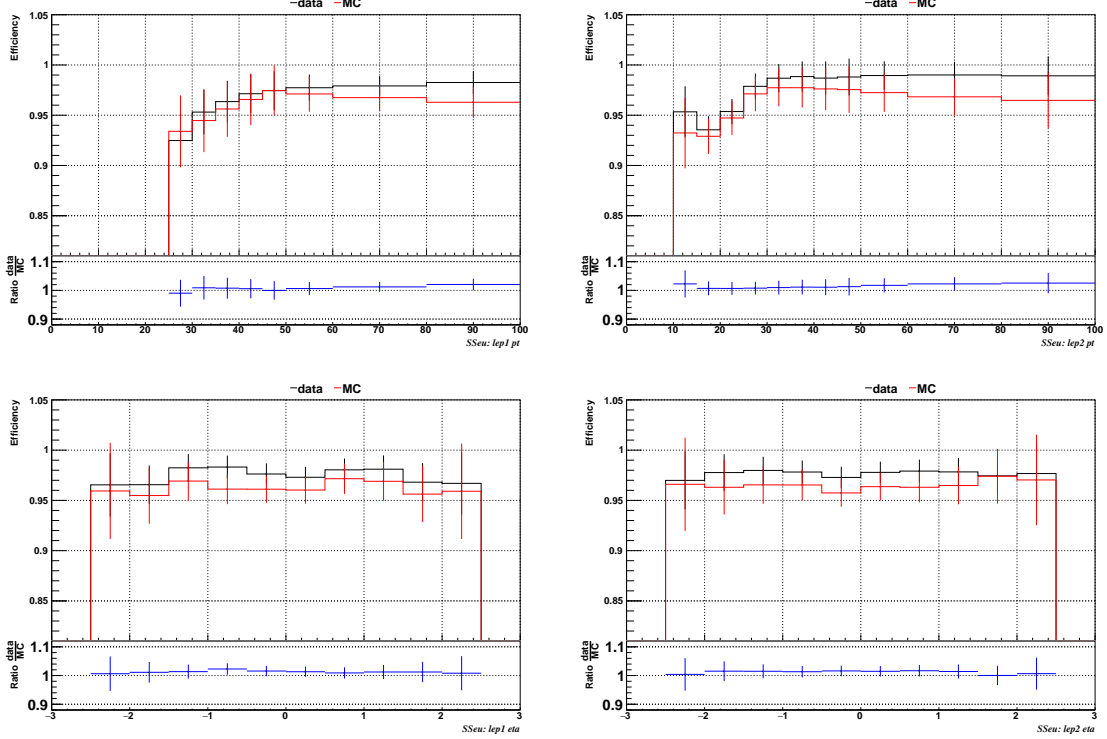


Figure 6.5: Comparison between data and MC trigger efficiencies in the same-sign $e\mu$ category as a function of the p_T (top) and η (bottom) of the leading lepton (left) and the sub-leading lepton (right) [149].

2525 6.4.3 MC samples

2526 Current event generators allow the adjustment of the kinematics of the generated
 2527 events, based on an event-wise reweighting; in this way, several generation parameters
 2528 phase spaces can be explored according to the experimental interests. The signal
 2529 samples used in this analysis were generated in such a way that not only the case κ_t
 2530 $= -1$, but an extended range of κ_t and κ_V values may be investigated.

2531 tHq and tHW cross section in the κ_t - κ_V phase space are shown in Figure 6.7. As
 2532 said in section 3.1, the tHq sample was generated using the 4F scheme which provides
 2533 a better description of the additional b quark from the initial gluon splitting, while the
 2534 tHW sample was generated using the 5F scheme in order to remove its interference

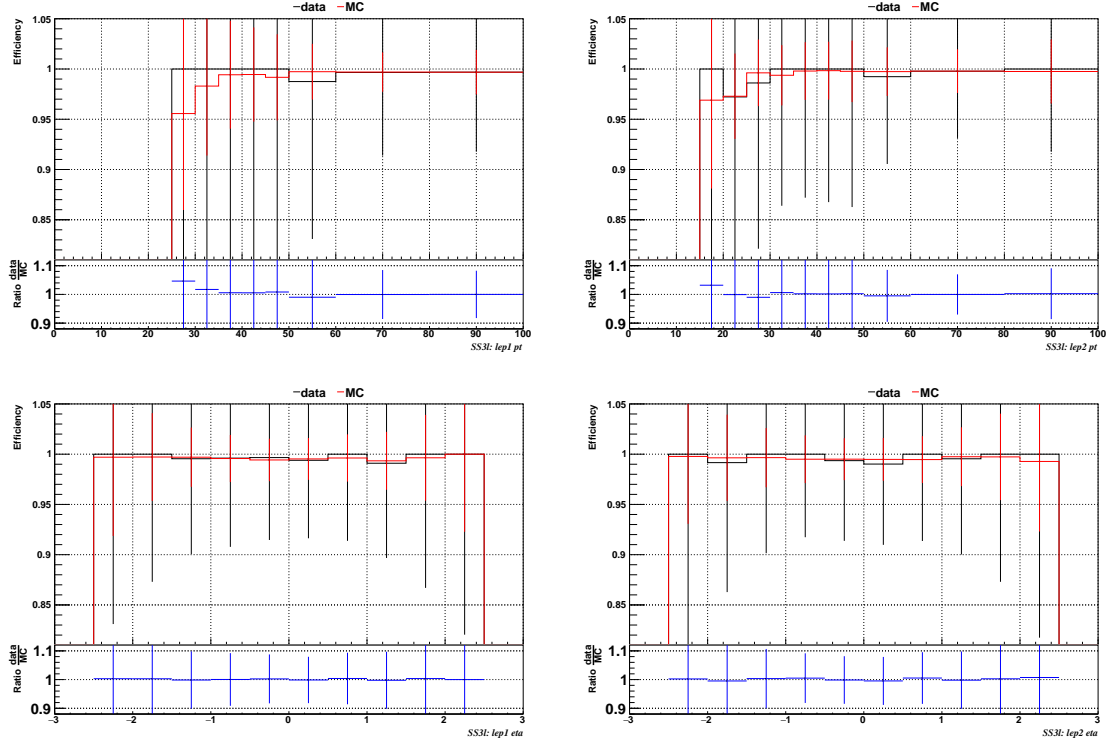


Figure 6.6: Comparison between data and MC trigger efficiencies in the $3l$ category, as a function of the p_T (top) and η (bottom) of the leading lepton (left) and the sub-leading lepton (right) [149].

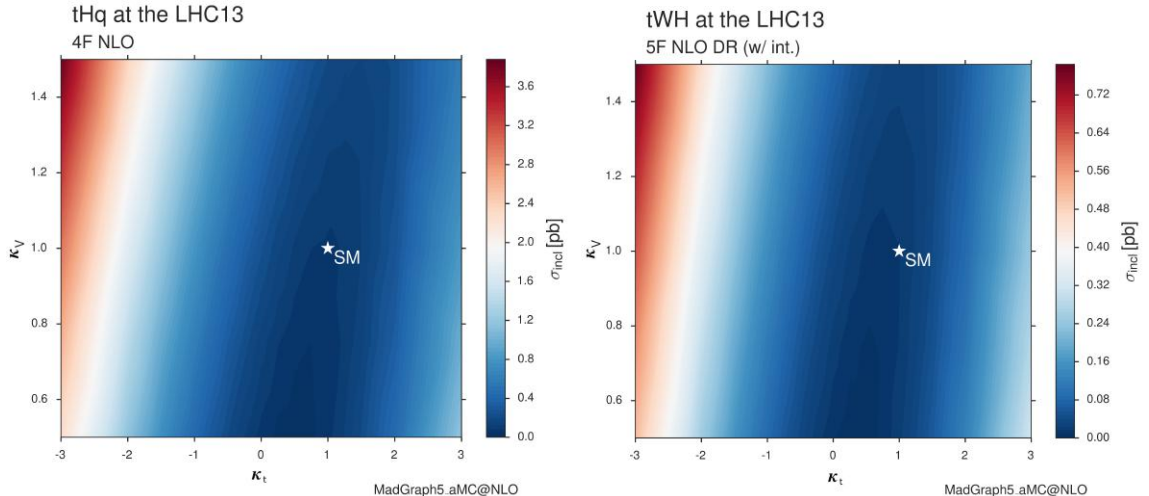


Figure 6.7: tHq and tHW cross section in the κ_t - κ_V phase space [150].

2535 with $t\bar{t}H$ at LO.

2536 **MC signal samples**

2537 The two signal samples, tHq and tHW , correspond to the `RunIISummer16MiniAODv2`
 2538 campaign produced with `CMSW_80X`; they were produced with `MG5_aMC@NLO`
 2539 (version 5.2.2.3), in LO mode at $\sqrt{s} = 13$ TeV, and are normalized to NLO cross sec-
 2540 tions (see Table 6.2). The Higgs boson is assumed to be SM-like except for the values
 2541 of its couplings to the top quark and W boson. Each sample was generated with a set
 2542 of event weights corresponding to 51 different values of (κ_t, κ_V) couplings, accessible
 2543 in terms of LHE event weights as shown in Table A.3; however, the main interest is
 2544 the $(\kappa_t = -1, \kappa_V = 1)$ case.

Sample	σ [pb]	BF
<code>/THQ_Hincl_13TeV-madgraph-pythia8_TuneCUETP8M1/</code>	0.7927	0.324
<code>/THW_Hincl_13TeV-madgraph-pythia8_TuneCUETP8M1/</code>	0.1472	1.0
<code>/tTHJetToNonbb_M125_13TeV_amcatnloFXFX_madspin_pythia8_mWCutfix/</code>	0.2151	1.0

2545 **Table 6.2:** MC signal samples used in this analysis; cross section and branching fraction
 2546 are also listed [150].

2545 The $t\bar{t}H$ sample was produced using `AMC@NLO` interfaced to `PYTHIA 8` for
 2546 the parton shower, and is scaled to NLO cross sections. The $t\bar{t}H$ cross section depends
 2547 quadratically on κ_t ; however, in contrast to the tHq and tHW samples, the scaling
 2548 is not performed during the sample generation process but in the analysis code since
 2549 it was decided to include the $t\bar{t}H$ process as a part of the signal in the course of the
 2550 analysis.

2551 **MC background samples**

2552 Several MC generators were used to generate the samples of the background processes.
 2553 The dominant background sources ($t\bar{t}$, $t\bar{t}W$, $t\bar{t}Z$) were produced using `AMC@NLO`

2554 interfaced to PYTHIA8, and are scaled to NLO cross sections. Other minor back-
 2555 ground processes are simulated using POWHEG interfaced to PYTHIA, or bare
 2556 PYTHIA as stated in the sample names in Table A.4. Pileup interactions are in-
 2557 cluded in the simulation in order to reflect the observed multiplicity in data; the
 2558 simulated events are weighted according to the actual pileup in data, estimated from
 2559 the measured bunch-to-bunch instantaneous luminosity and the total inelastic cross
 2560 section, 69.2 mb. All events are finally passed through a full simulation of the CMS
 2561 detector using GEANT4, and reconstructed using the same algorithms as used for
 2562 the data.

2563 6.5 Object Identification

2564 In this section, the specific definitions of the physical objects in terms of the recon-
 2565 struction parameters are presented; thus, the provided details summarize and com-
 2566 plement the descriptions presented in previous chapters. The object reconstruction
 2567 and selection strategy used in this thesis are inherited from the analyses in Refer-
 2568 ences [145, 149].

2569 6.5.1 Lepton reconstruction and identification

2570 Two types of leptons are defined in this analysis: *signal leptons* are those coming from
 2571 W, Z and τ decays which usually are isolated from other particles; *background leptons*
 2572 are defined as leptons produced in b -jet hadron decays, light-jets misidentification,
 2573 and photon conversions.

2574 The process of reconstruction and identification of electron and muon candidates
 2575 was described in chapter 3, hence, the identification variables used in order to retain

2576 the highest possible efficiency for signal leptons while maximizing the rejection of
 2577 background leptons are listed and described in the following sections ².

2578 The identification variables include not only observables related directly to the re-
 2579 constructed leptons themselves, but also to the clustered energy deposits and charged
 2580 particles in a cone around the lepton direction (jet-related variables); an initial loose
 2581 preselection of leptons candidates is performed and then an MVA discriminator, re-
 2582 fered to as *lepton MVA* discriminator, is used to distinguish signal leptons from
 2583 background leptons.

2584 Muons

2585 The Physics Objects Groups (POG) at CMS, are in charge of studying and defining
 2586 the set of selection criteria applied on the course of reconstruction and identification
 2587 of particles. These selection criteria are implemented in the CMS framework in the
 2588 form of several object identification working points according to the strength of the
 2589 requirements.

2590 The muon candidates are reconstructed by combining information from the tracker
 2591 system and the muon detection system of CMS detector and the POG defined three
 2592 working points for muon identification *MuonID* [153];

- 2593 • *POG Loose Muon ID* is a particle identified as a muon by the PF event re-
 2594 construction and also reconstructed either as a global-muon or as an arbitrated
 2595 tracker-muon. This identification criteria is designed to be highly efficient for
 2596 prompt muons and for muons from heavy and light quark decays; it can be com-
 2597 plemented by applying impact parameter cuts in analyses with prompt muon
 2598 signals.

² The studies performed to optimize the identification are far from the scope of this thesis,
 therefore, only general descriptions are provided

- 2599 • *POG Medium Muon ID* is a Loose muon with additional track-quality and
 2600 muon-quality (spatial matching between the individual measurements in the
 2601 tracker and the muon system) requirements. This identification criteria is de-
 2602 signed to be highly efficient in the separation of the muons coming from decay
 2603 in flight of heavy quarks and muons coming from B meson decays as well as
 2604 prompt muons. An additional category *MVA Prompt ID* is defined in this iden-
 2605 tification criteria directed to discriminated muons from B mesons and prompt
 2606 muons (from W,Z and τ decays). The Medium ID provides the same fake rate as
 2607 the Tight Muon ID but a higher efficiency on prompt and B-decays muons. [154]
- 2608 • *POG Tight Muon ID* is a global muon with additional muon-quality require-
 2609 ments Tight Muon ID selects a subset of the PF muons.
- 2610 Only muons within the muon system acceptance $|\eta| < 2.4$ and minimum p_T of 5
 2611 GeV are considered.

2612 **Electrons**

2613 Electrons are reconstructed using information from the tracker and from the electro-
 2614 magnetic calorimeter and identified by an MVA algorithm (*MVA eID* discriminant)
 2615 using the shape of the calorimetric shower variables like the shape in η and ϕ , the clus-
 2616 ter circularity, widths along η and ϕ ; track-cluster matching variables like E_{tot}/p_{in} ,
 2617 E_{Ele}/p_{out} , $\Delta\eta_{in}$, $\Delta\eta_{out}$, $\Delta\phi_{in}$, $1/E - 1/p$; and track quality variables like χ^2 of the
 2618 GSF tracks, the number of hits used by the GSF filter [155].

2619 A loose selection based on η -dependent cuts on this discriminant is used to prese-
 2620 lect electron candidates, the full shape of the discriminant is used in the lepton MVA
 2621 selection to separate signal leptons from background leptons (described in Section
 2622 6.5.1).

2623 In order to reject electrons from photon conversions, electron candidates with
 2624 missing hits in the pixel tracker layers or matched to a conversion secondary vertex
 2625 are discarded. Electrons are selected for the analysis if they have $p_T > 7$ GeV and
 2626 are located within the tracker system acceptance region ($|\eta| < 2.5$).

2627 **Lepton vertexing and pile-up rejection**

2628 The impact parameter in the transverse plane d_0 , impact parameter along the z -
 2629 axis d_z , and the impact parameter significance in the detector space SIP_{3D} , are
 2630 considered to perform the identification and rejection of pile-up, misreconstructed
 2631 tracks, and background leptons from b-hadron decays; pile-up and misreconstructed
 2632 track mitigation is achieved by imposing loose cuts on the impact parameter variables.
 2633 The full shape of those variables is used in a lepton MVA classifier to achieve the best
 2634 separation between the signal and the background leptons.

2635 **Lepton isolation**

2636 PF is able to recognize leptons from two different sources: on one side, leptons from
 2637 the decays of heavy particles, such as W and Z bosons, which are normally isolated in
 2638 space from the hadronic activity in the event; on the other side, leptons from decays
 2639 of hadrons and jets misidentified as leptons, which are not isolated as the former. For
 2640 highly boosted systems, like the lepton and the b -jet generated in the semileptonic
 2641 decay of a boosted top, the decay products tend to be more closer and sometimes they
 2642 even overlap; thus, the PF standard definition of isolation in terms of the separation
 2643 ΔR between lepton candidates (l) and other PF objects (i) in the η - ϕ plane,

$$\Delta R = \sqrt{(\eta^l - \eta^i)^2 + (\phi^l - \phi^i)^2} < 0.3 \quad (6.1)$$

which considers all the neutral, charged hadrons and photons in a cone around the leptons, is refocused to the local isolation of the leptons through the mini-isolation I_{mini} [156] defined as the sum of particle flow candidates p_T within a cone around the lepton, corrected for the effects of pileup and divided by the lepton p_T

$$I_{mini} = \frac{\sum_R p_T(h^\pm) - \max\left(0, \sum_R p_T(h^0) + p_T(\gamma) - \rho \mathcal{A}\left(\frac{R}{0.3}\right)^2\right)}{p_T(l)} \quad (6.2)$$

where ρ is the pileup energy density, h^\pm, h^0, γ, l , represent the charged hadron, neutral hadrons, photons, and the lepton, respectively. The radius R of the cone depends on the p_T of the lepton according to

$$R = \frac{10\text{GeV}}{\min(\max(p_T(l), 50\text{GeV}), 200\text{GeV})}, \quad (6.3)$$

The p_T dependence of the cone size allows for greater signal efficiency. Setting a cut on I_{mini} below a given threshold ensures that the lepton is locally isolated, even in boosted systems. The effect of pileup is mitigated using the so-called effective area correction \mathcal{A} listed in Table 6.3.

$ \eta $ range	$\mathcal{A}(e)$ neutral/charged	$\mathcal{A}(\mu)$ neutral/charged
0.0 - 0.8	0.1607 / 0.0188	0.1322 / 0.0191
0.8 - 1.3	0.1579 / 0.0188	0.1137 / 0.0170
1.3 - 2.0	0.1120 / 0.0135	0.0883 / 0.0146
2.0 - 2.2	0.1228 / 0.0135	0.0865 / 0.0111
2.2 - 2.5	0.2156 / 0.0105	0.1214 / 0.0091

Table 6.3: Effective areas, for electrons and muons used to mitigate the effect of pileup by using the so-called effective area correction.

A loose cut on I_{mini} is applied to pre-select the muon and electron candidates; however, the full shape is used in the lepton MVA discriminator when performing the signal lepton selection.

2658 **Jet-related variables**

2659 In order to reject misidentified leptons from b -jets, mostly coming from $t\bar{t}$ +jets,
 2660 Drell-Yan+jets, and W+jets events, the vertexing and isolation described in previous
 2661 sections are complemented with additional variables related to the closest recon-
 2662 structed jet to the lepton, i.e., the PF jets reconstructed³ around the leptons with
 2663 $\Delta R = \sqrt{(\eta^l - \eta^{jet})^2 + (\phi^l - \phi^{jet})^2} < 0.5$. The identification variables used in the lep-
 2664 ton MVA discriminator are the ratio p_T^l/p_T^{jet} , the CSV b-tagging discriminator value
 2665 of the jet, the number of charged tracks of the jet, and the relative p_T given by

$$p_T^{rel} = \frac{(\vec{p}_{jet} - \vec{p}_l) \cdot \vec{p}_l}{\|\vec{p}_{jet} - \vec{p}_l\|}. \quad (6.4)$$

2666 **LeptonMVA discriminator**

2667 Electrons and muons passing the basic selection process described above are referred
 2668 to as *loose leptons*. Additional discrimination between signal leptons and background
 2669 leptons is crucial considering that the rate of $t\bar{t}$ production is much larger than the
 2670 signal, hence, an overwhelming background from $t\bar{t}$ production is present. To maxi-
 2671 mally exploit the available information in each event to that end, the dedicated lepton
 2672 MVA discriminator, based on a boosted decision tree (BDT) algorithm, has been built
 2673 so that all the identification variables can be used together.

2674 The lepton MVA discriminator training is performed using simulated signal Loose
 2675 leptons from the $t\bar{t}H$ MC sample and fake leptons from the $t\bar{t}$ +jets MC sample,
 2676 separately for muons and electrons. The input variables used include vertexing, iso-
 2677 lation and jet-related variables, the p_T and η of the lepton, the electron MVA eID
 2678 discriminator and the muon segment-compatibility variables. An additional require-
 2679 ment known as *tight-charge* requirement, is imposed by comparing two independent

³ Charged hadrons from PU vertices are not removed prior to the jet clustering.

measurement of the charge, one from the ECAL supercluster and the other from the tracker; thus, the consistency in the measurements of the electron charge is ensured so that events with a wrong electron charge assignment are rejected; this variable is particularly used in the $2lss$ channel to suppress opposite-sign events for which the charge of one of the leptons has been mismeasured. The tight-charge requirement for muons is represented by the requirement of a consistently well measured track transverse momentum given by $\Delta p_T/p_T < 0.2$. Leptons are selected for the final analysis if they pass a given threshold of the BDT output, and are referred to as *tight leptons* in the following.

The validation of the lepton MVA algorithm and the lepton identification variables is performed using data in various control regions; the details about that validation are not discussed here but can be found in Reference [149].

Selection definitions

Electron and muon object identification is defined in three different sets of selections criteria; the *Loose*, *Fakeable Object*, and *Tight* selection. These three levels of selection are designed to serve for event level vetoes, the fake rate estimation application region (see Section 6.7.2), and the final signal selection, respectively. The p_T of fakeable objects is defined as $0.85 \times p_T(\text{jet})$, where the jet is the one associated to the lepton object. This mitigates the dependence of the fake rate on the momentum of the fakeable object and thereby improves the precision of the method.

Tables 6.4 and 6.5 list the full criteria for the different selections of muons and electrons.

In addition to the previously defined requirements for jets, they are required to be separated from any lepton candidates passing the fakeable object selections by $\Delta R > 0.4$.

Cut	Loose	Fakeable object	Tight
$ \eta < 2.4$	✓	✓	✓
p_T	$> 5\text{GeV}$	$> 15\text{GeV}$	$> 15\text{GeV}$
$ d_{xy} < 0.05$ (cm)	✓	✓	✓
$ d_z < 0.1$ (cm)	✓	✓	✓
$\text{SIP}_{3D} < 8$	✓	✓	✓
$I_{\text{mini}} < 0.4$	✓	✓	✓
is Loose Muon	✓	✓	✓
jet CSV	—	< 0.8484	< 0.8484
is Medium Muon	—	—	✓
tight-charge	—	—	✓
lepMVA > 0.90	—	—	✓

Table 6.4: Requirements on each of the three muon selections. In the cases where the cut values change between the selections, those values are listed in the table. Otherwise, whether the cut is applied is indicated.

Cut	Loose	Fakeable Object	Tight
$ \eta < 2.5$	✓	✓	✓
p_T	$> 7\text{GeV}$	$> 15\text{GeV}$	$> 15\text{GeV}$
$ d_{xy} < 0.05$ (cm)	✓	✓	✓
$ d_z < 0.1$ (cm)	✓	✓	✓
$\text{SIP}_{3D} < 8$	✓	✓	✓
$I_{\text{mini}} < 0.4$	✓	✓	✓
MVA eID $> (0.0, 0.0, 0.7)$	✓	✓	✓
$\sigma_{in\eta} < (0.011, 0.011, 0.030)$	—	✓	✓
H/E $< (0.10, 0.10, 0.07)$	—	✓	✓
$\Delta\eta_{in} < (0.01, 0.01, 0.008)$	—	✓	✓
$\Delta\phi_{in} < (0.04, 0.04, 0.07)$	—	✓	✓
$-0.05 < 1/E - 1/p < (0.010, 0.010, 0.005)$	—	✓	✓
p_T^{ratio}	—	$> 0.5^\dagger / -$	—
jet CSV	—	$< 0.3^\dagger / < 0.8484$	< 0.8484
tight-charge	—	—	✓
conversion rejection	—	—	✓
Number of missing hits	< 2	$= 0$	$= 0$
lepton MVA > 0.90	—	—	✓

Table 6.5: Criteria for each of the three electron selections. In cases where the cut values change between selections, those values are listed in the table. Otherwise, whether the cut is applied is indicated. In some cases, the cut values change for different η ranges. These ranges are $0 < |\eta| < 0.8$, $0.8 < |\eta| < 1.479$, and $1.479 < |\eta| < 2.5$ and the respective cut values are given in the form (value₁, value₂, value₃). For the two p_T^{ratio} and CSV rows, the cuts marked with a \dagger are applied to leptons that fail the lepton MVA cut, while the loose cut value is applied to those that pass the lepton MVA cut.

2705 6.5.2 Lepton selection efficiency

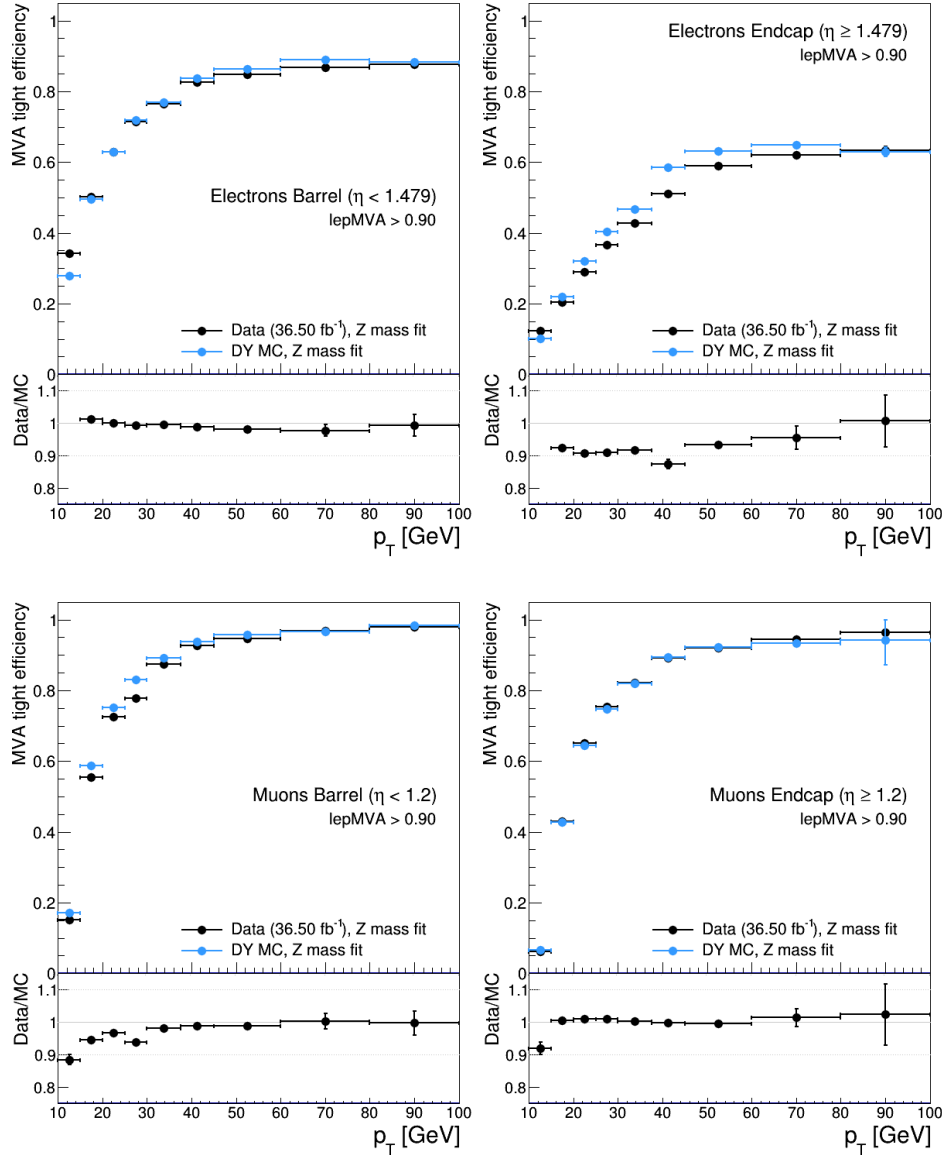


Figure 6.8: Tight vs loose selection efficiencies for electrons (top), and muons (bottom), for the $2lss$ definition, i.e., including the tight-charge requirement.

2706 Efficiencies of reconstruction and selecting loose leptons are measured both for
 2707 muons and electrons using a tag and probe method on both data and MC, using
 2708 $Z \rightarrow \ell^+ \ell^-$ [157]. The scale factors are derived from the ratio of efficiencies $\varepsilon_i(p_T, \eta)$

2709 measured for a given lepton in data/MC, according to

$$\rho(p_T, \eta) = \frac{\varepsilon_{data}(p_T, \eta)}{\varepsilon_{MC}(p_T, \eta)}. \quad (6.5)$$

2710 The scale factor for each event is used to correct the weight of the event in the

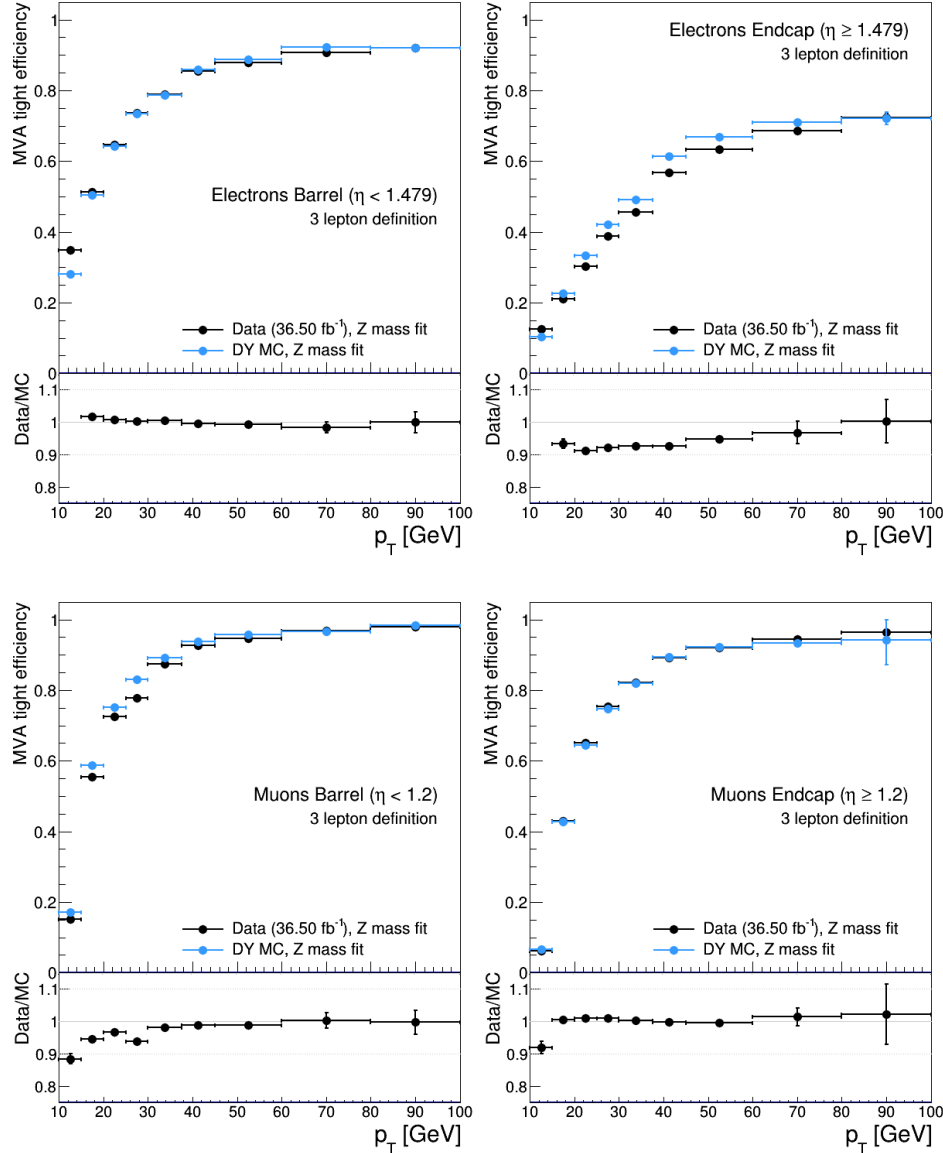


Figure 6.9: Tight vs loose selection efficiencies for electrons (top), and muons (bottom), for the $3l$ channel not including the tight-charge requirement.

2711 full sample; therefore, the full simulation correction is given by the product of all
 2712 the individual scale factors. The scale factors used in this thesis are inherited from
 2713 Reference [149] which in turns inherited them from leptonic SUSY analyses using
 2714 equivalent lepton selections.

2715 The efficiency of applying the tight selection as defined in Tables 6.4 and 6.5, on
 2716 the loose leptons is determined by using a tag and probe method on a sample of Drell-
 2717 Yan enriched events. Figures 6.8 and 6.9 show the efficiencies for the $2lss$ channel and
 2718 $3l$ channel respectively. Efficiencies in the $2lss$ channel have been produced including
 2719 the tight-charge requirement, while for the $3l$ channel it is not included. Number
 2720 of passed and failed probes are determined from a fit to the invariant mass of the
 2721 dilepton system. Simulation is corrected using these scale factors; note that they
 2722 depend on η and p_T .

2723 **6.5.3 Jets and b -jet tagging**

2724 In this analysis, jets are reconstructed by clustering PF candidates using the anti- k_t
 2725 algorithm with parameter distance $\Delta R = 0.4$; those charged hadrons that are not
 2726 consistent with the selected primary vertex are discarded from the clustering. The
 2727 jet energy is then corrected for the varying response of the detector as a function of
 2728 transverse momentum p_T and pseudorapidity η . Jets are selected for being used in the
 2729 analysis only if they have $p_T > 25$ GeV and are separated from any selected leptons
 2730 by $\Delta R > 0.4$.

2731 Jets coming from the primary vertex and jets coming from pile-up vertices are
 2732 distinguished using a MVA discriminator based on the differences in the jet shapes,
 2733 in the relative multiplicity of charged and neutral components, and in the different
 2734 fraction of transverse momentum which is carried by the most energetic components.

2735 Jet tracks are also required to be compatible with the primary vertex.

2736 Jets originated from the hadronization of a b quark are selected using a MVA
 2737 likelihood discriminant which uses track-based lifetime information and reconstructed
 2738 secondary vertices (CSV algorithm). Only jets within the CMS tracker acceptance
 2739 ($\eta < 2.4$) are identified with this tool. Data samples are used to measure the efficiency
 2740 of the b -jet tagging and the probability to misidentify jets from light quarks or gluons;
 2741 in both cases the measurements are parametrized as a function of the jet p_T and η
 2742 and later used to correct differences between the data and MC simulation in the b
 2743 tagging performance, by applying per-jet weights to the simulation, dependent on
 2744 the jet p_T , η , b tagging discriminator, and flavor (from the MC generation/simulation
 2745 truth information) [151]. The per-event weight is taken as the product of the per-jet
 2746 weights, including those of the jets associated to the leptons. The weights are derived
 2747 on $t\bar{t}$ and Z+jets events.

2748 Two working points are defined, based on the CSV algorithm output: *loose* work-
 2749 ing point ($\text{CSV} > 0.46$) with a b signal tagging efficiency of about 83%, and *medium*
 2750 working point ($\text{CSV} > 0.80$) with b -tagging efficiency of about 69% [152]. Tagging of
 2751 jets from charm quarks have efficiencies of about 40% and 18% for loose and medium
 2752 working points respectively. Separate scale factors are applied to jets originating from
 2753 bottom/charm quarks and from light quarks in simulated events to match the tagging
 2754 efficiencies measured in the data.

2755 6.5.4 Missing Energy MET

2756 As stated in Section 3.4.1, the MET vector is calculated as the negative of the vector
 2757 sum of transverse momenta of all PF candidates in the event and its magnitude is
 2758 referred to as E_T^{miss} . Due to pile-up interactions, the performance in determining

2759 MET is degraded; in order to correct for that, the energy from the selected jets and
 2760 leptons that compose the event is assigned to the variable H_T^{miss} . It is calculated in
 2761 the same way as E_T^{miss} and although it has worse resolution than E_T^{miss} , it is more
 2762 robust in the sense that it does not rely on the soft part of the event. The event
 2763 selection uses a linear discriminator based on the two variables given by

$$E_T^{miss, LD} = 0.00397 * E_T^{miss} + 0.00265 * H_T^{miss} \quad (6.6)$$

2764 taking advantage of the fact that the correlation between E_T^{miss} and H_T^{miss} is less
 2765 for events with instrumental missing energy than for events with real missing energy.
 2766 The working point $E_T^{miss, LD} > 0.2$ was chosen to ensure a good signal efficiency while
 2767 keeping an efficient background rejection.

2768 6.6 Event selection

2769 Events are selected considering the features of the signal process and the decay sig-
 2770 nature as described in Section 6.2. At the trigger level, events are selected to contain
 2771 either one, two, or three leptons with minimal p_T thresholds:

- 2772 • single-lepton trigger → 24 GeV for muons and at 27 GeV for electrons
- 2773 • double-lepton triggers → leading and sub-leading leptons: 17 and 8 GeV for
 2774 muons and 23 and 12 GeV for electrons.
- 2775 • three-lepton triggers → threshold on the third hardest lepton in the event: 5
 2776 and 9 GeV for muons and electrons, respectively.

2777 The offline event selection level targets the specific topology of the tHq signal
 2778 with $H \rightarrow WW$ and $t \rightarrow Wb \rightarrow l\nu b$; therefore, the resulting state is composed of three

2779 W bosons, one b quark, and a light spectator quark at high rapidity. The selection
 2780 criteria for the two channels exploited in this analysis are summarized in Table 6.6.
 2781 This selection includes contributions from $H \rightarrow \tau\tau$ and $H \rightarrow ZZ$ as well.

Same-sign $\ell\ell$ channel $e^\pm\mu^\pm, \mu^\pm\mu^\pm$	$\ell\ell\ell$ channel
Have fired one of the corresponding trigger paths	
No loose leptons with $m_{\ell\ell} < 12\text{GeV}$	
One or more b tagged jets (CSV medium) $ \eta < 2.4$	
One or more non-tagged jets: central $\rightarrow p_T > 25\text{ GeV}, \eta < 2.4$	
	forward $\rightarrow p_T > 40\text{ GeV}, \eta > 2.4$
$E_T^{miss}_{LD} > 0.2$	
Exactly two tight same-sign leptons	Exactly three tight leptons
Lepton $p_T > 25/15\text{GeV}$	Lepton $p_T > 25/15/15\text{GeV}$
Electrons are triple-charge consistent.	No OSSF lepton pair with $ m_{\ell\ell} - m_Z < 15\text{GeV}$
Muon p_T resolution: $\Delta p_T/p_T < 0.2$.	
No ee pair with $ m_{ee} - m_Z < 10\text{GeV}$	

Table 6.6: Summary of event pre-selection.

2782 In the $2lss$ channel, events with additional tight leptons are vetoed as well as those
 2783 for which a loose lepton pair has an invariant mass below 12 GeV. A threshold in p_T of
 2784 the leading and sub-leading leptons is also required. Events where the two electrons
 2785 have invariant mass within 10 GeV of the Z boson mass (Z -veto) are discarded in
 2786 order to reject events from DY+jets production with charge misidentified electrons.
 2787 In addition, contribution from the associated production of two W bosons of equal
 2788 charge and two light jets $W^\pm W^\pm qq$ and from same-sign W boson pairs can also be
 2789 produced in double parton scattering (DPS) processes, where each of the colliding
 2790 protons gives two partons, resulting in two hard interactions.

2791 In the $3l$ lepton channel, leptons are required to have respectively $p_T > 25\text{GeV}, >$
 2792 $> 15\text{ GeV}$, and $> 15\text{ GeV}$. Events with an opposite-sign same-flavor lepton combination
 2793 (OSSF) with invariant mass within 15 GeV of the Z boson mass are discarded in order
 2794 to reject events from $WZ + \text{jets}$ production.

2795 6.7 Background modeling and predictions

2796 The dominant background contribution is expected to arise from top quark produc-
 2797 tion processes, either $t\bar{t}$ pair production or in $t\bar{t}$ associated production with a W/Z.
 2798 Processes with production of single top quarks also contribute, mainly in the associ-
 2799 ated production with a Z boson (tZq) or when produced with both a W and a Z boson
 2800 (tZW). Background contamination from diboson processes is strongly suppressed by
 2801 imposing the Z-veto, vetoing additional leptons and requiring b -jets in the event.

2802 The selection criteria in Table 6.6 represent a relatively loose selection that allows
 2803 to maintain a large signal efficiency while suppressing the main backgrounds; thus
 2804 that selection is called *pre-selection*. The events obtained from the pre-selection are
 2805 then used to extract the signal contribution in a second analysis step, using BDT dis-
 2806 criminators against the main backgrounds of $t\bar{t}W/t\bar{t}Z$ and non-prompt leptons from
 2807 $t\bar{t}$. The shape of the discriminator variables is then fit to the observed data distribu-
 2808 tion to estimate the signal and background yields, simultaneously for all channels.

2809 Irreducible backgrounds are reliably estimated from MC simulated events; there-
 2810 fore, in this analysis all backgrounds involving prompt leptons are estimated in this
 2811 way. Reducible backgrounds, like non-prompt lepton backgrounds, are not well pre-
 2812 dicted by simulation, hence, they are estimated using data-driven methods.

2813 6.7.1 $t\bar{t}V$ and diboson backgrounds

2814 Backgrounds from $t\bar{t}W$ and $t\bar{t}Z$ processes are estimated using simulated events, cor-
 2815 rected for data/MC differences and inefficiencies (trigger and lepton selection) in the
 2816 same way as signal events. Their production cross sections are calculated at NLO of
 2817 QCD and EWK, considering theoretical uncertainties from unknown higher orders of
 2818 12% for $t\bar{t}W$ and 10% for $t\bar{t}Z$. Additional uncertainties arise from the knowledge of

2819 PDFs and α_s of about 4% each for $t\bar{t}W$ and $t\bar{t}Z$.

2820 The diboson contribution is also estimated from simulated events; however, the
 2821 overall normalization of this process is obtained from a dedicated control region.
 2822 The motivation behind that strategy is that even though the measured inclusive
 2823 cross section for diboson processes (WZ, ZZ) is in good agreement with the NLO
 2824 calculations [149], that agreement is perturbed when leptonic Z decays and hadronic
 2825 jets in the final state are required; those requirements are precisely the ones that
 2826 make the diboson production a background for the tHq signal. Thus, by using a
 2827 dedicated control region dominated by WZ production⁴, the overall normalization is
 2828 constrained.

2829 The control region is defined by the presence of at least three leptons, of which
 2830 one opposite-sign pair must be compatible with a Z boson decay, i.e., invert the Z -
 2831 veto which makes the control region orthogonal to signal region; the b-jet tagging
 2832 requirements is also inverted with respect to the signal region, i.e., require two not
 2833 b -jets. A scale factor is extracted from the predicted distribution of WZ events in the
 2834 control region, and the observed data, while keeping other processes fixed; this factor
 2835 is used to scale the diboson prediction in the signal selection region. More details
 2836 about the procedure used can be found in Reference [149] from where the scale factor
 2837 is taken.

2838 In order to test the usability of the diboson background scale factor in this analysis,
 2839 a Z -enriched control region⁵ was defined by inverting the Z -veto and requiring exactly
 2840 three tight leptons with $p_T > 25/15/15$ GeV, one or more jets passing the CSVv2 loose
 2841 working point and less than four central jets. Figure 6.10 shows the distribution of
 2842 three variables in the diboson control region; the good agreement between MC and

⁴ ZZ background is strongly reduced by the cut on MET.

⁵ This control region is different to the one used to find the scale factor.

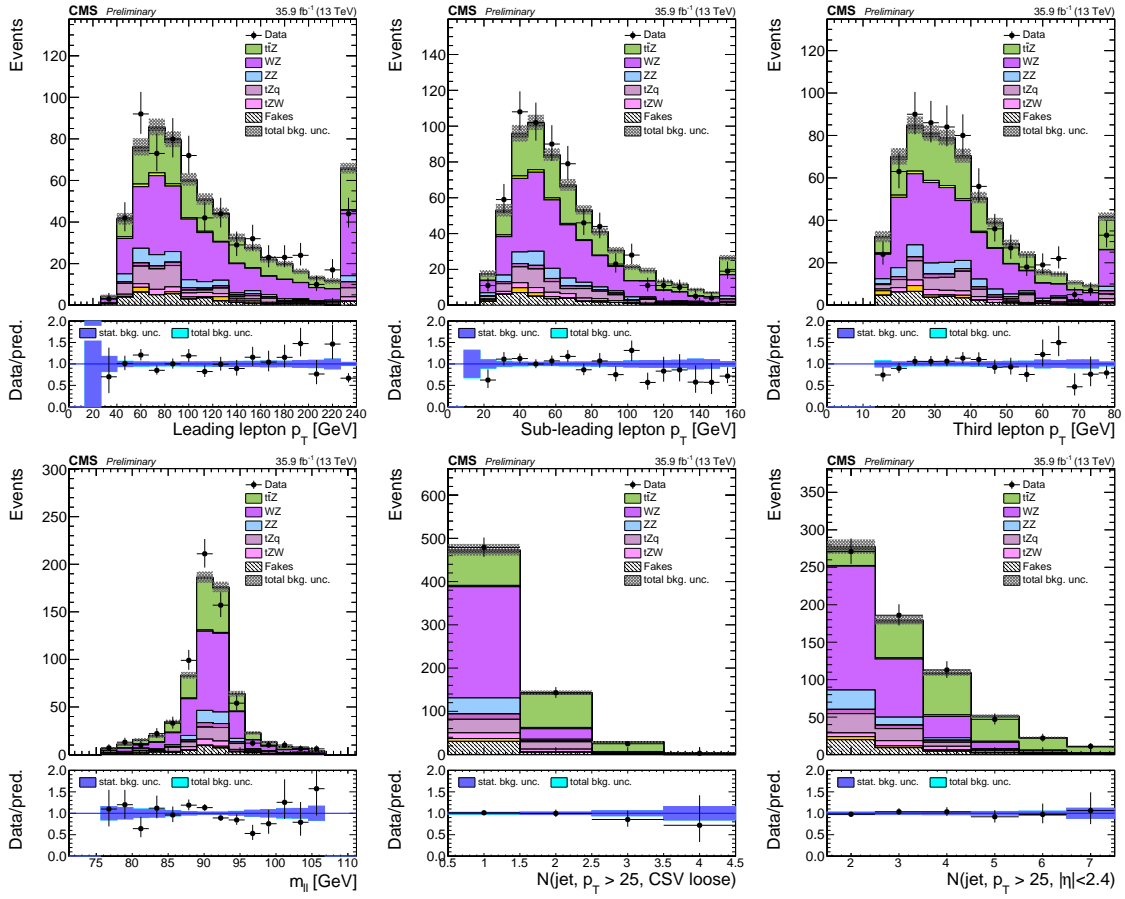


Figure 6.10: Kinematic distributions in the diboson control region.

2843 data motivates the adoption of the diboson background scale factor.

2844 Most of the diboson events passing the signal selection contain jets from light
 2845 quarks and gluons that are incorrectly tagged as b -jets; it makes the estimate mainly
 2846 sensitive to the experimental uncertainty in the mis-tag rate rather than the theore-
 2847 tical uncertainty in the jet flavor composition. The overall uncertainty assigned to
 2848 the diboson prediction is estimated from the statistical uncertainty due to the limited
 2849 sample size in the control region (30%), the residual background in the control region
 2850 (20%), the uncertainties on the b -tagging rate (10-40%), and from the knowledge of
 2851 PDFs and the theoretical uncertainties of the extrapolation (up to 10%).

2852 **6.7.2 Non-prompt and charge mis-ID backgrounds**

2853 The non-prompt lepton background contribution to the final selection is estimated
 2854 using the fake factor method. The main idea of the method is to define a control
 2855 region of events enriched in the background to estimate and determine a factor that
 2856 relates (extrapolates) these events to those in the signal region. The method is data-
 2857 driven in the sense that the control sample is selected from data, and the extrapolation
 2858 factor is measured from data.

2859 In the signal region of this analysis, non-prompt leptons are predominantly pro-
 2860 duced in $t\bar{t}$ events, with a much smaller contribution, from Drell-Yan production;
 2861 therefore, the control region also known as *application region*, is defined by modifying
 2862 the event selection criteria in such a way that most of the events after selection are
 2863 $t\bar{t}$ events and thus the misidentification rate is increased. The application regions
 2864 for electrons and muons are defined by the *fakeable* object definitions in Tables 6.4
 2865 and 6.5. Since the fakeable definition is a loosened version of the tight definition, in
 2866 the context of fake rates, the fakeable definition becomes the loose selection.

2867 The ratio between the number of events that pass both, the loose and tight se-
 2868 lections, and the number of events that pass the loose selection but fail the tight
 2869 one, corresponds to the *loose-to-tight ratio or fake factor/rate (f)*. The measurement
 2870 of the fake factor is made using two background dominated data samples, collected
 2871 with dedicated triggers, as a function of p_T and $|\eta|$ and separately for muons and
 2872 electrons:

- 2873 • A sample dominated by QCD multijet events, collected using single lepton trig-
 2874 gers at relatively high p_T thresholds. It is used to extract ratios for lepton
 2875 candidates with p_T above 30 GeV.
- 2876 • A sample dominated by Z + jets events, where the two high p_T leptons resulting

2877 from the Z decay are used to trigger the events without biasing the p_T spectrum
 2878 of a third lepton at low transverse momentum. It is used to determine the ratios
 2879 for low p_T leptons.

2880 Processes like $W + \text{jets}$, $Z + \text{jets}$, WZ and ZZ produce prompt leptons that
 2881 contaminate the samples; thus, they are suppressed by vetoing additional leptons in
 2882 the selection, and the residual contamination is then subtracted using the transverse
 2883 mass as a discriminating variable.

2884 The extrapolation from the application region to the signal region is performed
 2885 by weighting the events in the application region using the fake factor according to
 2886 the following rules:

- 2887 • events with one lepton failing the tight criteria are weighted with the factor
 2888 $\frac{f}{(1-f)}$ for the estimate to the signal region.
- 2889 • events with two leptons (i,j) failing the tight criteria are weighted with the factor
 2890 $-\frac{f_i f_j}{(1-f_i)(1-f_j)}$ for the estimate to the signal region.
- 2891 • events with three leptons (i,j,k) failing the tight criteria are weighted with the
 2892 factor $\frac{f_i f_j f_k}{(1-f_i)(1-f_j)(1-f_k)}$ for the estimate to the signal region.

2893 Figure 6.11 shows the fake rates for electrons and muons used in this analysis
 2894 which were taken from the studies in Reference [149].

2895 The resulting prediction of the event yield in the signal selection carries an uncer-
 2896 tainty of 30-50% which is composed of the statistical uncertainty in the measurement
 2897 of the fake rates due to prescaling of lepton triggers, the uncertainty in the subtraction
 2898 of residual prompt leptons from the control region, and from testing the closure of the
 2899 method in simulated background events; hence, it is one of the dominant limitations
 2900 on the performance of multilepton analyses in general and this analysis in particular.

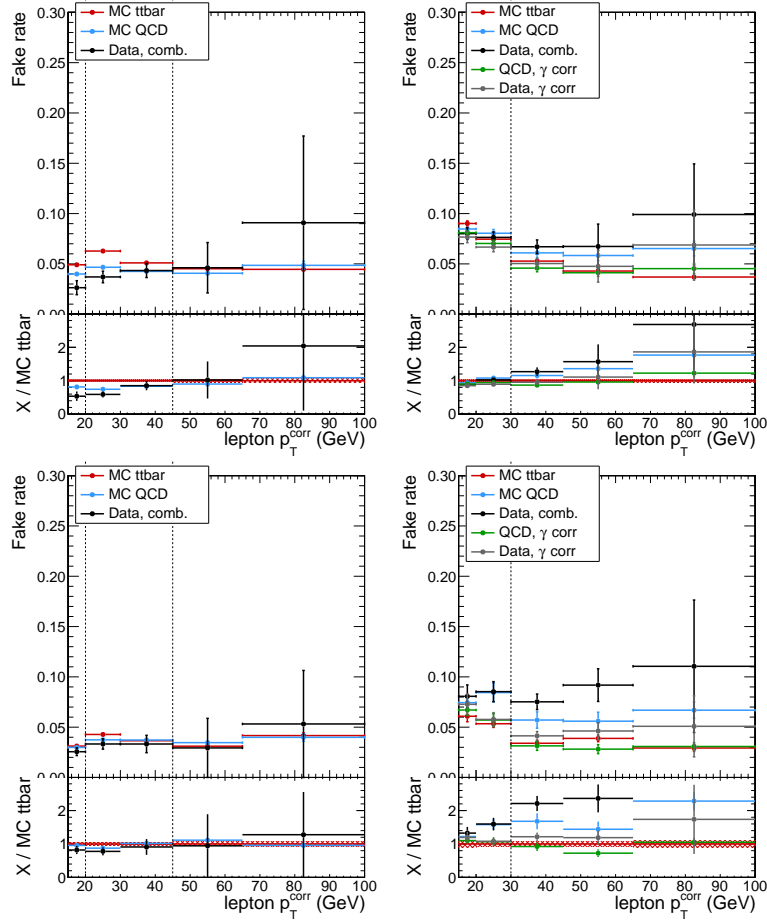


Figure 6.11: Fake rate measurement in events in data for muons (left column) and electrons (right column). Predictions from simulated events in the measurement region (blue) and from non-prompt leptons in $t\bar{t}$ (red) are included for comparison. Top row is for $|\eta| < 2.5$ and bottom row for $|\eta| > 2.5$.

Finally, an additional source of background arises in the $2lss$ channel from events with an originally opposite-sign lepton pair for which the charge of one of the leptons is misidentified (*charge mis-ID*); usually this happens because of the conversion of hard bremsstrahlung photons emitted from the initial lepton, hence, it is more likely to happen for electrons than for muons.

The charge mis-ID background is estimated from the yield of opposite-sign event in the signal region by measuring the charge mis-ID probability in same-sign and opposite-sign events compatible with a Z boson decay, in several bins of p_T and η ,

2909 and weighting events with opposite-sign leptons in the signal selection.

Data	$10 \leq p_T < 25$ GeV	$25 \leq p_T < 50$ GeV	$50 \text{ GeV} \leq p_T$
$0 \leq \eta < 1.48$	0.0442 ± 0.0011	0.0179 ± 0.0004	0.0262 ± 0.0020
$1.48 \leq \eta < 2.5$	0.1329 ± 0.0066	0.1898 ± 0.0014	0.3067 ± 0.0113
MC			
$0 \leq \eta < 1.48$	0.0378 ± 0.0016	0.0222 ± 0.0003	0.0233 ± 0.0015
$1.48 \leq \eta < 2.5$	0.0956 ± 0.0044	0.2108 ± 0.0027	0.3157 ± 0.0018

Table 6.7: Electron charge mis-ID probabilities (in percent), determined in data (top) and Drell-Yan MC (bottom) [149].

2910 The charge mis-ID probability is found to be negligible for this analysis for muons,
 2911 whereas for electrons it ranges from about 0.02% in the barrel section ($|\eta| < 1.48$)
 2912 up to about 0.35% in the detector endcaps ($1.48 < |\eta| < 2.5$). as shown in Table 6.7
 2913 and Figure 6.12.

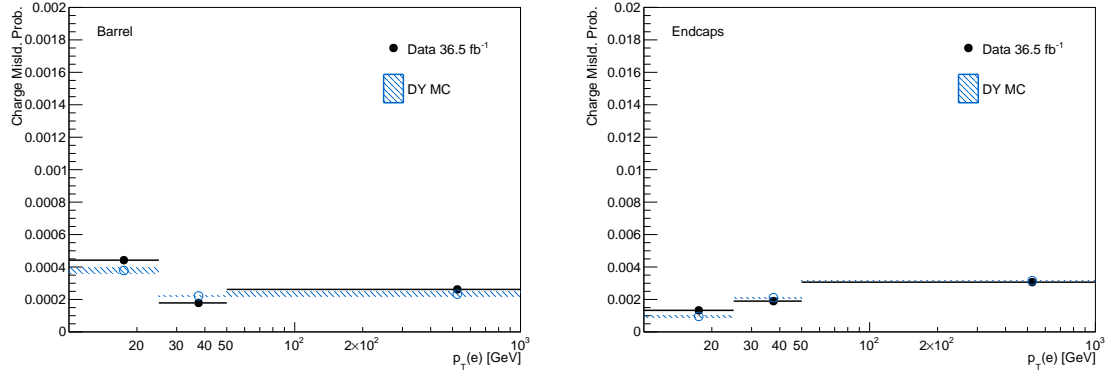


Figure 6.12: Electron charge mis-ID probabilities as a function of p_T for $|\eta| < 2.5$ (left) and $|\eta| < 2.5$ (right) [149].

2914 The contribution from charge mis-ID electrons in signal selection of this analysis
 2915 comes mainly from $t\bar{t}$ and Drell-Yan events. The systematic uncertainty of the nor-
 2916 malization of the charge mis-ID estimate is evaluated at about 30%, arising from a
 2917 slight disagreement of the mis-ID probability between data and simulation. Given
 2918 that it only affects the $e\mu$ channel, its impact on the final sensitivity is very limited.

2919 6.8 Pre-selection yields

2920 The expected and observed event yields of the pre-selection are shown in Table 6.8;
 2921 Figure 6.13 shows the distributions of some relevant kinematic variables, normalized
 2922 to the cross section of the respective processes and to the integrated luminosity. The
 2923 remaining variables distributions are shown in Appendix B.1.

	3ℓ	$\mu^\pm \mu^\pm$	$e^\pm \mu^\pm$
$t\bar{t}W$	22.50 ± 0.35	68.03 ± 0.61	97.00 ± 0.71
$t\bar{t}Z/\gamma^*$	32.80 ± 1.79	25.89 ± 1.12	64.82 ± 2.42
WZ	8.22 ± 0.86	15.07 ± 1.19	26.25 ± 1.57
ZZ	1.62 ± 0.33	1.16 ± 0.29	2.86 ± 0.45
$W^\pm W^\pm qq$	–	3.96 ± 0.52	6.99 ± 0.69
$W^\pm W^\pm(\text{DPS})$	–	2.48 ± 0.42	4.17 ± 0.54
VVV	0.42 ± 0.16	2.99 ± 0.34	4.85 ± 0.43
ttt	1.84 ± 0.44	2.32 ± 0.45	4.06 ± 0.57
tZq	3.92 ± 1.48	5.77 ± 2.24	10.73 ± 3.03
tZW	1.70 ± 0.12	2.13 ± 0.13	3.91 ± 0.18
γ conversions	7.43 ± 1.94	–	23.81 ± 6.04
Non-prompt	25.61 ± 1.26	80.94 ± 2.02	135.34 ± 2.83
Charge mis-ID	–	–	58.50 ± 0.31
All backgrounds	106.05 ± 3.45	210.74 ± 3.61	443.30 ± 8.01
tHq ($\kappa_t = -1.0$)	7.48 ± 0.14	18.48 ± 0.22	27.41 ± 0.27
tHW ($\kappa_V = -1.0$)	7.38 ± 0.16	7.72 ± 0.17	11.23 ± 0.20
$t\bar{t}H$	18.29 ± 0.41	24.18 ± 0.48	35.21 ± 0.58
Data ($35.9 fb^{-1}$)	127	280	525

Table 6.8: Expected and observed yields for $35.9 fb^{-1}$ after the pre-selection in all final states. Uncertainties are statistical only.

2924 For the tH and $t\bar{t}H$ processes, the largest contribution comes from Higgs decays
 2925 to WW (about 75%), followed by $\tau\tau$ (about 20%) and ZZ (about 5%). Other Higgs
 2926 production modes contribute negligible event yields (< 5% of the $tH + t\bar{t}H$ yield) as
 2927 shown in Table 6.9.

2928 A significant fraction of selected data events (about 50% in the dilepton channels,
 2929 and about 80% in the trilepton channel) also passes the selection used in the dedicated

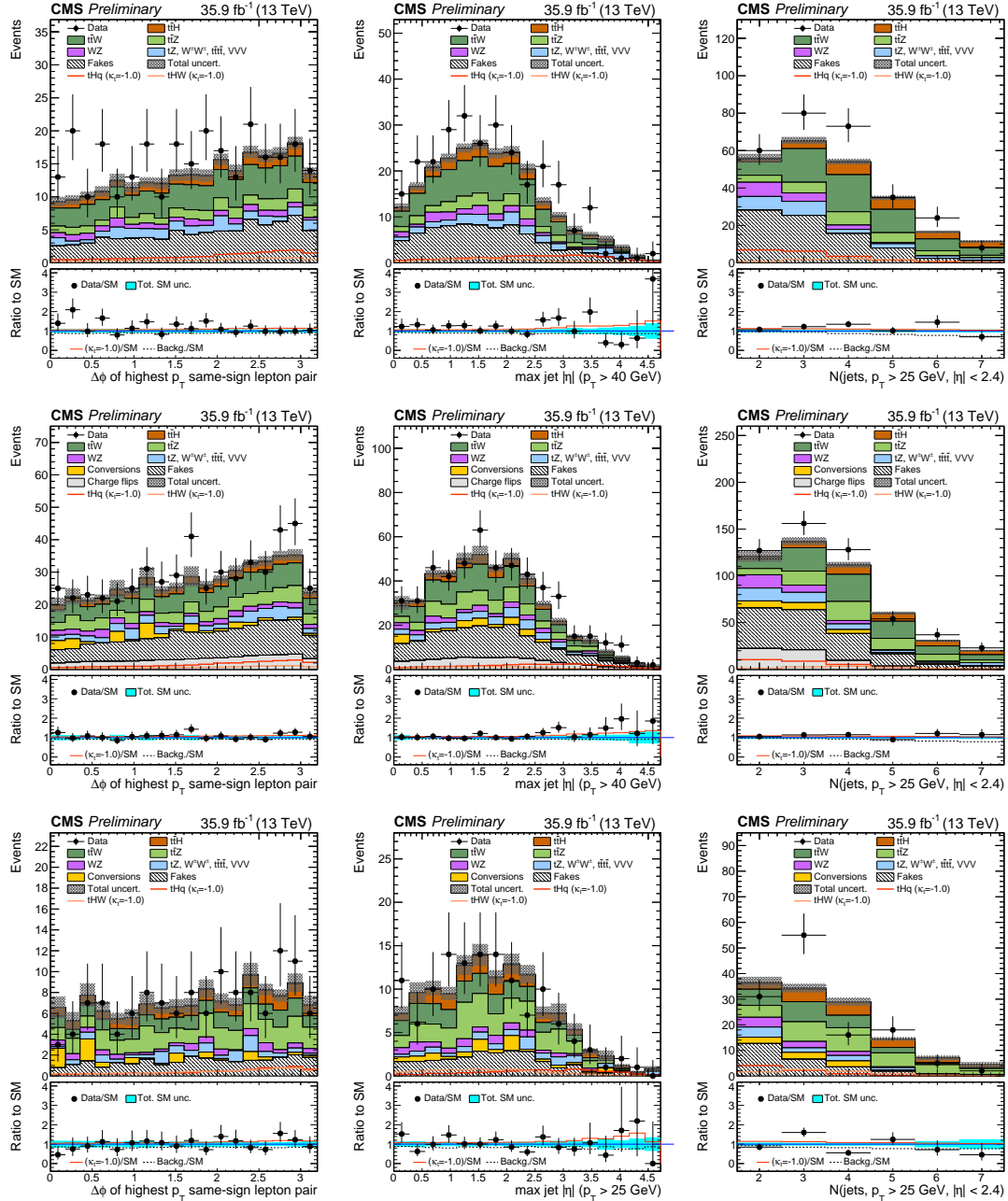


Figure 6.13: Distributions of discriminating variables for the event pre-selection for the same-sign $\mu^{\pm}\mu^{\pm}$ channel (top row), the same-sign $e^{\pm}\mu^{\pm}$ channel (middle row) and three lepton channel (bottom row), normalized to 35.9 fb^{-1} , before fitting the signal discriminant to the observed data. Uncertainties are statistical and unconstrained (pre-fit) normalization systematics. The shape of the two tH signals for $\kappa_t = -1.0$ is shown, normalized to their respective cross sections for $\kappa_t = -1.0, \kappa_V = 1.0$.

	3ℓ	$\mu^\pm \mu^\pm$	
tHq (Inclusive)	6.57	100.0%	17.38 100.0%
$tHq(H \rightarrow WW)$	4.84	73.9%	13.33 76.9%
$tHq(H \rightarrow \tau\tau)$	1.04	15.9%	3.62 20.6%
$tHq(H \rightarrow ZZ)$	0.48	7.2%	0.37 2.2%
$tHq(H \rightarrow \mu\mu)$	0.21	3.0%	0.04 0.2%
$tHq(H \rightarrow \gamma\gamma)$	< 0.01	0.1%	0.02 0.1%
$tHq(H \rightarrow bb)$	< 0.01	< 0.1%	0.01 < 0.1%
tHW (Inclusive)	7.32	100.0%	7.62 100.0%
$tHW(H \rightarrow WW)$	5.50	76.9%	5.60 74.1%
$tHW(H \rightarrow \tau\tau)$	1.40	20.6%	1.81 23.1%
$tHW(H \rightarrow ZZ)$	0.31	2.2%	0.21 2.7%
$tHW(H \rightarrow \mu\mu)$	0.12	0.2%	0.01 0.1%
$tHW(H \rightarrow \gamma\gamma)$	< 0.01	< 0.1%	< 0.01 < 0.1%
$tHW(H \rightarrow bb)$	< 0.01	< 0.1%	< 0.01 < 0.1%

Table 6.9: Signal yields split by decay channels of the Higgs boson. Forward jet p_T cut at 25 GeV.

2930 search for $t\bar{t}H$ in multilepton channels [149]. This is particularly important when
 2931 considering a possible combination of the measurements from both studies. More
 2932 details about the overlap between these two analyses are presented in Appendix E.

2933 6.9 Signal discrimination

2934 The production cross section for the signal processes tHq , tHW , and $t\bar{t}H$ is only
 2935 about 600 fb (the enhancement provided by inverted couplings, $\kappa_t = -1$ almost double
 2936 it), resulting in a small signal to background ratio even for a tight selection. A
 2937 multivariate method is hence employed to train discriminators to separate tH signal
 2938 events from the dominant background events.

2939 **6.9.1 MVA classifiers evaluation**

2940 Several MVA classifier algorithms were evaluated in order to determine the most
 2941 appropriate method for this analysis⁶. The comparison is based on the performance
 2942 of the classifiers, encoded in the plot of the background rejection as a function of the
 2943 signal efficiency (ROC curve). The top row of Figure 6.14 shows the ROC curves for
 2944 evaluated methods; two separated training were performed in the $3l$ channel: against
 2945 $t\bar{t}$ (right) and $t\bar{t}V$ (left) processes.

2946 In both cases, the gradient boosted decision tree *BDTG* (*BDTA_GRAD* in the
 2947 plot) classifier offers the best results, followed by the adaptive BDT classifier (*BDTA*);
 2948 the several Fisher classifiers tested, which differ in their parameters and/or boosting
 2949 method, they offer similar performance among them, while the k-Nearest Neighbour
 2950 (kNN) classifier performance is below the rest of the classifiers. The corresponding
 2951 ROC curves and in the $2lss$ channel for trainings against $t\bar{t}V$ (left) and $t\bar{t}$ (right)
 2952 processes are shown in the bottom row of Figure 6.14; the BDTG performance is
 2953 similar to that in the $3l$ channel.

2954 **6.9.2 Discriminating variables**

2955 The classifier chosen to separate the tHq signal from the main backgrounds is the
 2956 *BDTG* classifier, trained on simulated signal and background events. The samples
 2957 used in the training are the tHq sample in Table 6.2, the samples in the third section
 2958 of Table A.4 and the samples marked with an * in the same table.

2959 As explained in Section 5.1.1, a set of discriminating variables are given as input to
 2960 the *BDTG* which combines the individual discrimination power of each input variable

⁶ The choice of the tested algorithms was based on the recommendations provided by the official TMVA user guide, the experience from previous analyses and considering the expertise of the members of the tHq and $t\bar{t}H$ analyses groups. Only the BDT classifier is described in this thesis and a detailed description of all available methods can be found in Reference [127]

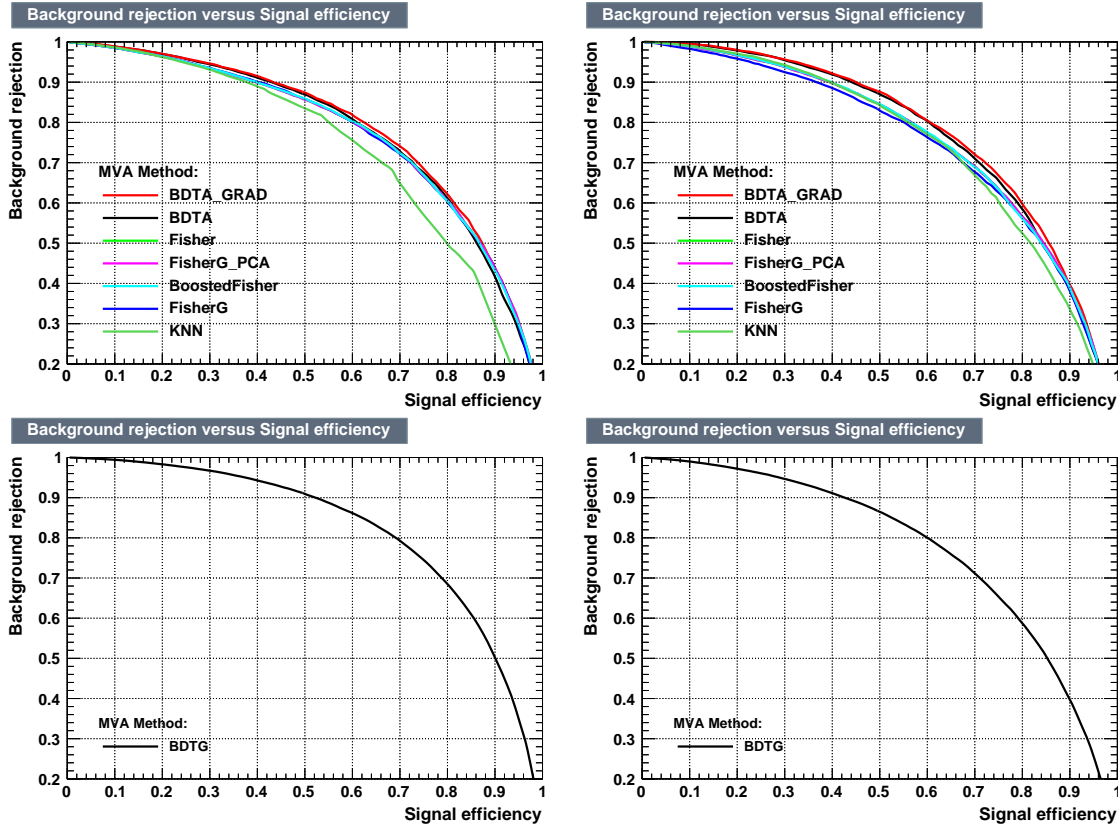


Figure 6.14: Top: Background rejection vs signal efficiency (ROC curves) for various MVA classifiers in the $3l$ channel for training against $t\bar{V}$ (left) and $t\bar{t}$ (right). Bottom: background rejection vs signal efficiency (ROC curve) in the $2lss$ channel for a single discriminator: BDTG, against $t\bar{V}$ (left) and $t\bar{t}$ (right).

2961 to produce a discriminator with the maximum discrimination power. Table 6.10 lists
 2962 the input variables used in the BDTG trainings for this analysis. The same set of
 2963 input variables was used to produce the plots for MVA classifiers evaluation.

2964 Plots in Figure 6.15 shows the BDTG input variables distributions for the signal
 2965 and background samples, in the $3l$ channels.

2966 All the input variables have some discrimination power, however, that power is
 2967 bigger for some of them; for instance, the third lepton p_T plot (top left in Figure 6.15)
 2968 shows some discrimination power against WZ and VVV backgrounds for which there
 2969 is a peak around 30 GeV while tHq peak around 18 GeV; although the discrimination

Variable name	Description
nJet25	Number of jets with $p_T > 25$ GeV, $ \eta < 2.4$
nJetEta1	Number of jets with $ \eta > 1.0$, non-CSV-loose
MaxEtaJet25	Max. $ \eta $ of any (non-CSV-loose) jet with $p_T > 25$ GeV
deltaFwdJetClosestLep	$\Delta\eta$ forward light jet and closest lepton
deltaFwdJetBJet	$\Delta\eta$ forward light jet and hardest CSV loose jet
deltaFwdJet2BJet	$\Delta\eta$ forward light jet and second hardest CSV loose jet
Lep3Pt/Lep2Pt	p_T of the 3 rd lepton (2 nd for ss2l)
totCharge	Sum of lepton charges
minDRll	Min ΔR any two leptons
dphiHighestPtSSPair	$\Delta\phi$ of highest p_T same-sign lepton pair

Table 6.10: BDTG input variables. First section lists variables related to jet multiplicities; second section lists variables related to forward jet activity, and third section lists variables related to lepton kinematics.

2970 power does not cover all the backgrounds, it counts for the final discriminator. A
 2971 similar situation can be seen in the plot for the number of jets (row three, column two);
 2972 $t\bar{t}W$, $t\bar{t}Z$ and $t\bar{t}H$ processes tend to have more jets compared to the tHq process. The
 2973 discrimination power is more evident in other plots like in the plot of the maximum
 2974 $|\eta|$ of the jets in the event (row two, column three). The same or equivalent input
 2975 variables are found to be performing well for both $3l$ and $2lss$ channels. Figure B.4
 2976 shows the corresponding input variables distribution plots for the $2lss$ channel.

2977 Discrimination power from BDTG classifier

2978 The Discrimination power of the input variables can also be evaluated from the BDTG
 2979 training, exclusively for the training samples, i.e., dominant backgrounds ($t\bar{t}$ and $t\bar{t}V$);
 2980 the training samples are submitted to the selection cuts on Table 6.6.

2981 Figure 6.16 shows the comparison between input variables for the two trainings
 2982 in the $3l$ channel; it reveals that some variables show opposite behavior for the two
 2983 background sources, which results in potentially screening the discrimination power
 2984 if they were to be used in a single discriminant, i.e., if the training would join $t\bar{t}$ and

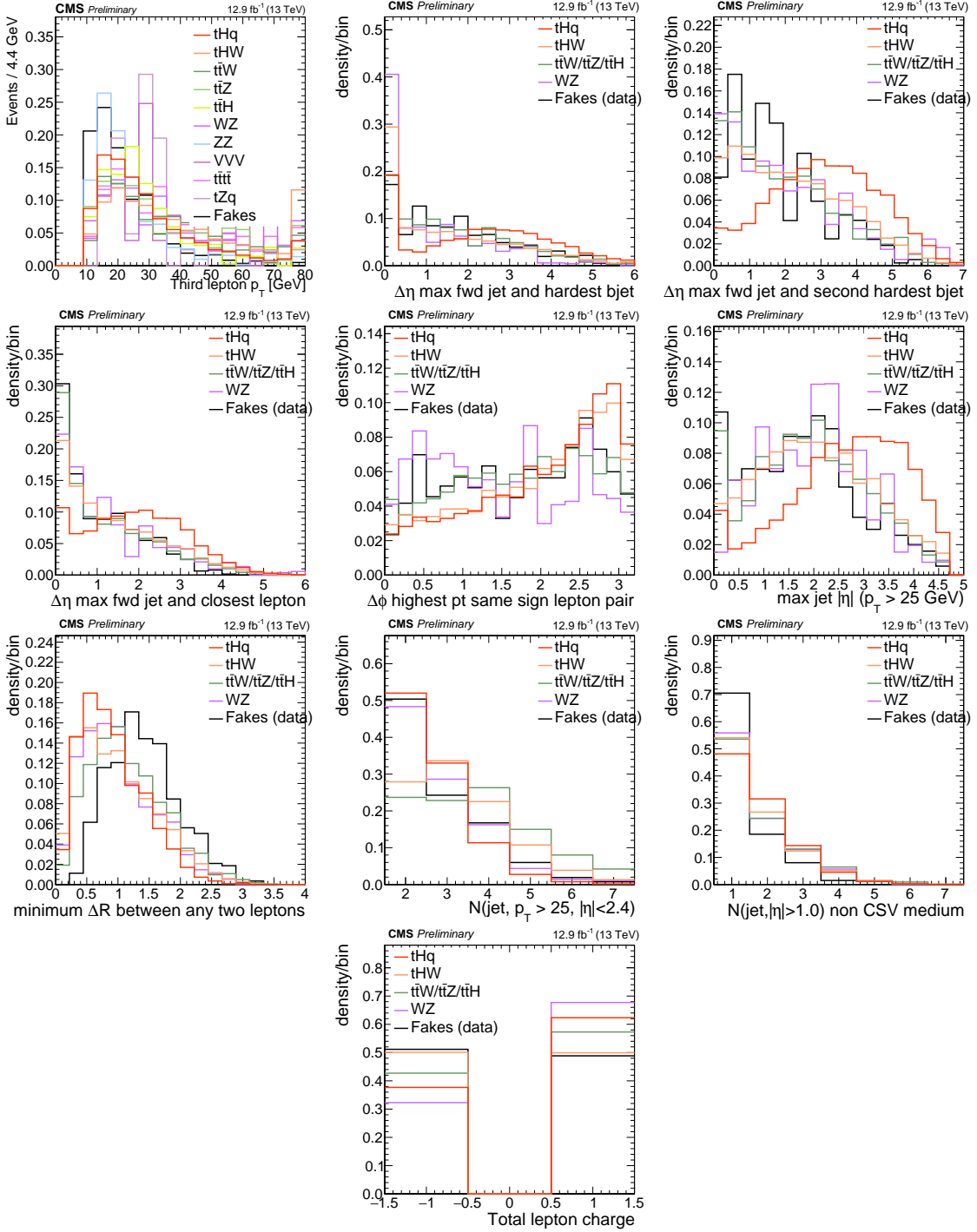


Figure 6.15: Distributions of the BDTG classifier input variables (not normalized) for signal discrimination in the $3l$ channel.

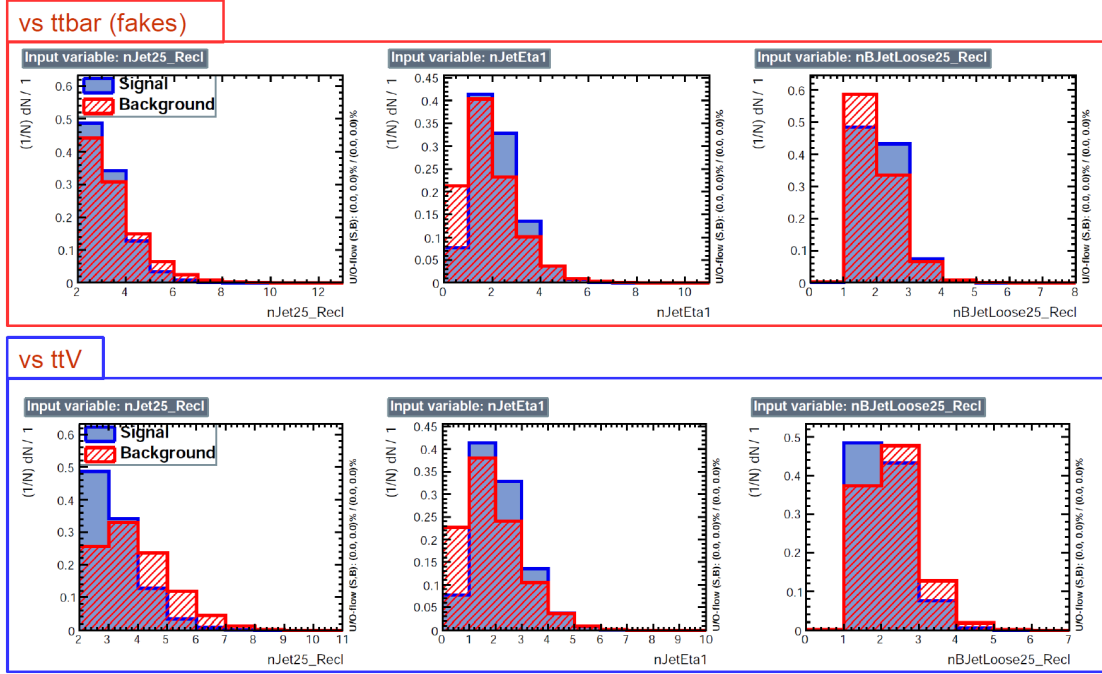


Figure 6.16: BDT input variables as seen by BDTG classifier for the $3l$ channel, tHq signal(blue) discriminated against $t\bar{t}V$ background (red).

2985 $t\bar{t}V$. For some other variables the distributions are similar in both background cases.

2986 In contrast to the distributions in Figure 6.15 only the dominant backgrounds are
2987 included; however, the discrimination power agrees among plots.

2988 Figures in the Appendix B.5, B.6, B.7, and B.8 show the input variables
2989 distributions for the $2lss$ and $3l$ channel as seen by the BDTG classifier.

2990 Input variables correlations

2991 From Table 6.10, it is clear that the input variables are correlated to some extent.
2992 These correlations play an important role for some MVA methods like the Fisher
2993 discriminant method in which the first step consist of performing a linear transfor-
2994 mation to an phase space where the correlations between variables are removed. In
2995 the case of BDT, correlations do not affect the performance. Figure 6.17 shows the

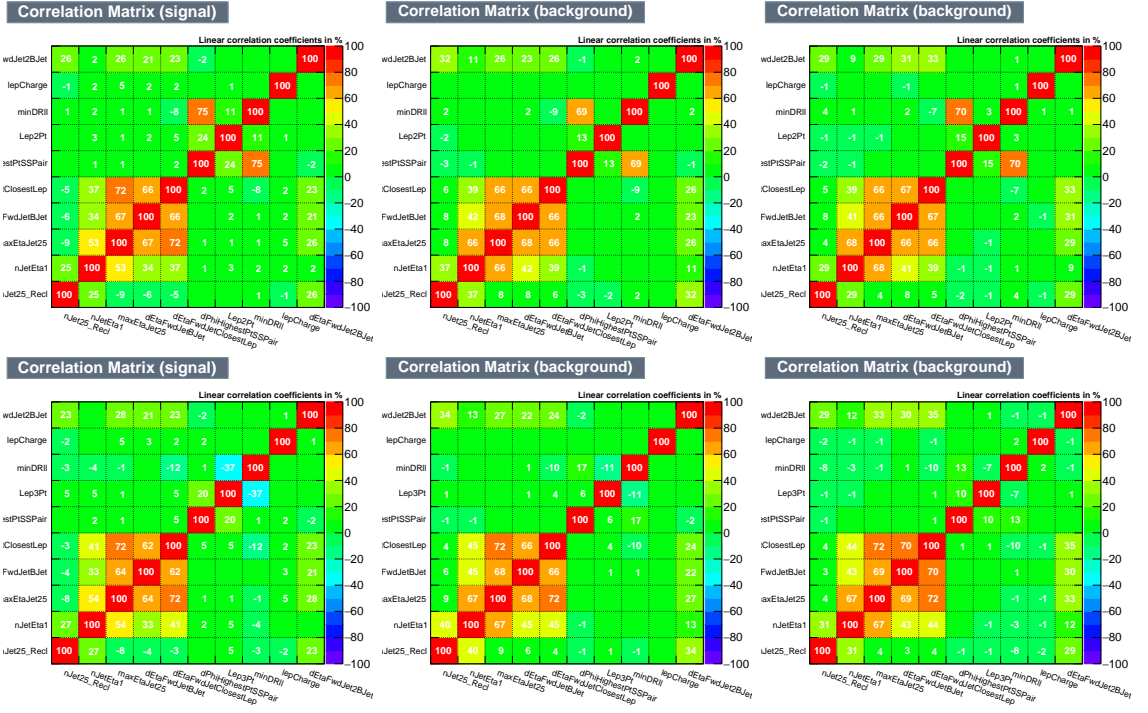


Figure 6.17: Signal (left), $t\bar{t}$ background (middle), and $t\bar{t}V$ background (right.) correlation matrices for the input variables in the BDTG classifier for the $2lss$ (top) and $3l$ (bottom) channels.

2996 linear correlation coefficients for signal and background for the two training cases (the
2997 signal values are identical by construction). As expected, strong correlations appears
2998 for variables related to the forward jet activity.

2999 6.9.3 BDTG classifiers response

After the training stage, the BDTG classifier is tested to ensure its ability to discriminate between simulated signal and background events. The BDTG classifier output distributions for signal and backgrounds in the $3l$ channel are shown in Figure 6.18. As expected, a good discrimination power is obtained using default discriminator parameter values; some overtraining is also visible.

3005 In order to explore further optimization in the BDTG performance, several changes

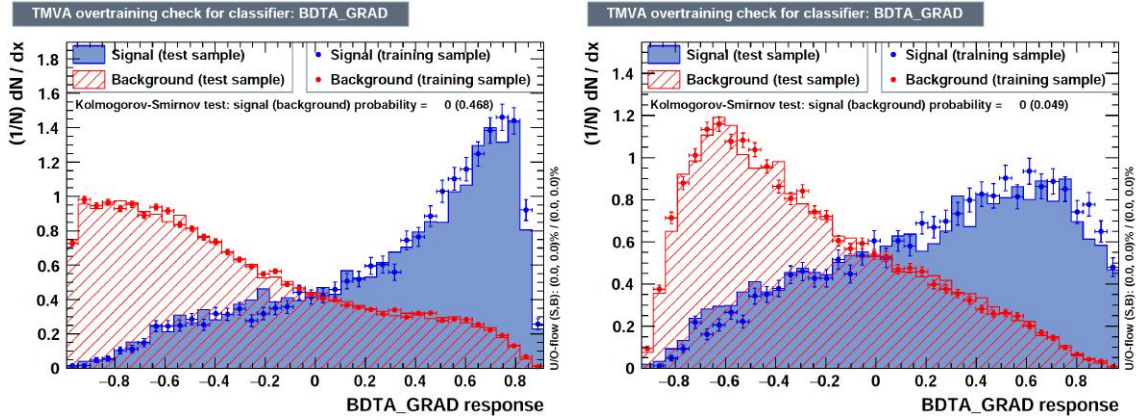


Figure 6.18: BDTG classifier output for trainings against $t\bar{t}V$ (left) and $t\bar{t}$ (right). Default BDTG parameters have been used.

3006 from the default BDTG parameters were tested; Table 6.11 list the set of parameters
 3007 found to be most discriminant with minimal overtraining as shown in Figure 6.19.

TMVA.Types.kBDT		
Option	Default	Used
NTrees	200	800
BoostType	AdaBoost	Grad
Shrinkage	1	0.1
nCuts	20	50
MaxDepth	3	

Table 6.11: Configuration used in the final BDTG training. Parameters not listed were not tested.

3008 The ranking of the input variables by their importance in the classification process
 3009 is shown in Table 6.12; for both trainings the rankings show almost the same five
 3010 variables in the first places.

3011 6.9.4 Additional discriminating variables

3012 Given that the forward jet in background processes could be originated from pileup,
 3013 two additional discriminating variables accounting for that were tested. These ad-
 3014 ditional variables describe the forward jet momentum (`fwdJetPt25`) and the forward

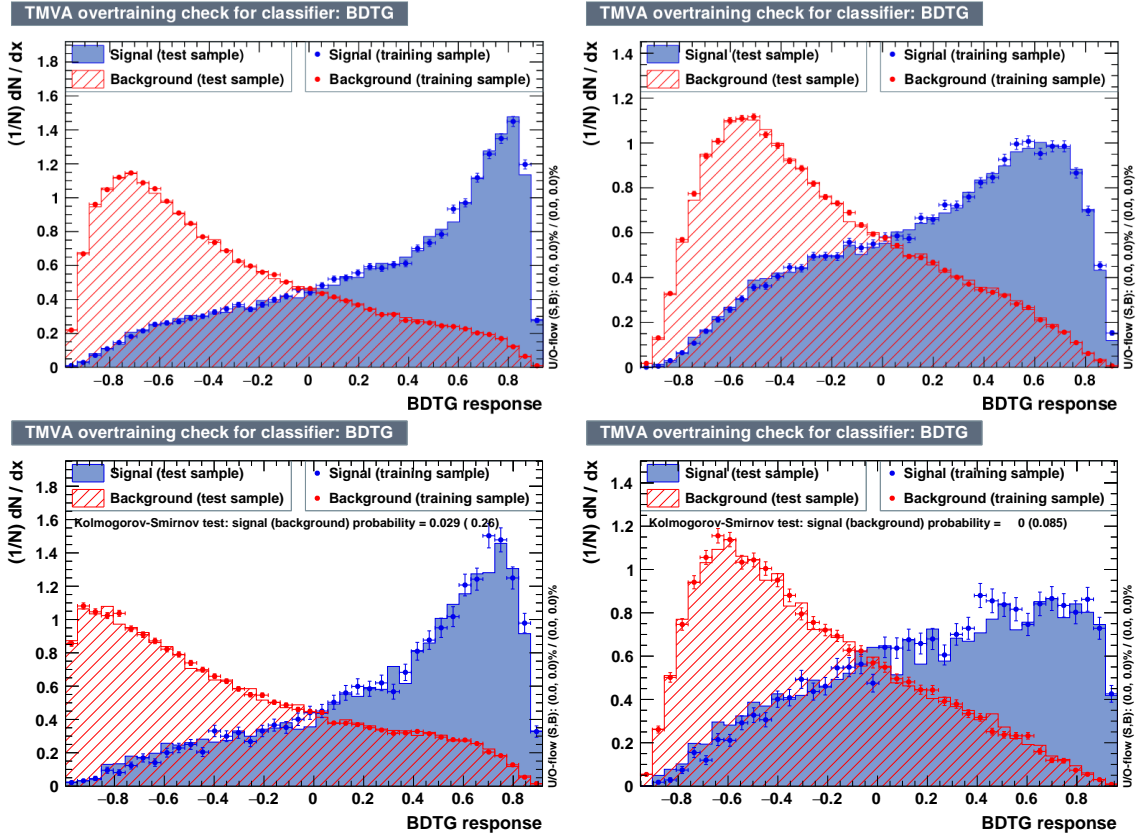


Figure 6.19: BDTG classifiers output for training against $t\bar{t}V$ (left) and $t\bar{t}$ (right) for $2lss$ channel(top) and $3l$ channel (bottom) .

3015 jet identification (fwdJetPUID); their distributions in the $3l$ channel are shown in
 3016 Figure 6.20. The forward jet identification distribution shows that for both, signal
 3017 and background, jets are mostly originated in the primary vertex.

3018 The testing was performed by including in the BDTG input one variable at a
 3019 time, so the discrimination power of each variable can be evaluated individually, and
 3020 then both simultaneously. fwdJetPUID was ranked the last place in importance (11)
 3021 in both training ($t\bar{t}V$ and $t\bar{t}$) while fwdJetPt25 was ranked 3 in the $t\bar{t}V$ training and
 3022 7 in the $t\bar{t}$ training. When training using 12 variables, fwdJetPt25 was ranked 5 and
 3023 7 in the $t\bar{t}V$ and $t\bar{t}$ trainings respectively, while fwdJetPUID was ranked 12 in both
 3024 cases.

Rank	$t\bar{t}$ training		$t\bar{t}V$ training	
	Variable		Variable	
1	minDRll		dEtaFwdJetBJet	
2	dEtaFwdJetClosestLep		Lep3Pt	
3	dEtaFwdJetBJet		maxEtaJet25	
4	dPhiHighestPtSSPair		dEtaFwdJet2BJet	
5	Lep3Pt		dEtaFwdJetClosestLep	
6	maxEtaJet25		minDRll	
7	dEtaFwdJet2BJet		dPhiHighestPtSSPair	
8	nJetEta1		nJet25_Recl	
9	nJet25_Recl		nJetEta1	
10	lepCharge		lepCharge	
1	dEtaFwdJetClosestLep		maxEtaJet25	
2	minDRll		dEtaFwdJet2BJet	
3	maxEtaJet25		dEtaFwdJetBJet	
4	dPhiHighestPtSSPair		Lep2Pt	
5	Lep2Pt		dEtaFwdJetClosestLep	
6	dEtaFwdJetBJet		minDRll	
7	dEtaFwdJet2BJet		nJet25_Recl	
8	nJetEta1		dPhiHighestPtSSPair	
9	nJet25		nJetEta1	
10	lepCharge		lepCharge	

Table 6.12: Input variables ranking for BDTG classifiers for the trainings in the $2lss$ channel (first section) and $3l$ channel (second section). For both trainings the rankings show almost the same five variables in the first places.

3025 The improvement in the discrimination performance provided by the additional
 3026 variables is about 1%, so it was decided not to include them in the procedure. Table
 3027 6.13 shows the ROC-integral for all the testing cases performed.

	ROC-integral	
	$t\bar{t}V$	$t\bar{t}$
base 10 var	0.848	0.777
+ fwdJetPUID	0.849	0.777
+ fwdJetPt25	0.856	0.787
12 var	0.856	0.787

Table 6.13: ROC-integral for all the testing cases performed in the evaluation of the additional variables discriminating power. The improvement in the discrimination performance provided by the additional variables is about 1% .

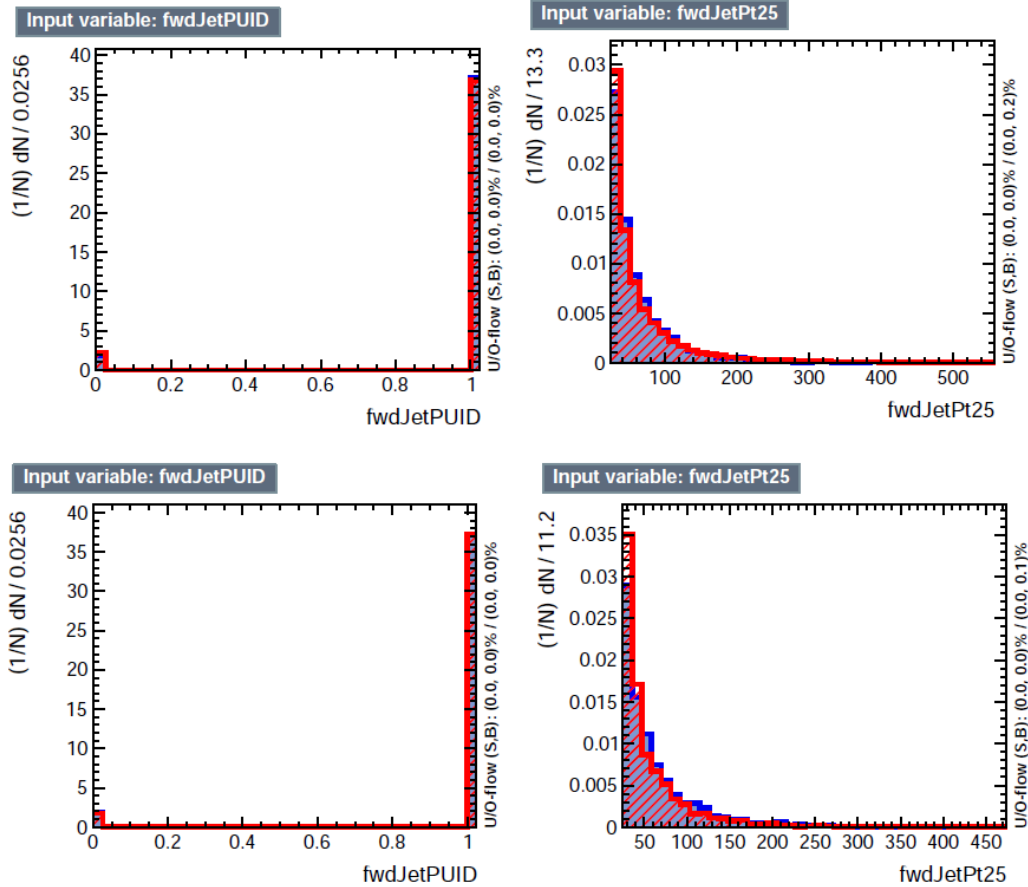


Figure 6.20: Additional discriminating variables distributions for $t\bar{t}V$ training (top row) and $t\bar{t}$ training (bottom row) in the $3l$ channel. The origin of the jets in the forward jet identification distribution is tagged as 0 for *pileup jets* while *primary vertex jets* are tagged as 1.

3028 6.9.5 Signal extraction procedure

3029 Once the two BDTG classifiers, introduced in the previous section, are trained against
 3030 the dominant backgrounds in each channel, they are used to classify the events in the
 3031 samples; their outputs are then used to evaluate the signal cross section limits in a
 3032 fit to the classifier shape. Figure 6.21 shows the expected output distributions in a
 3033 2D plane of one training vs. the other, i.e., $t\bar{t}V$ vs. $t\bar{t}$. Top row shows the 2D planes
 3034 for tHq and tHW signals, while the bottom left plot shows the corresponding 2D

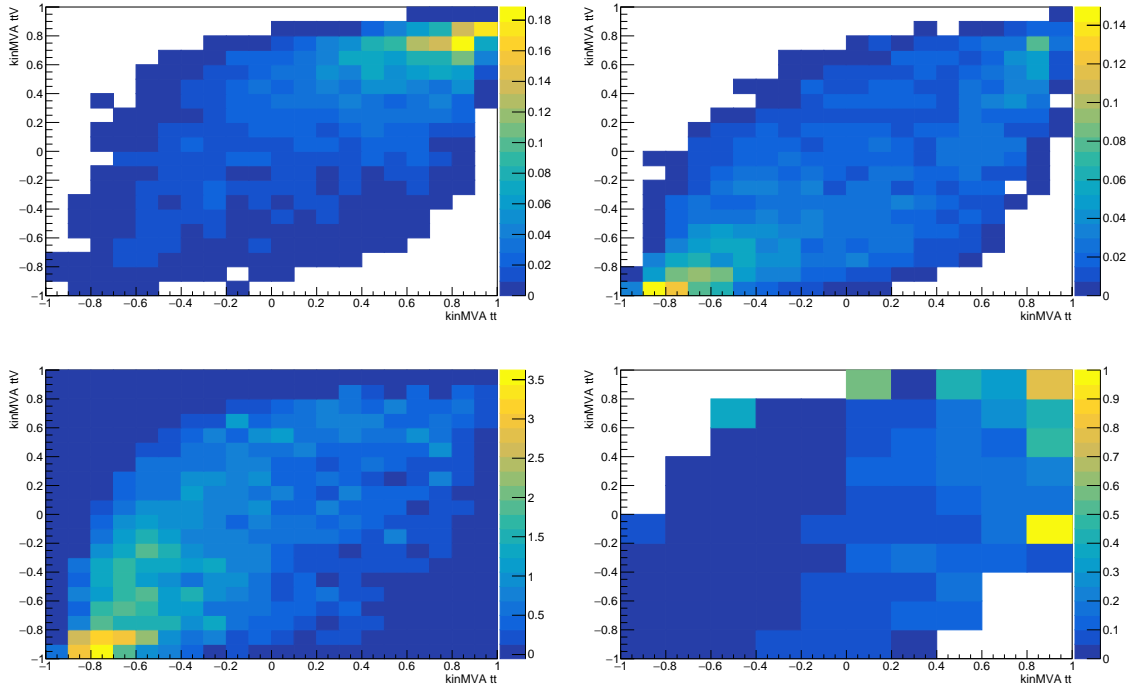


Figure 6.21: BDT classifier output planes (training vs $t\bar{t}$ on x-axis and vs $t\bar{t}V$ on y-axis) for the tHq and tHW signals (top row), and for the combined backgrounds (bottom left). Bottom right: S/B ratio (combining tHq and tHW) in the same plane. Plots are for $3l$ channel.

3035 plane for the combined backgrounds, which are evaluated as in the final background
 3036 prediction, i.e., these are not the samples used in the BDTG training and this includes
 3037 data-driven backgrounds. The signal (combining of tHq and tHW) to background
 3038 ratio (S/B) is showed in the bottom right plot of Figure 6.21.

3039 Each event is now classified into one of ten 2D-bins according to its position in the
 3040 plane, as shown in Figure 6.22. The number of bins is chosen such that no bins are
 3041 entirely empty for any process. The bin boundary positions and number of bins have
 3042 been studied and optimized with respect to the expected limit on the signal strength
 3043 (see Sec. 6.9.6).

3044 From this event categorization, a 1D histogram of expected distribution is pro-
 3045 duced for each signal and background process, and fit to the observed data (or the

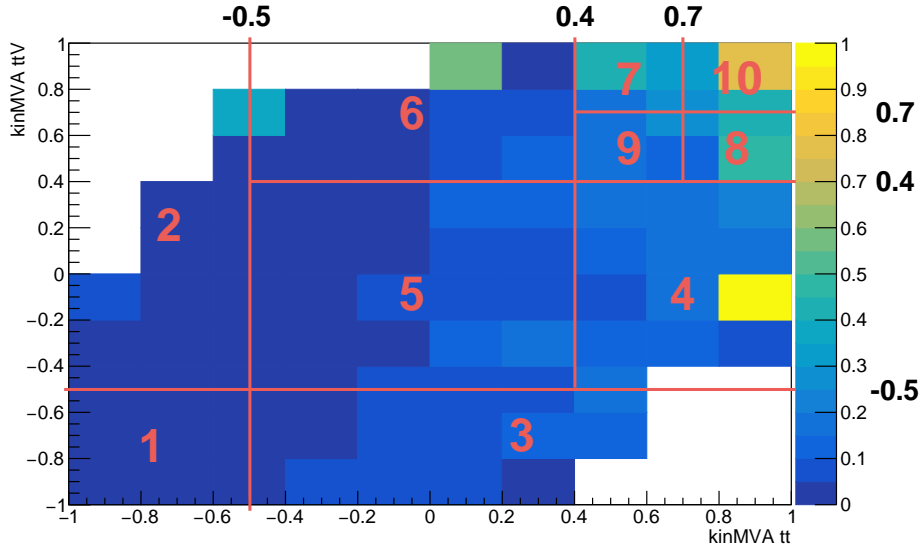


Figure 6.22: Binning overlaid on the S/B ratio map on the plane of classifier outputs.

3046 Asimov dataset for expected limits).

3047 6.9.6 Binning and selection optimization

3048 The effect of the choice of pre-selection cuts and the number of bins of the 1D his-
 3049 togram on the cross section limit is evaluated by varying the most important cuts and
 3050 re-calculating the limit in each case. In this analysis, the optimization was performed
 3051 in the $3l$ channel, by evaluating the upper limits on the $tHq + tHW$ expected signal
 3052 strength only (without $t\bar{t}H$ component), always evaluated at $\kappa_t = -1.0$, $\kappa_V = 1.0$.

3053 Table 6.14 shows several explored variations, compared with a baseline; the base-
 3054 line is similar to the selection reported in Table 6.6 but only a loose CSV jet and a Z
 3055 veto of ± 10 GeV are required.

3056 The optimal limit is found when requiring a slightly tighter selection with respect
 3057 to the baseline. The optimal selection is reported in Table 6.6.

3058 The signal strength limit also depends on the chosen binning in the 2D plane as
 3059 the S/B ratio varies across the plane, hence, several sizes and binning combinations

Selection	Variation	Expected limit
Baseline		< 2.93
Loose CSV tags	$\geq 1 \rightarrow \geq 2$	< 3.81
Medium CSV tags	$\geq 0 \rightarrow \geq 1$	< 2.76
Light forward jet η	$\geq 0 \rightarrow \geq 1$	< 2.94
Light forward jet η	$\geq 0 \rightarrow \geq 1.5$	< 3.00
MET > 30 GeV		< 2.91
Z veto ($ m_{\ell\ell} - m_Z $)	$> 10 \text{ GeV} \rightarrow > 15 \text{ GeV}$	< 2.79
One medium CSV + 15 GeV Z veto	combined	< 2.62

Table 6.14: Signal strength limit variation as a function of tighter cuts. The baseline selection corresponds to a looser selection compared to the one reported in Table 6.6 where only a CSV-loose b -jet is required, and the Z veto is loosened to ± 10 GeV. The optimal selection determined here corresponds to the baseline plus the two variations in the last row.

were tested in order to improve the limit. Figure 6.23 shows some of the binning combinations tested; in the default combination all the bins have the same size, while the best limit was found for a set of 10 bins. The bin borders and the resulting limits are shown in Table 6.15.

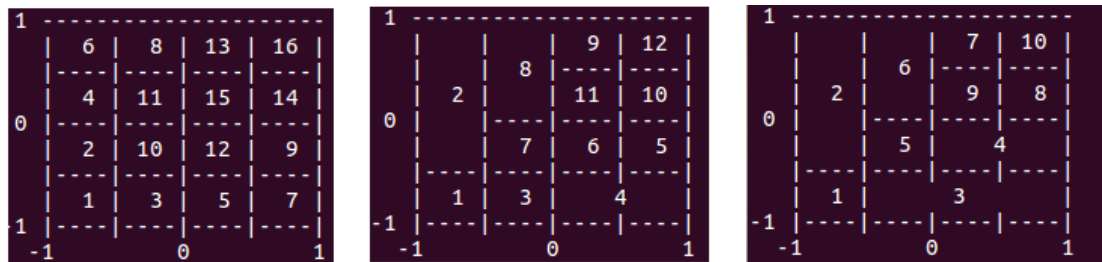


Figure 6.23: Binning combination scheme.

Combining the optimization of binning and using the tighter pre-selection cuts, the expected limit in the $3l$ channel alone reaches $\mathbf{r} < 2.59$.

A similar binning optimization was made for $2lss$ channel, including other binning combinations. First, the $3l$ channel binning was used to estimate the expected limit, then, bin borders were varied to obtain the best possible expected limit. The bin

Number of bins	Bin borders						Expected limit
	x_1	x_2	x_3	y_1	y_2	y_3	
16 (default)	-0.5	0.0	0.5	-0.5	0.0	0.5	< 2.91
16	-0.5	0.3	0.7	-0.5	0.3	0.7	< 2.83
10	-0.5	0.0	0.5	-0.5	0.0	0.5	< 2.93
10	-0.5	0.0	0.7	-0.5	0.0	0.7	< 2.86
10	-0.5	0.0	0.7	-0.5	0.0	0.5	< 2.84
10	-0.5	0.0	0.5	-0.5	0.0	0.7	< 2.87
10	-0.5	0.4	0.7	-0.5	0.4	0.7	< 2.81

Table 6.15: Limit variation as a function of bin size. The final bin borders used in the $3l$ channel are indicated in bold.

3069 borders and the resulting signal strength limits for the same-sign dimuon channel are
 3070 shown in Table 6.16.

Number of bins	Bin borders						Expected limit
	x_1	x_2	x_3	y_1	y_2	y_3	
16	-0.5	0.4	0.7	-0.5	0.4	0.7	< 1.72
12	-0.5	0.4	0.7	-0.5	0.4	0.7	< 1.72
12	-0.3	0.4	0.7	-0.5	0.4	0.7	< 1.71
12	-0.3	0.3	0.7	-0.5	0.4	0.7	< 1.71
12	-0.3	0.3	0.7	-0.4	0.4	0.7	< 1.70
12	-0.3	0.3	0.7	-0.3	0.4	0.7	< 1.70
12	-0.3	0.3	0.7	-0.3	0.2	0.7	< 1.68
12	-0.3	0.3	0.7	-0.3	0.1	0.7	< 1.70
12	-0.3	0.3	0.7	-0.3	0.2	0.6	< 1.70
10	-0.5	0.4	0.7	-0.5	0.4	0.7	< 1.75
10	-0.3	0.3	0.7	-0.3	0.2	0.6	< 1.69

Table 6.16: Limit variation as a function of bin size in the same-sign dimuon channel. (In bold: the final bin borders used in the $2lss$ channel.)

3071 The expected limit was found to be **r<1.69** for optimized bin borders in 10 bins
 3072 and optimized pre-selection cuts.

3073 Two additional binning strategies were tested, however, the obtained limits are
 3074 degraded; they are documented in Appendix C.

3075 6.10 Forward jet mismodeling

3076 As said in previous section, among the features of the tHq signature that serves as a
 3077 powerful discriminating variable is the presence of a forward jet; unfortunately, its η
 3078 distribution is poorly modeled in simulation. To estimate the effect of a mismodeled
 3079 forward jet distribution, a reweighting of the events in simulation based on the nor-
 3080 malized data/MC ratio in a control region is performed; as a result, an alternative
 3081 shape of the BDT output distributions that reflects a hypothetical perfect data/MC
 3082 agreement is derived.

3083 Using a sample of dileptonic $t\bar{t}$ events, the control region is defined by requiring
 3084 two opposite-sign tight leptons in the $e\mu$ channel, with at least two jets and at least
 3085 one medium CSV tagged jet. (Otherwise the selection is identical to the same-sign
 3086 $e^\pm\mu^\pm$ channel selection). Some distributions related to the forward jet for MC and
 3087 data are shown in Figure 6.24.

3088 The disagreement of the η distribution of forward jets for a p_T cut of 25 GeV is
 3089 well visible especially at higher values of $|\eta|$. The multiplicity for central jets is poorly
 3090 described by the MadgraphMLM sample used here; consistent with other observations
 3091 of the same sample. The $t\bar{t}$ background in this analysis is modeled with a data-driven
 3092 method and these disagreements do not directly affect the $t\bar{t}$ contribution in the
 3093 analysis. They do however reflect the expected agreement in these distributions for
 3094 the irreducible backgrounds and the signal.

3095 The effect of higher p_T cuts on the forward jet has been studied for three values:
 3096 25, 30 and 40 GeV. In order to take into account the data/MC disagreement in the
 3097 high η regions, the events are weighted accordingly to the data/MC ratio of the
 3098 unity normalized control plots shown in Figure 6.25. The data/MC agreement in the
 3099 forward jet η distribution improves significantly at higher jet p_T s.

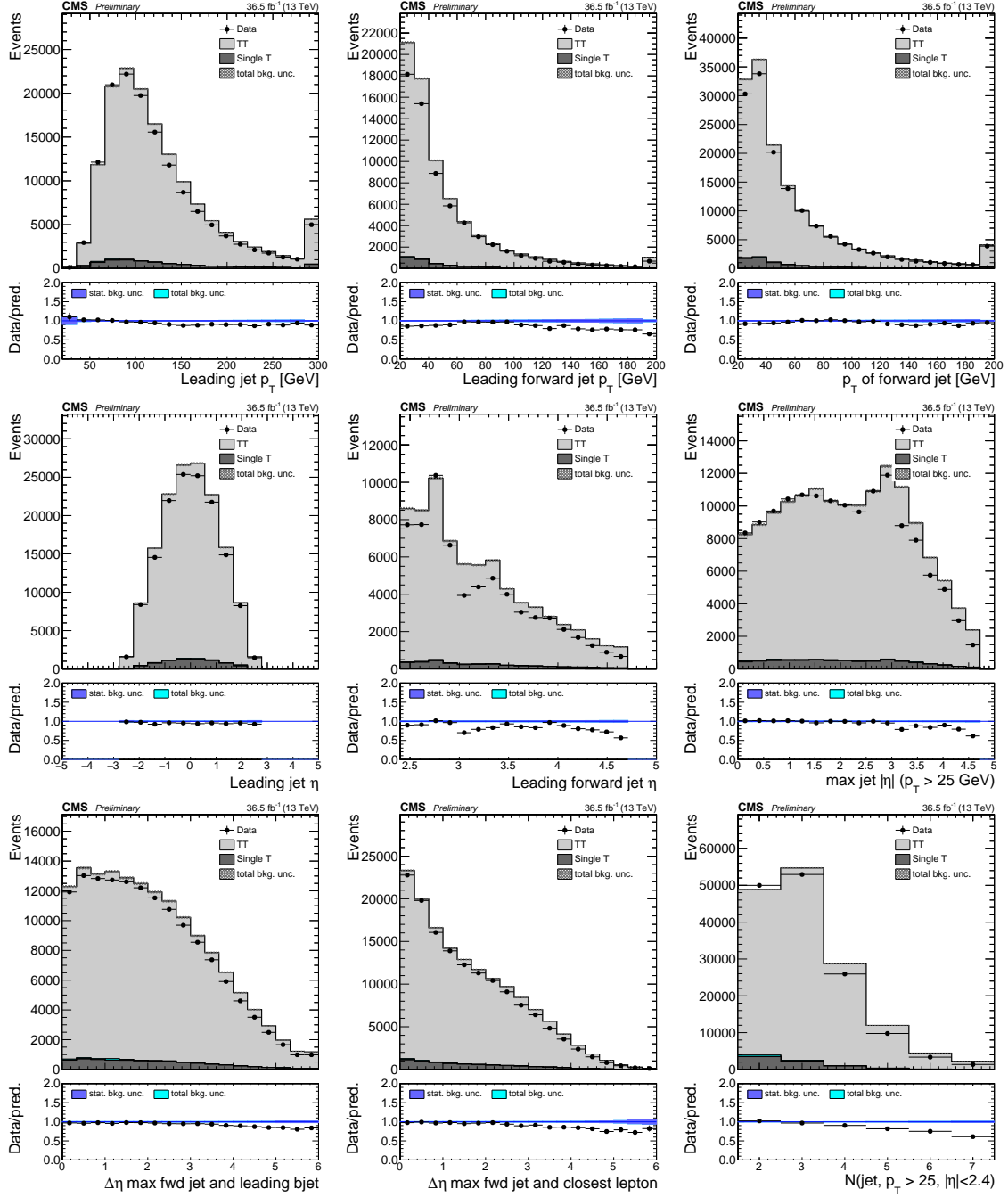


Figure 6.24: Kinematic distributions in the $t\bar{t}$ -enriched opposite-sign $e\mu$ selection. Top row, left to right: leading central ($\eta < 2.4$) jet p_T , leading forward ($\eta > 2.4$) jet p_T , p_T of non-CSV-loose jet with highest η ("light forward jet"). Middle row: η distribution of those same jets. Bottom row: $\Delta\eta$ between light forward jet and leading CSV-loose tagged jet; $\Delta\eta$ between light forward jet and closest lepton; number of central jets.

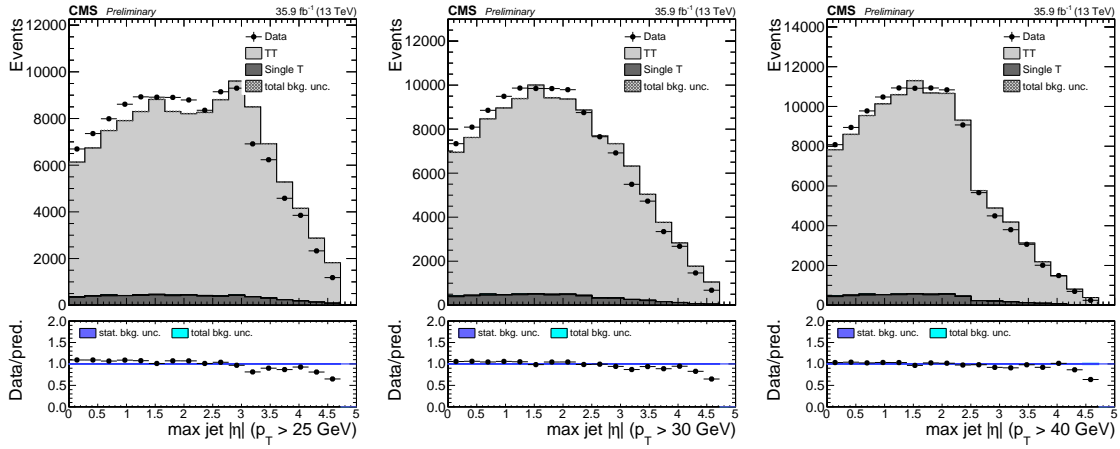


Figure 6.25: Pseudorapidity distributions of the most forward, non-CSV-loose tagged jet in the tt-enriched opposite-sign $e\mu$ selection for the three p_T cut values studied.

3100 Table 6.17 shows the scale factors obtained for the three p_T values. The expected
 3101 limit on cross section in the $3l$ was used to determine the most appropriate forward
 3102 jet p_T cut; higher p_T cut improves from 1.54 at 25 GeV to 1.51 at 30 GeV and 1.50
 3103 at 40 GeV. The impact of the data/MC disagreement for forward jet η is observed
 3104 to reduce with higher p_T cuts. Figures F.1, F.2 and F.3 show this reduction in the
 3105 impact of the forward jet η nuisance in the fit.

3106 6.11 Signal model

3107 It is worth to remind that the main goal of this analysis is to test the compatibility
 3108 of points in the parameter space of Higgs-to-vector boson and Higgs-to-top quark
 3109 couplings. This is achieved by using simulated tHq , tHW , and $t\bar{t}H$ signal events
 3110 which are weighted to reflect the impact of the couplings on kinematic distributions,
 3111 and together with different predictions of the respective production cross sections and
 3112 branching ratios, to produce limits on the cross section for different values of κ_V and
 3113 κ_t . See Section 6.4.3 and Table A.3 for the set of κ_t and κ_V values generated. The
 3114 slight shape-dependence of the BDTG classifier outputs as a function of the couplings

η range	$p_T > 25$ GeV	$p_T > 30$ GeV	$p_T > 40$ GeV
0 – 0.278	1.0925	1.0566	1.0326
0.278 – 0.556	1.0920	1.0617	1.0407
0.556 – 0.833	1.0675	1.0459	1.0244
0.833 – 1.111	1.0888	1.0593	1.0340
1.111 – 1.389	1.0759	1.0508	1.0322
1.389 – 1.667	1.0109	0.9847	0.9661
1.667 – 1.944	1.0727	1.0448	1.0239
1.944 – 2.222	1.0715	1.0457	1.0169
2.222 – 2.500	1.0112	0.9871	0.9746
2.500 – 2.778	1.0387	0.9942	0.9816
2.778 – 3.056	0.9687	0.9427	0.9200
3.056 – 3.333	0.8137	0.8695	0.9092
3.333 – 3.611	0.9010	0.9387	0.9807
3.611 – 3.889	0.8685	0.8887	0.9213
3.889 – 4.167	0.9277	0.9466	1.0135
4.167 – 4.444	0.8111	0.8278	0.8637
4.444 – 4.722	0.6497	0.6485	0.6367
4.722 – 5.000	1.0000	1.0000	1.0000
Exp. limit ($\ell\ell\ell$)	$r < 1.54$	$r < 1.51$	$r < 1.50$

Table 6.17: Data/MC scale factors for η distribution of most forward, non-tagged jet with three different p_T cuts, see Figure 6.25.

3115 is showed in Appendix D.

3116 In addition to the (κ_t, κ_V) dependence of the tHq and tHW production cross
 3117 sections, due to interferences, the cross section of $t\bar{t}H$ depends quadratically on κ_t
 3118 according to [158]:

$$\sigma(tHq) = (2.633\kappa_t^2 + 3.578\kappa_V^2 - 5.211\kappa_t\kappa_V) * \sigma_{SM}(tHq), \quad (6.7)$$

$$\sigma(tHW) = (2.909\kappa_t^2 + 2.310\kappa_V^2 - 4.220\kappa_t\kappa_V) * \sigma_{SM}(tHW), \quad (6.8)$$

$$\sigma(t\bar{t}H) = \kappa_t^2 * \sigma_{SM}(t\bar{t}H). \quad (6.9)$$

3119 The Higgs branching fractions to vector bosons depend on κ_V , and the overall

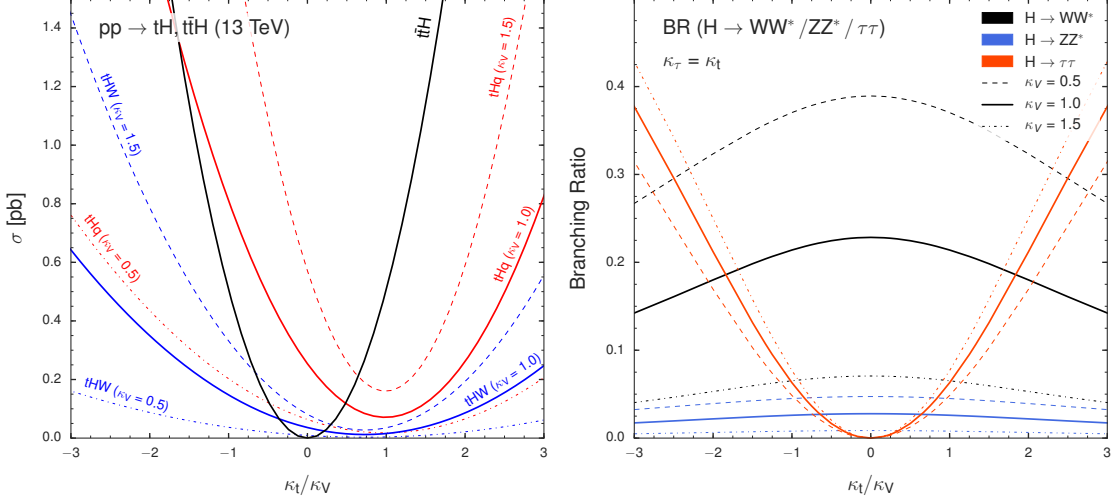


Figure 6.26: Scaling of the tHq , tHW , and $t\bar{t}H$ production cross sections (left) and of the $H \rightarrow WW^*$, $H \rightarrow \tau\tau$, and $H \rightarrow ZZ^*$ branching ratios (right), as a function of κ_t/κ_V , for three different values of κ_V .

3120 Higgs decay width depend both on κ_t and κ_V when considering resolved top quark
 3121 loops in the $H \rightarrow \gamma\gamma$, $H \rightarrow Z\gamma$, and $H \rightarrow gg$ decays. The relative contributions from
 3122 $H \rightarrow WW$, $H \rightarrow ZZ$, and $H \rightarrow \tau\tau$ also changes with changing κ_V .

3123 If the Higgs-to-tau coupling modifier (κ_τ) is assumed to be equal to κ_t , the relative
 3124 fractions of WW , ZZ , and $\tau\tau$ in the event selection will only depend on the ratio of
 3125 κ_t/κ_V ; thus, any limit set at any given value of κ_t/κ_V is valid for all values of κ_t and
 3126 κ_V with that ratio, and could then be compared with theoretical predictions of cross
 3127 sections at different values of either modifier. Figure 6.26 shows the tHq , tHW and
 3128 $t\bar{t}H$ cross sections(left) and the Higgs boson branching ratios $H \rightarrow WW$, $H \rightarrow ZZ$,
 3129 and $H \rightarrow \tau\tau$ (right) as a function of the κ_t/κ_V ratio.

3130 Thus, this analysis sets an upper limit on the combined cross section times branch-
 3131 ing ratio of tHq , tHW , and $t\bar{t}H$ as a function of the ratio κ_t/κ_V .

3132 Similar interpretation can be made if instead of reporting the limits as a function
 3133 of the κ_t/κ_V ratio, they are reported as a function of the relative strength of Higgs-top
 3134 and Higgs-vector-boson couplings, multiplied by the relative sign

$$f_t = \text{sign}\left(\frac{\kappa_t}{\kappa_V}\right) \times \frac{\kappa_t^2}{\kappa_t^2 + \kappa_V^2}. \quad (6.10)$$

3135 this parameter covers the full space between -1.0 and 1.0 , with the SM at 0.5 .
 3136 Absolute values of 1.0 or 0.0 would correspond to purely Higgs-top and purely Higgs-
 3137 V couplings, respectively.

3138 Table 6.18 shows the points in the κ_t/κ_V and f_t parameter space that are mapped
 3139 by the 51 individual κ_t and κ_V points.

3140 The overall Higgs decay width (modified by both κ_t and κ_V) becomes irrelevant
 3141 if limits are quoted as absolute cross sections rather than multiples of the expected
 3142 cross section (which depends on it).

3143 The 1D histograms of events as categorized in regions of the 2D BDTG plane are
 3144 then used in a maximum likelihood fit of signal and background shapes, where the
 3145 tHq , tHW , and $t\bar{t}H$ signals are floating with a common signal strength modifier r ,
 3146 producing a 95% C.L. upper limit the observed cross section of $tHq + tHW + t\bar{t}H$.

3147 This procedure is done separately for each point (κ_t, κ_V) where the cross sections
 3148 and branching fractions are scaled accordingly in each point. Limits at fixed values
 3149 of κ_t/κ_V are by construction identical. Tables G.1–G.3 and G.4–G.6 in Appendix G
 3150 show the scalings of cross section times branching fraction, as well as branching
 3151 fractions alone for each of the Higgs decay modes and each of the signal components.

3152 6.12 Systematic uncertainties

3153 The uncertainties present in this analysis can be either of statistical nature given
 3154 the size of the samples and the probabilistic nature of the processes, or of system-
 3155 atic nature. The systematic uncertainties are associated to theoretical uncertainties
 3156 originating in the limited knowledge of the processes, and also to experimental uncer-

f_t	κ_t/κ_V	$\kappa_V = 0.5$	$\kappa_V = 1.0$	$\kappa_V = 1.5$
-0.973	-6.000	-3.00		
-0.941	-4.000	-2.00		
-0.900	-3.000	-1.50	-3.00	
-0.862	-2.500	-1.25		
-0.800	-2.000	-1.00	-2.00	-3.00
-0.692	-1.500	-0.75	-1.50	
-0.640	-1.333			-2.00
-0.610	-1.250		-1.25	
-0.500	-1.000	-0.50	-1.00	-1.50
-0.410	-0.833			-1.25
-0.360	-0.750		-0.75	
-0.308	-0.667			-1.00
-0.200	-0.500	-0.25	-0.50	-0.75
-0.100	-0.333			-0.50
-0.059	-0.250		-0.25	
-0.027	-0.167			-0.25
0.000	0.000	0.00	0.00	0.00
0.027	0.167			0.25
0.059	0.250		0.25	
0.100	0.333			0.50
0.200	0.500	0.25	0.50	0.75
0.308	0.667			1.00
0.360	0.750		0.75	
0.410	0.833			1.25
0.500	1.000	0.50	1.00	1.50
0.610	1.250		1.25	
0.640	1.333			2.00
0.692	1.500	0.75	1.50	
0.800	2.000	1.00	2.00	3.00
0.862	2.500	1.25		
0.900	3.000	1.50	3.00	
0.941	4.000	2.00		
0.973	6.000	3.00		

Table 6.18: The 33 distinct values of κ_t/κ_V and f_t as mapped by the 51 κ_t and κ_V points.

3157 tainties originating for instance from the limited resolution of the detectors. In this
 3158 section, the contributions to the systematic uncertainties from all the sources in this
 3159 analysis are considered.

3160 Rate uncertainties associated to the application of scaling factors for the affected
3161 processes, and shape uncertainties which affect not only the normalization but also
3162 the shape of certain distributions, compose the systematic uncertainties. The latter
3163 can affect the analysis during the event selection; therefore, these systematic shape
3164 uncertainties are applied to the simulation samples.

3165 **Experimental uncertainties.**

3166 • *Luminosity.* The measurement of the luminosity delivered by the LHC is af-
3167 fected by experimental conditions like pileup and the number of protons per
3168 bunch. Due to variations in the LHC running parameters an uncertainty of
3169 2.6% is applied.

3170 • *Lepton efficiencies.* Systematic uncertainties in the signal selection efficiency
3171 arise from correction factors applied to the simulated events in order to better
3172 match the measured detector performance; also from theoretical uncertainties in
3173 the modeling of the signal process. Data/MC differences in the trigger efficiency
3174 accounted with scale factors applied to correct for them, lepton reconstruction
3175 and identification performance, and lepton selection efficiency carry a combined
3176 uncertainty of about 5% per lepton.

3177 • *Jets related uncertainties.* Jet energy corrections affect the uncertainty in the
3178 signal selection efficiency it is evaluated by varying the correction factors within
3179 their uncertainties and propagating the effects to the final results by recalculat-
3180 ing the kinematic quantities. The effects of the jet energy scale uncertainties,
3181 b -tagging efficiency and forward jet mismodeling are evaluated using dedicated
3182 shape templates derived from a variation of the jet energy scale within its uncer-
3183 tainty and from varying the b -tagging forward jet data/MC scale factors within
3184 their uncertainty.

3185 **Theory uncertainties**

3186 The uncertainties from unknown higher orders of tHq and tHW production are
 3187 estimated from a change in the Q^2 scale of double and half the initial value, evaluated
 3188 for each point of κ_t and κ_V . The $t\bar{t}H$ signal component has an uncertainty of about
 3189 $+5.8/-9.2\%$ from Q^2 scale variations and a further 3.6% from the knowledge of PDFs
 3190 and α_s [57]. Uncertainties related to the choice of PDF set and its scale are estimated
 3191 to be about 3.7% for tHq and about 4.0% for tHW .

3192 The theoretical uncertainties from unknown higher orders for $t\bar{t}W$ and $t\bar{t}Z$ are
 3193 12% and 10% respectively; additional uncertainties from the knowledge of PDFs and
 3194 α_s of about 4% each for $t\bar{t}W$ and $t\bar{t}Z$ are estimated.

3195 **Backgrounds**

3196 Besides the theory uncertainties on $t\bar{t}W$ and $t\bar{t}Z$, uncertainties of the smaller
 3197 irreducible backgrounds and the charge mis-identification estimate are covered with
 3198 flat normalization uncertainties. The WZ contribution due to the scale factor is
 3199 derived during the background estimation using the control region.

3200 The dominant uncertainty is associated to the estimate of the non-prompt lepton
 3201 contribution using a fake rate method; the main normalization uncertainty comes from
 3202 limited statistics in the data control region, and the subtraction of residual prompt
 3203 lepton contribution as stated in section 6.7.2. Shape variations resembling data/MC
 3204 differences and deviations in closure test are evaluated as shape uncertainties.

3205 **Fake rate closure uncertainties**

3206 In order to determine the systematic uncertainties associated to the fake rates,
 3207 the BDTG classifier output shapes from a pure MC estimation of fake leptons (in
 3208 $t\bar{t}$) and from the application of fake-rates as measured in QCD MC, applied in $t\bar{t}$
 3209 MC events, are compared. The difference in the resulting normalization and output
 3210 shapes, for both trainings vs. $t\bar{t}$ and vs. $t\bar{t}V$, are estimated and propagated to the

3211 fit as normalization and shape variations; Figures 6.27 and 6.28 show the results of
3212 these closure tests.

3213 Table 6.19 list all the systematic uncertainties currently considered in the analysis.

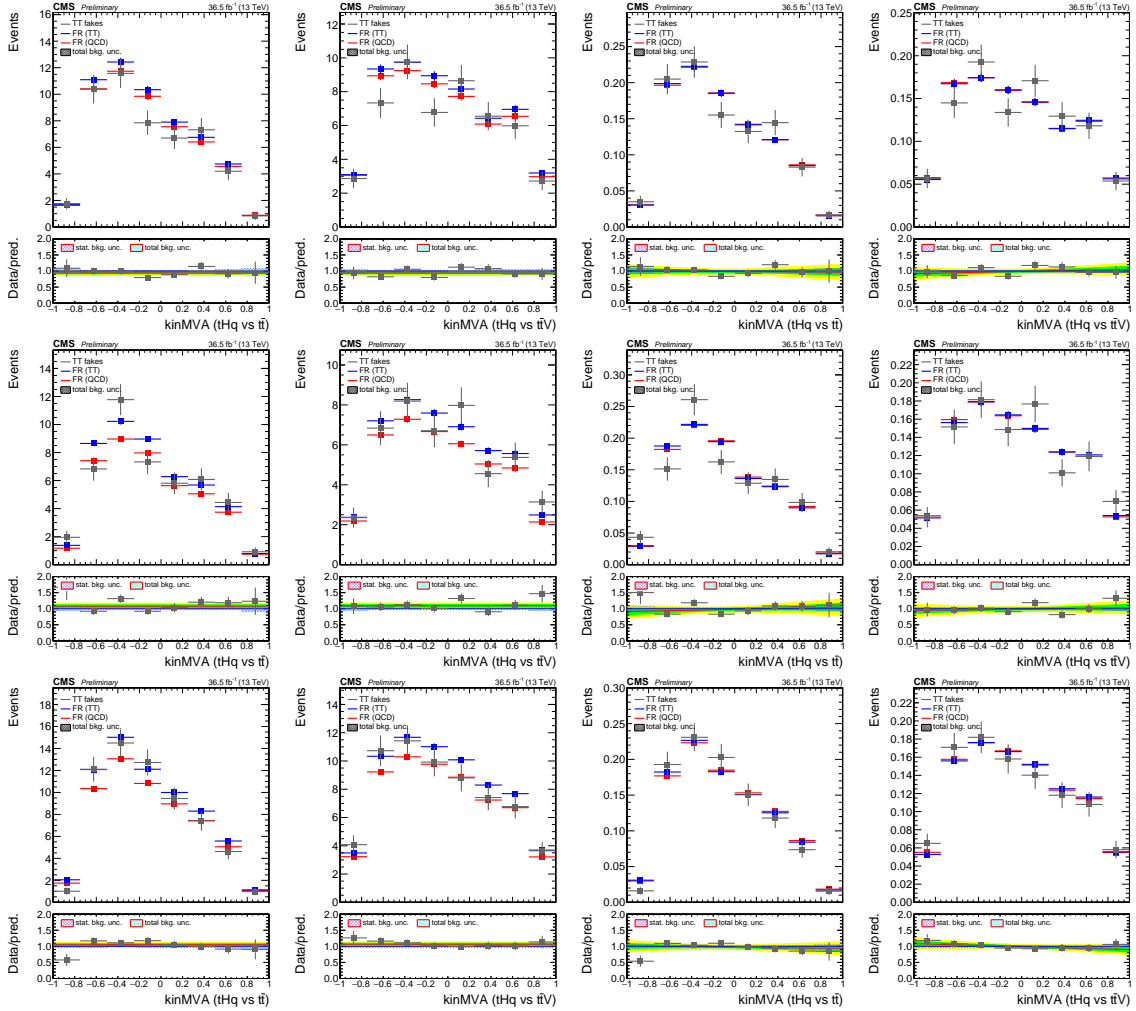


Figure 6.27: BDT outputs comparing $t\bar{t}$ MC to a fake-rate prediction using fake rates measured in QCD MC. Agreement in normalization is estimated from the plots in the two left columns, shape disagreement is estimated from the (normalized) plots in the two right columns. From top to bottom rows: same-sign $e^\pm \mu^\mp$ selection with electron fakes, same-sign $e^\pm \mu^\mp$ selection with muon fakes, same-sign $\mu^\pm \mu^\pm$ selection.

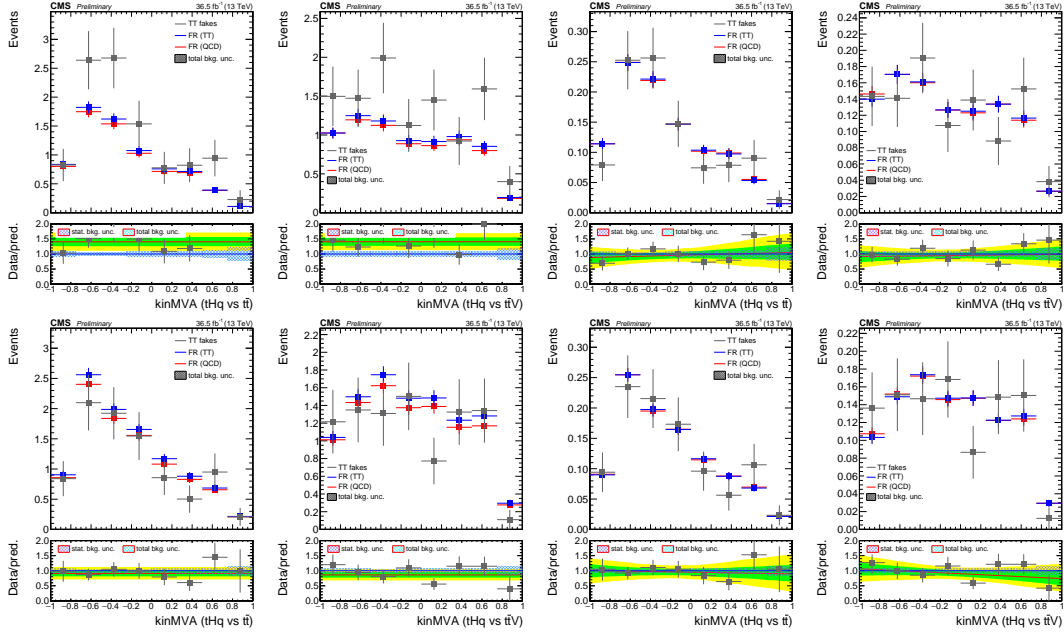


Figure 6.28: BDT outputs comparing $t\bar{t}$ MC to a fake-rate prediction using fake rates measured in QCD MC. Agreement in normalization is estimated from the plots in the two left columns, shape disagreement is estimated from the (normalized) plots in the two right columns. From top to bottom rows: three lepton selection with electron fakes, three lepton selection with muon fakes.

Source	Channel	Size
Experimental uncertainties		
Luminosity	all	1.026
Loose lepton efficiency		1.02 per lepton
Tight lepton efficiency		1.03 per lepton
Trigger efficiency	$\mu^\pm \mu^\pm$ $e^\pm \mu^\pm$ $\ell\ell\ell$	1.01 1.01 1.03
Jet energy scale	all	templates
Forward jet modeling	all	templates, see Table 6.17
_tagging efficiency	all	templates
Theory uncertainties		
Q^2 scale (tHq)	all	0.92–1.06 (depending on κ_t, κ_V)
Q^2 scale (tHW)	all	0.93–1.05 (depending on κ_t, κ_V)
Q^2 scale ($t\bar{t}H$)	all	0.915/1.058
Q^2 scale ($t\bar{t}W$)	all	1.12
Q^2 scale ($t\bar{t}Z$)	all	1.11
pdf ($t\bar{t}H$)	all	1.036
pdf gg ($t\bar{t}Z$)	all	0.966
pdf $q\bar{q}$ ($t\bar{t}W$)	all	1.04
pdf qg (tHq)	all	1.037
pdf qg (tHW)	all	1.040
Higgs branching fractions		
param_alphaS	all	1.012
param_mB	all	0.981
HiggsDecayWidthTHU_hqq	all	0.988
HiggsDecayWidthTHU_hvv	all	1.004
HiggsDecayWidthTHU_hll	all	1.019
Backgrounds		
WZ control region statistics	$\ell\ell\ell$	1.10
WZ control region backgrounds	$\ell\ell\ell$	1.20
WZ modeling	$\ell\ell\ell$	1.07
$WZ + 2\text{jet}$ background	$\mu^\pm \mu^\pm, e^\pm \mu^\pm$	1.50
Rare SM processes	all	1.50
Charge flips	$e^\pm \mu^\pm$	1.30
Fake rate estimate		
Electron FR measurement		templates
Muon FR measurement		templates
Electron closure	$e^\pm \mu^\pm$	0.94 norm., (0.98 ($t\bar{t}$))/1.07 ($t\bar{t}V$)) shape var.
	$\ell\ell\ell$	1.40 norm., (1.09 ($t\bar{t}$))/1.05 ($t\bar{t}V$)) shape var.
Muon closure	$\mu^\pm \mu^\pm$	1.07 norm., (0.97 ($t\bar{t}$))/0.91 ($t\bar{t}V$)) shape var.
	$e^\pm \mu^\pm$	1.09 norm., (1.06 ($t\bar{t}$))/1.03 ($t\bar{t}V$)) shape var.
	$\ell\ell\ell$	1.09 norm., (0.95 ($t\bar{t}$))/0.83 ($t\bar{t}V$)) shape var.

Table 6.19: Pre-fit size of systematic uncertainties.

3214 6.13 Results

3215 As a result of applying the event pre-selection on the dataset, 127 events are observed
 3216 in the $3l$ channel, 280 in the $2lss \mu^\pm \mu^\pm$ channel and 525 in the $2lss e^\pm \mu^\pm$ channel
 3217 as shown in Table 6.8. These events are then classified into one of ten categories,
 3218 depending on the output of the two BDTG classifiers and according to the optimized
 binning strategy.

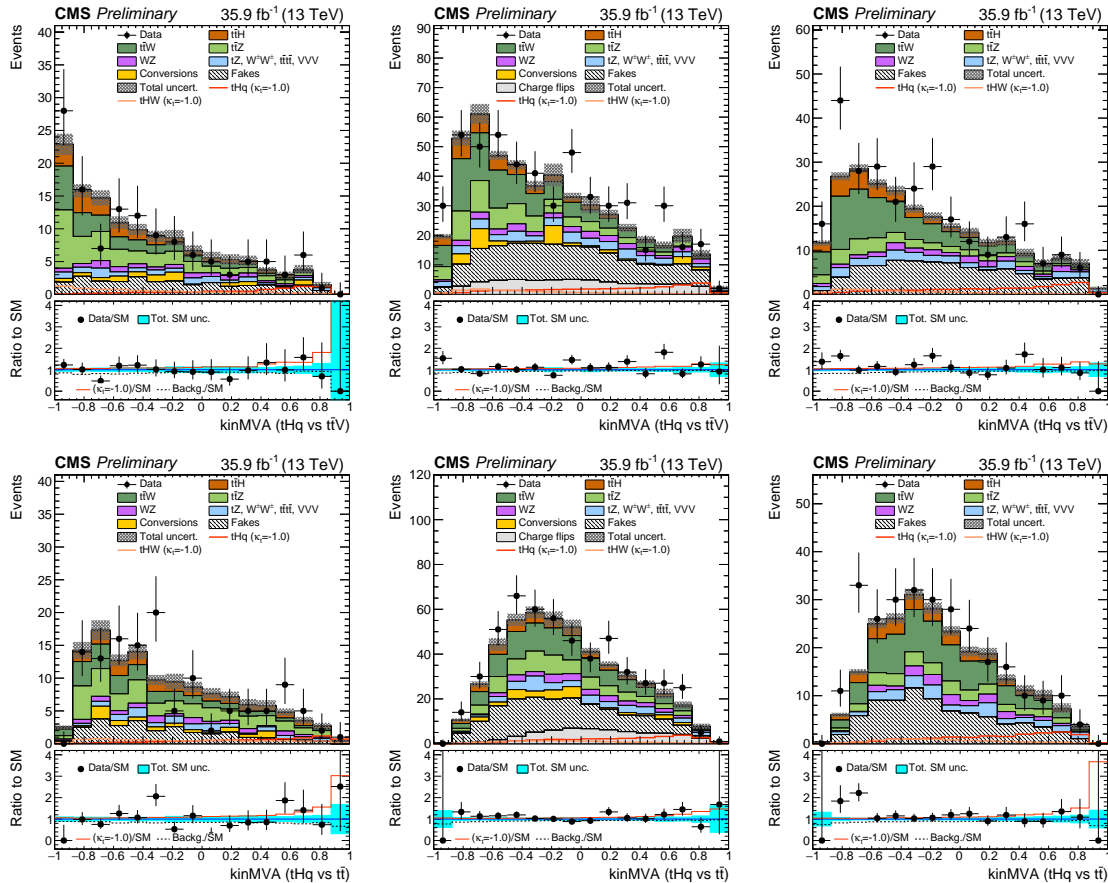


Figure 6.29: Pre-fit BDT classifier outputs, for the three-lepton channel (left), $e^\pm \mu^\pm$ (center), and $\mu^\pm \mu^\pm$ (right), for 35.9 fb^{-1} , for training against $t\bar{t}V$ (top row) and against $t\bar{t}$ (bottom row). In the box below each distribution, the ratio of the observed and predicted event yields is shown. The shape of the two tH signals for $\kappa_t = -1.0$ is shown, normalized to their respective cross sections for $\kappa_t = -1.0, \kappa_V = 1.0$. The grey band represents the unconstrained (pre-fit) statistical and systematical uncertainties.

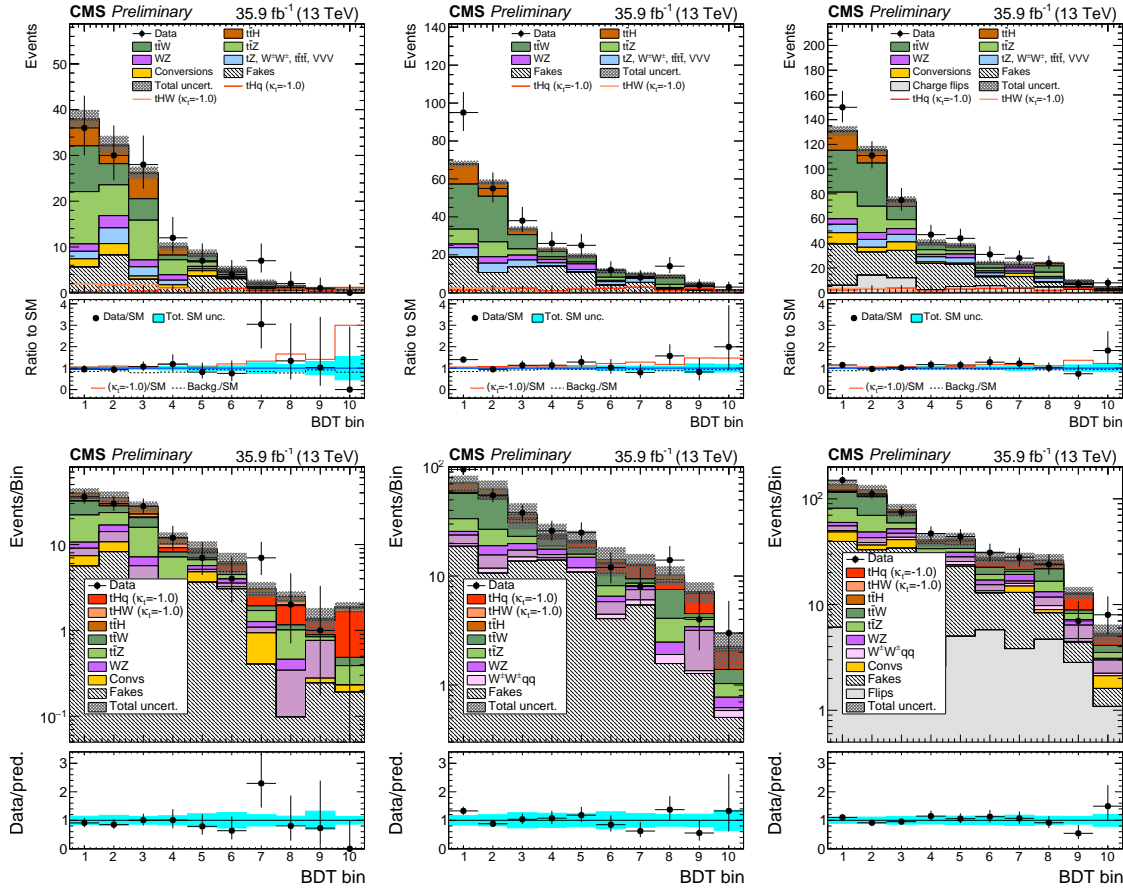


Figure 6.30: Expected (pre-fit) distributions in the final binning used for the signal extraction, for (from left to right) the three lepton channel, the $\mu^\pm\mu^\pm$ channel, and the $e^\pm\mu^\pm$ channel. Linear scale (top row), and logarithmic scale (bottom row).

3220 The pre-fit distributions of BDTG outputs are shown in Figure 6.29, while the
 3221 pre-fit distributions in the final binning used in the signal extraction are shown in
 3222 Figure 6.30.

3223 The expected signal and background shapes for the distribution in the 1D his-
 3224 togram (with ten bins) are fit to the observed data in a maximum likelihood fit, for
 3225 all three channels simultaneously and separately for the signal shapes for each of the
 3226 33 κ_t/κ_V coupling configuration points.

3227 The tH and $t\bar{H}$ production cross sections and the Higgs decay branching ratios are
 3228 modified in each point with the Higgs-top (κ_t) and Higgs-vector boson (κ_V) coupling

strength and the Higgs-tau coupling strength modifier (κ_τ) is assumed to be equal to κ_t ; the rest of the parameters are assumed to be at the SM predicted values. The combined signal shape is then uniquely defined by the ratio of κ_t/κ_V . In the fit, the signal components, tH and $t\bar{t}H$, are floated with a common signal strength modifier (defined as the ratio to the expected cross section) to produce a 95% confidence level (C.L) upper limit on the observed $tH + t\bar{t}H$ cross section times the combined branching ratio of $H \rightarrow WW^* + ZZ^* + \tau\tau$.

The post-fit categorized BDTG output distributions obtained in the maximum likelihood fit to extract the limits, are shown in Figure 6.31.

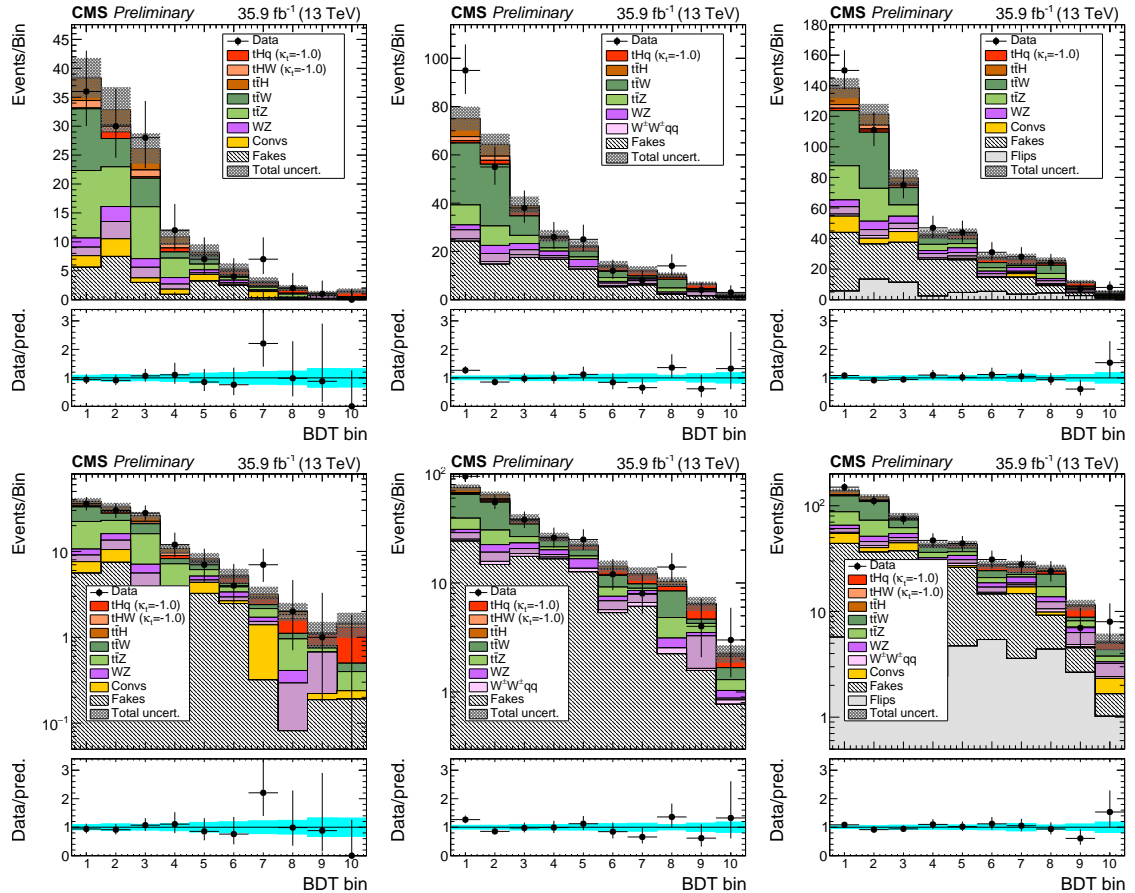


Figure 6.31: Post-fit distributions in the final binning used for the signal extraction, for (from left to right) the three lepton channel, the $\mu^\pm\mu^\pm$ channel, and the $e^\pm\mu^\pm$ channel. Linear scale (top row), and logarithmic scale (bottom row).

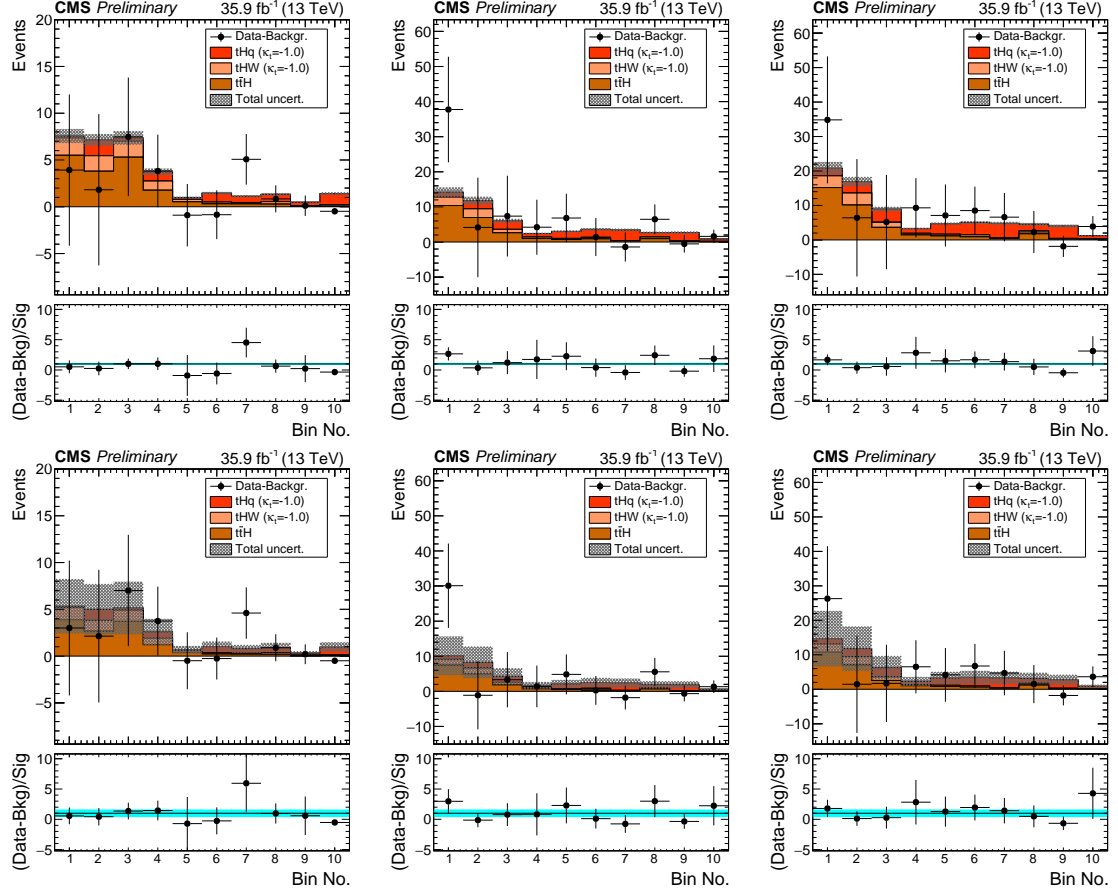


Figure 6.32: Background-subtracted pre- (top) and post-fit (bottom) distributions in the final binning used for the signal extraction, for three lepton channel (left), the $\mu^{\pm}\mu^{\pm}$ channel (center), and the $e^{\pm}e^{\pm}$ channel (right). For a fit in the inverted couplings scenario ($\kappa_V = 1, \kappa_t = -1$).

3238 As expected, the signal contribution is very small compared to the background
 3239 ground contribution; however, it is possible to see the signal contribution by subtracting the background from the overall BDT output distributions as shown in Figure
 3240 6.32 for the inverted coupling scenario ($\kappa_V = 1, \kappa_t = -1$) and Figure 6.33 for the SM-like
 3241 scenario ($\kappa_V = 1, \kappa_t = 1$).
 3242

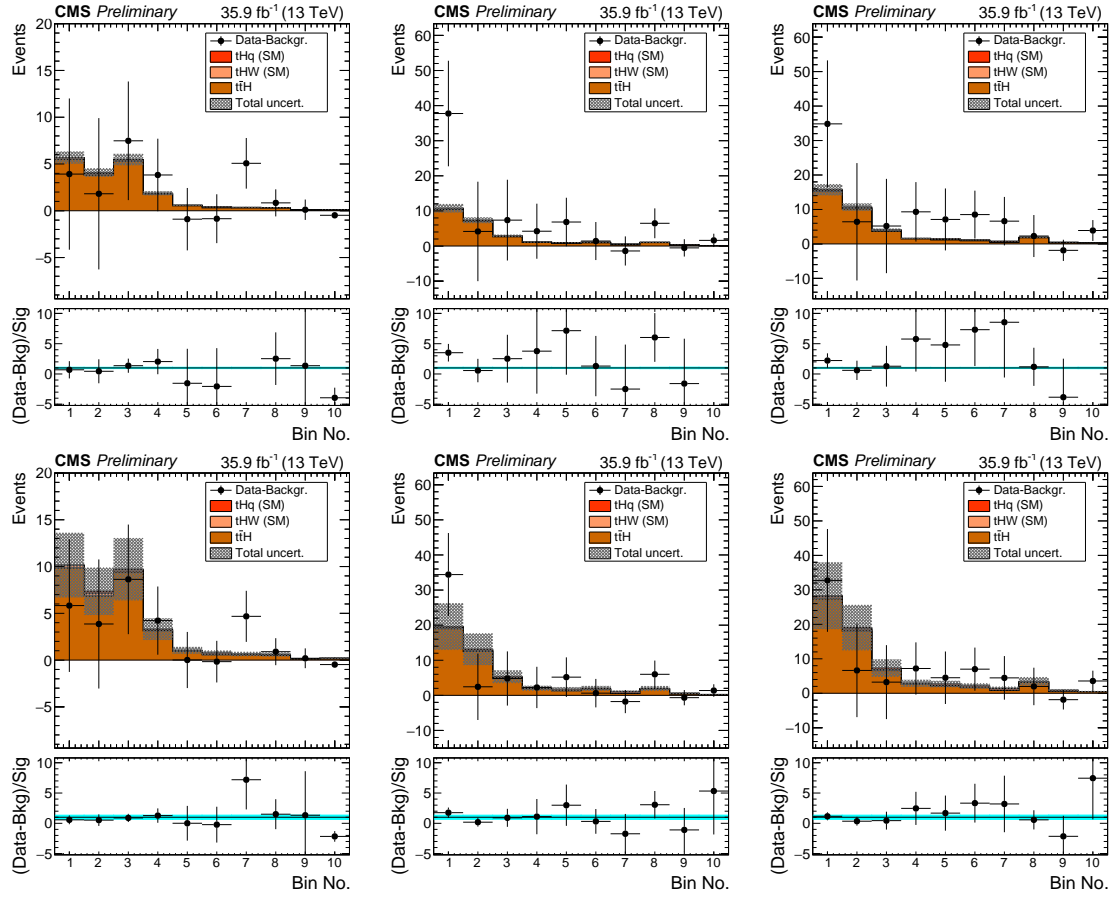


Figure 6.33: Background-subtracted pre- (top) and post-fit (bottom) distributions in the final binning used for the signal extraction, for the three lepton channel (left), the $\mu^{\pm}\mu^{\pm}$ channel (center), and the $e^{\pm}\mu^{\pm}$ channel (right). For a fit in the SM-like scenario ($\kappa_t = \kappa_V = 1$).

3243 6.13.1 CL_S and cross section limits

3244 Table 6.20 lists the expected background only, the expected SM-like Higgs signal, and
 3245 the observed 95% C.L. upper limits on the $tH + t\bar{H}$ production cross section times
 3246 $H \rightarrow WW^* + ZZ^* + \tau\tau$ branching ratio (in pb); the corresponding plots are shown
 3247 in Figure 6.34 for $\kappa_V = 1$. The expected background-only limit is calculated on an
 3248 Asimov dataset, while the expected SM-like limit is calculated on an Asimov dataset
 3249 that includes the SM-like tH and $t\bar{H}$ signals.

3250 An excess of more than 2σ is observed for the SM configuration ($\kappa_t/\kappa_V = 1$) for the

f_t	κ_t/κ_V	Exp. lim.	SM exp.	Obs. lim.	Best fit σ [pb]	Best fit r
-0.973	-6.000	0.328 $^{+0.136}_{-0.090}$	0.507 $^{+0.206}_{-0.158}$	0.603	0.305 $^{+0.155}_{-0.169}$	0.013 $^{+0.007}_{-0.007}$
-0.941	-4.000	0.335 $^{+0.137}_{-0.098}$	0.509 $^{+0.215}_{-0.166}$	0.627	0.322 $^{+0.157}_{-0.174}$	0.036 $^{+0.018}_{-0.020}$
-0.900	-3.000	0.335 $^{+0.138}_{-0.096}$	0.510 $^{+0.215}_{-0.172}$	0.639	0.334 $^{+0.160}_{-0.173}$	0.075 $^{+0.036}_{-0.039}$
-0.862	-2.500	0.334 $^{+0.139}_{-0.097}$	0.505 $^{+0.217}_{-0.173}$	0.649	0.341 $^{+0.160}_{-0.174}$	0.119 $^{+0.056}_{-0.061}$
-0.800	-2.000	0.330 $^{+0.141}_{-0.095}$	0.500 $^{+0.212}_{-0.176}$	0.656	0.345 $^{+0.165}_{-0.176}$	0.202 $^{+0.097}_{-0.103}$
-0.692	-1.500	0.325 $^{+0.139}_{-0.095}$	0.485 $^{+0.209}_{-0.172}$	0.660	0.340 $^{+0.164}_{-0.176}$	0.369 $^{+0.178}_{-0.191}$
-0.640	-1.333	0.325 $^{+0.139}_{-0.097}$	0.482 $^{+0.210}_{-0.173}$	0.659	0.334 $^{+0.169}_{-0.174}$	0.456 $^{+0.231}_{-0.238}$
-0.610	-1.250	0.321 $^{+0.140}_{-0.095}$	0.474 $^{+0.210}_{-0.169}$	0.653	0.328 $^{+0.164}_{-0.177}$	0.505 $^{+0.252}_{-0.272}$
-0.500	-1.000	0.315 $^{+0.142}_{-0.093}$	0.450 $^{+0.213}_{-0.160}$	0.638	0.304 $^{+0.175}_{-0.176}$	0.685 $^{+0.395}_{-0.396}$
-0.410	-0.833	0.312 $^{+0.138}_{-0.095}$	0.424 $^{+0.210}_{-0.147}$	0.615	0.276 $^{+0.168}_{-0.177}$	0.819 $^{+0.498}_{-0.526}$
-0.360	-0.750	0.307 $^{+0.138}_{-0.093}$	0.409 $^{+0.200}_{-0.136}$	0.593	0.256 $^{+0.170}_{-0.176}$	0.874 $^{+0.581}_{-0.601}$
-0.308	-0.667	0.301 $^{+0.138}_{-0.092}$	0.384 $^{+0.198}_{-0.124}$	0.566	0.231 $^{+0.165}_{-0.174}$	0.915 $^{+0.655}_{-0.689}$
-0.200	-0.500	0.292 $^{+0.136}_{-0.090}$	0.345 $^{+0.181}_{-0.109}$	0.497	0.166 $^{+0.163}_{-0.162}$	0.895 $^{+0.879}_{-0.871}$
-0.100	-0.333	0.278 $^{+0.132}_{-0.086}$	0.303 $^{+0.156}_{-0.092}$	0.409	0.092 $^{+0.157}_{-0.092}$	0.679 $^{+1.159}_{-0.679}$
-0.059	-0.250	0.268 $^{+0.129}_{-0.083}$	0.283 $^{+0.152}_{-0.085}$	0.365	0.059 $^{+0.148}_{-0.059}$	0.515 $^{+1.285}_{-0.515}$
-0.027	-0.167	0.260 $^{+0.125}_{-0.081}$	0.266 $^{+0.135}_{-0.077}$	0.328	0.029 $^{+0.142}_{-0.029}$	0.297 $^{+1.434}_{-0.297}$
0.000	0.000	0.254 $^{+0.123}_{-0.079}$	0.252 $^{+0.123}_{-0.073}$	0.294	0.000 $^{+0.132}_{-0.000}$	0.002 $^{+1.776}_{-0.002}$
0.027	0.167	0.275 $^{+0.132}_{-0.086}$	0.284 $^{+0.148}_{-0.084}$	0.357	0.040 $^{+0.154}_{-0.040}$	0.650 $^{+2.514}_{-0.650}$
0.059	0.250	0.297 $^{+0.141}_{-0.093}$	0.329 $^{+0.171}_{-0.099}$	0.458	0.119 $^{+0.183}_{-0.119}$	2.015 $^{+3.098}_{-2.015}$
0.100	0.333	0.322 $^{+0.148}_{-0.099}$	0.405 $^{+0.220}_{-0.135}$	0.611	0.246 $^{+0.166}_{-0.184}$	4.147 $^{+2.802}_{-3.103}$
0.200	0.500	0.324 $^{+0.141}_{-0.096}$	0.505 $^{+0.212}_{-0.181}$	0.730	0.413 $^{+0.150}_{-0.177}$	5.982 $^{+2.174}_{-2.559}$
0.308	0.667	0.281 $^{+0.122}_{-0.082}$	0.462 $^{+0.172}_{-0.159}$	0.651	0.382 $^{+0.136}_{-0.144}$	4.186 $^{+1.492}_{-1.574}$
0.360	0.750	0.268 $^{+0.116}_{-0.079}$	0.442 $^{+0.160}_{-0.154}$	0.620	0.364 $^{+0.130}_{-0.135}$	3.392 $^{+1.214}_{-1.253}$
0.410	0.833	0.258 $^{+0.112}_{-0.075}$	0.427 $^{+0.162}_{-0.147}$	0.599	0.351 $^{+0.127}_{-0.130}$	2.754 $^{+0.999}_{-1.022}$
0.500	1.000	0.244 $^{+0.105}_{-0.072}$	0.401 $^{+0.154}_{-0.137}$	0.562	0.328 $^{+0.118}_{-0.121}$	1.821 $^{+0.657}_{-0.671}$
0.610	1.250	0.240 $^{+0.104}_{-0.070}$	0.394 $^{+0.154}_{-0.133}$	0.545	0.315 $^{+0.118}_{-0.119}$	1.072 $^{+0.399}_{-0.403}$
0.640	1.333	0.242 $^{+0.105}_{-0.071}$	0.398 $^{+0.156}_{-0.136}$	0.547	0.316 $^{+0.122}_{-0.121}$	0.921 $^{+0.354}_{-0.352}$
0.692	1.500	0.244 $^{+0.106}_{-0.071}$	0.401 $^{+0.159}_{-0.136}$	0.543	0.312 $^{+0.120}_{-0.120}$	0.678 $^{+0.262}_{-0.261}$
0.800	2.000	0.256 $^{+0.109}_{-0.075}$	0.416 $^{+0.169}_{-0.138}$	0.552	0.311 $^{+0.121}_{-0.127}$	0.317 $^{+0.123}_{-0.129}$
0.862	2.500	0.268 $^{+0.114}_{-0.078}$	0.433 $^{+0.169}_{-0.142}$	0.558	0.310 $^{+0.127}_{-0.130}$	0.170 $^{+0.070}_{-0.072}$
0.900	3.000	0.276 $^{+0.118}_{-0.080}$	0.442 $^{+0.177}_{-0.144}$	0.563	0.308 $^{+0.128}_{-0.134}$	0.102 $^{+0.042}_{-0.044}$
0.941	4.000	0.290 $^{+0.122}_{-0.084}$	0.459 $^{+0.184}_{-0.149}$	0.566	0.304 $^{+0.134}_{-0.140}$	0.046 $^{+0.020}_{-0.021}$
0.973	6.000	0.306 $^{+0.122}_{-0.081}$	0.474 $^{+0.192}_{-0.150}$	0.571	0.300 $^{+0.131}_{-0.150}$	0.016 $^{+0.007}_{-0.008}$

Table 6.20: Expected (for background only, and for a SM-like Higgs signal) and observed 95% C.L. upper limits (in pb), and best fit signal strength r and corresponding best fit cross section for the combined $tH + t\bar{t}H$ cross section times modified branching ratio for the combination of all three channels, for different values of κ_t/κ_V or the equivalent f_t numbers.

background-only expected limit; however, the inclusion of the SM-like tH and $t\bar{t}H$ signals reveals that the excess is actually about 1σ ; furthermore, looking at $\kappa_t/\kappa_V = 0$, i.e., the $t\bar{t}H$ component in the signal is zero, it is evident that the origin of the excess is mostly due to the presence of the $t\bar{t}H$ component in the signal, given that the

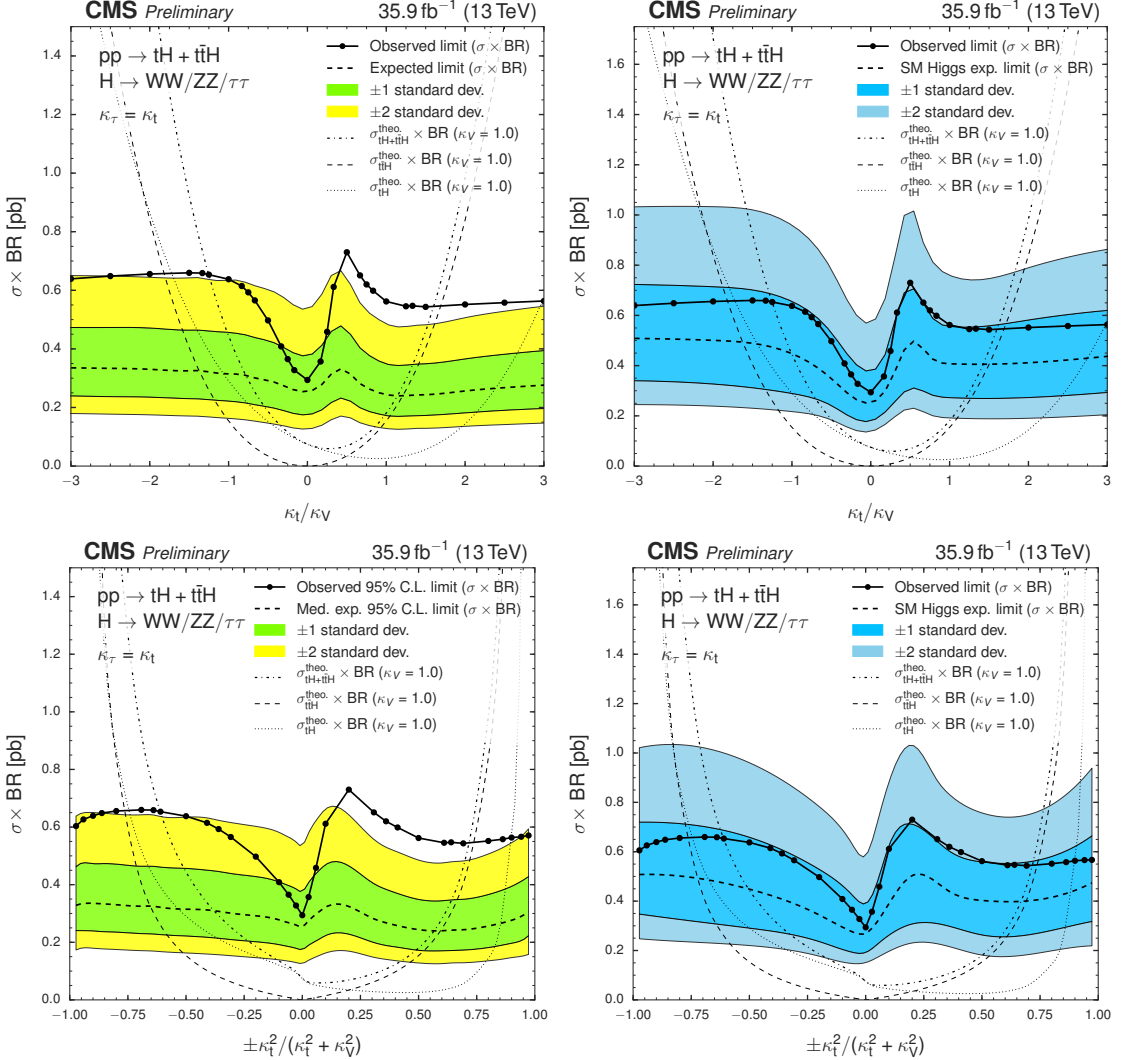


Figure 6.34: Left (Right): Expected background-only (SM-like including $t\bar{t}H$ and tH signals) and observed asymptotic limits on the combined $tH + t\bar{t}H$ cross section times modified BR as a function of κ_t/κ_V (top) and $\text{sign}(\kappa_t/\kappa_V) \times \frac{\kappa_t^2}{(\kappa_t^2 + \kappa_V^2)}$ (bottom) for the combination of three lepton channel, $\mu^\pm\mu^\pm$, and $e^\pm\mu^\pm$ channel.

3255 deviation of the observed limit from the expected one is much smaller than 1σ ; this is
 3256 consistent with the results presented in Reference [149]. It is also evident that, given
 3257 the dependence of the $t\bar{t}H$ cross section on κ_t^2 , the source of the asymmetry in both,
 3258 background-only and SM-like, limits is induced by the tH component of the signal.

3259 Comparing the observed upper limit with the theoretical prediction of the $tH +$

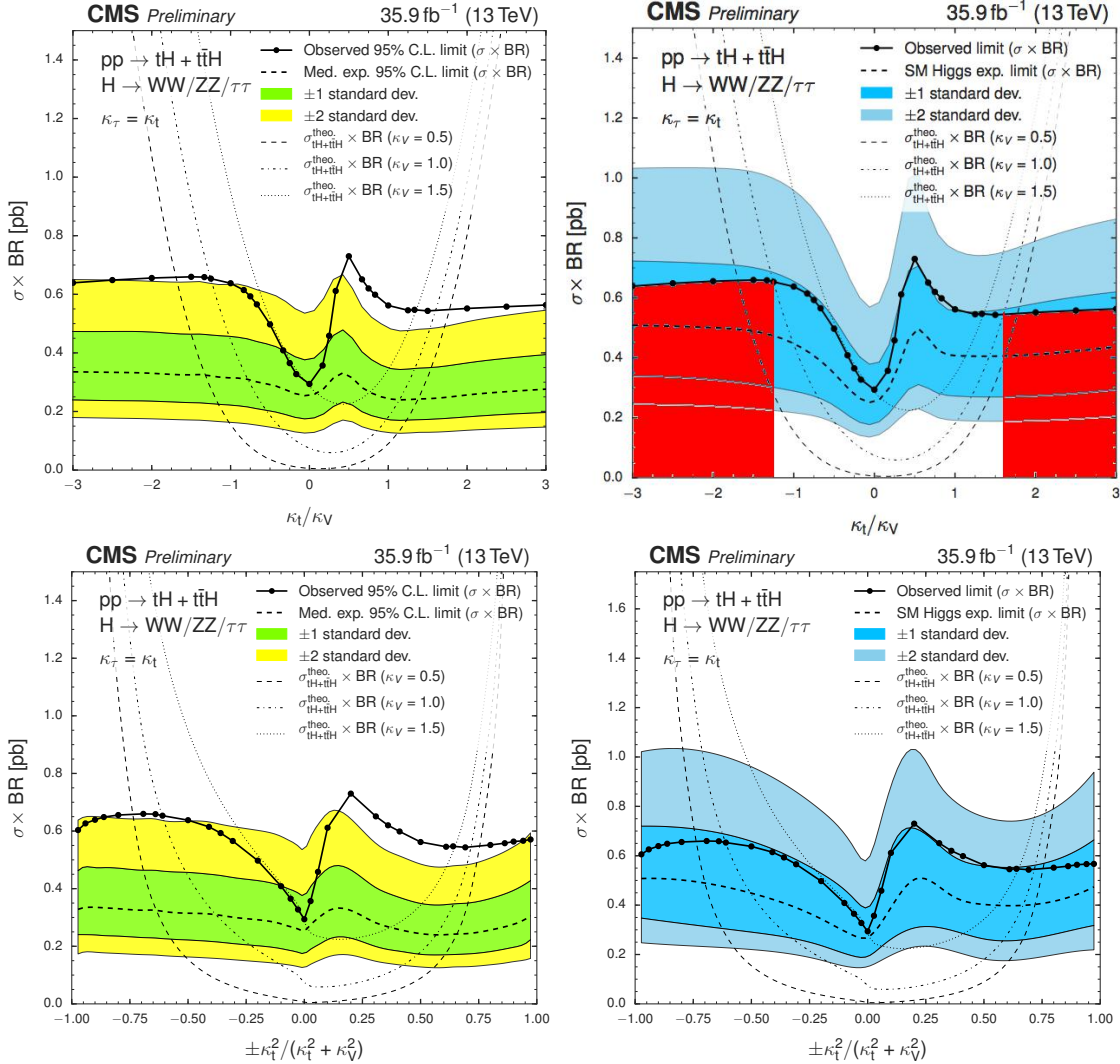


Figure 6.35: Left (Right): Expected background-only (SM-like including $t\bar{t}H$ and tH signals) and observed asymptotic limits on the combined $tH + t\bar{t}H$ cross section times modified BR as a function of κ_t/κ_V (top) and $\text{sign}(\kappa_t/\kappa_V) \times \frac{\kappa_t^2}{(\kappa_t^2 + \kappa_V^2)}$ (bottom) for the combination of three lepton channel, $\mu^\pm \mu^\pm$, and $e^\pm \mu^\pm$ channel. Theoretical $tH + t\bar{t}H$ cross section curves have been included for $\kappa_V = 0.5, 1.0, 1.5$. Red areas on the top right plot correspond to the excluded regions.

3260 $t\bar{t}H$ cross section times BR for $\kappa_V = 1.0$ constrains the allowed range of coupling
 3261 configurations κ_t/κ_V to between about -1.25 and +1.60. as shown in the top right
 3262 plot in Figure 6.35.

3263 The observed limit of about 0.64 pb on a signal shape expected for $\kappa_t/\kappa_V = -1.0$

Scenario	Channel	Obs. Limit (pb)	Exp. Limit (pb)		
			Median	$\pm 1\sigma$	$\pm 2\sigma$
$\kappa_t/\kappa_V = -1$	$\mu^\pm \mu^\pm$	1.00	0.58	[0.42, 0.83]	[0.31, 1.15]
	$e^\pm \mu^\pm$	0.84	0.54	[0.39, 0.76]	[0.29, 1.03]
	$\ell\ell\ell$	0.70	0.38	[0.26, 0.56]	[0.19, 0.79]
	Combined	0.64	0.32	[0.22, 0.46]	[0.16, 0.64]
$\kappa_t/\kappa_V = 1$ (SM-like)	$\mu^\pm \mu^\pm$	0.87	0.41	[0.29, 0.58]	[0.22, 0.82]
	$e^\pm \mu^\pm$	0.59	0.37	[0.26, 0.53]	[0.20, 0.73]
	$\ell\ell\ell$	0.54	0.31	[0.22, 0.43]	[0.16, 0.62]
	Combined	0.56	0.24	[0.17, 0.35]	[0.13, 0.49]

Table 6.21: Expected and observed 95% C.L. upper limits on the $tH + t\bar{t}H$ production cross section times $H \rightarrow WW^* + \tau\tau + ZZ^*$ branching ratio for a scenario of inverted couplings ($\kappa_t/\kappa_V = -1.0$, top rows) and for a standard-model-like signal ($\kappa_t/\kappa_V = 1.0$, bottom rows), in pb. The expected limit is calculated on a background-only Asimov dataset and quoted with $\pm 1\sigma$ and $\pm 2\sigma$ probability ranges.

Scenario	Channel	Obs. Limit	Exp. Limit				
			-2σ	-1σ	Median	$+1\sigma$	$+2\sigma$
$\kappa_V = 1.0$	$\mu^\pm \mu^\pm$	2.3	0.71	0.94	1.32	1.88	2.60
	$e^\pm \mu^\pm$	1.9	0.65	0.87	1.21	1.71	2.32
	$\ell\ell\ell$	1.6	0.43	0.59	0.86	1.26	1.78
	Combined ($\mu\mu, 3\ell$)	1.6	0.40	0.54	0.78	1.12	1.57
	Combined ($\mu\mu, e\mu, 3\ell$)	1.4	0.37	0.50	0.71	1.03	1.43
(SM)	$\mu^\pm \mu^\pm$	4.9	1.20	1.61	2.27	3.24	4.54
	$e^\pm \mu^\pm$	3.3	1.10	1.48	2.07	2.95	4.06
	$\ell\ell\ell$	3.0	0.91	1.22	1.73	2.49	3.47
	Combined ($\mu\mu, 3\ell$)	3.4	0.79	1.07	1.51	2.17	3.01
	Combined ($\mu\mu, e\mu, 3\ell$)	3.1	0.71	0.96	1.36	1.94	2.70

Table 6.22: Expected and observed CL_S limits (at 95% C.L.) on the signal strength of combined $tH + t\bar{t}H$ production in each channel, and for different combinations of them, for a scenario with inverted couplings ($\kappa_V = 1.0$, $\kappa_t = -1.0$, top section), and for the standard model ($\kappa_V = \kappa_t = 1.0$, bottom section). Numbers are for $35.9 fb^{-1}$.

and for the combination of all three channels, corresponds to 1.4 times the expected $tH + t\bar{t}H$ cross section with $\kappa_t = -1.0$, $\kappa_V = 1.0$. In the SM scenario ($\kappa_t/\kappa_V = 1.0$), the observed upper limit on the cross section times branching ratio is 0.56 pb, corresponding to 3.1 times the expected SM cross section of $tH + t\bar{t}H$. The summary of the results for the ITC and SM-like scenarios split by channel are presented in Table

3269 6.21, whereas, the summary of the expected and observed CL_S limits (at 95% C.L.)
 3270 on the signal strength of combined $tH + t\bar{t}H$ production in each channel, and for
 3271 different combinations thereof, for the ITC and SM-like scenarios are presented in
 3272 Table 6.26.

3273 **6.13.2 Best fit**

3274 The best-fit results for the signal strength in all the 33 κ_t/κ_V configurations are also
 3275 listed in Table 6.20; the inverted top coupling (ITC) and the SM-like scenarios are
 3276 highlighted there and summarized in Table 6.23. The individual contributions from
 3277 all the channels to the best-fit signal strength for the SM-like Higgs signal are listed
 3278 in Table 6.24.

Scenario	Best fit signal strength	Best fit $\sigma \times BR$	Significance Obs.(exp.)
$\kappa_t/\kappa_V = -1.0$	0.68 ± 0.40	0.30 ± 0.18 pb	$1.70\sigma(2.51\sigma)$
$\kappa_t/\kappa_V = 1.0$	$1.82^{+0.66}_{-0.67}$	0.33 ± 0.12 pb	$2.73\sigma(1.50\sigma)$

Table 6.23: Best fit for signal strength r and corresponding best fit cross section for the combined $tH + t\bar{t}H$ cross section times modified branching ratio for the combination of all three channels, for the ITC and the SM-like scenarios.

$\ell\ell\ell$	$r = 1.44^{+0.91}_{-0.84}$
$e^\pm \mu^\pm$	$r = 1.42^{+1.06}_{-1.03}$
$\mu^\pm \mu^\pm$	$r = 2.75^{+1.22}_{-1.11}$
Combined	$r = 1.82^{+0.76}_{-0.69}$
Expected	$r = 1.00^{+0.70}_{-0.65}$

Table 6.24: Best-fit signal strengths for a SM-like Higgs signal for the individual channels.

3279 In the SM scenario, a signal strength of 1.82 is obtained which corresponds to a
 3280 cross section of 0.33 pb. The observed significance of the signal, in a background-
 3281 only hypothesis, is 2.7σ , with an a-priori expected significance of 1.5σ . For the
 3282 ITC scenario, the best fit signal strength is 0.68, corresponding to a significance

of 1.7σ (2.5σ expected); a scan of the observed and expected significances over the κ_t/κ_V configurations is shown in Fig. 6.36. Note that the fit favors a signal strength compatible with zero for a scenario with $\kappa_t = 0$ (where the $t\bar{t}H$ component vanishes).

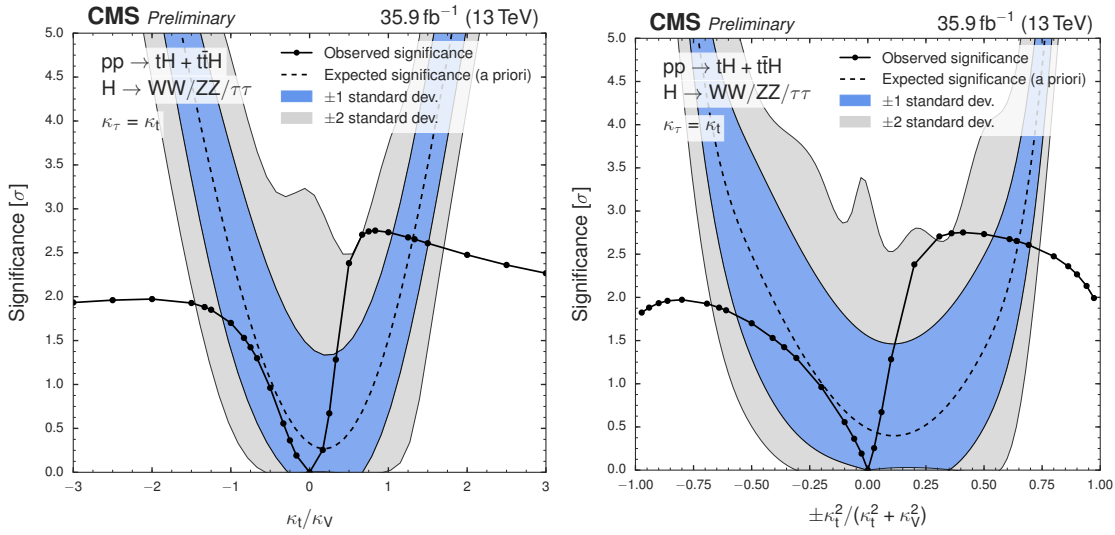


Figure 6.36: Observed and a priori expected significance of the fit result (in a background-only hypothesis) as a function of κ_t/κ_V (top) and f_t (bottom) for the combination of three lepton channel, $\mu^\pm\mu^\pm$, and $e^\pm\mu^\pm$ channel.

A scan over the best fit values of the combined cross section times modified BR is shown in Figure 6.37. The fact that the best fit signal strength at $\kappa_t = 0$, where the $t\bar{t}H$ component of the signal is zero, is compatible with zero implies that the best fit for the cross section is also compatible with zero, which again reveals that the excess in the cross section limit with respect to the expectation is not tH -like but $t\bar{t}H$ -like.

6.13.3 Effect of the nuisance parameters

The post-fit behavior of the most important nuisance parameters is presented in the pulls and impacts plots in Figures B.9, B.9 and B.9; additional pulls and impacts can be found in Appendix B.4

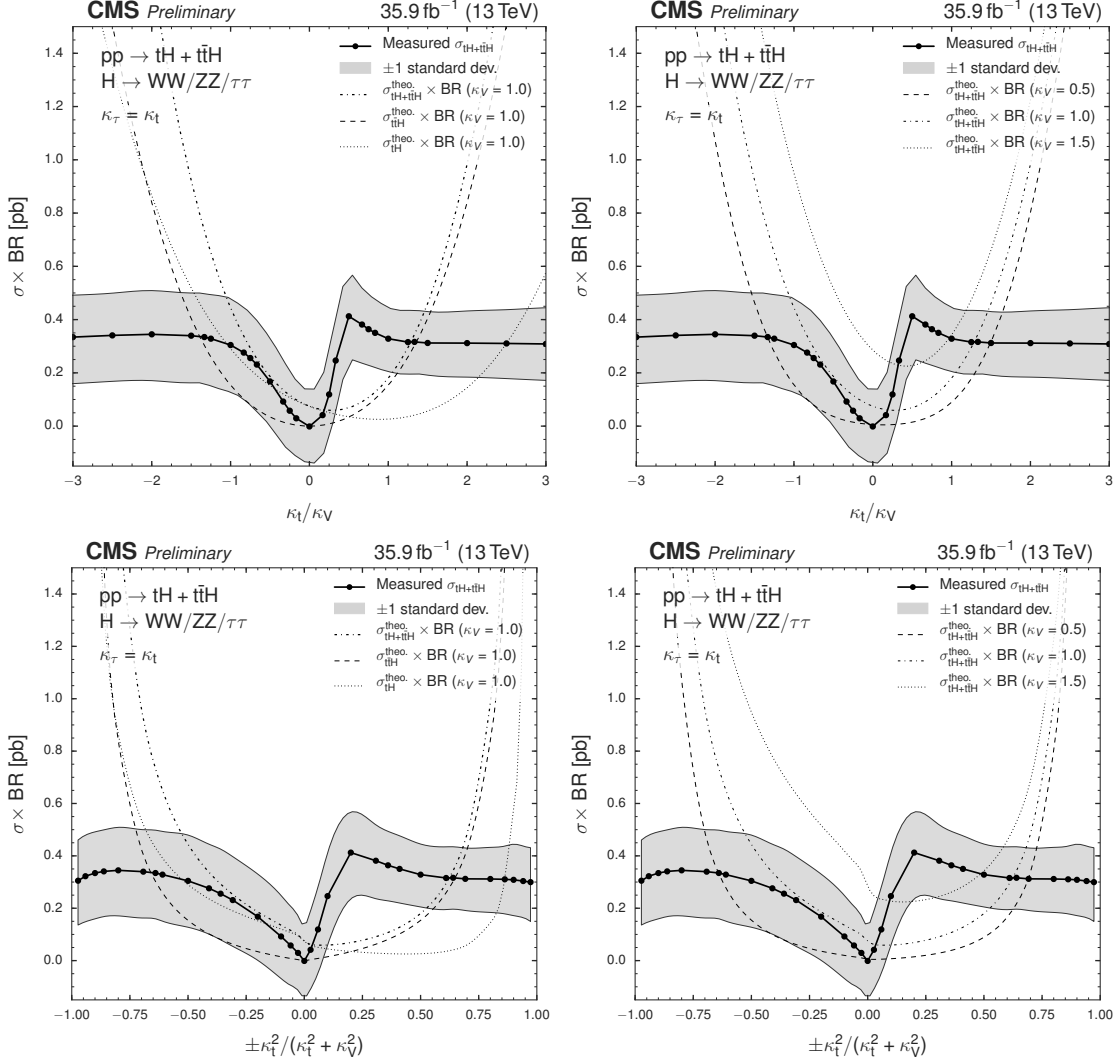


Figure 6.37: Best fit values of the combined $tH + t\bar{t}H$ cross section times modified BR as a function of κ_t/κ_V (top) and $\text{sign}(\kappa_t/\kappa_V) \times \frac{\kappa_t^2}{(\kappa_t^2 + \kappa_V^2)}$ (bottom) for the combination of three lepton channel, $\mu^\pm\mu^\pm$, and $e^\pm\mu^\pm$ channel.

3295 Most of the nuisance parameters stay close to their initial values. The biggest
 3296 impact on the signal strength limits is associated to the fake rates for muons, followed
 3297 by the lepton efficiencies and nuisances associated to the QCD scales. The lower
 3298 impact in the ITC scenario is associated to the b-tag and tHq closure normalization
 3299 and shape nuisances, while in the SM scenario, nuisances associated to the forward
 3300 jet in tHq and P.D.F.s have the lower impact in the signal strength limit .

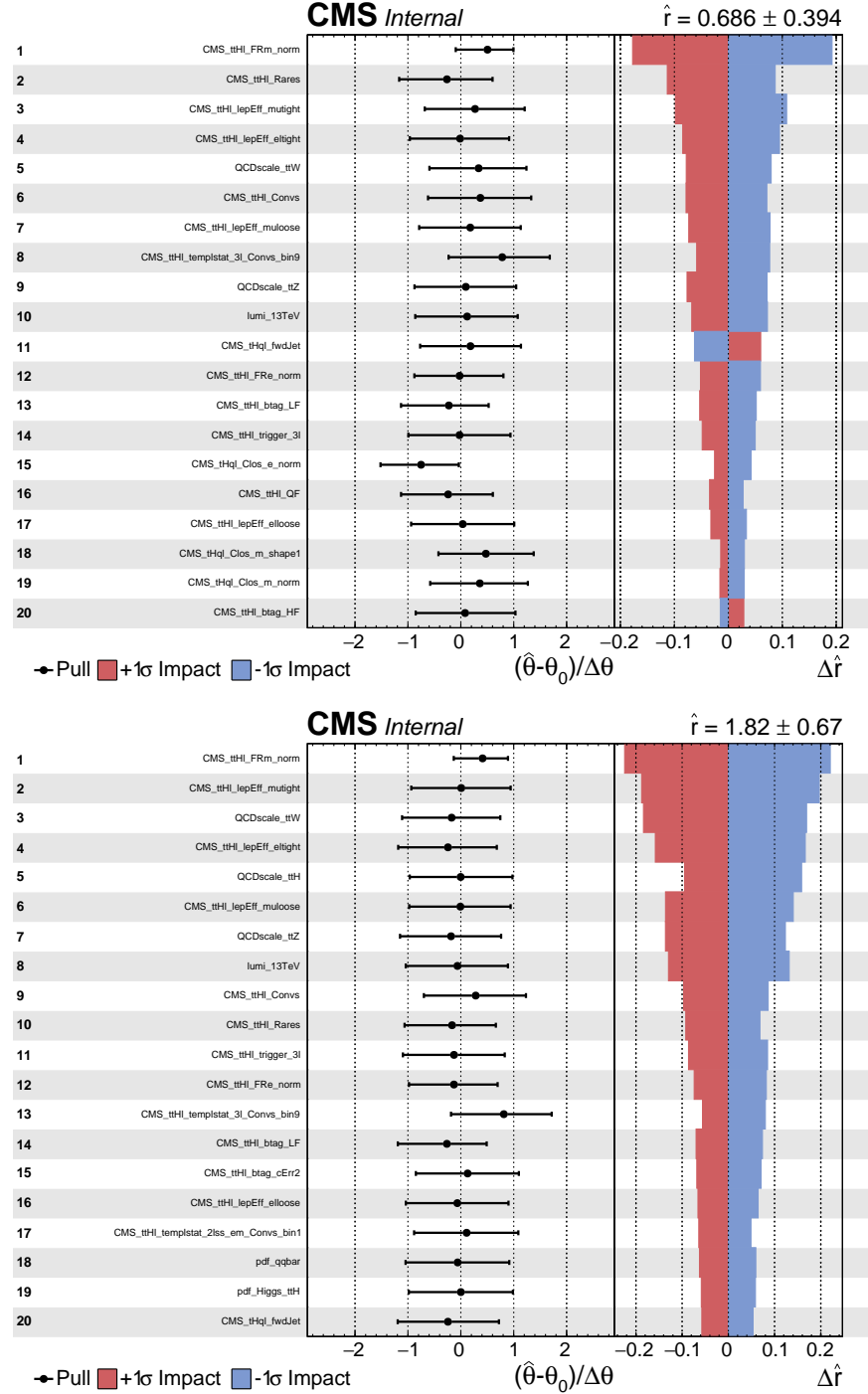


Figure 6.38: Post-fit pulls and impacts of the 20 nuisance parameters with largest impacts for the fit on the observed data, for the ITC (top) and SM (bottom) hypotheses.

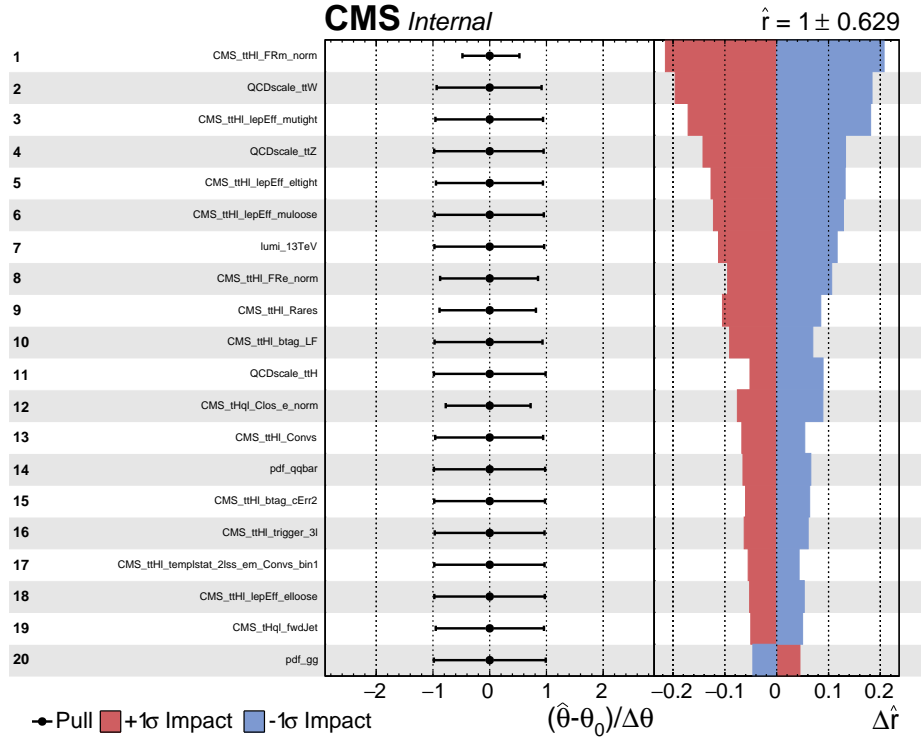


Figure 6.39: Post-fit pulls and impacts of the 20 nuisance parameters with largest impacts for a fit to the Asimov dataset with fixed signal strength, for the $\kappa_t/\kappa_V = -1.0$ hypothesis.

The sensitivity of the analysis is limited by systematic uncertainties, predominantly by those concerning the normalizations of the main background components, i.e., the non-prompt lepton estimation, the scale uncertainties for $t\bar{t}W$ and $t\bar{t}Z$, as well as by the uncertainties on the measured lepton efficiency.

3305 6.14 CP-mixing in tHq

3306 The sensitivity of the tH production process to the CP-mixing in the Higgs boson
 3307 sector was explored in Section 1.6; the theoretical model postulates the existence of a
 3308 generic spin-0 particle X_0 with CP-symmetry violating interaction with the top quark
 3309 but SM-like interaction with the W boson.

3310 The LHE reweighting procedure used in the ITC analysis is used in this CP-

$\cos(\alpha_{CP})$	Cross section (pb)		
	tHq	tHW	$t\bar{t}H$
-1.0	$0.794^{+2.8}_{-4.0}$	$0.146^{+0.2}_{-0.2}$	0.503
-0.9	$0.728^{+2.7}_{-4.1}$	$0.135^{+0.2}_{-0.2}$	0.426
-0.8	$0.664^{+2.7}_{-4.2}$	$0.123^{+0.2}_{-0.2}$	0.356
-0.7	$0.601^{+2.8}_{-4.0}$	$0.112^{+0.2}_{-0.2}$	0.296
-0.6	$0.546^{+2.9}_{-4.3}$	$0.102^{+0.2}_{-0.2}$	0.242
-0.5	$0.497^{+3.1}_{-4.2}$	$0.092^{+0.2}_{-0.2}$	0.198
-0.4	$0.446^{+3.1}_{-4.5}$	$0.083^{+0.2}_{-0.2}$	0.160
-0.3	$0.398^{+3.2}_{-4.6}$	$0.074^{+0.2}_{-0.2}$	0.132
-0.2	$0.353^{+3.5}_{-4.8}$	$0.066^{+0.2}_{-0.2}$	0.112
-0.1	$0.314^{+3.7}_{-4.9}$	$0.059^{+0.2}_{-0.2}$	0.100
0.0	$0.275^{+3.6}_{-5.2}$	$0.052^{+0.2}_{-0.2}$	0.095
0.1	$0.242^{+4.0}_{-5.5}$	$0.045^{+0.2}_{-0.2}$	0.100
0.2	$0.211^{+4.1}_{-5.8}$	$0.040^{+0.2}_{-0.2}$	0.112
0.3	$0.182^{+4.1}_{-6.1}$	$0.035^{+0.2}_{-0.2}$	0.132
0.4	$0.156^{+4.4}_{-6.5}$	$0.030^{+0.2}_{-0.2}$	0.160
0.5	$0.134^{+4.5}_{-6.6}$	$0.026^{+0.2}_{-0.2}$	0.198
0.6	$0.116^{+4.7}_{-6.9}$	$0.023^{+0.2}_{-0.2}$	0.242
0.7	$0.100^{+5.0}_{-7.1}$	$0.020^{+0.2}_{-0.2}$	0.296
0.8	$0.087^{+4.8}_{-7.1}$	$0.018^{+0.2}_{-0.2}$	0.357
0.9	$0.077^{+4.7}_{-7.0}$	$0.017^{+0.2}_{-0.2}$	0.426
1.0	$0.071^{+4.2}_{-6.7}$	$0.016^{+0.2}_{-0.2}$	0.503

Table 6.25: Production cross sections for tHq , tHW and $t\bar{t}H$ at $\sqrt{s} = 13$ TeV, as a function of $\cos(\alpha_{CP})$. Uncertainties on the cross section are based on scale variations and given in %. The used $t\bar{t}H$ NLO cross sections are provided by the authors of Reference [47] and are interpolated to the angles for which the LHE weights in the signal MC samples are available.

mixing analysis; thus, a tX_0q simulation sample was produced, containing 21 event weights for different CP-mixing angles (α_{CP}) ranging from values of $\cos(\alpha_{CP}) = 1$ to $\cos(\alpha_{CP}) = -1$ in steps of 0.1. The extremes of that range correspond to the previously studied points SM ($\kappa_t = 1$) and the ITC ($\kappa_t = -1$). The sample was produced at LO with MadGraph5_aMCatNLO, requiring the leptonic decay of the top quark. The tHq , tHW , and $t\bar{t}H$ cross sections are scaled to their NLO prediction and are listed in Table 6.25. The shape variations of the $t\bar{t}H$ process with $\cos(\alpha_{CP})$ are expected to be negligible in the range of values studied here where the cross section contribution is dominated by tH processes; however, the production of a private $t\bar{t}H$

sample including the CP-mixing weights is ongoing so that they can be included in a future refinement of the analysis.

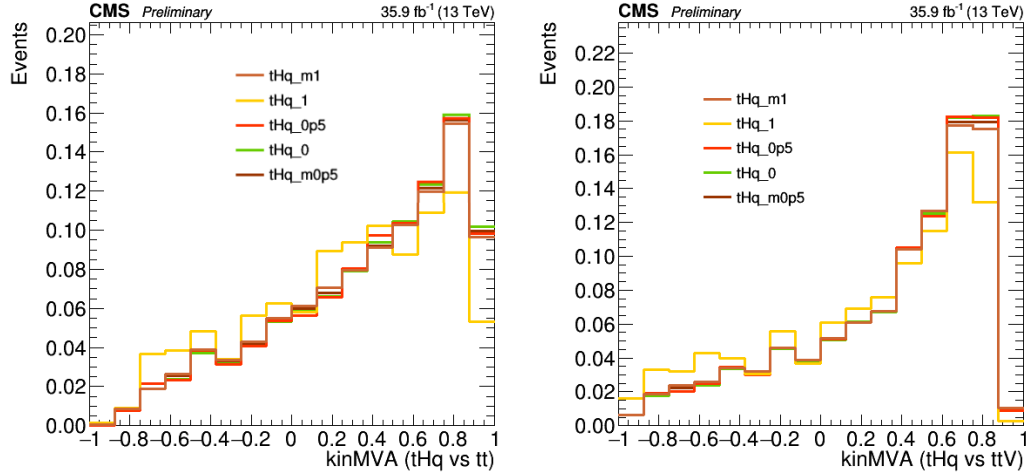


Figure 6.40: BDT shape variations for five CP-mixing angles. The trainings use the same set of input variables and samples as for the κ_t - κ_V study. Since there are no big variations between BDT output, only one training was performed.

The set of BDTG input variables and training parameters are the same as for the κ_t - κ_V analysis, as they already were optimized. Figure 6.40 shows that the shape variations for five values of $\cos(\alpha_{CP})$; since there are no significant variations, it is not necessary to perform BDT trainings for each CP-mixing angle.

After performing the simultaneous fit to the observed data for all channels, the asymptotic limits are calculated for each of the CP-mixing angles. Figure 6.41 shows the expected background-only, SM-like, and observed asymptotic Cl_S limits at 95% C.L. on the combined $tH + t\bar{t}H$ cross section times BR as a function of $\cos(\alpha_{CP})$ for the combination of the $3l$, $\mu^\pm\mu^\pm$, and $e^\pm\mu^\pm$ channels for all studied CP-mixing angles; the corresponding values are listed in Table G.7. The SM-like limits and cross section limits have been calculated on an Asimov dataset that includes SM-like tH and $t\bar{t}H$ signals.

The interpolation between estimated values was made using a cubic spline fit.

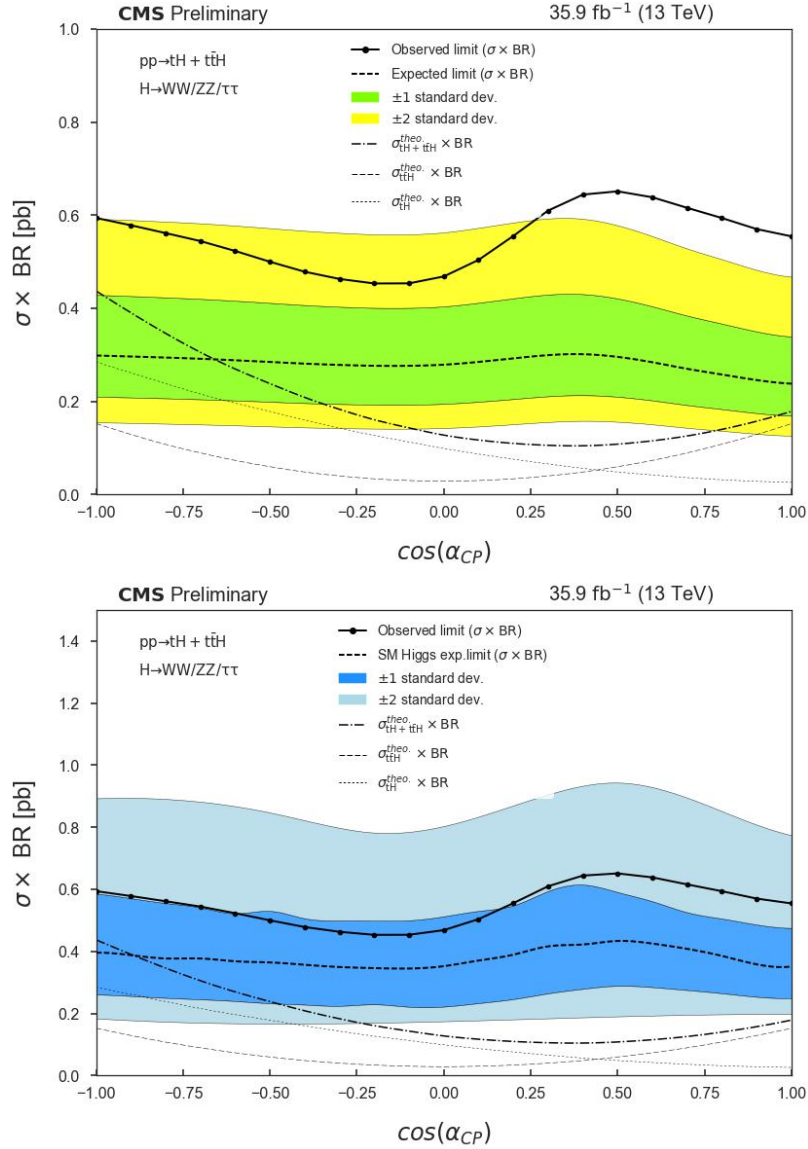


Figure 6.41: Left (Right): Expected background-only (SM-like including $t\bar{t}H$ and tH signals) and observed asymptotic limits on the combined $tH + t\bar{t}H$ cross section times BR as a function of $\cos(\alpha_{CP})$ for the combination of three lepton channel, $\mu^\pm\mu^\pm$, and $e^\pm\mu^\pm$ channel. Theoretical $tH + t\bar{t}H$ cross section curves have been included.

3335 Table 6.26 summarizes the upper limits for the ITC ($\cos(\alpha_{CP}) = -1$), SM ($\cos(\alpha_{CP}) =$
 3336 1), and fully pseudo-scalar ($\cos(\alpha_{CP}) = 0$) CP-mixing configurations.

3337 The CP-mixing limits are consistent with the limits obtained in the κ_t - κ_V anal-
 3338 ysis as expected; however, in the CP-mixing case it is not possible to exclude any

Scenario	Obs. Limit	Exp. Limit		
		Median	$\pm 1\sigma$	$\pm 2\sigma$
$\cos(\alpha_{CP}) = -1$	0.594	0.299	[0.210,0.423]	[0.155,0.592]
$\cos(\alpha_{CP}) = 1$	0.555	0.238	[0.170,0.340]	[0.126,0.470]
$\cos(\alpha_{CP}) = 0$	0.469	0.279	[0.195,0.404]	[0.143,0.563]

Table 6.26: Expected (for background only) and observed 95% C.L. upper limits (in pb), for the combined $tH + t\bar{H}$ cross section times branching ratio for the combination of all three channels, for different ITC, SM, and fully pseudo-scalar CP-mixing scenarios.

region/value in the α_{CP} phase space. The excess of more than 2σ observed in the SM scenario for the background-only expected limit, and that was also observed in the κ_t - κ_V analysis, is again reduced to about 1σ when the SM-like tH and $t\bar{H}$ signals are included in the calculation of the expectations; however, as said above, the fact that the $t\bar{H}$ sample does not include the CP-mixing weights implies that no conclusive sentence can be stated.

Finally, the best fit values of the combined $tH + t\bar{H}$ cros sections times the BR as a function of the CP-mixing angle, are showed in Figure 6.42.

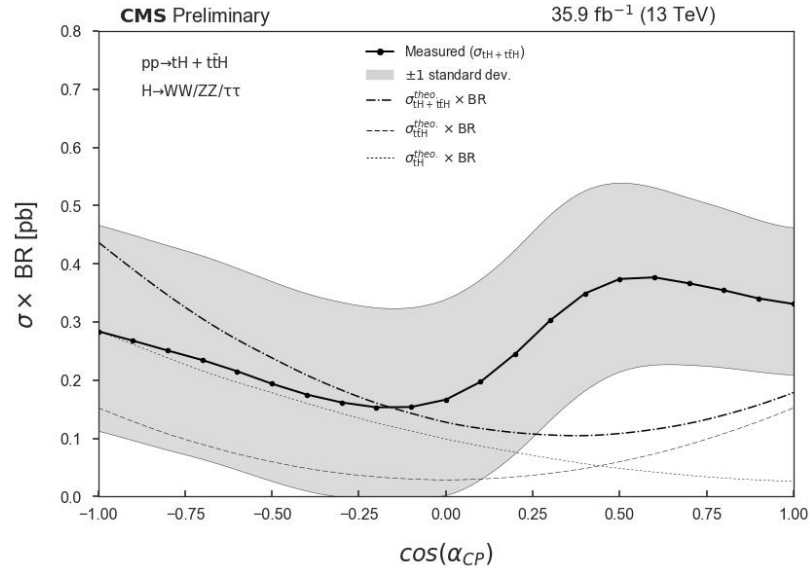


Figure 6.42: Best fit combined $tH + t\bar{H}$ $\sigma \times BR$ as a function of the CP-mixing angle, for the combination of three lepton channel, $\mu^\pm\mu^\pm$, and $e^\pm\mu^\pm$ channel. Theoretical $tH + t\bar{H}$ cross section curves have been included.

³³⁴⁷ **Chapter 7**

³³⁴⁸ **Phase 1 FPix upgrade modules**

³³⁴⁹ In chapter 2, a description of the CMS pixel detector used during the collection
³³⁵⁰ of the data sets used in this analysis, was presented. During the extended year-end
³³⁵¹ technical stop (EYETS) 2017, the complete CMS pixel detector was replaced in order
³³⁵² to support the full performance of the CMS experiment under the higher radiation
³³⁵³ conditions produced by the increasing instantaneous luminosity delivered by the LHC
³³⁵⁴ accelerator. It also was designed to address and mitigate the identified weaknesses in
³³⁵⁵ the previous system.

³³⁵⁶ In this chapter, a description of the upgraded detector will be presented. Emphasis
³³⁵⁷ will be put on the contributions made by the University of Nebraska - Lincoln (UNL)
³³⁵⁸ HEP group, which consisted of the assembly of about 600 of the modules that make
³³⁵⁹ up the phase 1 upgraded forward pixel detector (FPix); in particular, the gluing and
³³⁶⁰ encapsulation stages will be described in detail since they are my contributions. A
³³⁶¹ complete description of the upgrade design and plans is presented in Reference [?]
³³⁶² which is the main source of the information contained in this section unless additional
³³⁶³ references are provided.

3364 7.1 CMS pixel detector upgrade

3365 The previous pixel detector was designed to record efficiently and with high precision
 3366 the first three space-points near the interaction region, in the range of $|\eta| < 2.5$, at
 3367 instantaneous luminosity of $1 \times 10^{34} \text{ cm}^{-2}\text{s}^{-1}$ and a bunch crossing each 25 ns
 3368 An average pileup of about 25 simultaneous overlapping events is expected. The
 3369 increasing luminosity would affect the performance of the detector reducing track
 3370 reconstruction efficiency, and increasing the data losses caused by the degradation of
 3371 the readout system; furthermore, if the LHC runs with 50 ns bunch spacing at twice
 3372 the luminosity, then the data losses would increase almost exponentially, to losses of
 3373 50% for the innermost layer. An illustration of the foreseen reduced performance in
 3374 tracking efficiency and data loss is shown in Figure 7.1 in the case of simulated $t\bar{t}$
 3375 events at instantaneous luminosities up to $2 \times 10^{34} \text{ cm}^{-2}\text{s}^{-1}$ with 25 ns and 50 ns
 3376 bunch spacing. The increasing fake rate is also showed. In conclusion, the previous
 3377 pixel detector was not able to perform efficiently under the new luminosity, pileup,
 3378 radiation, and running conditions.

3379 The pre-trigger system is designed to offer high performance under these new oper-
 3380 ational conditions; it is composed of four-layers/three-disks, low mass silicon pixel
 3381 detectors providing a high performance tracking in the high luminosity environment.
 3382 The design was leaded by the following requirements¹

- 3383 • In running with 50 or more pile-up, maintain the high efficiencies and low fake
 3384 rates.
- 3385 • New pixel readout chip (ROC) to minimize data loss due to latencies and limited
 3386 buffering in high luminosity running.

¹ Taken literally from the technical design report.

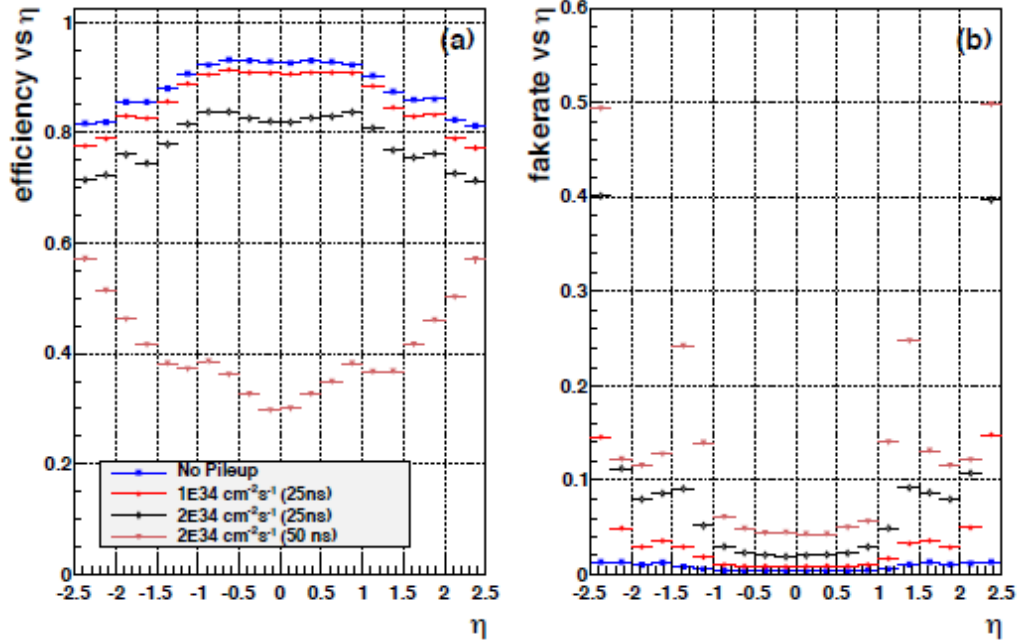


Figure 7.1: Expected performance of the previous pixel detector in simulated $t\bar{t}$ events: a) efficiency; b) fake rate. Conventions are the same for both plots, considering zero pileup (blue squares), average pileup of 25 (red dots), average pileup of 50 (black diamonds), and average pileup of 100 (magenta triangles).

- 3387 • Minimize degradation due to radiation damage.
- 3388 • Optimized detector layout for 4-pixel-hit coverage over the η range with minimal
3389 innermost layer radius improving pattern recognition and track reconstruction.
- 3390 • To reduce material, adopt two-phase CO_2 cooling and light-weight mechani-
3391 cal support, moving the electronic boards and connections out of the tracking
3392 volume.
- 3393 • To reuse the current patch panel and off-detector services, cooling pipes, cables
3394 and fibers, adopt DC-DC power converters and higher bandwidth electronics.
- 3395 • Reduce number of module types and interfaces simplifying production and main-
3396 tenance.

3397 • New smaller diameter beam pipe to accommodate the placement of the inner
 3398 pixel layer closer to the interaction region.

3399 The upgraded  detector is expected to provide higher efficiencies, lower fake rates,
 3400 lower dead-time/data-loss, and an extended lifetime of the detector, which translate
 3401 in better muon ID, b-tagging, photon/electron ID, and tau reconstruction, in both
 3402 HLT and offline levels. No details about the performance of the current pixel detector
 3403 are given here since that matter falls beyond the purpose of this document; however,
 3404 it is documented in Reference [159].

3405 Figure 7.2 shows the layout of the upgraded pixel detector. The old 3-layer barrel
 3406 (BPIX), 2-disk endcap (FPix) system is replaced with a 4-layer barrel, 3-disk endcap
 3407 system. The additional barrel layer and forward disk provide redundancy for the
 3408 track pattern recognition and reconstruction.

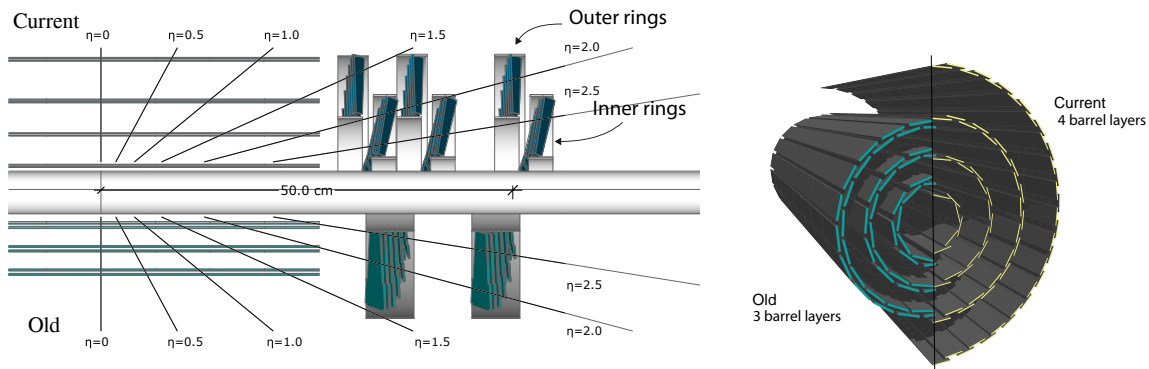


Figure 7.2: Layout and comparison of the layers and disks in the current and old pixel detectors.

3409 **7.2 Phase 1 FPix upgrade**

3410 The Phase 1 upgraded FPix system is composed of three disks in each endcap, located
 3411 at each end of the barrel detector, with a radial coverage ranging from 4.5 to 16.1

3412 cm. The first disk is located along the beam line at 29.1 cm from the IP; the second
 3413 and third disks are located at 39.6 cm and 51.6 cm from the IP; each disk consists of
 3414 two half disks. Some of the main features of the upgraded FPix System are:

- 3415 • Pixel size: $100 \times 150 \mu\text{m}$
- 3416 • Only one type of modules: 2x8 ROC modules
- 3417 • Modules oriented radially to improve resolution in $r - \phi$.
- 3418 • Minimize the gap in 4-hit coverage between the end of the 4th-barrel layer and
 the forward-most disk.
- 3420 • All three identical disks on each side of the IP.

3421 Figure 7.3 shows a schematic structure of the FPix half disk; each half disk is
 3422 composed of two sections, inner and outer, where the pixel modules are assembled.

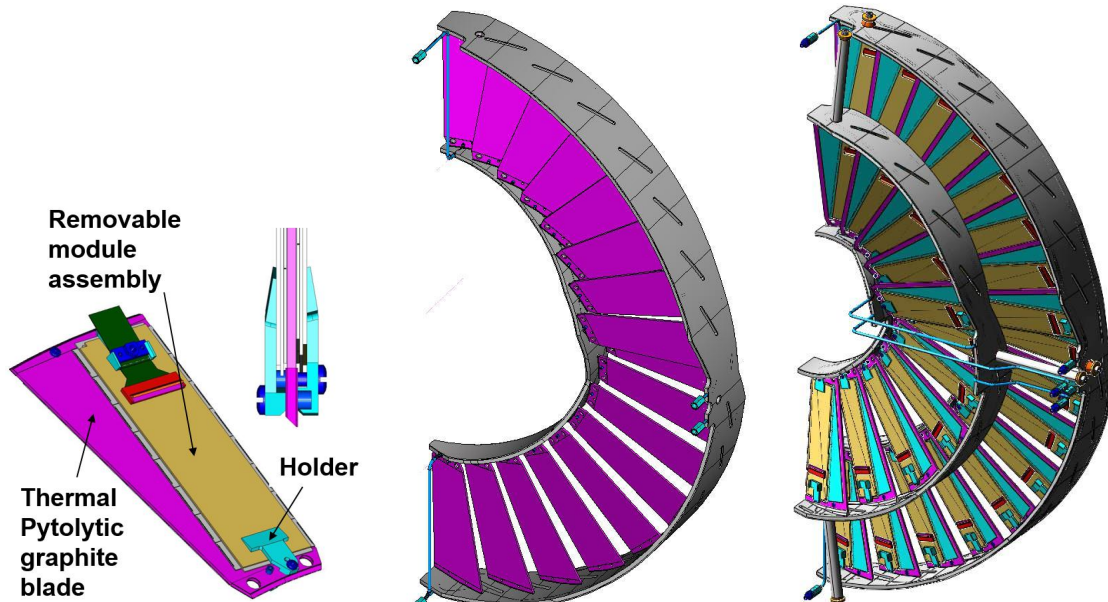


Figure 7.3: FPix half disk design; FPix module (left) mounted on a blade, outer half disk (center), assembled half disk (right).

3423 In total, there are 56 modules (896 ROCs) per half-disk, 34 modules in the outer
 3424 ring and 22 modules in the inner ring. The pixel modules are attached to the blades
 3425 by a pair of module holders. Modules are designed to be removable and replace-
 3426 able without disassembling the half-disks; thus those modules that suffer failure or
 3427 degradation can be easily replaced during an annual tech stop.

3428 Blades on the outer assembly are rotated by 20° forming a turbine-like geometry;
 3429 in addition, they are arranged in an inverted cone array with the blades tilted by 12°
 3430 with respect to the IP in order to guarantee excellent resolution in both the azimuthal
 3431 and radial directions throughout the FPIX acceptance angle for the inner assembly.

3432 7.3 FPix module structure

3433 The current CMS pixel detector is composed of 1184 pixel modules in the BPIX sector
 3434 with a total 79 million of pixels; the FPix sector contains 672 with approximately 45
 3435 million of pixels. Figure 7.4 shows an schematic view of the FPix modules structure.
 3436 The n^+ -in- n *Silicon sensor* is Bump-Bonded to the 16 ROC to form the detector
 3437 unit known as *Bump-Bonded Module* (BBM) with 66560 pixels. The *High Density*
 3438 *Interconnect* (HDI) is glued on top of the BBM and wirebonded to the ROCs to
 3439 provide them the required signals and power. The modules are attached to the
 3440 support structure using the end holders glued to the HDI.

3441 7.4 FPix module assembly

3442 The construction of the modules for the current FPix system was divided between
 3443 two sites located at Purdue University and ; testing facilities were located at
 3444 University of Kansas and Fermi National Accelerator Laboratory (Fermilab). The

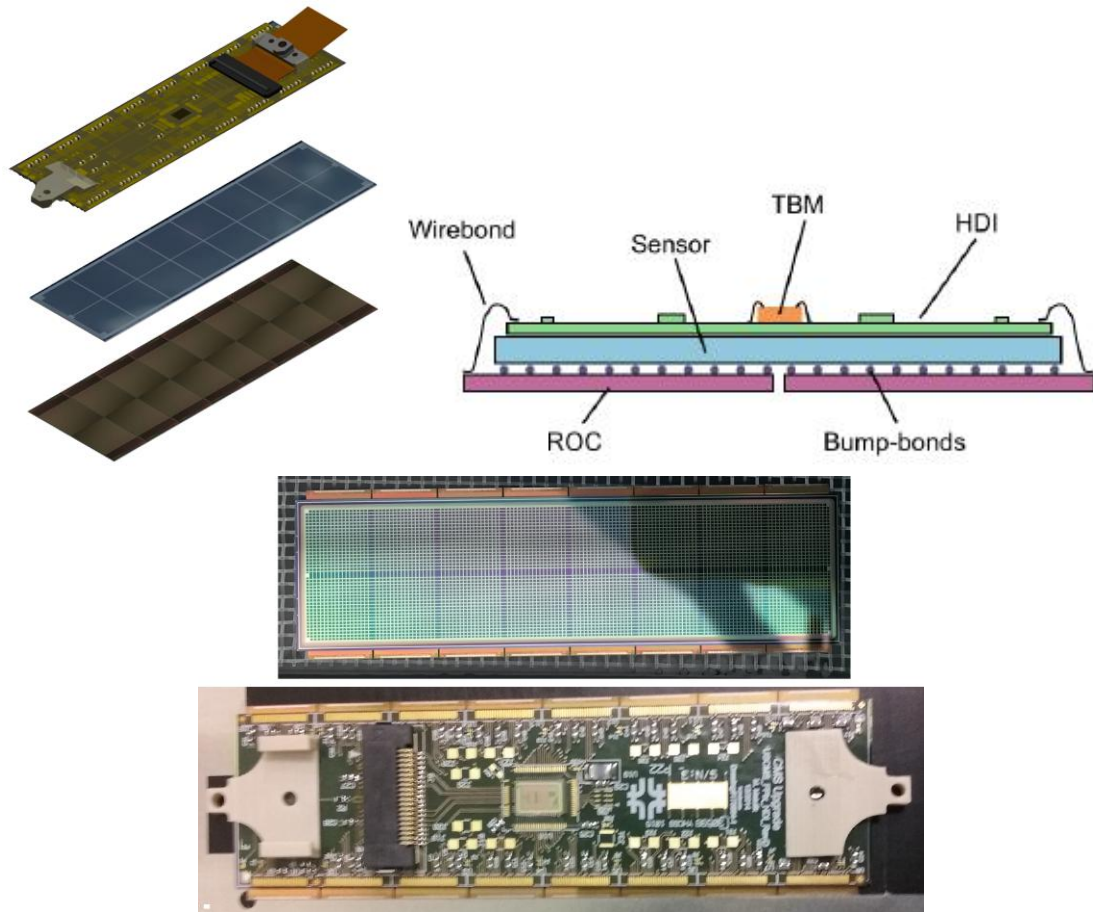


Figure 7.4: Top: FPix module structure; The bare silicon sensor is bump-bonded to the ROCs to form the BBM; then the HDI is glued on top of the BBM and wirebonded to the ROCs. Bottom: pictures of actual BBM and HDI.

3445 integration facility was based at Fermilab.

3446 The BBM was prepared by a commercial vendor, while the HDI was populated at
 3447 Fermilab, with all the electronic components like resistors, capacitors and the central
 3448 component known as *Token Bit Manager* (TBM) which is in charge of managing the
 3449 information coming from the silicon sensors and going to the ROCs. Both BBM and
 3450 HDI were sent to the assembly sites ready to be glued together.

3451 The module production procedure was designed following a production line struc-
 3452 ture. Figure 7.5 shows the work flow followed at the UNL assembly site. Once the

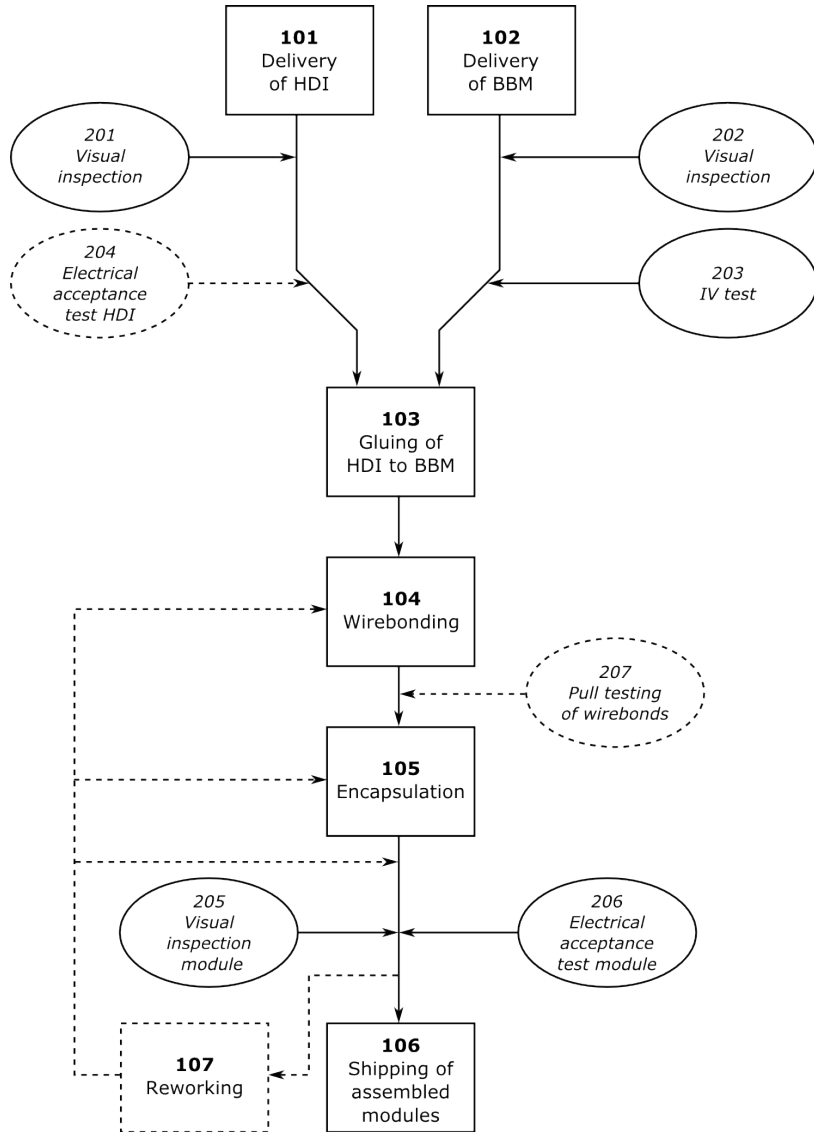


Figure 7.5: UNL module assembly work flow. Dashed lines represent occasional quality testing and reworking procedures; 10X numbers represent the stage within the assembly procedure while 20X numbers represent testing stages along the assembly procedure.

3453 BBM and HDI arrive, they are submitted to visual inspection looking for defects,
 3454 scratches, dents or short circuits. Modules passing the visual inspection are tested
 3455 for electrical acceptance and performance. BBM and HDI are then glued employ-
 3456 ing robotic pick-and-place mach**in**s that integ**ate** optic tools, pattern recognition
 3457 algorithms, and glue dispensing; the semi-automated gluing process improves the

3458 uniformity of the technique. After 10 hours of curing, glued modules are moved to
3459 the wirebonding station where ROCs and HDI are electrically connected employing
3460 semi-automated ultrasonic wirebonding machines; occasionally, some of the wires are
3461 pull tested for quality control. After this step, modules are fully functional, hence, a
3462 basic functionality test is done at a subset of modules to control the manufacturing
3463 process.

3464 In the next stage, the wirebonds are encapsulated with an elastomeric compound
3465 (*Sylgard*) in order to protect them against mechanical damage and electrical shorts;
3466 the encapsulation process is performed employing the robotic pick-and-place machine
3467 which also integrates the encapsulant dispensing system. Once the encapsulation
3468 ends, modules are mounted on module holders and submitted to a head cycle to cure
3469 the sylgard.

3470 The module assembly sites were also responsible for the testing and characteriza-
3471 tion of the assembled pixel modules. That testing included, visual inspection, elec-
3472 trical acceptance, performance testing under controlled temperature conditions that
3473 simulate the expected operational conditions; in case of any necessary reworking, the
3474 modules were returned to the appropriate stage.

3475 In the final stage, the assembled and tested modules were shipped to University
3476 of Kansas for further characterization.

3477 Each stage in the assembly procedure is documented with an *Standard Operat-*
3478 *ing Procedure* (SOP) document that describes the procedures to be followed by the
3479 operator. The full set of SOPs can be found in Reference [160].

3480 In the following sections a detailed description of the gluing and encapsulation
3481 stages will be presented. The full set of tools was designed by Dr. Frank Meier
3482 Aeschbacher.

3483 7.4.1 Pick and place machine setup

3484 Figure 7.6 shows the full setup used to perform the gluing and encapsulation steps.
 3485 The gantry used in the setup is a custom made *AGS15000 Series Gantry*, fabricated
 3486 by Aerotech [161], which offers translational motion in 3D ensuring coverage of any
 3487 position in the work field; in addition, rotational motion is provided in the *gantry*
 3488 *head* in the usual x-y plane (gantry table plane).

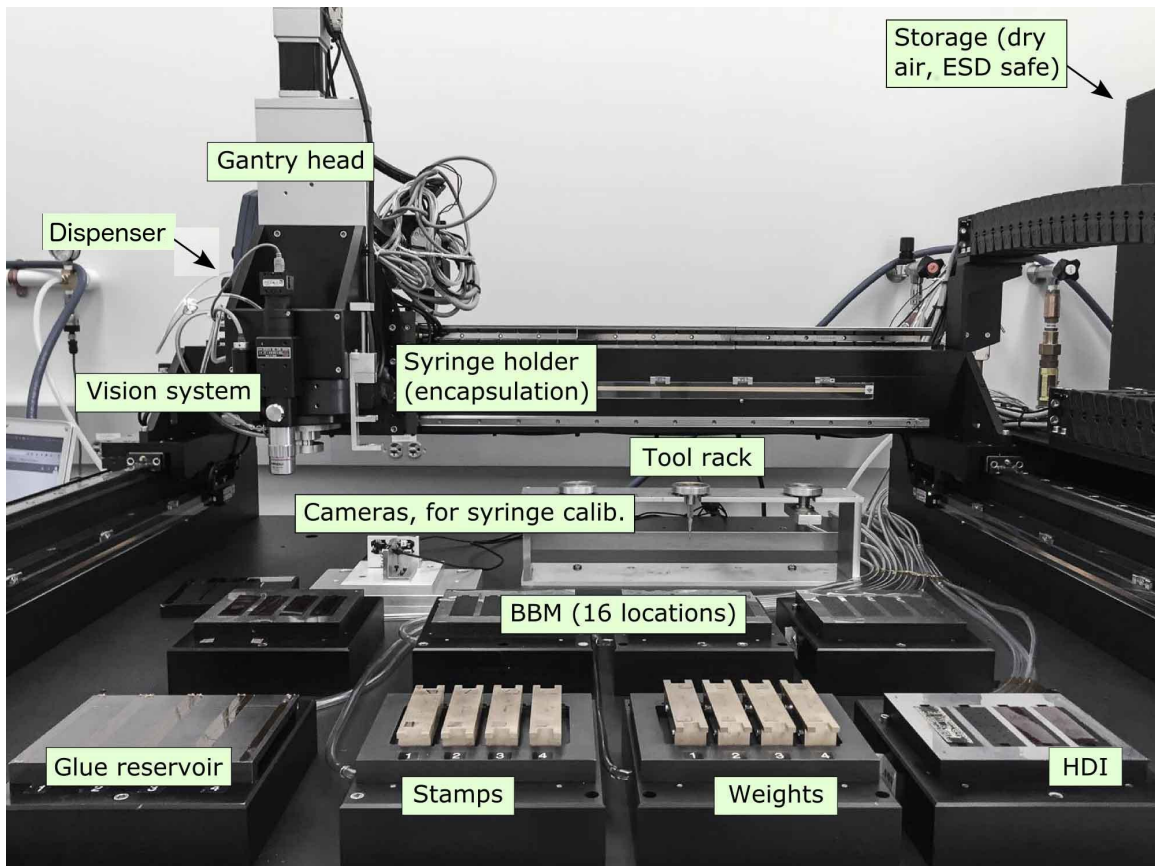


Figure 7.6: Full gluing and encapsulation setup.

3489 A set of eight hard-anodized aluminum chucks, composed of a *base chuck* and a
 3490 *plate chuck* each, henceforth chuck and plate respectively, were designed to house the
 3491 parts and tools needed along the gluing process; Figure 7.7 shows the details of a
 3492 chuck.

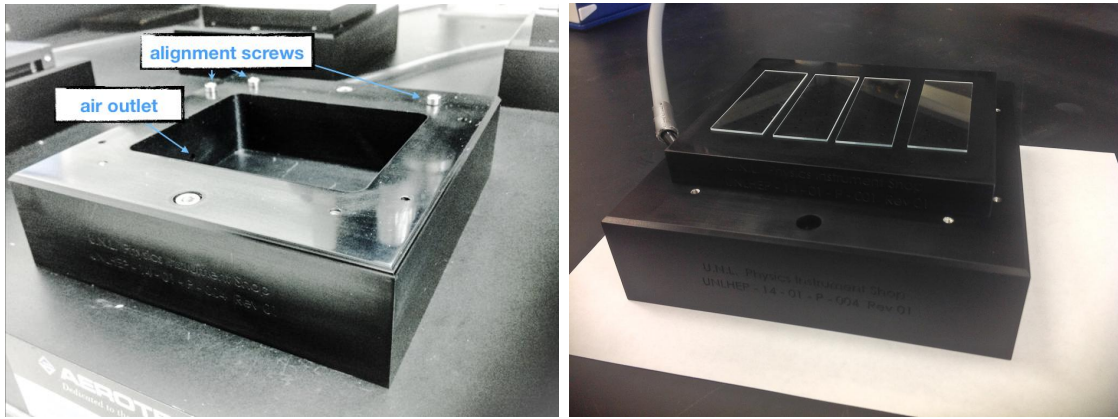


Figure 7.7: Left: Chuck detailed internal view. Right: full chuck housing glass slides. The vacuum connection is visible on the left.

3493 Each chuck is connected to an independent vacuum line such that the plate is
 3494 hold fixed; both pieces are polished to seal the vacuum with no use of O-rings. The
 3495 three screws serves as references for aligning the plates with the chucks. There are
 3496 four types of plates; HDI/BBM plate, the glue reservoir plate, stamp plate, weight
 3497 plate.

3498 Chucks

3499 Four chucks are used to accommodate sixteen BBMs (four per plate); the holes in
 3500 the BBM/HDI plate (see Figure 7.8) are intended to hold the BBM/HDI safely fixed
 3501 to the plate by the action of the vacuum, while the stencil (100 μm in thickness)
 3502 allows for a very accurate positioning of the BBM/HDI; it is thin enough that the
 3503 alignment is controlled by the edges of the ROC and no force is applied to the sensor.

3504 One chuck is dedicated to accommodate four HDIs. Although BBM/HDI plates
 3505 have the same design, the HDI chuck four independent pockets instead of only
 3506 a big one, in order to enable the release of one HDI at a time; hence, it is connected
 3507 to 4 vacuum lines. That is not required for the BBMs because they are oved
 3508 from their original location. An additional adjustment was made to the HDI plate in

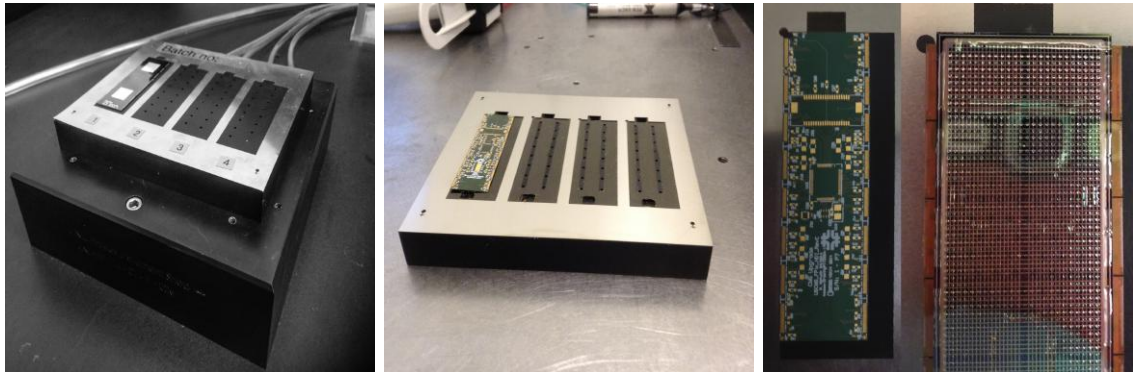


Figure 7.8: Left: BBM/HDI plate with a mock module that repro^{███} the BBM features. Center: the pockets in the top and bottom sides accommodate the module holders. Right: bare HDI and BBM showing the alignment provided by the stencil.

3509 response to the HDI back surface which is not totally flat but has irregularities; these
 3510 irregularities caused vacuum leaks that were addressed by adding a kapton tape layer
 3511 to the HDI plate, as shown in the center of Figure 7.8. The tracks ensure the vacuum
 3512 action and the tape flexibility ensures the sealing.

3513 One ch^{███} holds the *glue reservoir* plate, as shown in Figure 7.9. Each of the
 3514 four reservoirs is a pocket just 100 μm deep, suitable for retaining sufficient glue to
 3515 be applied to the BBM.



Figure 7.9: Glue reservoir plate. The four pockets are 100 μm deep.

3516 The remaining two chucks house the *stamp plate* and the *weight plate* which in

3517 turn house the *stamp tools* and the *weight tools* as shown in Figure 7.10.

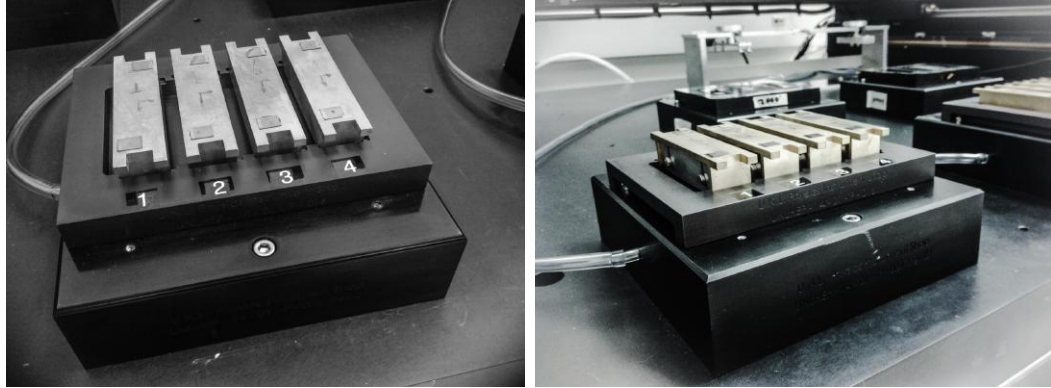


Figure 7.10: Chucks housing stamp tools(left) and weight tools(right).

3518 **Stamp and weight tools**

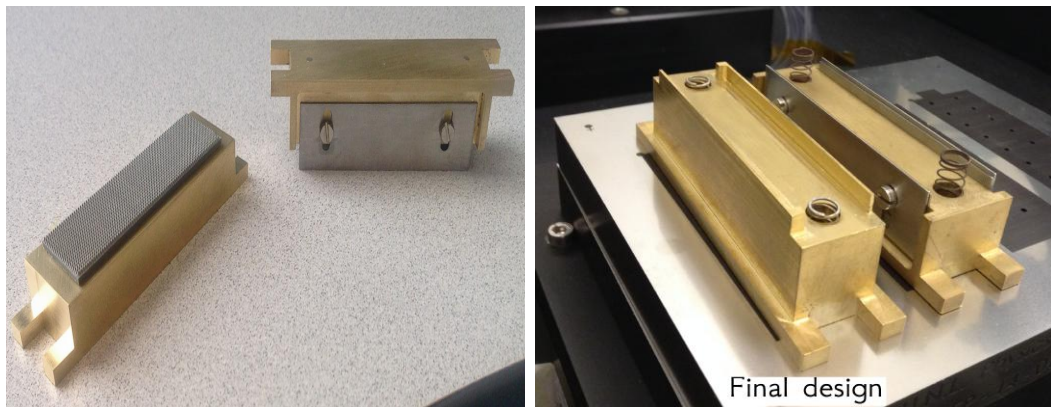


Figure 7.11: Stamp and weight tools. Both tools are made of brass; the stamp tool includes a rubber stamp while the weight tool includes four stainless steel blades to apply force while curing. The final weight tool design eliminates the blades (right).

3519 Stamp and weight tools are a set of custom made tools, all produced by the UNL
 3520 Physics department machine shop (see Figure 7.11). The very first design of the
 3521 weight tool included four stainless steel blades and two springs; the blades matched
 3522 the rows of 8 ROC bond pads on the HDI to apply force while curing. The springs
 3523 apply force to the module end holders on the HDI. The final design of the tool

3524 eliminates the issues associated to the alignment of the blades, by integrating them
 3525 into the design in the form of narrow blade-like brass edges. The weight tools a 
 3526 made with 260 g of brass.

3527 The stamp tool is composed of a brass piece of 200 g and a rubber stamp piece
 3528 attached to the bottom side of the brass piece; it is used to pick the glue from the glue
 3529 reservoir and then stamp it over the BBM. An extensive testing process was performed
 3530 in order to determine the most appropriate features of the gluing strategy. Figure 7.12
 3531 shows the four stamp patterns tested and a picture of the first two attached to the
 3532 stamp tools; the variations of the stamp pattern design were based on the results
 3533 from testing for:

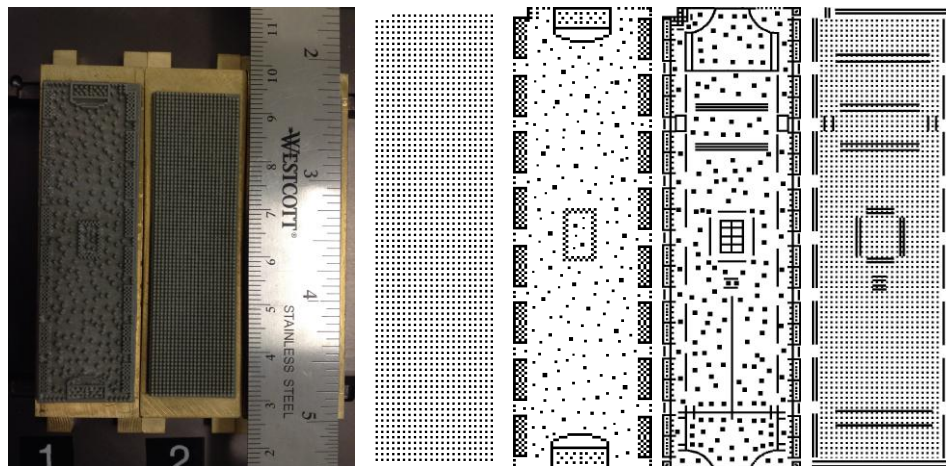


Figure 7.12: Stamp patterns evaluated along the glue testing process; the picture on the left show the first two versions mounted on the stamp tool while the final version is on the right.

3534 • *the amount of glue dispensed*, and in particular the glue spreading out of the HDI
 3535 area. An excess of glue, scattered beyond the HDI edge would go between the
 3536 ROC and the sensor, affecting the functionality of the bump bonds connecting
 3537 them; in the case of the high voltage (HV) pad, it was observed that excess of
 3538 glue cover  the pad on the sensor, making impossible to wire it. The amount

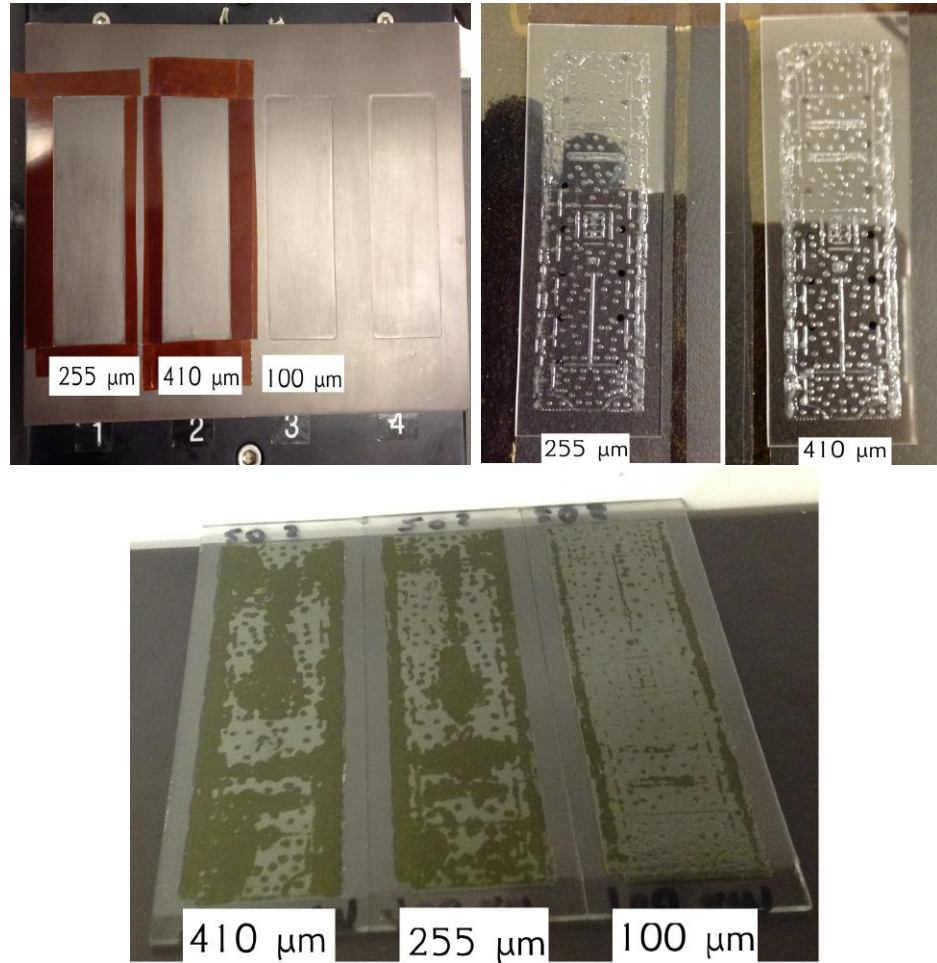


Figure 7.13: Pictures of a test of the amount of glue dispensed as a function of the glue reservoir depth. The glue reservoir depth was varied by adding kapton tape (left), and the test were conducted by gluing plain HDI on top of glass slides (middle and right.)

3539 of glue deposited on top of BBM depends on several variables: the dipping
 3540 time of the stamp tool in the glue reservoir, the time that the stamp tool is in
 3541 contact with the BBM, and the depth of the glue reservoir. In the case of the
 3542 dipping and stamping times, it was found that there is not a strong dependence
 3543 and those times were set to 10 seconds; in the case of the glue reservoir depth,
 3544 the dependence is stronger. Several glue tests where conducted by gluing plain
 3545 HDIs to glass slides; Figure 7.13 shows pictures from a glue test with three
 3546 different glue reservoir depths ($100\ \mu m$, $255\ \mu m$ and $410\ \mu m$). The results show

3547 not only that the deeper is the glue reservoir the bigger is the amount of glue
 3548 deposited, as expected, but also that the spreading out is critical for the depths
 3549 greater than 200 μm . A redesign of the rubber stamp pattern was made in
 3550 order to reduce the amount of glue deposited in the HDI pads regions; that
 3551 adjustment led to the final rubber stamp pattern.

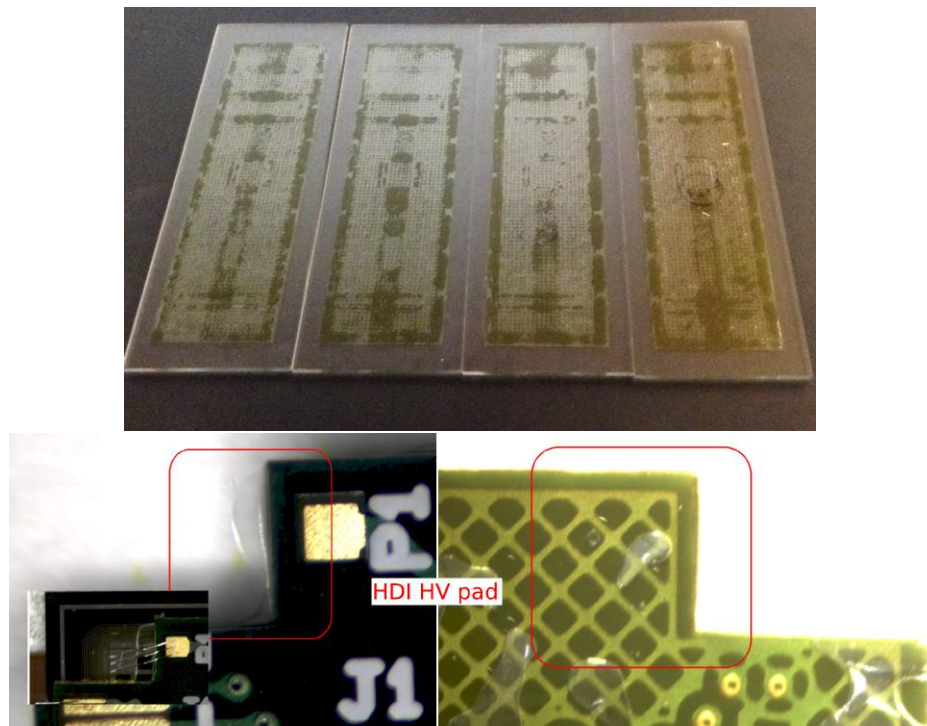


Figure 7.14: Results from a glue test using the final stamp pattern, which proves the support provided to the HDI bond pads and the HV pad and the almost null glue spreading out.

3552 • the size of contact area, and in particular the support given to the edges of the
 3553 HDI where the bond pads and the HV pad are located. This is a critical aspect,
 3554 given that the wirebonding relies on the steadiness of the pads to be connected.
 3555 Figure 7.14 shows the outcomes of a glue test using the final stamp pattern.
 3556 Note the support that it provides to the HDI bond pads and the HV pad and
 3557 the almost null glue spreading out, which justify why it was chosen.

3558 The final tools designs used during the module production are indicated in Figures
 3559 7.11 and 7.12, while the optimal glue reservoir depth was found to be $100 \mu\text{m}$.

3560 **Grabber and picker tools**

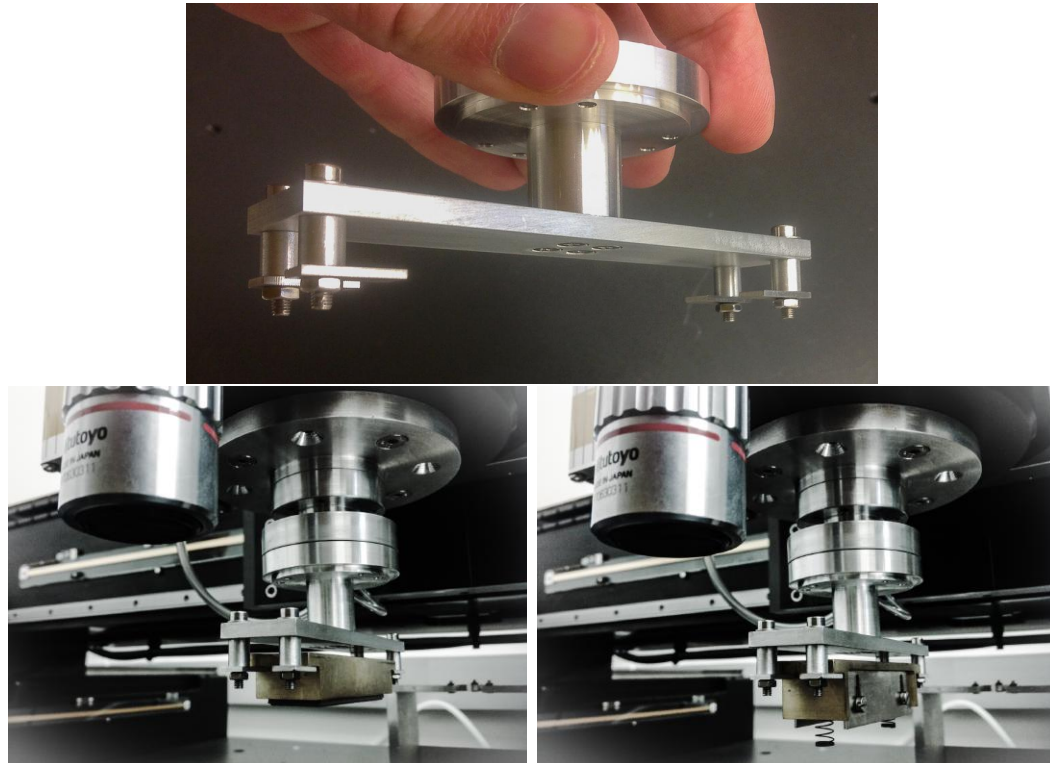


Figure 7.15: Top: Grabber tool used to grab the stamp and weight tools from their houses to the BBM location. Bottom: grabber tool holding the stamp (left) and weight (right) tools.

3561 In order to move the stamp and weight tools from their houses to the glue reservoir
 3562 and to the BBM location, a *grabber tool* was designed. The grabber tool is hold on a
 3563 tool rack located in the back of the gantry table and it gets attached to the gantry head
 3564 by using an adapter and the vacuum system as shown in Figure 7.15. The gantry head
 3565 adapter is attached to the rotary motor that provides the angular motion, therefore,
 3566 the grabber tool is able to grab the stamp and weight tools and adjust their alignment
 3567 in agreement with the BBM orientation. The force with which the glue is applied on

3568 the BBM is controlled by the weight of the brass piece; in a similar way, the force
 3569 applied to the HDI-BBM sandwich is controlled by the weight of the tool and the
 3570 springs.

3571 The pick of the HDI and place on top of the BBM is performed using the *Picker*
 3572 *tool* showed in Figure 7.16. Same as the grabber tool, the picker tool is hold at the
 3573 tool rack until the gantry head goes to its location and catch it using vacuum; an
 3574 independent vacuum line is use to capture the HDI from its chuck slot. The alignment
 is performed while the HDI is being moved to the BBM location.

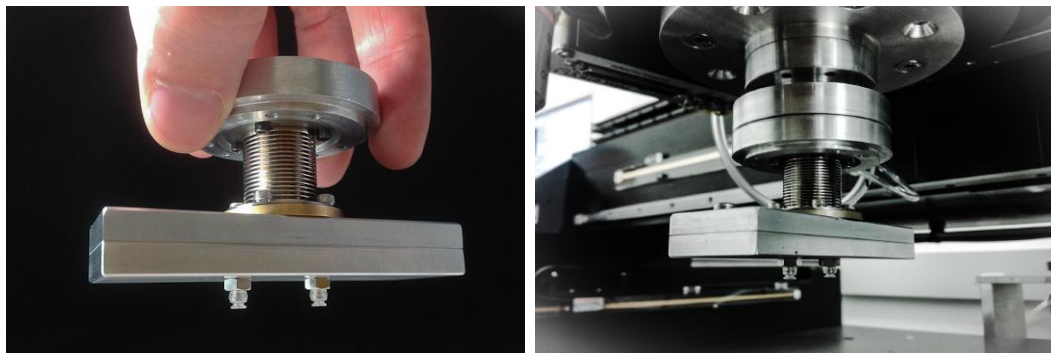


Figure 7.16: The pick and place tool, picks the HDI from its chuck and place it on top of the BBM.

3575

3576 Vision system

3577 A vision hardware system, attached to the gantry head, is used to locate the module
 3578 components and tools employed in the assembly process. It is composed of a IDS
 3579 HD digital camera and a Mitutoyo wide-field video microscope unit (WIDE VMU)
 3580 as shown in Figure 7.6. The vision hardware is complemented with auto-focus and
 3581 pattern recognition algorithms.

3582 Given that the coarse location of the HDIs, BBMs, stamp and weight tools are
 3583 well defined by the location of the stencils and plates on the gantry table, the vision
 3584 system is designed to search and find fiducial marks present on the materials and

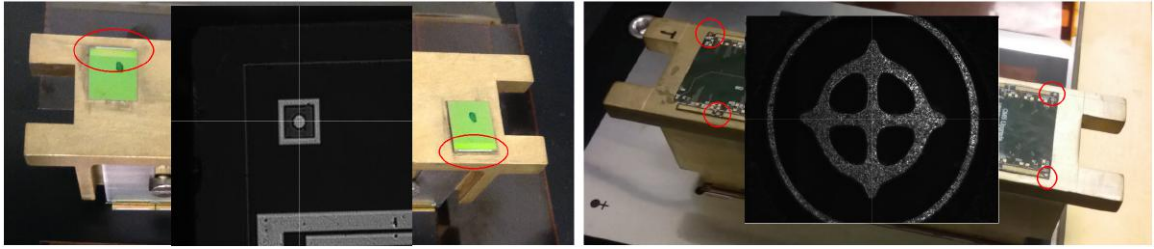


Figure 7.17: Fiducial marks attached to the stamp and weight tools. Initially, non-functional ROCs were glued on top of the tools (left) to provide the marks, located in the places indicated by red circles and shown overlapping the tool; later they were replaced by plane HDIs (right).

3585 tools; these fiducial marks are placed on the HDI and BBM during their fabrication
 3586 process. In the case of the tools, two methods were used to attach a fiducial mark
 3587 to them: non-functional ROCs, which have on themselves fiducial marks, were glued
 3588 on top of the tools as shown in Figure 7.17, however, during the gluing and cleaning
 3589 processes the fiducial marks used to be covered or broken making necessary their
 3590 replacement very often; the second method consisted of gluing plane HDIs on top of
 3591 the tools, which not only solved the issues with the destruction of the fiducial marks
 3592 but also simplified the pattern recognition.

3593 The procedure to find the fiducial marks starts by moving the camera to an initial
 3594 default calibrated position above the element, HDI, BBM or tool, such that the
 3595 image in the field of view of the camera contains the fiducial mark; then, the auto-
 3596 focus algorithm finds the best focus by measuring the contrast of pictures taken by
 3597 the camera at ten different positions in z direction around a default position where
 3598 it is assumed the best focus is; these ten contrasts are then fitted to a Gaussian
 3599 distribution where the maximum of the fitting corresponds to the best focus.

3600 Once the best focus is found, the gantry head moves the camera to that position,
 3601 takes a new picture and send it to feed the pattern recognition algorithm which
 3602 use k-means clustering to separate the foreground from the background; then, the

3603 foreground (Fiducial + noise) is dilated to close any small holes in image and to
 3604 extract contours from image.

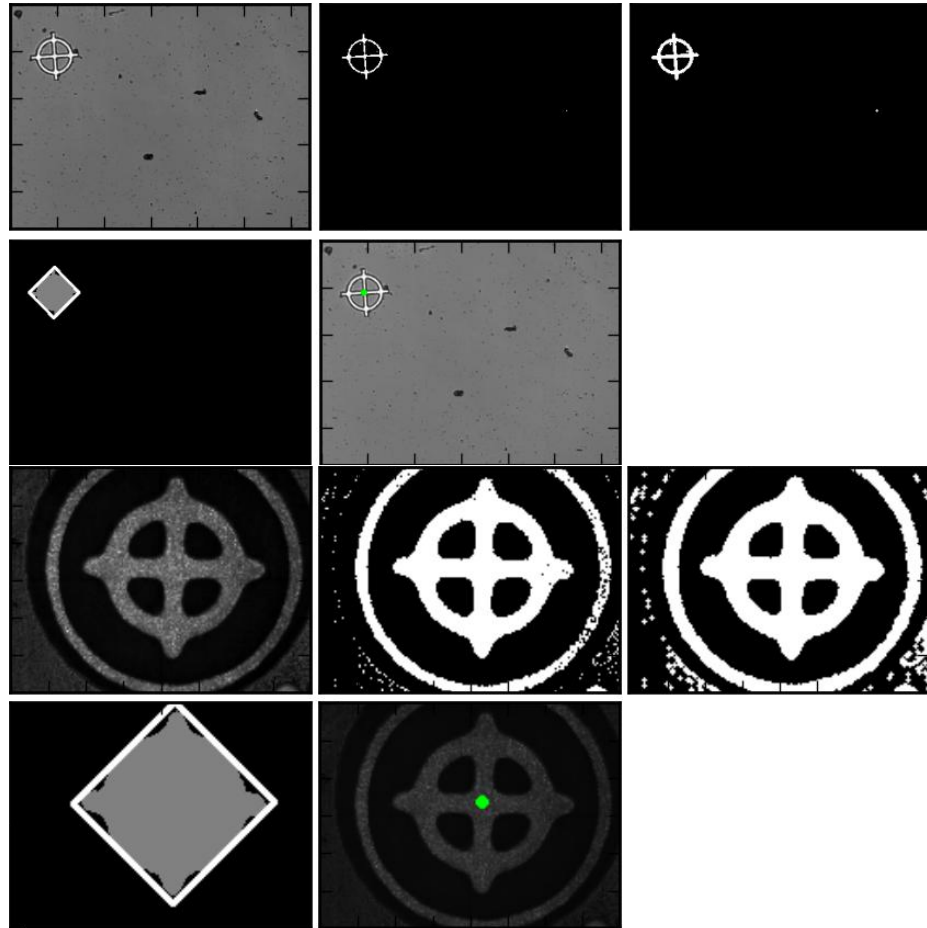


Figure 7.18: Fiducial mark recognition: BBM (two top rows) and HDI (two bottom rows). The input image is processed to define contours; after filtering, the centroid of the recognized fiducial mark is returned by the algorithm and indicated in the input image by the green dot.

3605 The fiducial mark features are parametrized in terms of its size and aspect ratio
 3606 with respect to the field of view of the camera, therefore, by filtering the contours on
 3607 size and aspect ratio it is assured that one and only one contour passes filters. Later,
 3608 the algorithm calculates the minimum bounding box and centroid of the fiducial mark
 3609 to finally return the centroid as fiducial mark center and distance between centroid
 3610 and box center as a measure of goodness. In order to reduce the processing time,

3611 the input image resolution is reduced by a factor of 8. The algorithm was written by
 3612 Caleb Fangmeier and is documented in Reference [162] from where Figure 7.18 was
 3613 taken.

3614 **Gantry head center-camera offset (GHCO)**

3615 The *global coordinate system* of the setup is centered in the so-called *home position*
 3616 located in the back-left side of the gantry table; thus, the origin of the coordinate
 3617 system is defined by the position of the gantry head center when it is placed in 
 3618 the home position. Any distance is then measured by comparing the gantry head
 3619 center position at a given location and the home position. While the tool adapter is
 3620 concentric to the gantry head (and then its coordinates are the same as the gantry),
 3621 the camera has an offset with respect to the origin of the global coordinate system
 3622 because the vision system is not located at the gantry head center, therefore, any
 3623 location provided by the vision system has to be corrected by this offset, known as
 3624 *Gantry head center-camera offset (GHCO)*.

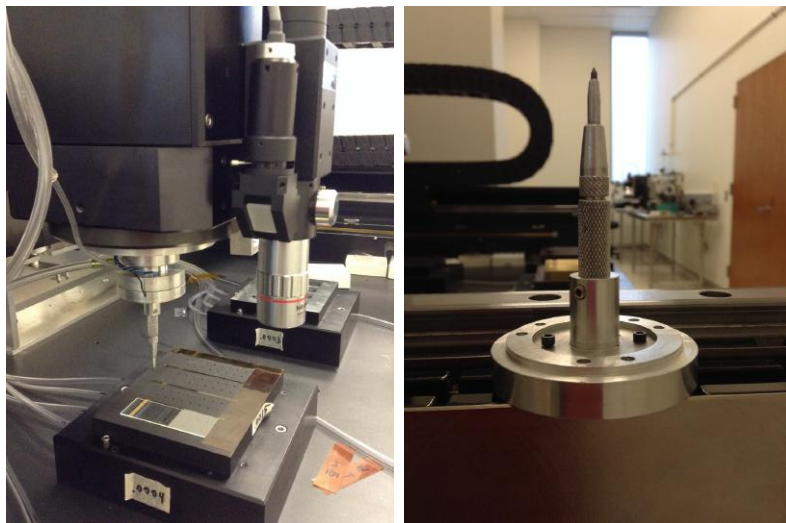


Figure 7.19: Setup used to measure the GHCO

3625 To determine the GHCO, a set of 40 marks (scratches) were made on a glass
 3626 slide using a needle shaped tool with the tip made of carbide (see Figure 7.19);
 3627 the locations of the scratches were predefined and known as commanded positions.
 3628 Later, the camera was moved to find the scratches and their locations were tagged
 3629 as observed positions. In principle, the difference between the commanded and the
 3630 observed positions provide a measurement of the GHCO, but it cannot be assumed
 3631 that the needle tool is straight, i.e., if the tip of the tool coincides with the gantry
 3632 head center; in order to take into account this fact when calculating the offset, an
 3633 scratching schema was designed; it is showed in Figure 7.20. In the ideal case the
 3634 scratch is made right in the commanded position (red circle), but if the needle is not
 3635 straight, the scratch will be shifted (black cross). A rotation of the tool can be used
 3636 to determine how bend is the needle tip.

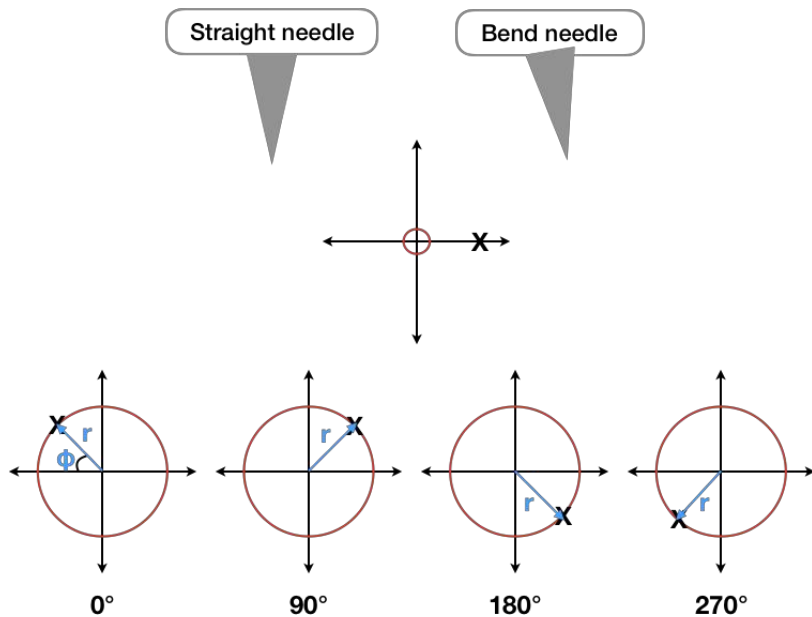


Figure 7.20: Scratches scheme if the tool is not straight

3637 The precise procedure:

- 3638 ● pick the needle tool from the tool rack,
 - 3639 ● move the gantry to the first scratch position (the commanded position),
 - 3640 ● make the scratch moving the tool down.
 - 3641 ● move the tool back up
 - 3642 ● move the gantry to the next scratch commanded position.
 - 3643 ● Repeat the process to make nine more scratches.
 - 3644 ● Rotate the tool by $\theta = 90^\circ$ and  make ten scratches.
 - 3645 ● Rotate the tool by additional 90° (now the total rotation is $\theta = 180^\circ$) and make
 - 3646 ten more scratches.
 - 3647 ● Rotate the tool by additional 90° (now the total rotation is $\theta = 270^\circ$) and make
 - 3648 ten more scratches.
 - 3649 ● Move the camera to the first scratch position and locate the center of the scratch,
 - 3650 capture the position.
 - 3651 ● Repeat the process to locate the rest of the scratches.
- 3652 The procedure is performed by a labVIEW program (*offset_fitting.vi*) which fol-
- 3653 lows the steps mentioned above automatically so that the user only interacts with the
- 3654 program by capturing the positions. The output of the program is a text file which
- 3655 contains all the commanded and observed positions.
- 3656 The set of measurements are statistically treated, using the linear least squares
- 3657 fitting technique. The model describing the location of the scratches system is
- 3658 parametrized by a linear combination of a set of functions weighted by a set of pa-
- 3659 rameters;

$$y(x) = f(y, \mathbf{a}) = a_1 f_1(x) + a_2 f_2(x) + \dots + a_p f_p(x) \quad (7.1)$$

3660 The residuals, which correspond to the difference between the predicted value
 3661 from model ($f(x_i, \mathbf{a})$) and the measured value y_i , are calculated using

$$r_i = y_i - f(x_i, \mathbf{a}), \quad (7.2)$$

3662 one want to minimize these residuals and more specifically their squares (S). The fit
 3663 will provide the values of the parameters \mathbf{a}  that the model is totally defined. In
 3664 matrix form, for a set of measurements (x, y) :

$$\mathbf{Y} = A\mathbf{a} \quad (7.3)$$

3665

$$S = \mathbf{r}^T \mathbf{r} \quad (7.4)$$

3666 The matrix A enc the features of the system/model, the vector \mathbf{a} enc the
 3667 parameters under evaluation and the vector \mathbf{Y} enc the measurements taken and
 3668 the predictions made by the model. After the minimization, the vector of parameters
 3669 can be written as:

$$\mathbf{a} = (A^T V^{-1} A)^{-1} A^T V^{-1} \mathbf{Y} \quad (7.5)$$

3670 where V is the covariance matrix; it contains the information about the correlation
 3671 among measurements and also the uncertainty of the measurements.

$$V = \begin{pmatrix} \sigma_1^2 & \sigma_{12} & \cdots & \sigma_{1n} \\ \sigma_{21} & \sigma_2^2 & \cdots & \sigma_{2n} \\ \vdots & \vdots & \ddots & \vdots \\ \sigma_{n1} & \sigma_{n2} & \cdots & \sigma_n^2 \end{pmatrix} \quad (7.6)$$

3672 The model for one measurement (x, y) , i.e. only one scratch, can be written as:

$$\begin{pmatrix} x \\ y \end{pmatrix} - \begin{pmatrix} x_g \\ y_g \end{pmatrix} = \begin{pmatrix} \Delta x_{GHCO} \\ \Delta y_{GHCO} \end{pmatrix} + \begin{pmatrix} c & s \\ -s & c \end{pmatrix} \begin{pmatrix} c' & s' \\ -s' & c' \end{pmatrix} \begin{pmatrix} 1 \\ 0 \end{pmatrix} \quad (7.7)$$

3673 where, (x_g, y_g) are the commanded positions, $(\Delta x_{GHCO}, \Delta y_{GHCO})$ are the offset com-
 3674 ponents in x, y directions respectively, $c = r \cos \phi$ and $s = r \sin \phi$, describe the bending
 3675 of the needle tool in terms of the radius r of the circle and the angle ϕ (see Figure 7.20)
 3676 and $c' = \cos \theta$ and $s' = \sin \theta$ describe the rotations of the tool ($\theta = 0^\circ, 90^\circ, 180^\circ, 270^\circ$)
 3677 with respect to the x direction.

3678 The matrix A and the vector of parameter \mathbf{a} can be written as:

$$A = \begin{pmatrix} 1 & 0 & c' & -s' \\ 0 & 1 & -s' & -c' \end{pmatrix}, \quad \mathbf{a} = \begin{pmatrix} \Delta x_{GHCO} \\ \Delta y_{GHCO} \\ c \\ s \end{pmatrix} \quad (7.8)$$

3679 The A matrix including the full set of forty pairs of measurements (x, y) is a 4×80
 3680 matrix where in the first ten rows $c' = \cos(\theta = 0) = 1, s' = \sin(\theta = 0) = 0$, while in the
 3681 second ten rows $c' = \cos(\theta = 90) = 0, s' = \sin(\theta = 90) = 1$ and so on.

3682 The offset_fitting.vi program integrates a Matlab script that solves the matrix
 3683 equation 7.5, using the commanded and observed positions measured by the vision
 3684 system; the uncertainties were assumed to be the same for all measurements and ad-

3685 ditionally it was assumed that the measurements are not correlated, so the covariance
 3686 matrix is the uncertainty ($\sigma = 0.01\mu\text{m}$) times the 80×80 identity matrix. The results
 3687 for the GHCO and the radius are:

$$\begin{aligned}\Delta x_{GHCO} &= 0.482 \pm 0.008\text{mm} \\ \Delta y_{GHCO} &= -102.362 \pm 0.008\text{mm} \\ r &= 0.042 \pm 0.007\text{mm}.\end{aligned}\tag{7.9}$$

3688 **The dispensing system**

3689 The dispensing system components are shown in Figure 7.21. The dispenser and sys-
 3690 ringe holder are attached to the gantry head as shown in Figure 7.6. The encapsulant
 3691 is a mixture of sylgard curing agent and sylgard base elastomer in a proportion 1:10;
 3692 the volumes are measured using common syringes, and the mixing is performed on
 3693 a plastic sheet. Several needle tip sizes were tested in order to optimize the amount
 3694 of sylgard dispensed in agreement with the pressure provided by the dispenser; the
 3695 needle chosen has an internal diameter of $150\ \mu\text{m}$.

3696 The encapsulation process consists of depositing a sylgard trace over the wires
 3697 connecting the HDI and the ROC; it is highly dependent not only on the ability to
 3698 measure the location of the regions to be encapsulated, which is well managed by
 3699 the vision system, but also on the ability to know with high precision the position of
 3700 the needle tip, which added to the fact that for each encapsulation session a new set
 3701 of syringe-needle has to be used, demands a robust method to locate the needle tip.

3702 The needle-tip calibration procedure was implemented using an additional vision
 3703 system composed of two regular web cameras disposed one perpendicular to each

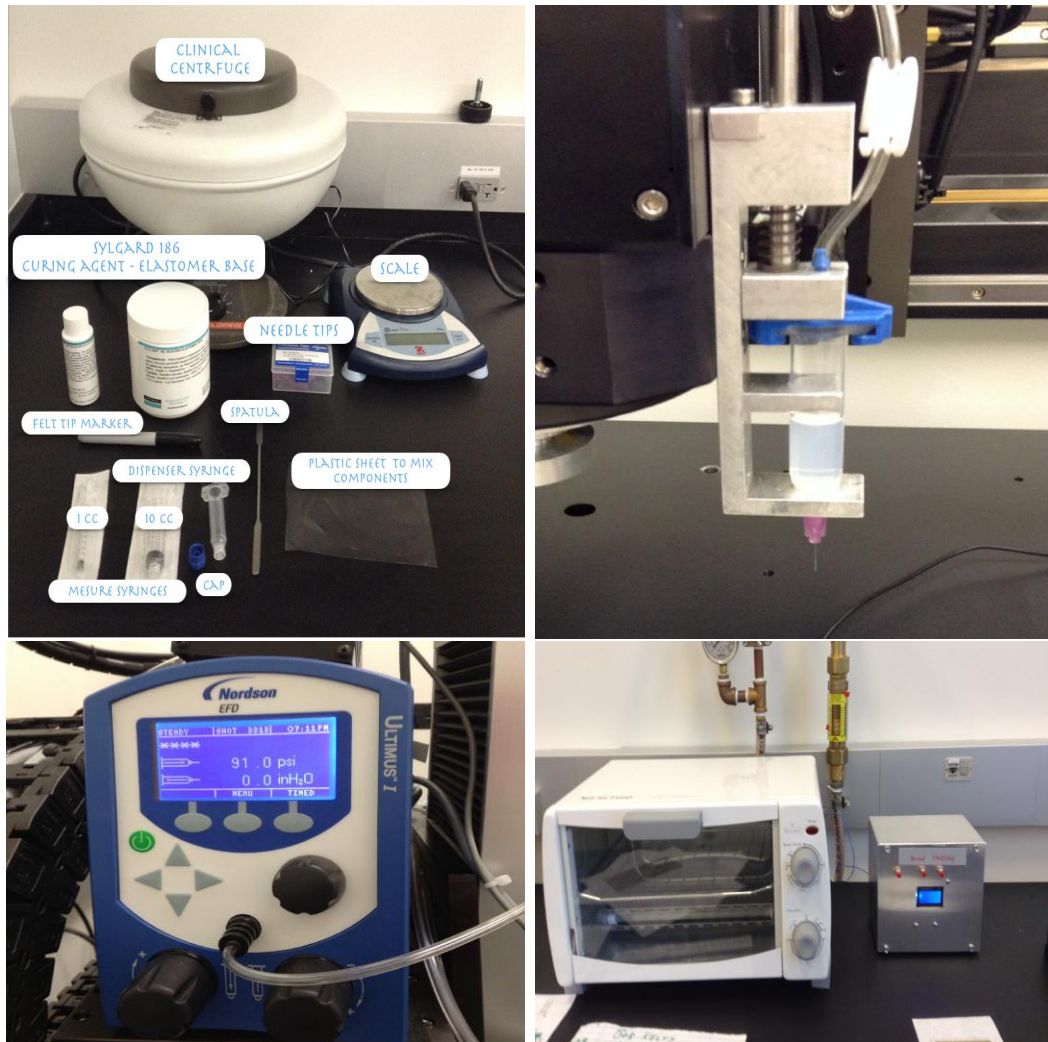


Figure 7.21: Dispensing system components.

3704 other as shown in Figure 7.22 known as *webcam setup*. The reference position acting
 3705 as the origin of the webcam setup coordinate system (RC) was defined by looking at a
 3706 ROC placed over a pedestal so that the horizontal plane of the webcams is adjusted;
 3707 then, using the gantry camera, a fiducial mark on the ROC was located and focused
 3708 so that the z coordinate of the fiducial is known (RC_z). Later, with a dispenser
 3709 syringe and a needle tip mounted on the syringe holder, the needle tip was moved
 3710 to the position of the fiducial mark on the ROC previously focused; the focuses of

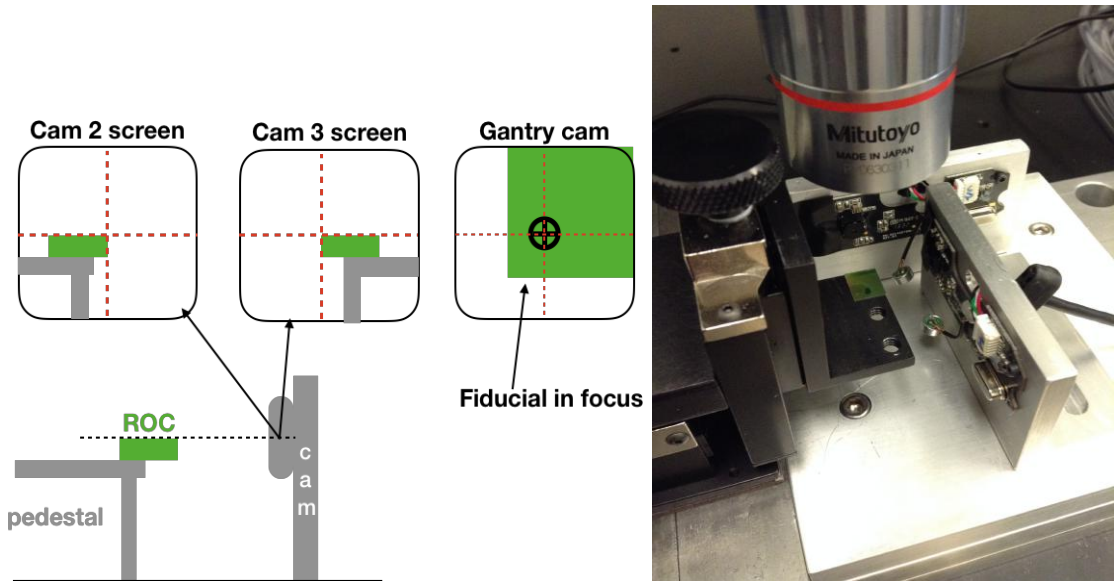


Figure 7.22: Webcam setup used to locate the needle tip in 3D.

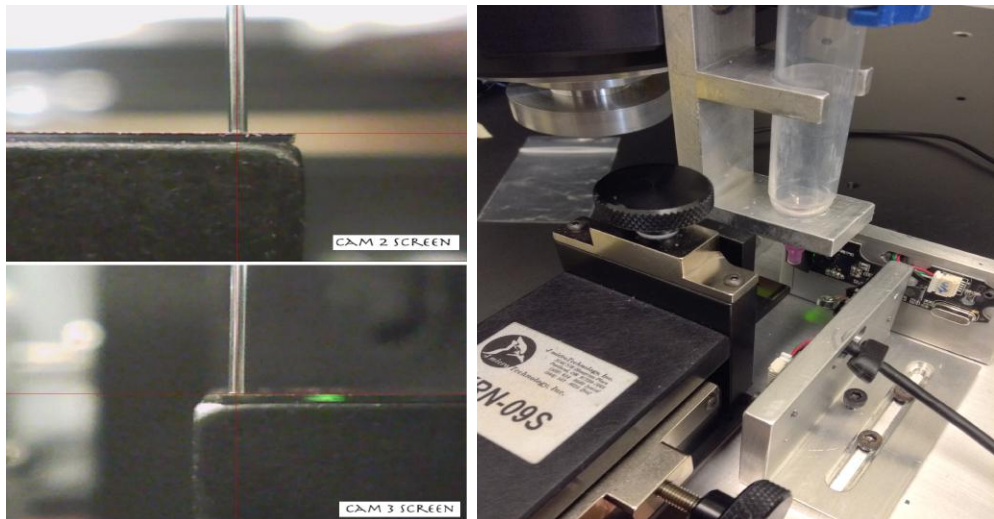


Figure 7.23: Webcam setup calibration. The 3D needle tip coordinates define the reference coordinates (origin) of the webcam setup.

3711 webcams were adjusted such that the needle is well visible in the screens (see Figure
 3712 7.23) and simultaneously in focus for both webcams, while the needle tip is centered
 3713 in the screen, thus, (x, y) gantry head coordinates at that position correspond to the

3714 (RC_x, RC_y) coordinates; after the calibration the RC is

$$RC = (17.337, 80.144, 88.486) \quad (7.10)$$

3715 For any new needle to be used, it is necessary to correct for the needle tip coor-
 3716 dinates deviation from the RC; the correction is obtained by moving the new needle
 3717 tip to the RC position and adjusting the position of the needle tip to get it focused
 3718 and centered in the webcam setup screens; these adjusted coordinates (MC) are com-
 3719 pared with RC, and the difference is called *Needle Tip Offset* (NTO); this calibration
 3720 is connected to the calibration made for the GHCO so that the coordinates provided
 3721 by the vision system for the regions to be encapsulated are also corrected for the
 3722 NTO.

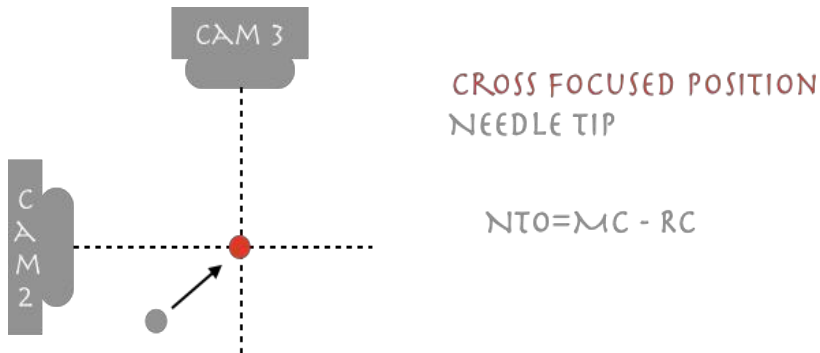


Figure 7.24: Needle tip offset measurement.

3723 **Space-time synchronization of the sylgard deposition**

3724 The requirement imposed to the sylgard deposition over the modules, HDI and BBM,
 3725 is to cover all the bond pads including the wire bonds; to do that, several parameters
 3726 were optimized. First, when the sylgard starts to flow out of the needle, it is necessary
 3727 that the sylgard drop gets in touch with a surface/object before it gets to heavy to

fall down and prevent a continuous flow. Also, it is desired that the sylgard drop to the HDI/BBM bondpads/surface first, rather than the wires themselves; in the former case, the sylgard spreads along the surface while in the latter case the sylgard sticks to the wires and it does not spread. Thus, the distance between the needle tip and the surface is a critical parameter.

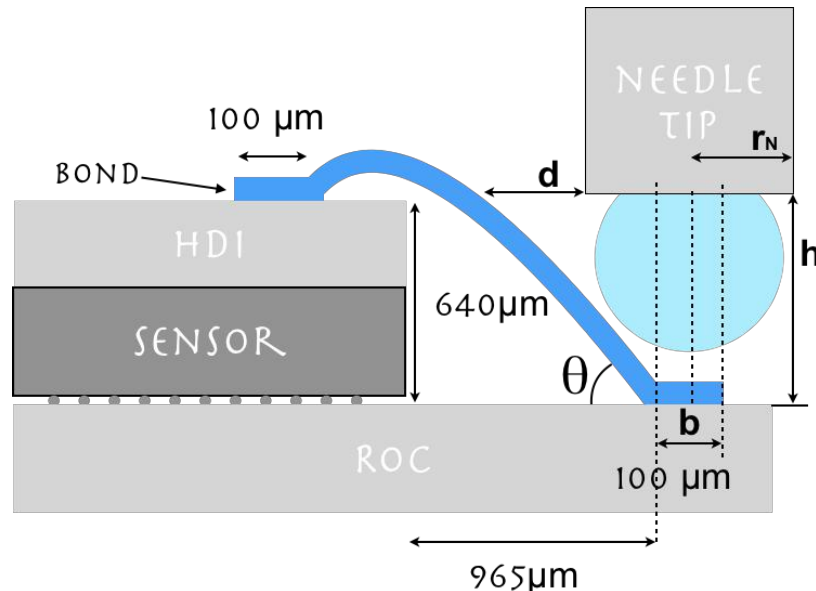


Figure 7.25: Wire bond region.

Figure 7.25 shows an schematic of the wire bond region and some typical dimensions involved. The slope of the wire is about 34° but can vary according to the wirebonding conditions. Going too close to the surface would make the needle tip to touch and break the wires. If the reference to deposit the sylgard is chosen to be the center of the bond, i.e., the center of the needle will be right above the center of the bond, then a simple calculation of the height (h) necessary to have the wire at a safe distance from the needle tip is given by

$$h = \left(d + r_N - \frac{b}{2} \right) \tan(\theta) \quad (7.11)$$

$\theta(^{\circ})$	d(μm)			
	100	150	200	250
30	207.8	236.7	265.6	294.4
45	360.0	410.0	460.0	510.0
60	623.5	710.1	796.7	883.3

Table 7.1: Values of the needle tip height h (μm) for several combinations of parameters d and θ .

3740 where d is the distance from the needle tip edge to the wire (safe distance), r_N is
 3741 the external needle radius ($310\mu\text{m}$), b is the size of the bond ($100\mu\text{m}$) and θ describe
 3742 the slope of the wire. Table 7.1 shows the values of h for several combinations of the
 3743 parameters d and θ (r_N and b fixed).

3744 Given the typical slope of the wires, it was chosen $h = 236.7 \mu\text{m}$ as the needle tip
 3745 height.

3746 The next optimization was performed on the parameters defining the sylgard depo-
 3747 sition kinematics. The basic sylgard deposition process consists of depositing a sylgard
 3748 trace along a path defined by an initial and final positions $(x_i, y_i, z_i), (x_f, y_f, z_f)$. To
 3749 ensure that all the wirebonds are covered, it is necessary to synchronize the dispenser
 3750 action and the gantry motion. The top side of Figure 7.26 shows a sketch of the
 3751 gantry velocity and dispenser action as a function of the time. When the dispenser
 3752 is open the sylgard starts to flow out of the needle, however, the sylgard needs some
 3753 time to flow out and get touch the surface of the HDI/BBM, thus, there should be a
 3754 time delay between the dispenser valve opening and that the gantry starts to move,
 3755 it is called Δt_0 . Accordingly, after the valve is closed, there is a remaining sylgard
 3756 flowing, so the valve should be closed before the gantry reach the final of the way;
 3757 this time delay is called Δt_1 .

3758 To find these time delays, the strategy sketched in the bottom side of Figure 7.26
 3759 was implemented in a LabVIEW program; it proceeds as follows: with the dispenser

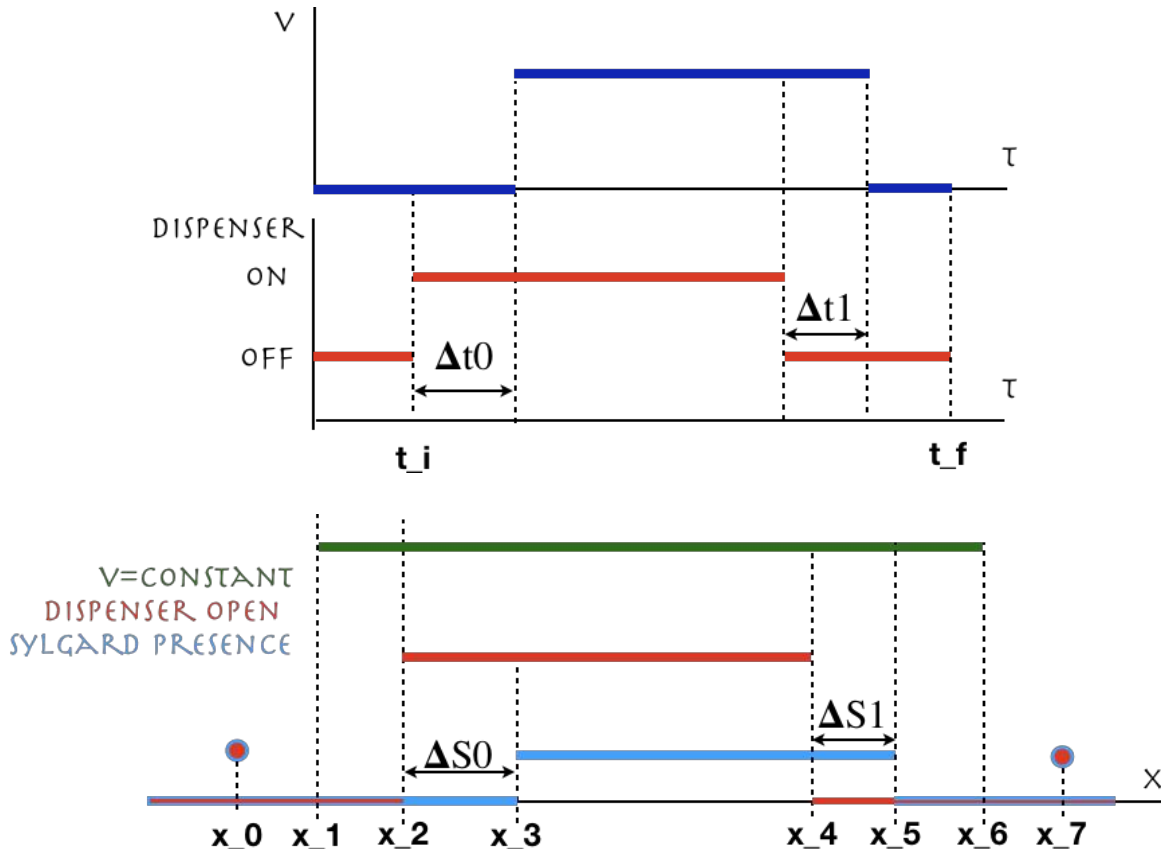


Figure 7.26: Sylgard deposition synchronization. Top: sketch of the gantry velocity and dispenser action as a function of the time. Bottom: sketch of the strategy designed to determine the time delays.

3760 needle loaded and mounted on the syringe holder, and the needle tip calibrated, a set
 3761 of sylgard marks are deposited over a glass slide. The first is a control mark at x_0 ,
 3762 then, at x_1 the gantry starts to move at constant speed v ; at x_2 the dispenser valve
 3763 is opened; at x_3 the sylgard gets in touch with the glass slide and it starts to spread.
 3764 At x_4 , the dispenser valve is closed, but some sylgard is still flowing out until x_5 . At
 3765 x_6 , the gantry stops and finally, at x_7 another sylgard control mark is deposited. The
 3766 time delays are given by

$$\Delta t_0 = \frac{\Delta S_0}{v} = \frac{x_3 - x_2}{v}, \quad (7.12)$$

$$\Delta t_1 = \frac{\Delta S_1}{v} = \frac{x_5 - x_4}{v} \quad (7.13)$$

3767 Figure 7.27 shows the results from two attempts to measure the time delays. In
 3768 the first attempt, the samples were taken in intervals of five minutes at 1 mm/s; the
 3769 sylgard traces started to break up after seven samples. The reason of the breaking
 3770 up is that the sylgard gets ticker with time, so that the speed of the gantry needs
 3771 to be decreased. In the second attempt, the speed was decreased when the breaking
 3772 up showed up; in total, forty samples spaced by five minutes were taken at six speed
 3773 values (0.6,0.5,0.4,0.3,0.25) mm/s.

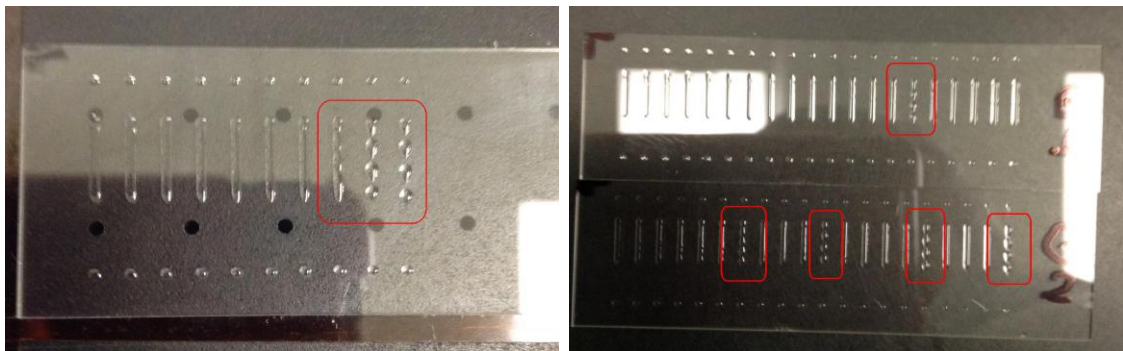


Figure 7.27: Time delay measurement. Left: ten samples spaced by 5 minutes at 1mm/s. Right: forty samples spaced by 5 minutes, adjusting the speed to eliminate the breaking up..

3774 Figure 7.28 (top) shows the evolution of the speed as a function of time for the
 3775 forty samples; the quadratic fit (modified) corresponds to a function that models a
 3776 consistent reduction of the gantry speed in time such that the breaking up of the
 3777 sylgard traces is avoided. This fitting function was implemented in the labVIEW
 3778 program used to take the samples for the time delay calculation; the results are

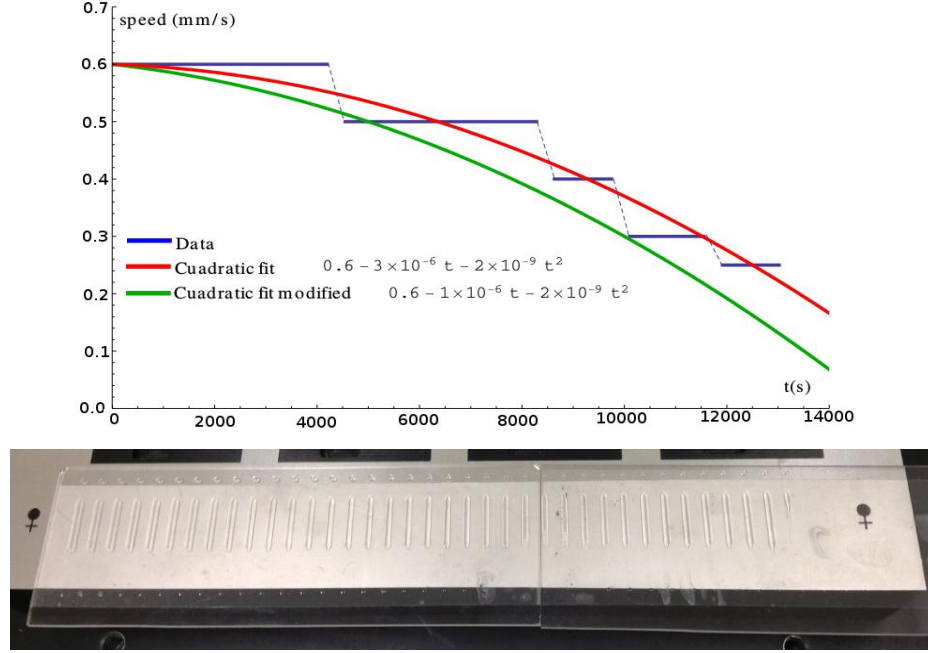


Figure 7.28: Top: speed evolution in time for the time delays determination. Bottom: time delays determination experiment after the implementation of the speed function. After 3.5 hours of data taking, there is no sign of sylgard breaking up.

3779 shown in the bottom side of Figure 7.28 where it is clear that the implementation of
 3780 the speed function meets the requirements. This speed function is called *deposition*
 3781 *speed*.

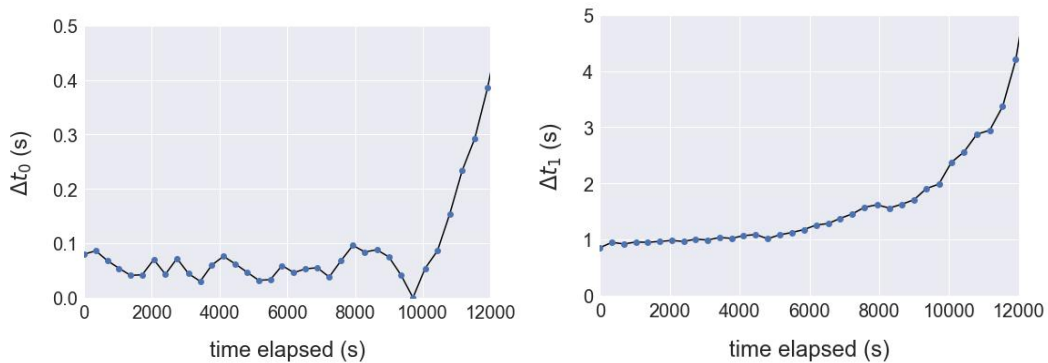


Figure 7.29: Time delay functions Δt_0 and Δt_1 . In the time range of the typical encapsulation process, time delays are approximated by a constant; conservative values were adopted: $\Delta t_0 = 0.1$ s, $\Delta t_1 = 1$ s.

3782 From this test it is also possible to extract the time delay functions (given that
 3783 the deposition speed is a function of the time it is expected that the time delays also
 3784 depends on time); they are shown in Figure 7.29.

3785 The typical encapsulation time per module is about five minutes, therefore, a full
 3786 encapsulation session would last about one and a half hours in total, counting the
 3787 time used to find the fiducial marks on the HDIs/BBMs and the regions where the
 3788 sylgard will be deposited. In that time range, Δt_0 and Δt_1 could be approximated by
 3789 a constant; a conservative choice was adopted: $\Delta t_0 = 0.1$ s, $\Delta t_1 = 1$ s.

3790 7.4.2 The gluing routine

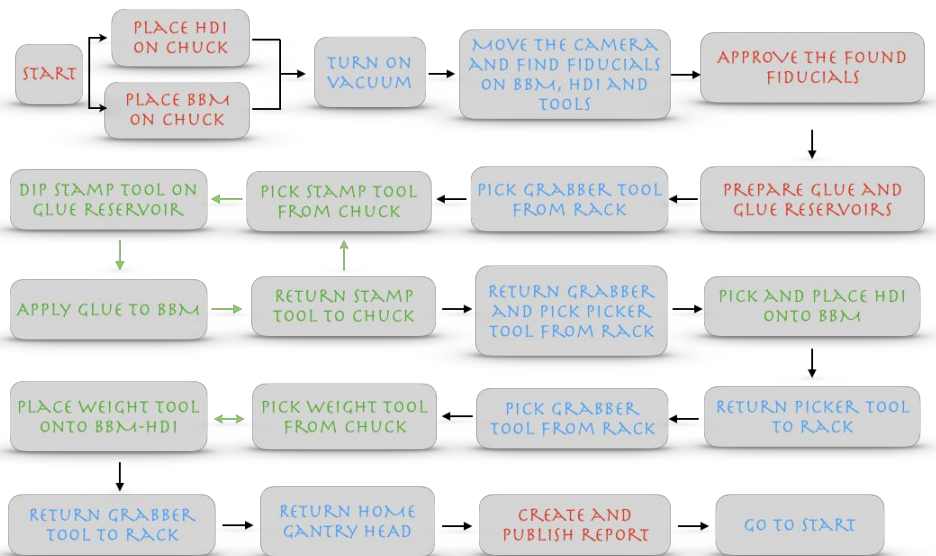


Figure 7.30: Gluing routine workflow.

3791 A gluing session was defined as the process where four modules are assembled. The
 3792 gluing routine workflow is shown in Figure 7.30; the green steps represent the steps
 3793 that are performed more than once in the same session, while the red steps represent
 3794 those performed by the operator. The routine was implemented in a LabVIEW

3795 program (*Gluing_main.vi*) that controls the sequence. The *Main front panel* of the
 3796 gluing routine, shown in Figure 7.32, gathers the most relevant information about
 3797 the gluing session, while each step in the routine has its dedicated front panel. The
 3798 module gluing sequence begins by manually placing pre-tested, BBMs, HDIs and tools
 3799 on their chucks. Figure 7.31 shows the materials used during the gluing session; the
 3800 aluminum squared tool is used to hold the gel-pack containing the BBMs while the
 3801 vacuum pen is used to manipulate the BBMs.

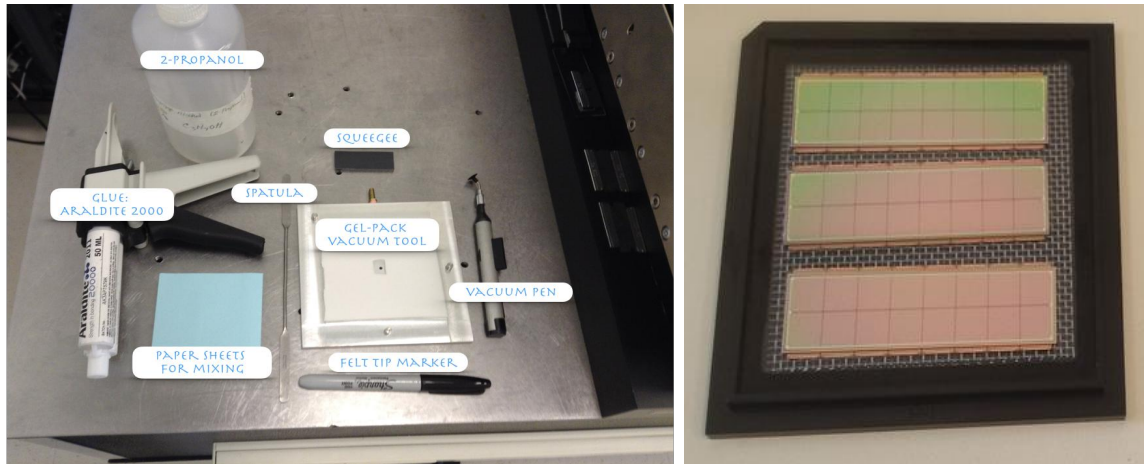


Figure 7.31: Materials used during gluing stage (left). BBMs on a Gel-pack.

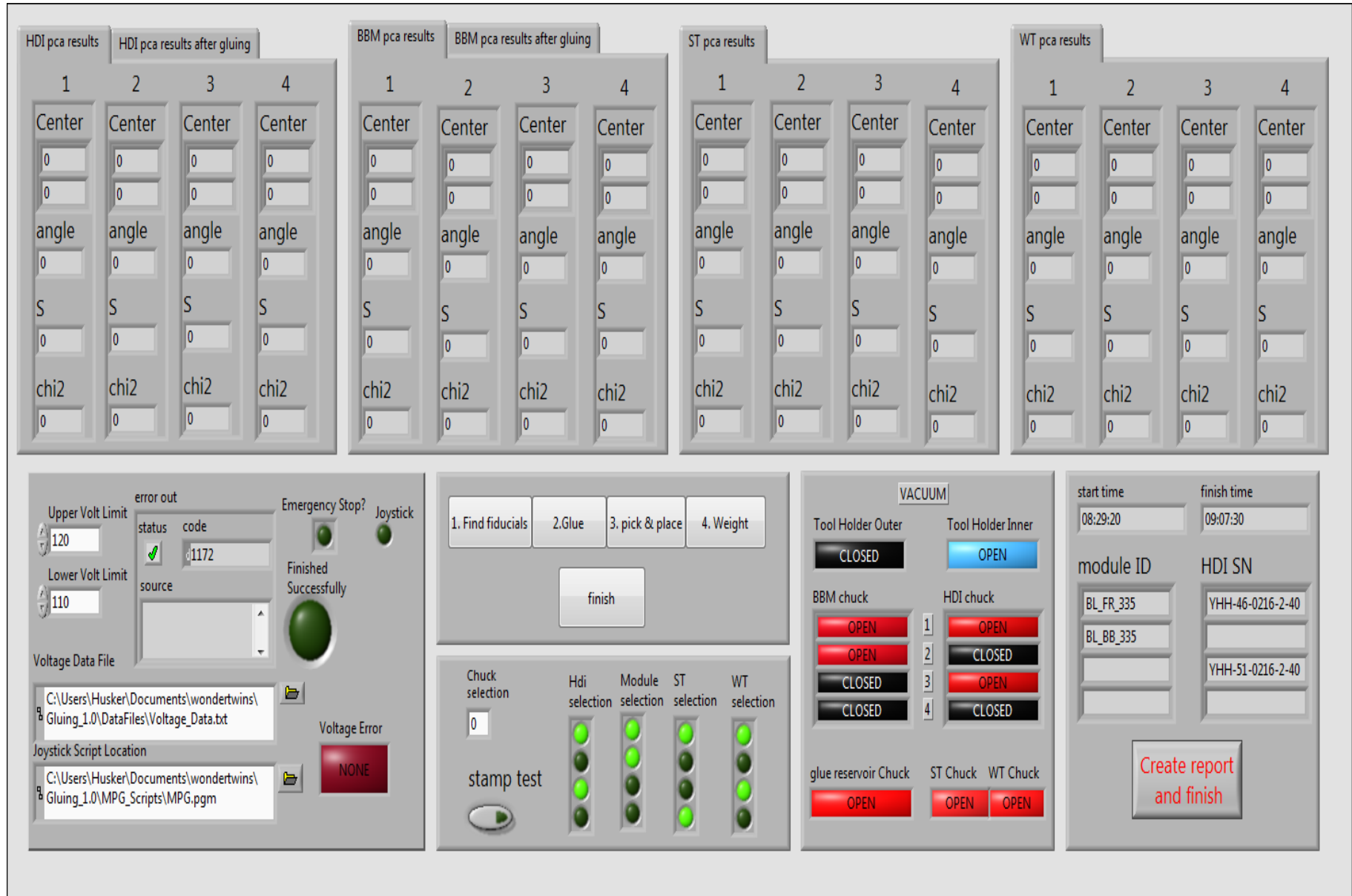


Figure 7.32: Gluing routine LabVIEW front panel.

3802 Once the parts are in place, and the program is run, the BBM and HDI iden-
3803 tification information (serial numbers)  collected² in the first step as well as the
3804 configuration of the gantry table, i.e., the BBM/HDI slots and tools to be used so
3805 that the vacuum system is properly activated.

3806 The camera is moved to view, recognize and find the fiducials locations on the
3807 BBMs, HDIs and tools. These locations are stored and shown in the Main and *Find*
3808 *fiducials* front panels, so that the operator can identify abnormal values from extreme
3809 misalignments and pattern recognition fails; that usually occurs when the plates are
3810 not properly placed on the chucks and/or when the fiducials do not appear in the
3811 camera field of view. In those cases, a manual fiducial finding option is available. The
3812 find fiducial front pannel is shown in Figure 7.33 and a sample of the found fiducials
3813 on a HDI and a BBM is shown in Figure 7.34 indicating the located center of the
3814 fiducial with a green dot. After all the fiducials are identified, the operator has to
3815 check them and perform the necessary adjustments. Usually, the glue was prepared
3816 in parallel to the fiducial identification, reducing the session time.

² A batch numbering strategy was designed in order to identify the modules internally at UNL. 

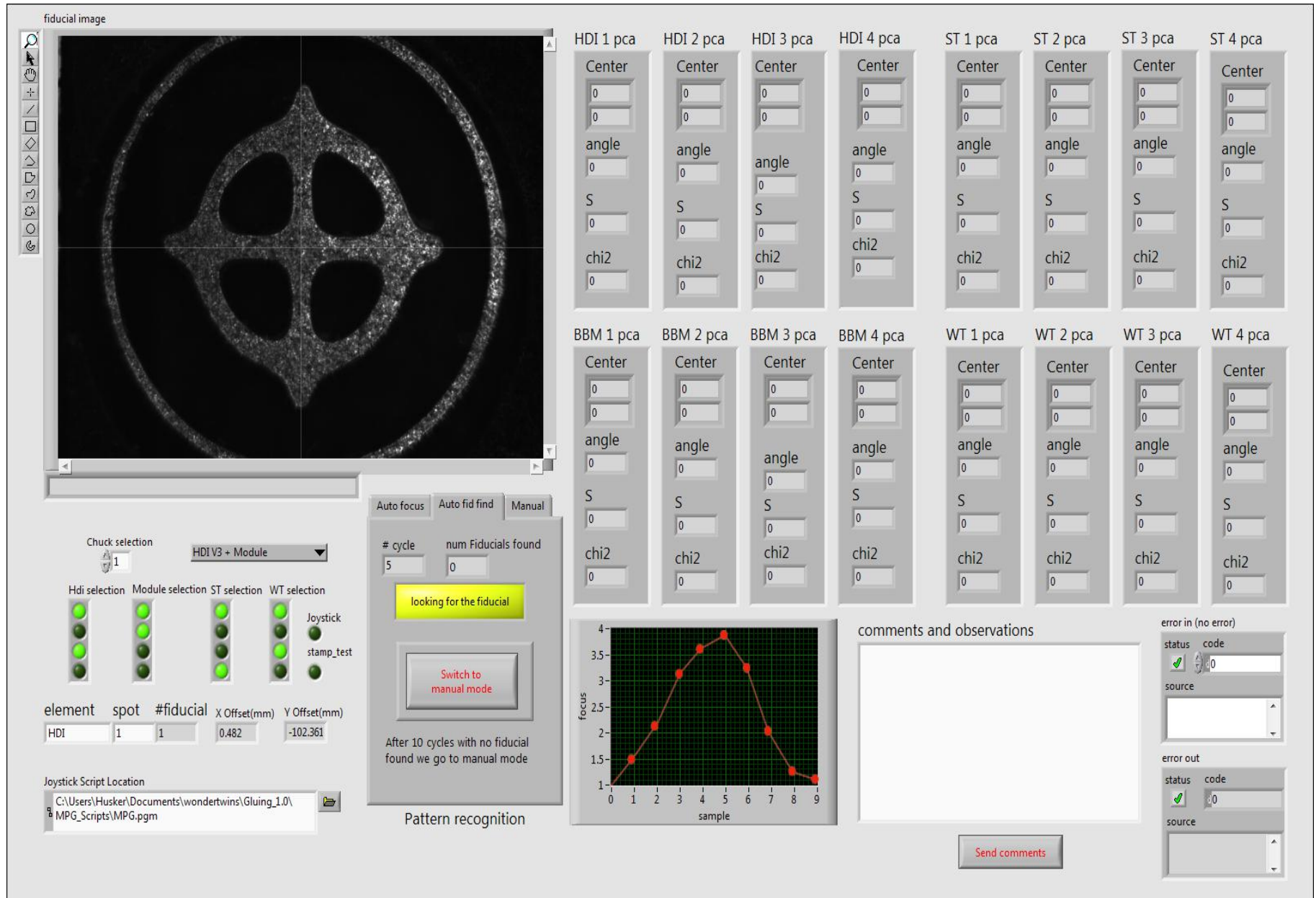


Figure 7.33: Fiducial finder LabVIEW front panel.

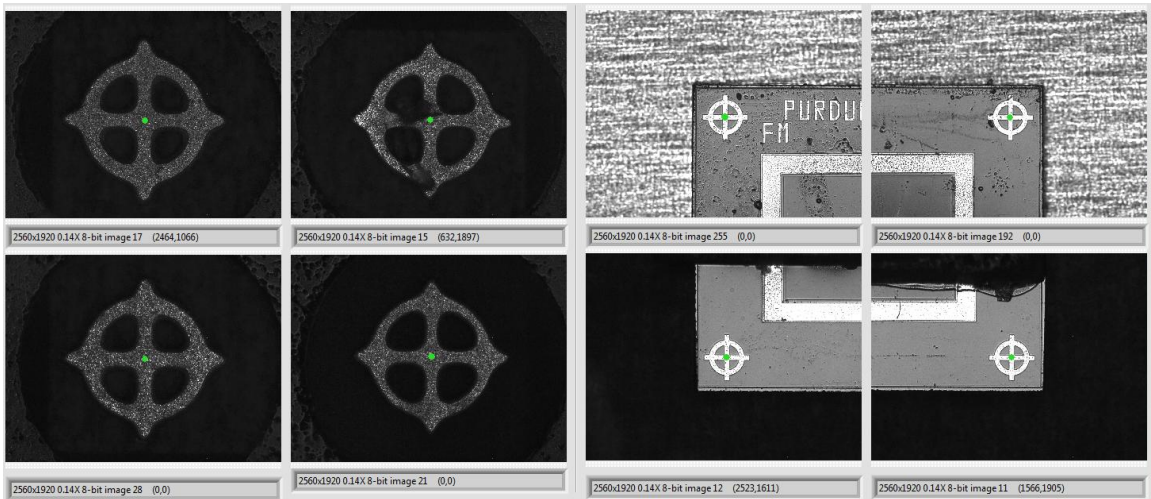


Figure 7.34: Fiducial finder step LabVIEW front panel.

3817 The glue application step starts by picking up the grabber tool from the tool
 3818 rack, and grabbing the stamp tools from their chuck; after dipping the stamp tool in
 3819 the glue reservoir, the epoxy is dispensed on the BBMs. The procedure is repeated
 3820 as many times as the number of modules involved in the session, each time using a
 3821 different stamp tool and a different glue reservoir slot. The step fin~~sh~~ by returning
 3822 the grabber tool to the tool rack. The routine provides full freedom to choose any
 3823 available combination of stamp tool, glue reservoir slot and BBM; this feature is
 3824 particularly useful for glue testing and commissioning. The grabber tool is then
 3825 returned to the tool rack and the picker tool is picked, so that the HDIs are picked
 3826 from their plate slots and placed on top of the BBMs (making the alignment with
 3827 respect to BBMs); again, the routine allows for different combinations of BBM-HDI.
 3828 The front panels for both, gluing and pick-and-place steps, are shown in Figure 7.35.
 3829 Later, the picker tool is returned to the tool rack.

3830 In the weight step of the routine, the grabber tool is picked again from the tool
 3831 rack in order to move the weight tools from their plate slots to the BBM locations.

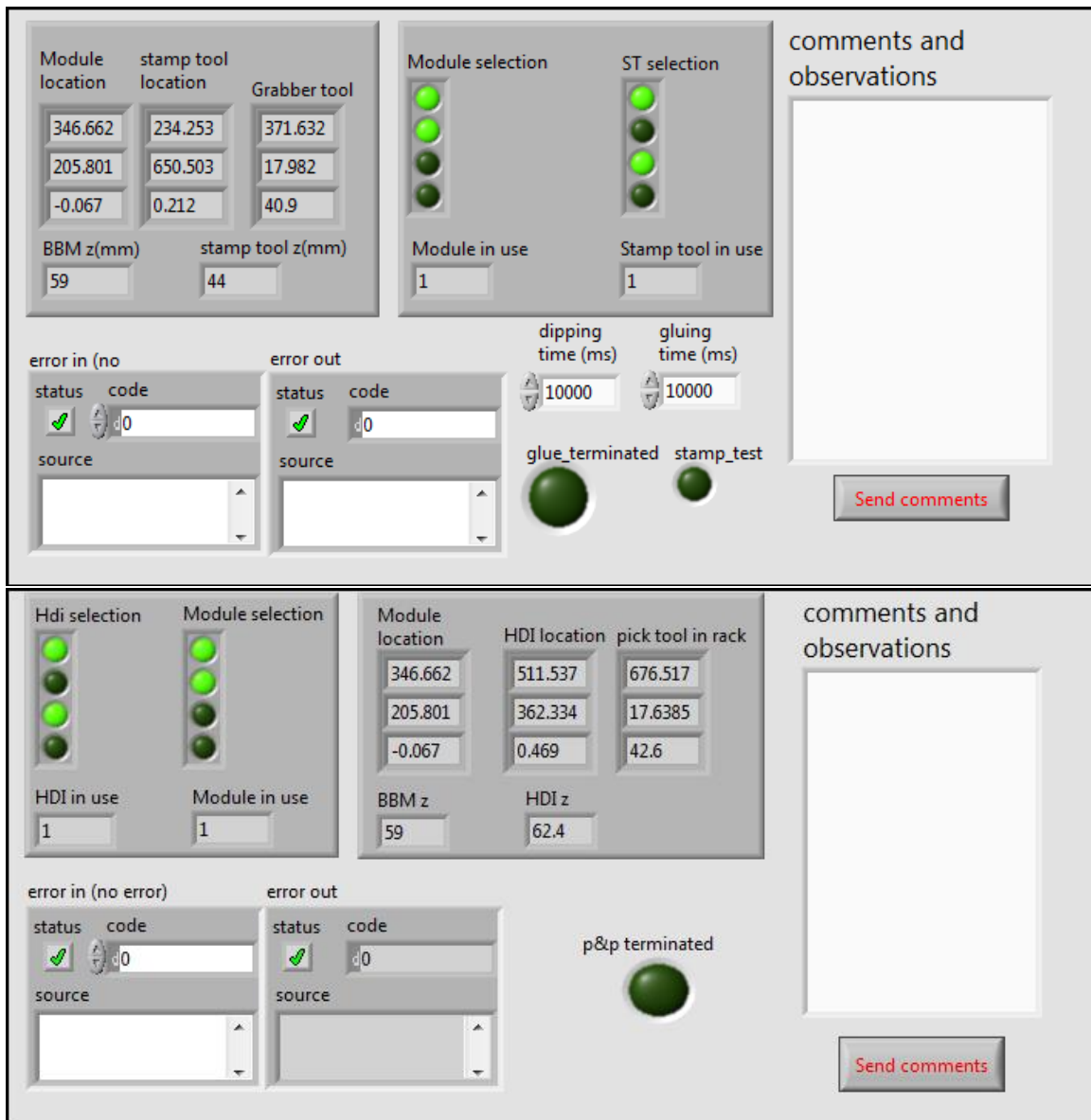


Figure 7.35: Gluing (top) and pick-and-place (bottom) LabVIEW front panels.

3832 The front panel for this step is similar to the gluing front panel. Later, the grabber
 3833 tool is returned to the tool rack and the gantry head is moved back to the home
 3834 position. Figure 7.36 shows pictures of the glue reservoir plate loaded with glue,
 3835 BBMs after the glue deposition, BBM-HDI after pick-and-place, and weight tools
 3836 over the assembled modules.

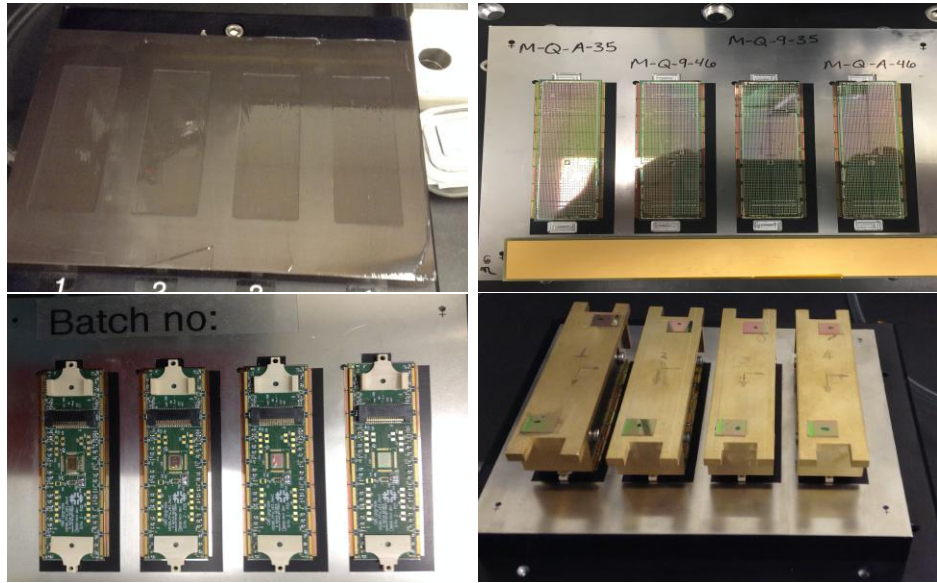


Figure 7.36: Gluing steps pictures. Top: glue reservoir loaded (left), glue dispensed on BBMs (right). Bottom: BBM-HDI after pick-and-place(left), weight tools over assembled modules(right).

3837 The last step of the routine of creating and publishing the gluing ses-
 3838 sion report (see Figure 7.37) in the UNL silicon lab. electronic logbook (ELOG) and
 3839 updating the database created to keep track of the assembly progress.

3840 At the end of the full cycle, the stamp plate with stamp tools is moved to be
 3841 cleaned thoroughly using water and 2-propanol at sink outside the cleanroom. Let
 3842 them dry and bring them back to gantry table. The assembled modules are left to
 3843 cure eight hours, typically overnight. The fully detailed SOP (SOP-103) for the gluing
 3844 stage can be found in Reference [163], while several videos showing the gluing routine
 3845 in action can be found in References [164, 165].

3846 7.4.3 The encapsulation routine

3847 Following the assembly, HDIs are wirebonded to the ROCs using semi-automated
 3848 ultrasonic irebonding machine. Pull tests of wirebonds are performed on a sample

Manufacturing of modules: Glued HDI on BBM

Procedure performed according to SOP 103-v0

Date: 7/3/2016

Finish time: 3/7/2016-09:07:30

Start time: 3/7/2016-08:29:20

pressure: 69

operator: Jmonroy

Araldite batch no. : ADE0254200

Software version: dev

Object status updated in Purdue database (Justify in comments): yes

List id of parts involved in table below:

Chuck No. :2

BBM ID	HDI S/N
BL FR 335	YHH46-0216-2-40
BL BB 335	
	YHH51-0216-2-40

Special observations and comments:

Orientation:

Glueing:

Pick&place:

Weight:

Others:

Figure 7.37: Gluing session report.

3849 of modules for quality control; a picture of one of the sixteen ROCs wirebonded to
 3850 its HDI counterpart is shown in Figure 7.38. The wirebonds were encapsulated with
 3851 an elastomeric compound in order to protect them from mechanical damage and to
 3852 avoid possible shortcut circuits.

3853 The encapsulation was performed using the robotic gantry and the dispensing
 3854 system described in Section 7.4.1; the step by step instructions are documented in
 3855 SOP-105 [166]. After the wirebonding, the plates with the modules were taken back to



Figure 7.38: ROC-HDI wirebonding.

3856 the gantry table and located in the BBM chucks. The encapsulation strategy is based
 3857 on a simple routine: by stating the initial conditions, i.e., the initial (R_i) and final
 3858 (R_f) reference positions, the time elapsed after sylgard preparation, time delays, and
 3859 needle tip location, move the gantry head to R_i and deposit the encapsulant following
 3860 the structure sketched in Figure 7.26 (top). The sylgard trace is required to fully cover
 3861 the HDI/BBM bond pads without spreading out in between the sensor and the ROC.

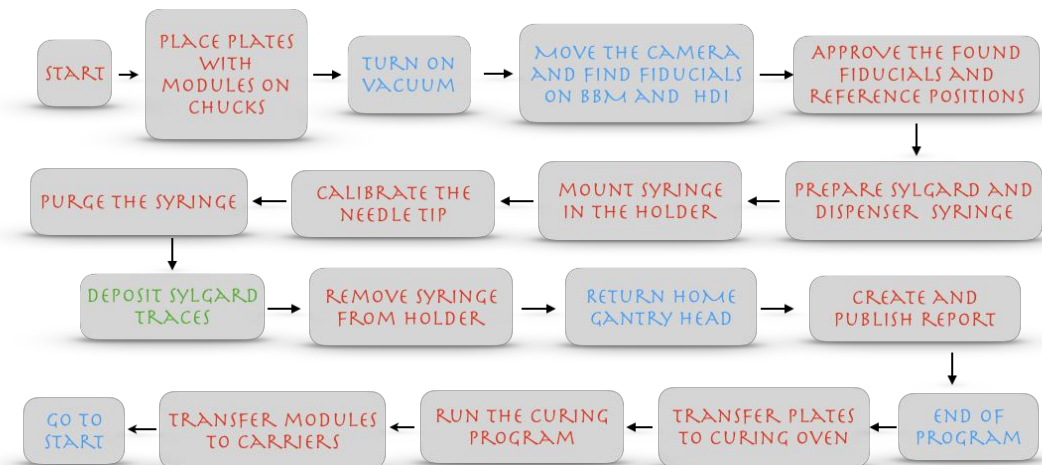


Figure 7.39: Encapsulation workflow. Steps in red correspond to interactions with the user; steps in blue are those performed by the gantry automatically while the step in green is performed by the gantry repeatedly during the same encapsulation session.

3862 An encapsulation session is defined as the process where 8 modules are encapsu-
3863 lated following the encapsulation routine workflow shown in Figure 7.39; steps in red
3864 correspond to actions performed by the user; steps in blue are those performed by the
3865 gantry automatically while the step in green is performed by the gantry repeatedly
3866 during the same encapsulation session. The routine was implemented in a LabVIEW
3867 program controlling the sequence, taking advantage of the routines created during
3868 the implementation of the gluing stage.

3869 The main routine is composed of two steps, although each step involves more than
3870 one substeps. Again, the most important information about the session is gathered
3871 in the main front panel as shown in Figure 7.40. The encapsulation routine involves
3872 much less vacuum manipulation given that there is no movable elements.

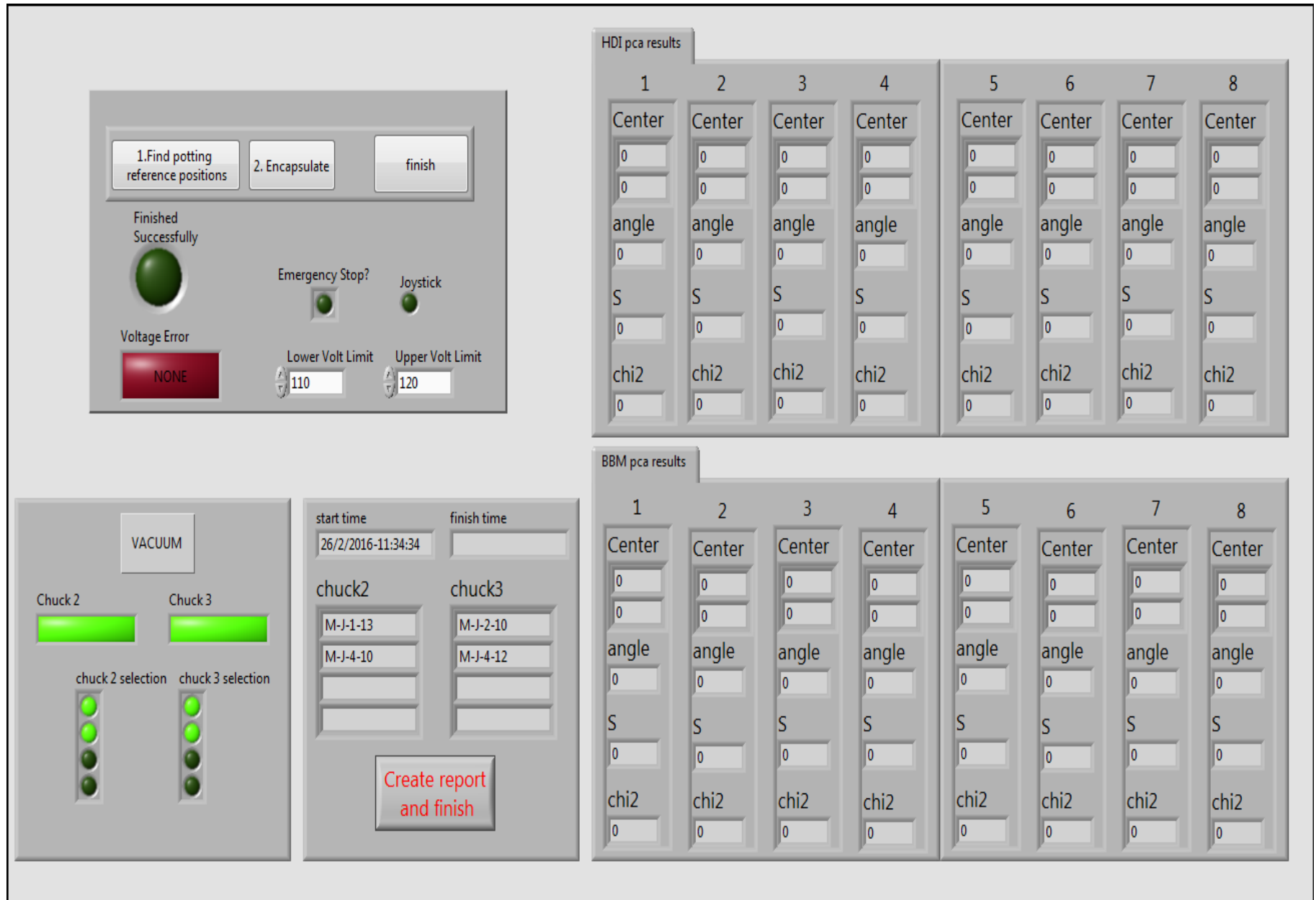


Figure 7.40: Encapsulation LabVIEW main front panel.

3873 The module encapsulation sequence begins by moving the wirebonded modules
 3874 from the storage cabinet to the chucks; since the session involves eight modules,
 3875 only two chucks are made available in the routine. Once the module identification
 3876 information and gantry table configuration is provided by the operator, the vacuum
 3877 is activated accordingly.

3878 In the first step, the vision system is used to locate the fiducial marks on the
 3879 BBMs and HDIs, the same used in the gluing stage, and the reference positions that
 3880 determine the sylgard traces to be deposited.

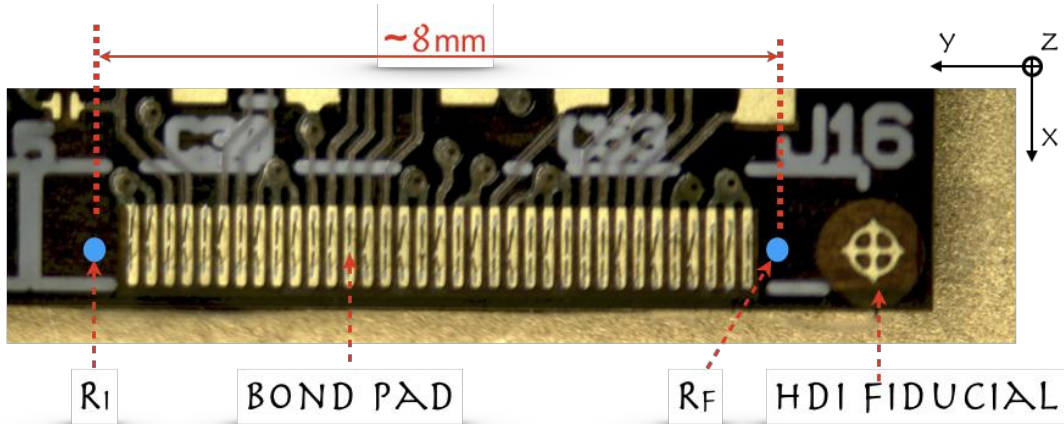


Figure 7.41: Encapsulation region. The sylgard trace, defined by the reference positions R_i and R_f , is required spread out to fully cover the bond pads.

3881 These reference positions R_i and R_f define the length of the sylgard trace as shown
 3882 in Figure 7.41; they are determined from the bond pad locations which in turn are
 3883 found using the information from the BBM/HDI design technical specifications, i.e.,
 3884 knowing the location of the fiducial marks on the BBM/HDI, it is possible to locate
 3885 with precision the location of the bond pads. Originally, R_i was identified with the
 3886 center of the first bond pad, while R_f was identified with the center of the last bond
 3887 pad; however, the initial testing showed that this identification resulted in some of
 3888 the pads not being fully covered. At first, the proposed solution was to extend Δt_0

3889 and eliminate Δt_i which would increase the amount of sylgard in the trace ends, but
 3890 further testing showed that the additional amount of sylgard, due to an extended
 3891 Δt_0 , did not provide a full solution and that the surface tension would be source of
 3892 the issue. A simple solution was to move the reference positions a bit away from
 3893 the bond pad center as showed in Figure 7.41; this adjustment was implement in the
 3894 routine.

3895 In general, the sylgard trace lives in 3D because the module is not perfectly
 3896 aligned with respect to the gantry coordinate system (neither the HDI ner) and
 3897 even though the ROCs are flat the HDI could be bent, therefore, the gantry motion
 3898 during the sylgard deposition is carried in 3D. The displacements in each direction are
 3899 determined from the reference positions and the motions are done in the same time
 3900 interval, thus, the speed for each direction is different; however, the displacement in
 3901 y -direction, i.e., the length of the set of bond pads which is about 8 mm, is much larger
 3902 than the displacement in x and z directions, which are expected to be about 10-50
 3903 μm , so essentially the speed in y -direction is essentially the same as the deposition
 3904 speed.

3905 The fact that re HDI is not perfectly flat, implies that et though the tech-
 3906 nical specifications can provide a very precise estimation of the references in the $x - y$
 3907 plane and at some extend the information from the fiducials locations can provide a
 3908 measurement of the variation in z -direction, it is still necessary to set the reference
 3909 positions independently for each sylgard trace in order to foreseen any bump in the
 3910 HDI.

3911 After the reference positions have been determined, they are approved by the
 3912 operator or adjusted according to the parameters described above; in case of failure,
 3913 a manual mode is available. Figure 7.42 shows pictures with the reference positions
 3914 chosen for a module.

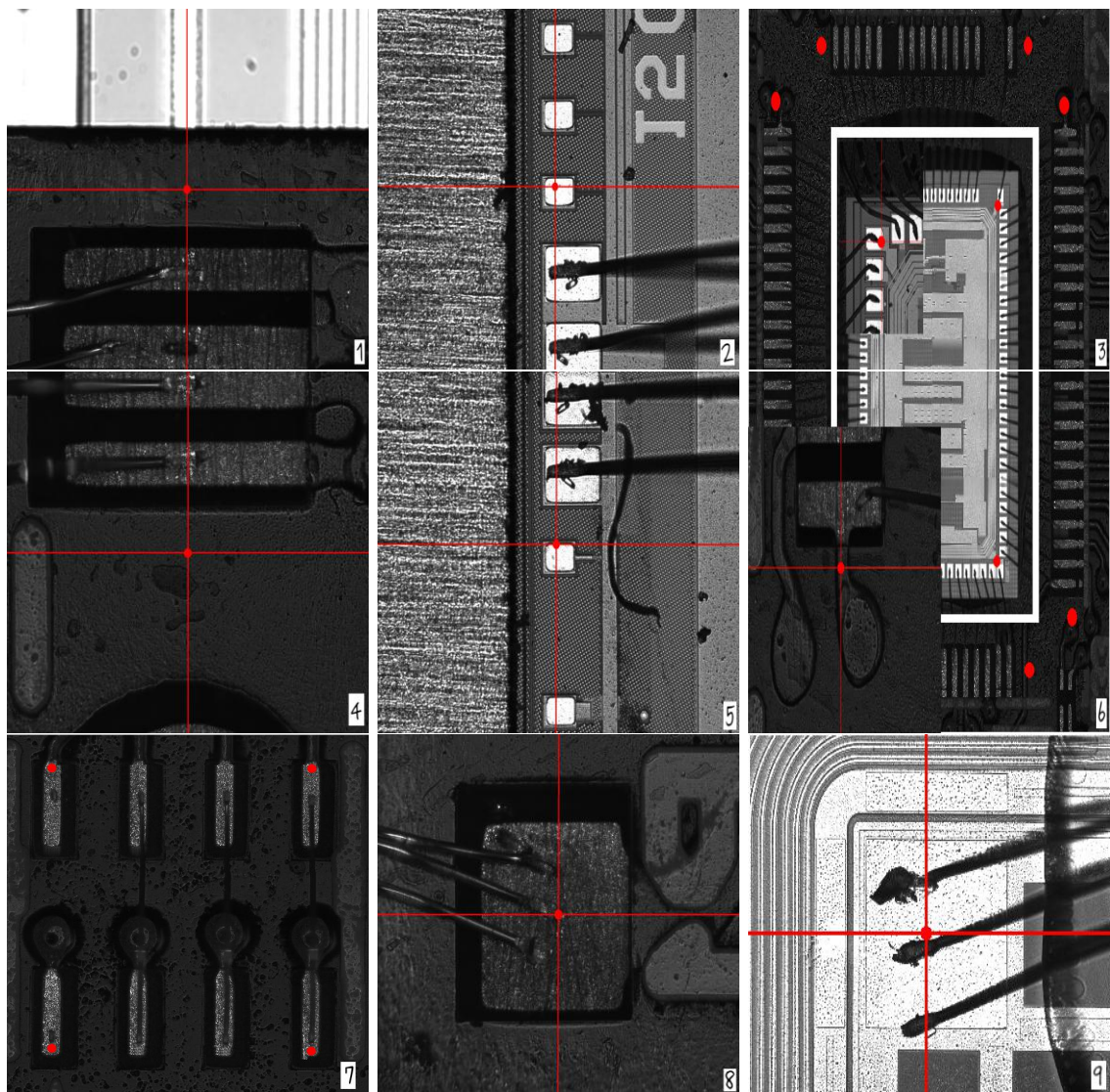


Figure 7.42: Encapsulation reference positions for one module. 1 and 4 show the reference positions for one of the HDI bond pads sets, while 2 and 5 show the corresponding reference positions for the bond pads on the BBM side. 3 and 6 show the reference points for the TBM; 7, 8 and 9 show the reference positions for the address pads, the HV pad on HDI and the HV pad on BBM respectively.

3915 The next step is the sylgard preparation; 1 cc of sylgard elastomer are mixed
 3916 with 0.1 cc of curing agent over a plastic sheet and then transferred to the dispenser
 3917 syringe using the spatula. Later, the dispenser syringe  is placed in a clinical centrifuge
 3918 in order to eliminate the air bubbles; finally the dispenser syringe is installed in the

3919 syringe holder attached to the gantry head. This process takes about ten minutes
3920 and is required to be done in the shortest time possible given that sylgard gets ticker
3921 with time; the mixing time has to be annotated and inputted into the program in
3922 order to control the deposition speed.

3923 The needle tip is installed once the dispenser syringe is mounted in the holder,
3924 then, the needle tip calibration is performed using the webcam setup; before to start
3925 dispensing the sylgard, the syringe is purged to eliminate the air trapped between the
3926 syringe mouth and the needle tip.

3927 In total, the encapsulation of one module is composed by 32 sylgard traces covering
3928 the bonds connecting the HDI and each of the 16 ROCs per module, 8 sylgard traces
3929 covering the bonds connection the TBM and the HDI, 2 sylgard traces covering the
3930 bonds of the address pads, and two sylgard drops covering the HV pads; each module
3931 is encapsulated in about five minutes.

3932 After the sylgard deposition step, the syringe is removed from the holder and the
3933 gantry head goes back to the home position. The work at the gantry table ends with
3934 the generation and publication of the encapsulation session report.

3935 At the end of the full cycle, a visual inspection of the sylgard traces is performed in
3936 order to ensure the quality of the encapsulation; in case of defects, the encapsulation
3937 procedure is repeated taking the reference positions in agreement with the regions
3938 that are not fully sylgard-covered.

3939 Later, the plates with the encapsulated modules are transferred into the curing
3940 oven where they are submitted to a thermal cycle keeping them at 50 °C degrees
3941 for one hour. The curing procedure is not included in the encapsulation routine and
3942 no details are provided about it in this document. Figure 7.43 shows a picture of
3943 an encapsulation test using a plain HDI glued on a glass slide; also, pictures of an
3944 encapsulated module confirming the quality of the encapsulation.

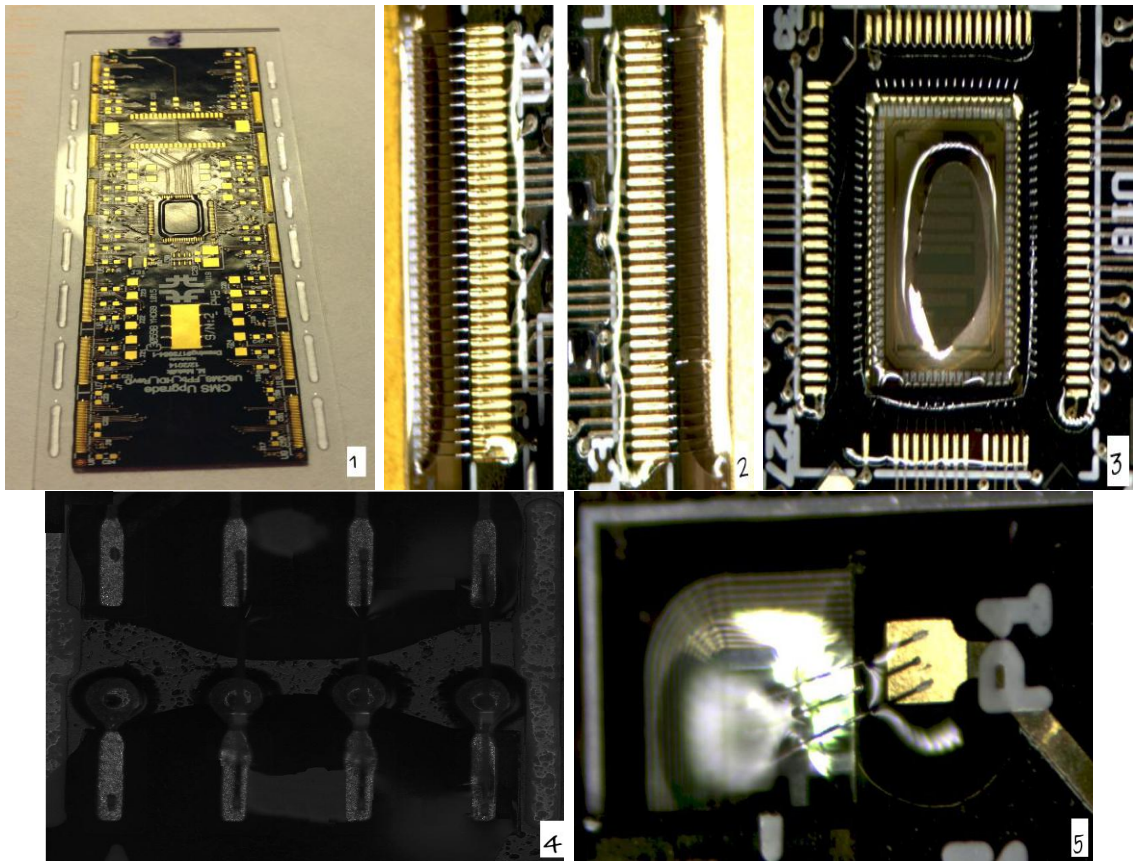


Figure 7.43: Encapsulation results. 1 shows an encapsulation test. 2-5 show the results from a module encapsulation for two sets of ROC-HDI traces, TBM, address pads and HV pads respectively.

3945 The module assembly sites were also responsible for the testing and characteriza-
 3946 tion of the assembled pixel modules; therefore, modules were tested at room tempera-
 3947 ture ($\sim 17^{\circ}\text{C}$) while monitoring ROC digital and analog currents. The very last step
 3948 in the production line was the shipment to the x -rays characterization site located
 3949 at University of Kansas.

3950 **7.4.4 The FPix module production yields**

³⁹⁵¹ **Appendix A**

³⁹⁵² **Datasets and triggers**

Dataset name
/JetHT/Run2016X-23Sep2016-vY/MINIAOD
/HTMHT/Run2016X-23Sep2016-vY/MINIAOD
/MET/Run2016X-23Sep2016-vY/MINIAOD
/SingleElectron/Run2016X-23Sep2016-vY/MINIAOD
/SingleMuon/Run2016X-23Sep2016-vY/MINIAOD
/SinglePhoton/Run2016X-23Sep2016-vY/MINIAOD
/DoubleEG/Run2016X-23Sep2016-vY/MINIAOD
/MuonEG/Run2016X-23Sep2016-vY/MINIAOD
/DoubleMuon/Run2016X-23Sep2016-vY/MINIAOD
/Tau/Run2016B-23Sep2016-v3/MINIAOD
/JetHT/Run2016H-PromptReco-v3/MINIAOD
/HTMHT/Run2016H-PromptReco-v3/MINIAOD
/MET/Run2016H-PromptReco-v3/MINIAOD
/SingleElectron/Run2016H-PromptReco-v3/MINIAOD
/SingleMuon/Run2016H-PromptReco-v3/MINIAOD
/SinglePhoton/Run2016H-PromptReco-v3/MINIAOD
/DoubleEG/Run2016H-PromptReco-v3/MINIAOD
/MuonEG/Run2016H-PromptReco-v3/MINIAOD
/DoubleMuon/Run2016H-PromptReco-v3/MINIAOD

Table A.1: Full 2016 dataset used in the analysis. In the first section of the table are listed the 23Sep2016 samples; in the Run2016X-23Sep-vY label, X:B-G tag the run while Y:1,3 tag the version of the data sample. Second section list the PromptReco version of the dataset.

Same-sign dilepton (==2 muons)
HLT_Mu17_TrkIsoVVL_Mu8_TrkIsoVVL_DZ_v*
HLT_Mu17_TrkIsoVVL_TkMu8_TrkIsoVVL_DZ_v*
HLT_IsoMu22_v*
HLT_IsoTkMu22_v*
HLT_IsoMu22_eta2p1_v*
HLT_IsoTkMu22_eta2p1_v*
HLT_IsoMu24_v*
HLT_IsoTkMu24_v*
Same-sign dilepton (==2 electrons)
HLT_Ele23_Ele12_CaloIdL_TrackIdL_IsoVL_DZ_v*
HLT_Ele27_eta2p1_WP Loose_Gsf_v*
HLT_Ele27_WPTight_Gsf_v*
HLT_Ele25_eta2p1_WPTight_Gsf_v*
Same-sign dilepton (==1 muon, ==1 electron)
HLT_Mu23_TrkIsoVVL_Ele8_CaloIdL_TrackIdL_IsoVL_v*
HLT_Mu8_TrkIsoVVL_Ele23_CaloIdL_TrackIdL_IsoVL_v*
HLT_Mu23_TrkIsoVVL_Ele8_CaloIdL_TrackIdL_IsoVL_DZ_v*
HLT_Mu8_TrkIsoVVL_Ele23_CaloIdL_TrackIdL_IsoVL_DZ_v*
HLT_IsoMu22_v*
HLT_IsoTkMu22_v*
HLT_IsoMu22_eta2p1_v*
HLT_IsoTkMu22_eta2p1_v*
HLT_IsoMu24_v*
HLT_IsoTkMu24_v*
HLT_Ele27_WPTight_Gsf_v*
HLT_Ele25_eta2p1_WPTight_Gsf_v*
HLT_Ele27_eta2p1_WP Loose_Gsf_v*
Three lepton
HLT_DiMu9_Ele9_CaloIdL_TrackIdL_v*
HLT_Mu8_DiEle12_CaloIdL_TrackIdL_v*
HLT_TripleMu_12_10_5_v*
HLT_Ele16_Ele12_Ele8_CaloIdL_TrackIdL_v*
HLT_Mu23_TrkIsoVVL_Ele8_CaloIdL_TrackIdL_IsoVL_v*
HLT_Mu23_TrkIsoVVL_Ele8_CaloIdL_TrackIdL_IsoVL_DZ_v*
HLT_Mu8_TrkIsoVVL_Ele23_CaloIdL_TrackIdL_IsoVL_v*
HLT_Mu8_TrkIsoVVL_Ele23_CaloIdL_TrackIdL_IsoVL_DZ_v*
HLT_Ele23_Ele12_CaloIdL_TrackIdL_IsoVL_DZ_v*
HLT_Mu17_TrkIsoVVL_Mu8_TrkIsoVVL_DZ_v*
HLT_Mu17_TrkIsoVVL_TkMu8_TrkIsoVVL_DZ_v*
HLT_IsoMu22_v*
HLT_IsoTkMu22_v*
HLT_IsoMu22_eta2p1_v*
HLT_IsoTkMu22_eta2p1_v*
HLT_IsoMu24_v*
HLT_IsoTkMu24_v*
HLT_Ele27_WPTight_Gsf_v*
HLT_Ele25_eta2p1_WPTight_Gsf_v*
HLT_Ele27_eta2p1_WP Loose_Gsf_v*

Table A.2: Table of high-level triggers considered in the analysis.

		<i>tHq</i>		<i>tHW</i>		
κ_V	κ_t	sum of weights	cross section [pb]	sum of weights	cross section [pb]	LHE weights
1.0	-3.0	35.700022	2.991	11.030445	0.6409	LHEweight_wgt[446]
1.0	-2.0	20.124298	1.706	5.967205	0.3458	LHEweight_wgt[447]
1.0	-1.5	14.043198	1.205	4.029093	0.2353	LHEweight_wgt[448]
1.0	-1.25	11.429338	0.9869	3.208415	0.1876	LHEweight_wgt[449]
1.0	-1.0		0.7927		0.1472	
1.0	-0.75	7.054998	0.6212	1.863811	0.1102	LHEweight_wgt[450]
1.0	-0.5	5.294518	0.4723	1.339886	0.07979	LHEweight_wgt[451]
1.0	-0.25	3.818499	0.3505	0.914880	0.05518	LHEweight_wgt[452]
1.0	0.0	2.627360	0.2482	0.588902	0.03881	LHEweight_wgt[453]
1.0	0.25	1.719841	0.1694	0.361621	0.02226	LHEweight_wgt[454]
1.0	0.5	1.097202	0.1133	0.233368	0.01444	LHEweight_wgt[455]
1.0	0.75	0.759024	0.08059	0.204034	0.01222	LHEweight_wgt[456]
1.0	1.0	0.705305	0.07096	0.273617	0.01561	LHEweight_wgt[457]
1.0	1.25	0.936047	0.0839	0.442119	0.02481	LHEweight_wgt[458]
1.0	1.5	1.451249	0.1199	0.709538	0.03935	LHEweight_wgt[459]
1.0	2.0	3.335034	0.2602	1.541132	0.08605	LHEweight_wgt[460]
1.0	3.0	10.516125	0.8210	4.391335	0.2465	LHEweight_wgt[461]
1.5	-3.0	45.281492	3.845	13.426212	0.7825	LHEweight_wgt[462]
1.5	-2.0	27.606715	2.371	7.809713	0.4574	LHEweight_wgt[463]
1.5	-1.5	20.476088	1.784	5.594971	0.3290	LHEweight_wgt[464]
1.5	-1.25	17.337465	1.518	4.635978	0.2749	LHEweight_wgt[465]
1.5	-1.0	14.483302	1.287	3.775902	0.2244	LHEweight_wgt[466]
1.5	-0.75	11.913599	1.067	3.014744	0.1799	LHEweight_wgt[467]
1.5	-0.5	9.628357	0.874	2.352505	0.1410	LHEweight_wgt[468]
1.5	-0.25	7.627574	0.702	1.789184	0.1081	LHEweight_wgt[469]
1.5	0.0	5.911882	0.5577	1.324946	0.08056	LHEweight_wgt[470]
1.5	0.25	4.479390	0.4365	0.959295	0.05893	LHEweight_wgt[471]
1.5	0.5	3.331988	0.3343	0.692727	0.04277	LHEweight_wgt[472]
1.5	0.75	2.469046	0.2558	0.525078	0.03263	LHEweight_wgt[473]
1.5	1.0	1.890565	0.2003	0.456347	0.02768	LHEweight_wgt[474]
1.5	1.25	1.596544	0.1689	0.486534	0.02864	LHEweight_wgt[475]
1.5	1.5	1.586983	0.1594	0.615638	0.03509	LHEweight_wgt[476]
1.5	2.0	2.421241	0.2105	1.170602	0.06515	LHEweight_wgt[477]
1.5	3.0	7.503280	0.5889	3.467546	0.1930	LHEweight_wgt[478]
0.5	-3.0	27.432685	2.260	8.929074	0.5136	LHEweight_wgt[479]
0.5	-2.0	13.956013	1.160	4.419093	0.2547	LHEweight_wgt[480]
0.5	-1.5	8.924438	0.7478	2.757611	0.1591	LHEweight_wgt[481]
0.5	-1.25	6.835341	0.5726	2.075247	0.1204	LHEweight_wgt[482]
0.5	-1.0	5.030704	0.4273	1.491801	0.08696	LHEweight_wgt[483]
0.5	-0.75	3.510528	0.2999	1.007273	0.05885	LHEweight_wgt[484]
0.5	-0.5	2.274811	0.1982	0.621663	0.03658	LHEweight_wgt[485]
0.5	-0.25	1.323555	0.1189	0.334972	0.01996	LHEweight_wgt[486]
0.5	0.0	0.656969	0.06223	0.147253	0.008986	LHEweight_wgt[487]
0.5	0.25	0.274423	0.02830	0.058342	0.003608	LHEweight_wgt[488]
0.5	0.5	0.176548	0.01778	0.068404	0.003902	LHEweight_wgt[489]
0.5	0.75	0.363132	0.03008	0.177385	0.009854	LHEweight_wgt[490]
0.5	1.0	0.834177	0.06550	0.385283	0.02145	LHEweight_wgt[491]
0.5	1.25	1.589682	0.1241	0.692099	0.03848	LHEweight_wgt[492]
0.5	1.5	2.629647	0.2047	1.097834	0.06136	LHEweight_wgt[493]
0.5	2.0	5.562958	0.4358	2.206057	0.1246	LHEweight_wgt[494]
0.5	3.0	14.843102	1.177	5.609519	0.3172	LHEweight_wgt[495]

Table A.3: κ_V and κ_t combinations generated for the two signal samples and their NLO cross sections. The *tHq* cross section is multiplied by the branching fraction of the enforced leptonic decay of the top quark (0.324) [150].

Sample	σ [pb]
TTWJetsToLNu_TuneCUETP8M1_13TeV-amcatnloFXFX-madspin-pythia8	0.2043 *
TTZToLLNuNu_M-10_TuneCUETP8M1_13TeV-amcatnlo-pythia8	0.2529 *
/store/cmst3/group/susy/gpetrucc/13TeV/u/TTLL_m1to10_L0_NoMS_for76X/	0.0283
WGToLNuG_TuneCUETP8M1_13TeV-madgraphMLM-pythia8	585.8
ZGTo2LG_TuneCUETP8M1_13TeV-amcatnloFXFX-pythia8	131.3
TGJets_TuneCUETP8M1_13TeV_amcatnlo_madspin_pythia8	2.967
TGJets_TuneCUETP8M1_13TeV_amcatnlo_madspin_pythia8	2.967
TTGJets_TuneCUETP8M1_13TeV-amcatnloFXFX-madspin-pythia8	3.697
WpWpJJ_EWK-QCD_TuneCUETP8M1_13TeV-madgraph-pythia8	0.03711
ZZZ_TuneCUETP8M1_13TeV-amcatnlo-pythia8	0.01398
WWZ_TuneCUETP8M1_13TeV-amcatnlo-pythia8	0.1651
WZZ_TuneCUETP8M1_13TeV-amcatnlo-pythia8	0.05565
WW_DoubleScattering_13TeV-pythia8	1.64
tZq_ll_4f_13TeV-amcatnlo-pythia8_TuneCUETP8M1	0.0758
ST_tW11_5f_LO_13TeV-MadGraph-pythia8	0.01123
TTTT_TuneCUETP8M1_13TeV-amcatnlo-pythia8	0.009103
WZTo3LNu_TuneCUETP8M1_13TeV-powheg-pythia8	4.4296
ZZTo4L_13TeV_powheg_pythia8	1.256
TTJets_SingleLeptFromTbar_TuneCUETP8M1_13TeV-madgraphMLM-pythia8	182.1754 *
TTJets_SingleLeptFromT_TuneCUETP8M1_13TeV-madgraphMLM-pythia8	182.1754 *
TTJets_DiLept_TuneCUETP8M1_13TeV-madgraphMLM-pythia8	87.3 *
DYJetsToLL_M-10to50_TuneCUETP8M1_13TeV-amcatnloFXFX-pythia8	18610
DYJetsToLL_M-50_TuneCUETP8M1_13TeV-madgraphMLM-pythia8	6024
WJetsToLNu_TuneCUETP8M1_13TeV-amcatnloFXFX-pythia8	61526.7
ST_tW_top_5f_inclusiveDecays_13TeV-powheg-pythia8_TuneCUETP8M1	35.6
ST_tW_antitop_5f_inclusiveDecays_13TeV-powheg-pythia8_TuneCUETP8M1	35.6
ST_t-channel_4f_leptonDecays_13TeV-amcatnlo-pythia8_TuneCUETP8M1	70.3144
ST_t-channel_antitop_4f_leptonDecays_13TeV-powheg-pythia8_TuneCUETP8M1	26.2278
ST_s-channel_4f_leptonDecays_13TeV-amcatnlo-pythia8_TuneCUETP8M1	3.68064
WWTo2L2Nu_13TeV-powheg	10.481
ttWJets_13TeV_madgraphMLM	0.6105
ttZJets_13TeV_madgraphMLM	0.5297/0.692

Table A.4: List of background samples used in this analysis (CMSSW 80X). The first section of the table lists the samples used in simulation to extract the final yields and shapes; the second section lists the samples of the processes for which the yields are estimated from data. The MC simulation is used to design the data driven methods and in the derivation of the associated systematic uncertainties. The third section list the leading order $t\bar{t}W$ and $t\bar{t}Z$ samples, which in addition to the ones marked with a *, where used in the BDT training.

³⁹⁵³ **Appendix B**

³⁹⁵⁴ **Aditional plots**

³⁹⁵⁵ **B.1 Pre-selection kinematic variables**

³⁹⁵⁶ Figures B.1, B.2 and B.3 show the distributions of some relevant kinematic variables,
³⁹⁵⁷ normalized to the cross section of the respective processes and to the integrated
³⁹⁵⁸ luminosity.

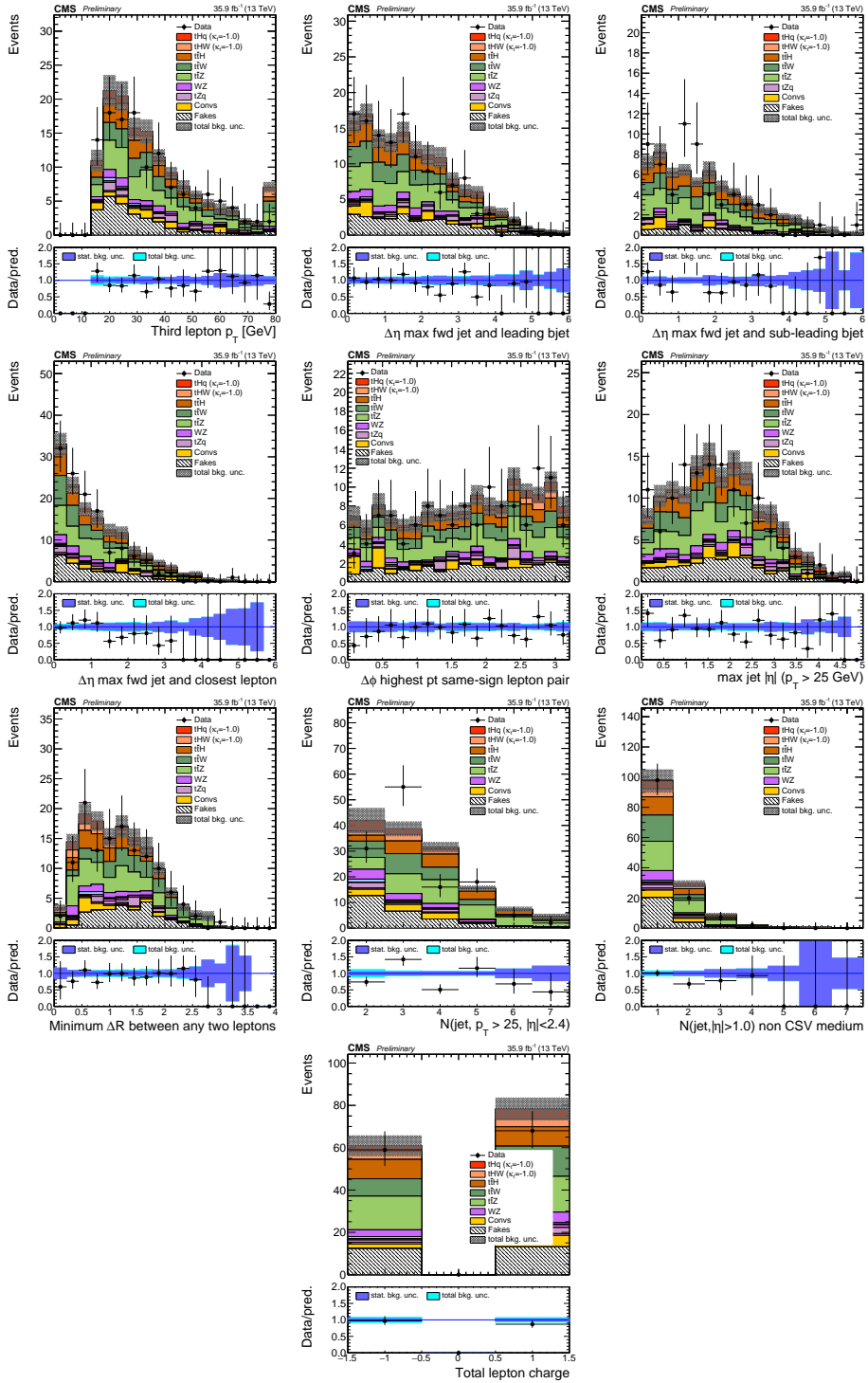


Figure B.1: Distributions of input variables to the BDT for signal discrimination, three lepton channel, normalized to their cross section and to 35.9 fb^{-1} .

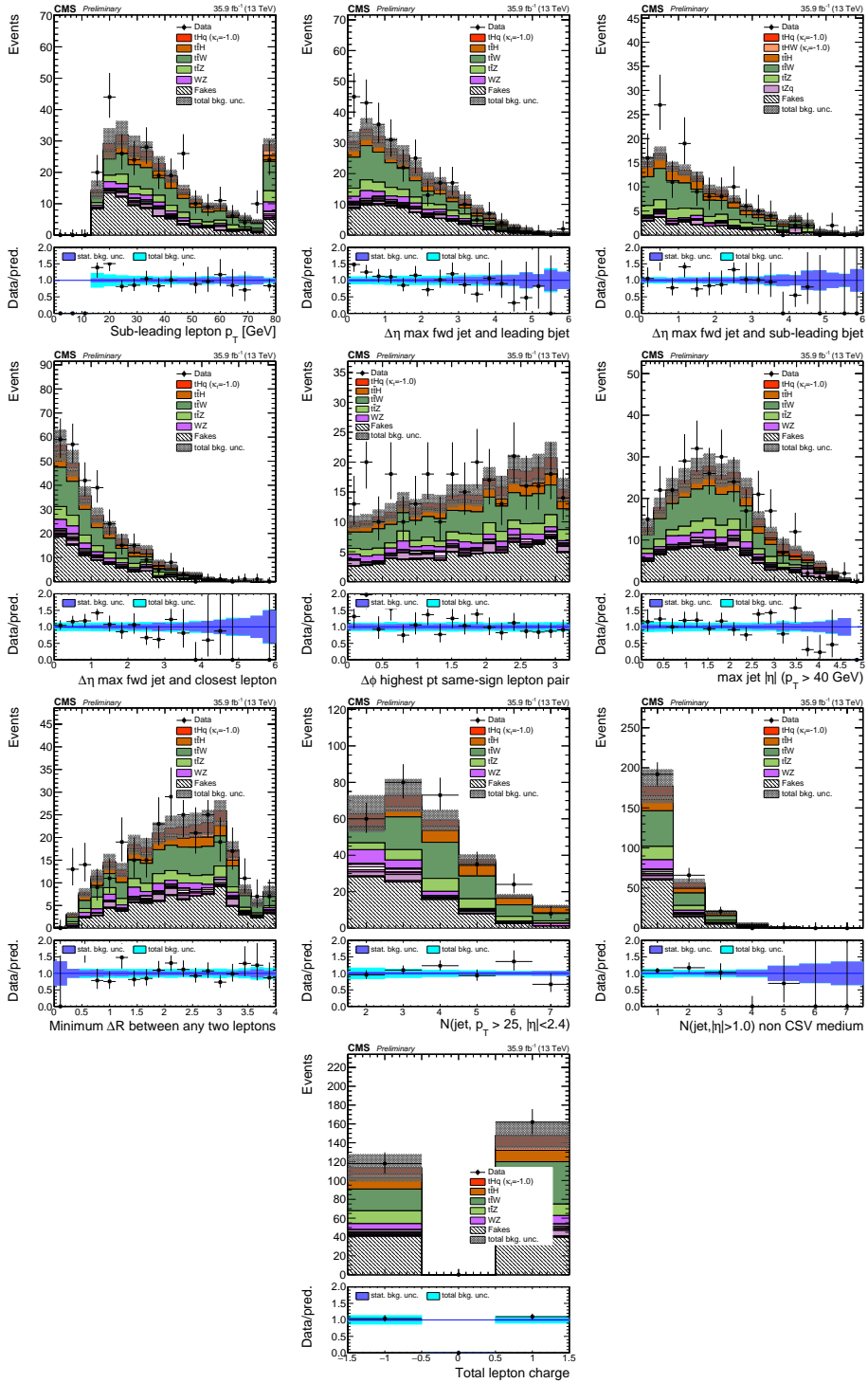


Figure B.2: Distributions of input variables to the BDT for signal discrimination, in $\mu^\pm\mu^\pm$ channel, normalized to their cross section and to 35.9fb^{-1} .

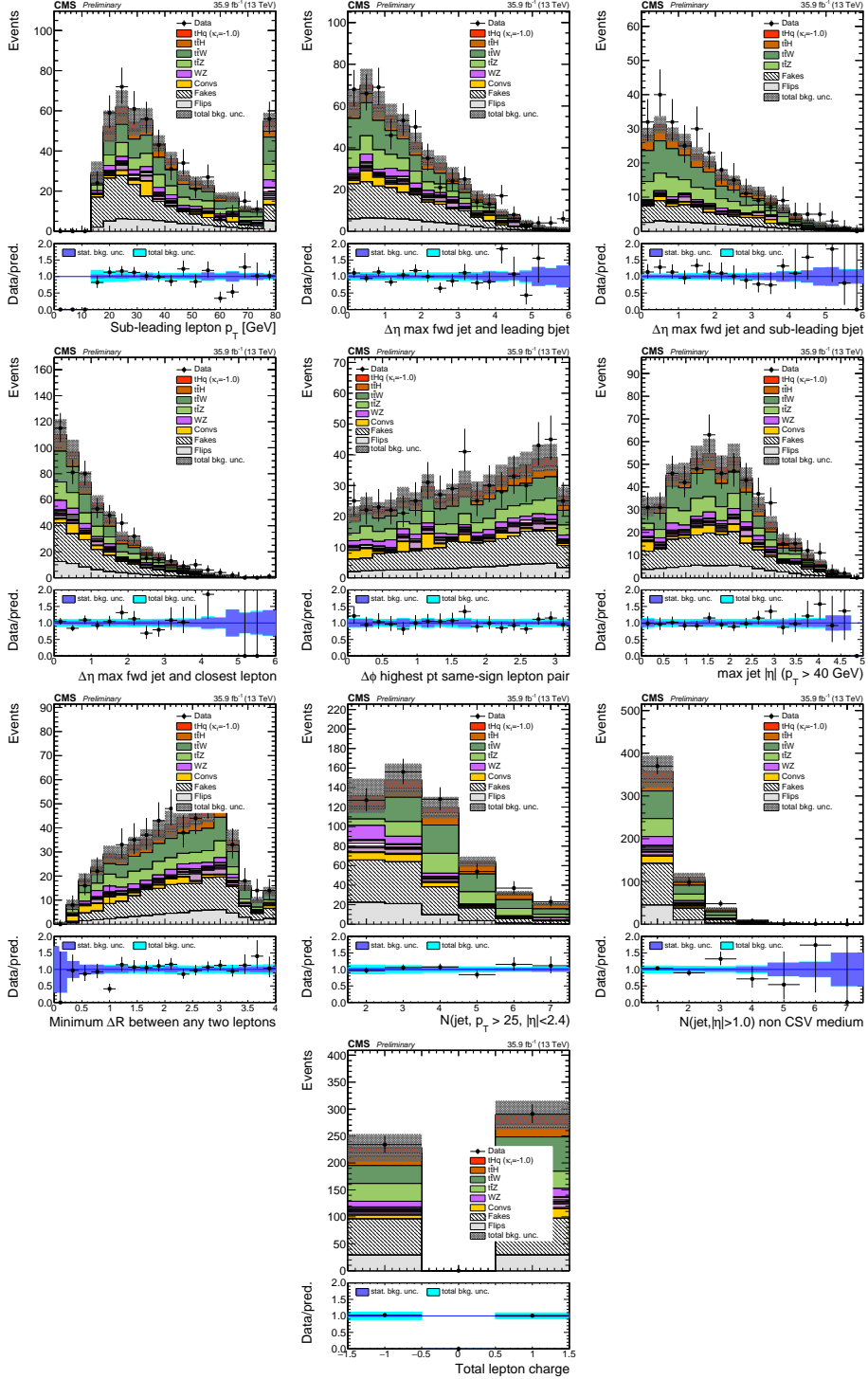


Figure B.3: Distributions of input variables to the BDT for signal discrimination, in $e^\pm\mu^\pm$ channel, normalized to their cross section and to 35.9 fb^{-1} .

3959 B.2 BDTG input variables for $2lss$ channel

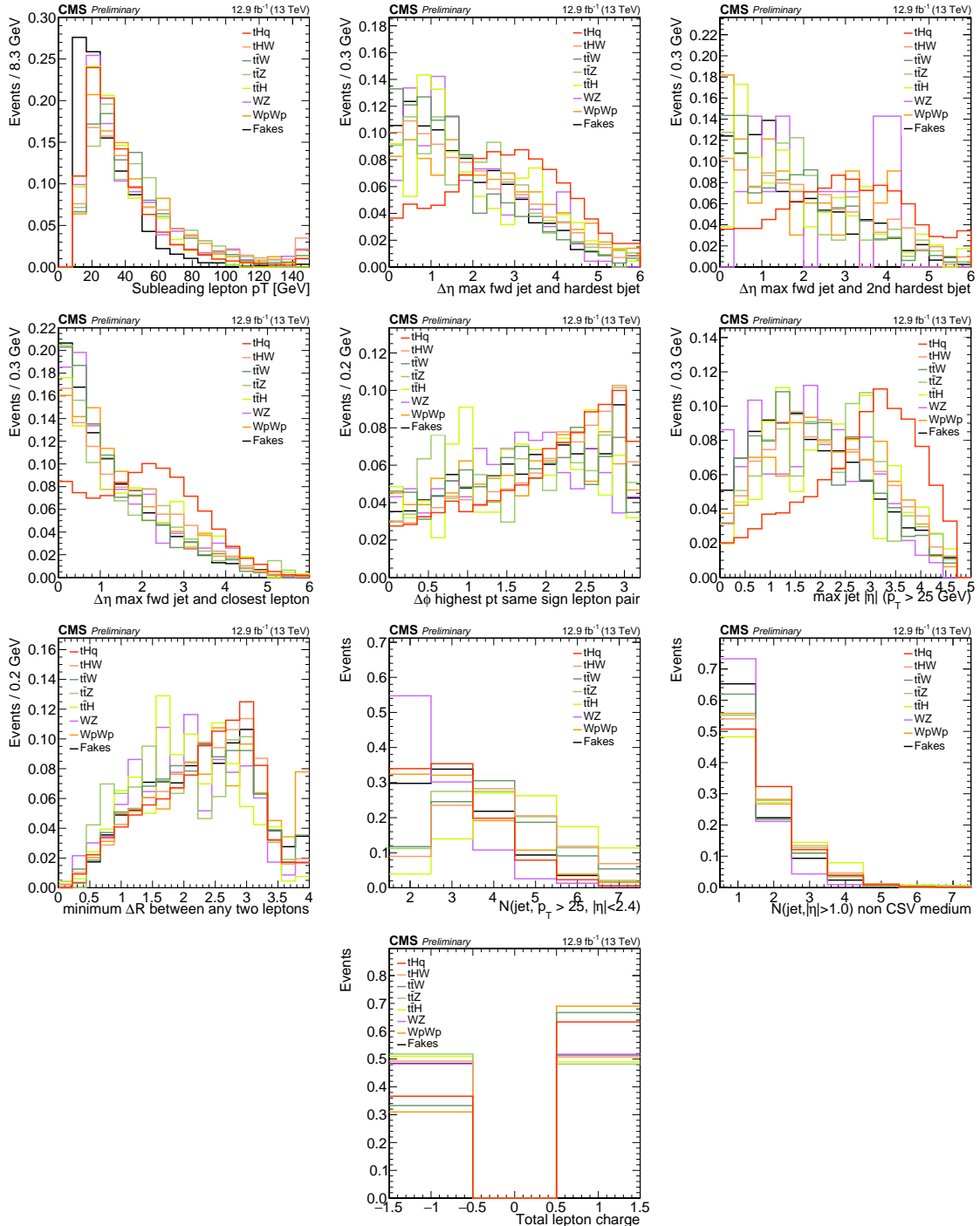


Figure B.4: Distributions of input variables to the BDT for signal discrimination, two lepton same sign channel.

3960 **B.3 Input variables distributions from BDTG**
 3961 classifiers

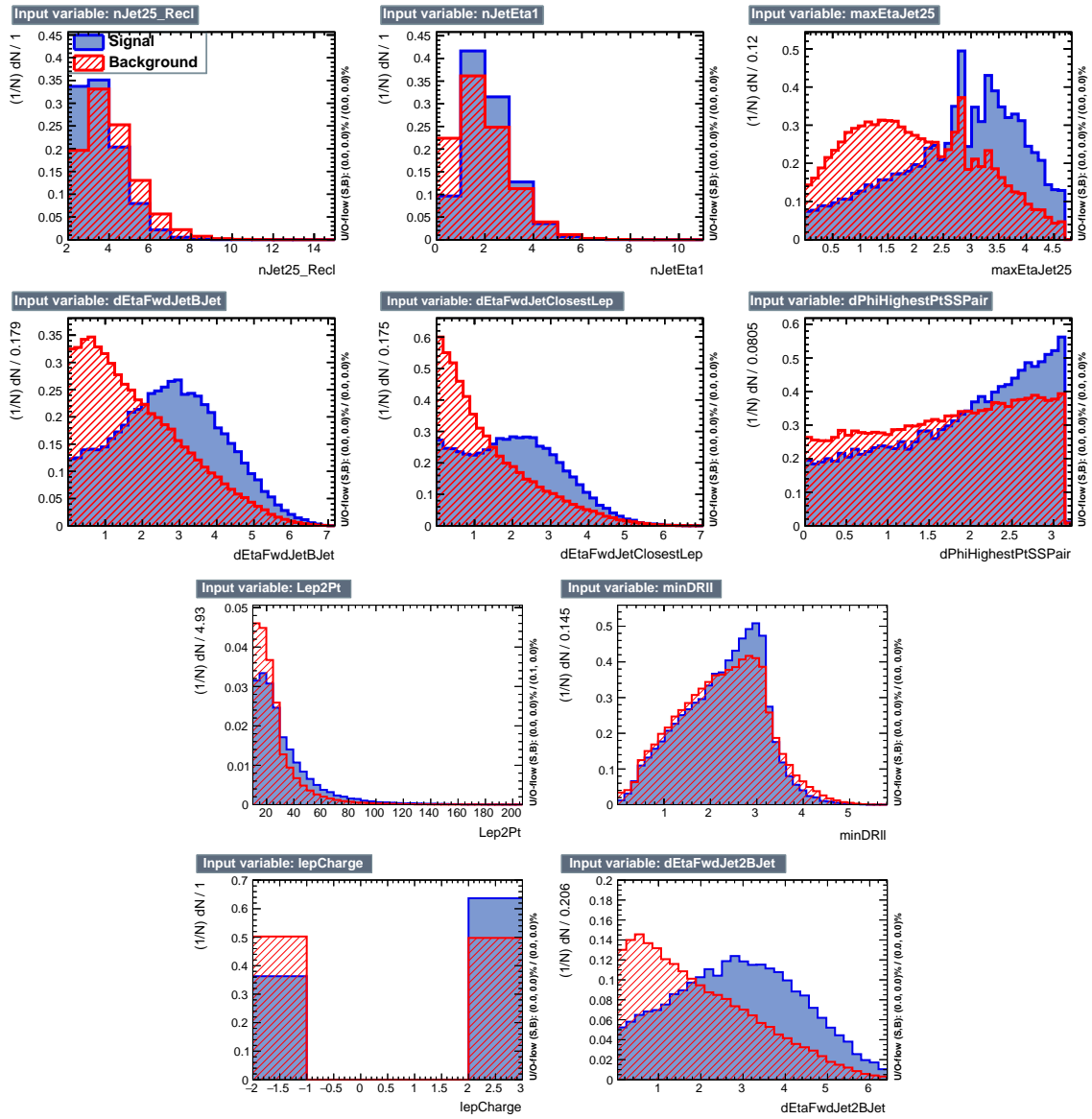


Figure B.5: BDT input variables as seen by BDTG classifier for the $2lss$ channel, tHq signal (blue) discriminated against $t\bar{t}$ background (red).

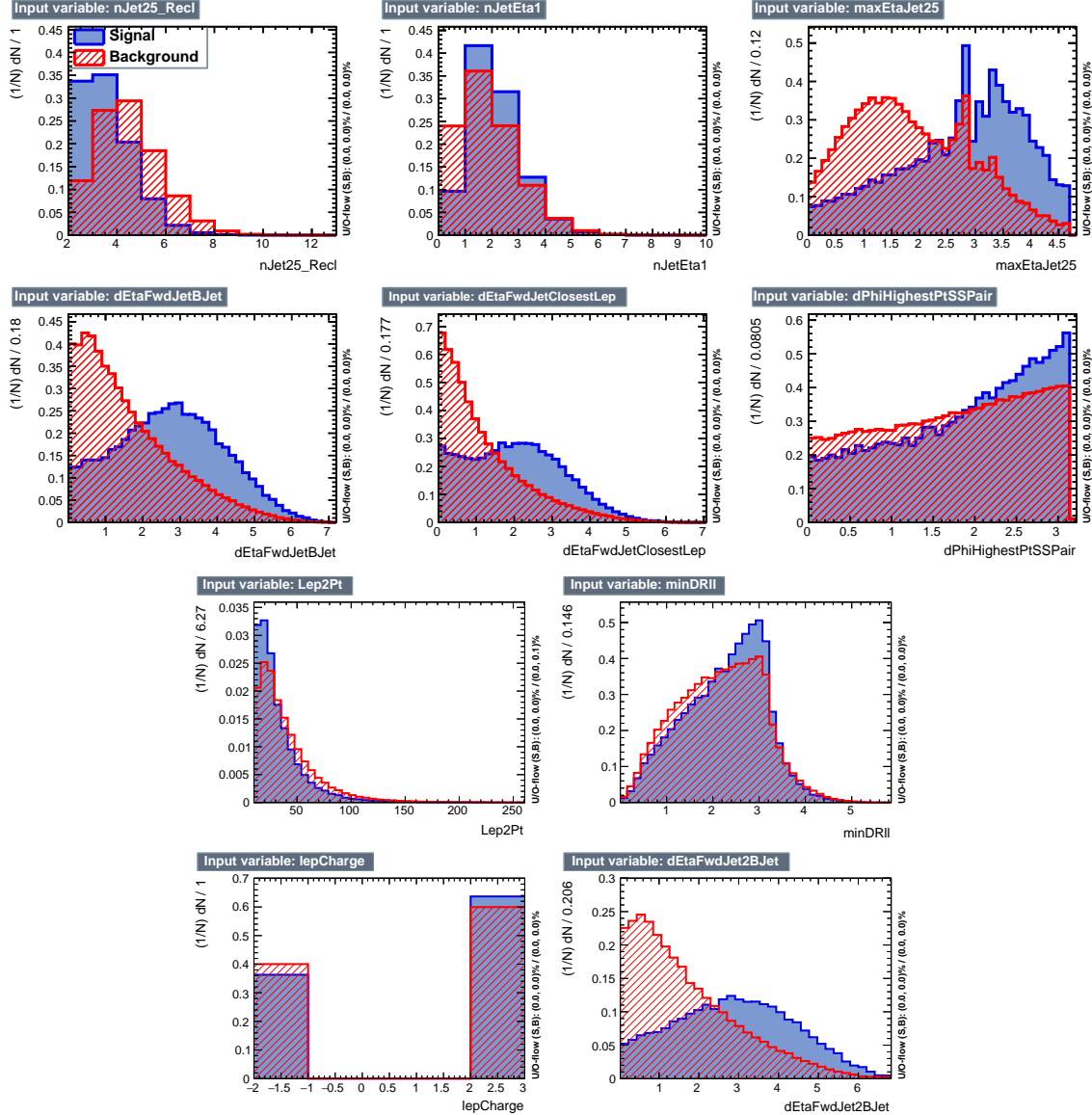


Figure B.6: BDT input variables as seen by BDTG classifier for the $2lss$ channel, tHq signal(blue) discriminated against $t\bar{t}V$ background (red).

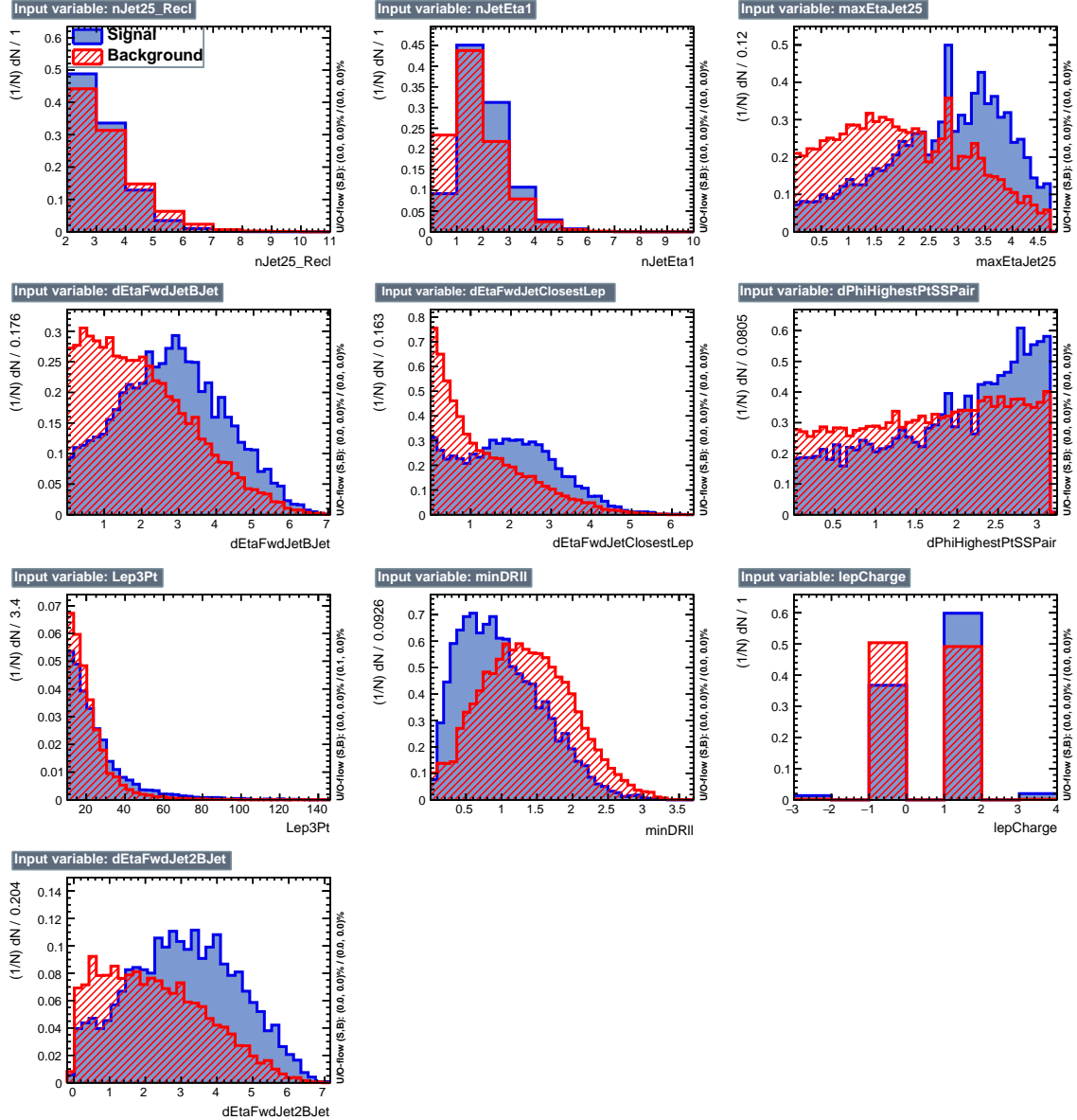


Figure B.7: BDT input variables as seen by BDTG classifier for the $3l$ channel, tHq signal (blue) discriminated against $t\bar{t}$ background (red).

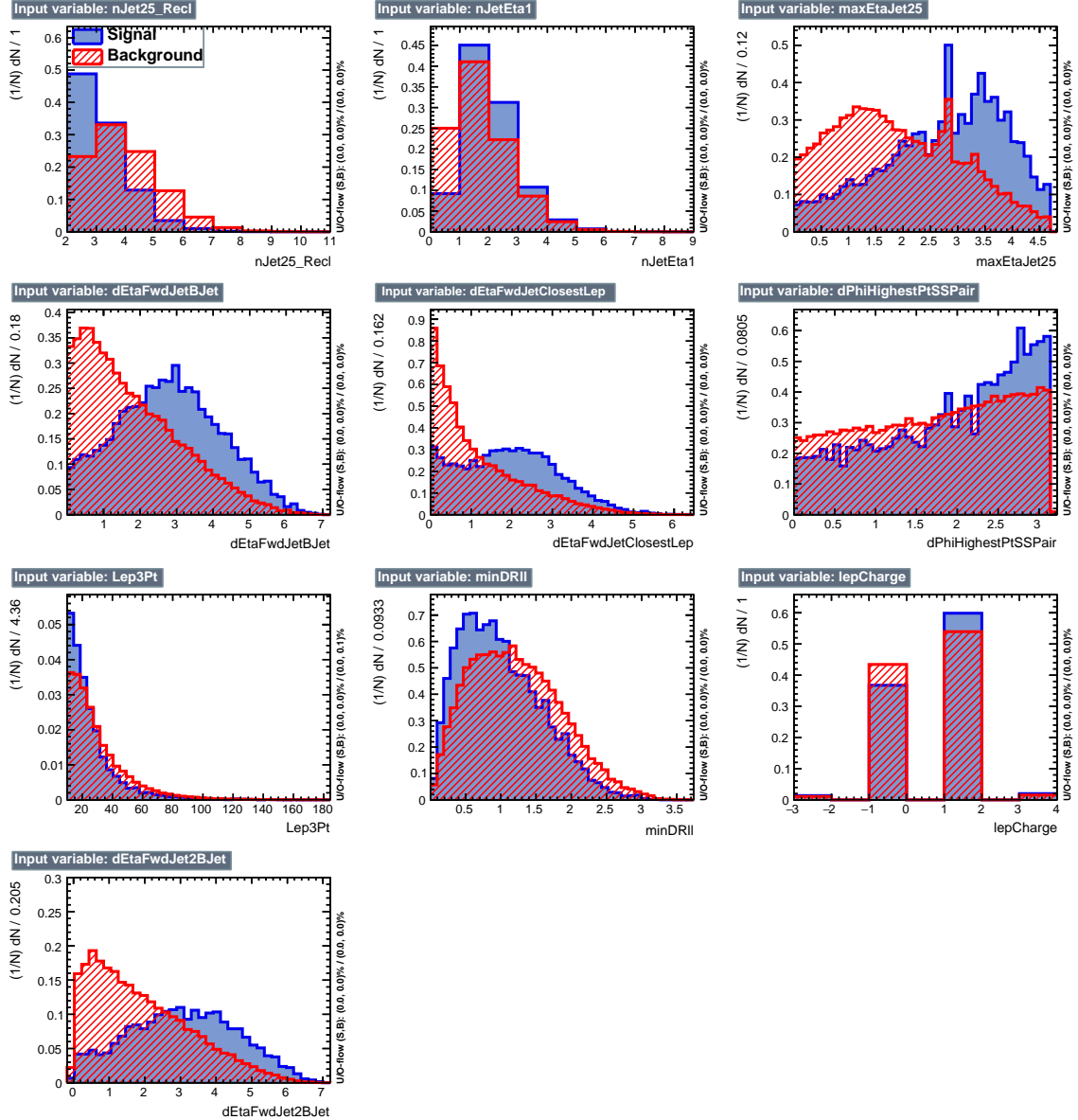


Figure B.8: BDT input variables as seen by BDTG classifier for the $3l$ channel, tHq signal (blue) discriminated against $t\bar{t}V$ background (red).

3962 **B.4 Pulls and impacts**

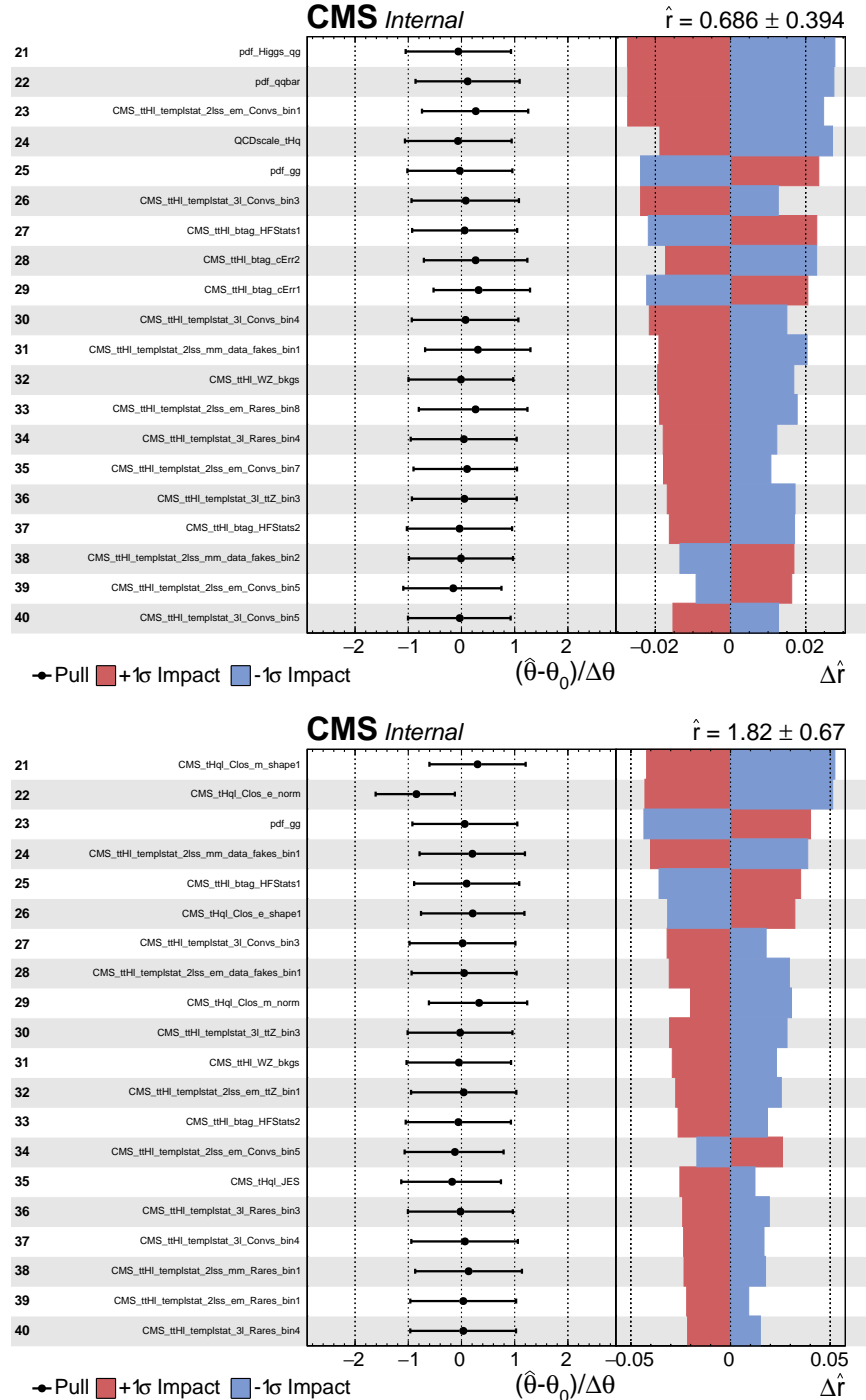


Figure B.9: Post-fit pulls and impacts of the next 20 nuisance parameters with largest impacts for the fit on the observed data, for the ITC (top) and SM (bottom) hypotheses.

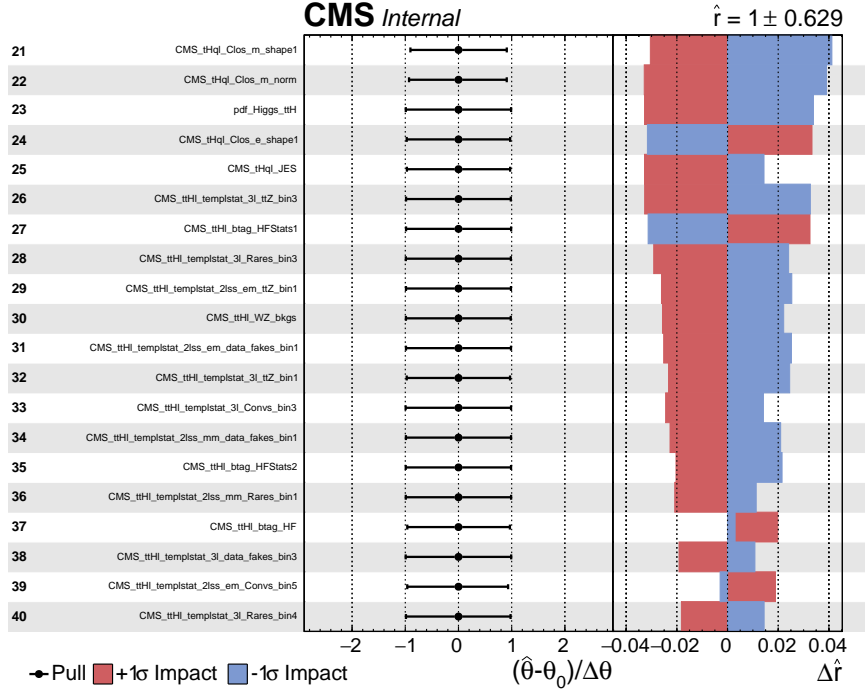


Figure B.10: Post-fit pulls and impacts of the next 20 nuisance parameters with largest impacts for a fit to the Asimov dataset with fixed signal strength, for the $\kappa_t/\kappa_V = -1.0$ hypothesis.

3963 **Appendix C**

3964 **Other binning strategies**

3965 Two additional strategies of clustering regions in the 2D plane of $BDTG_{tt}$ vs $BDTG_{ttV}$
3966 into bins were attempted, following studies done and documented in great detail in
3967 Reference [149]. A brief description is provided in the following.

3968 **Clustering by S/B ratio**

3969 In this method, the 2D plane is clustered into a given number of bins corresponding
3970 to regions where S/B is within a certain range. The bin borders are determined
3971 such that the number of background events in each bin is approximately equal. The
3972 resulting regions for $2lss$ and $3l$ events are shown in Figure C.1, while the expected
3973 distribution of signal and dominant backgrounds are shown in Figure C.2.

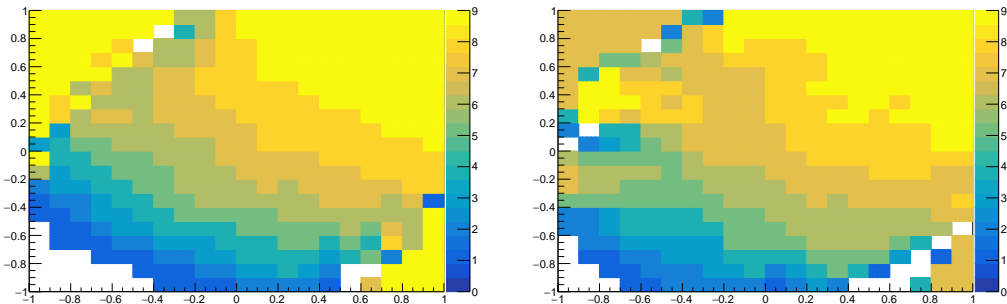


Figure C.1: Binning by S/B regions for $2lss$ (left) and $3l$ (right).

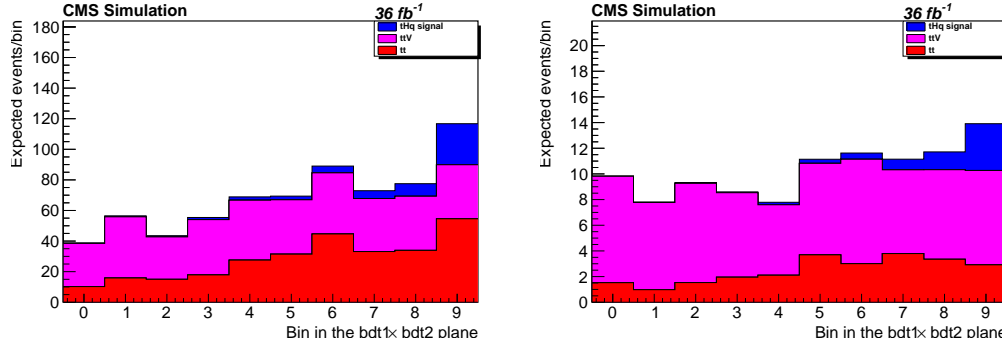


Figure C.2: Final bins (corresponding to S/B regions in the 2D plane) for $2lss$ and $3l$ (right).

Using this method, the resulting limits (for the $\kappa_t = -1, \kappa_V = 1$ scenario) are about 20% worse than with the binning in Section 6.9.6: $\mu^\pm\mu^\pm$ changed from 1.82 to 2.15, $3l$ changed from 1.52 to 1.75.

3977 *k*-Means geometric clustering

This method employs a recursive application of the *k*-means algorithm (see Appendix D in Reference [149]) to separate the 2D plane into geometric regions. The resulting clustering (using the $t\bar{t}H$ multilepton code on tHq signal and $t\bar{t}$ and $t\bar{t}V$ background events) are shown in Figure C.3. The expected distribution of events for the signal and dominant backgrounds in these bins is shown in Fig. C.4.

Similarly to the S/B ratio binning, the limits using the *k*-means clustering are significantly worse than those of the bins described before. In the $\mu^\pm\mu^\pm$ channel, the limit deteriorates from 1.82 to 2.05, whereas in $3l$ it changes from 1.58 to 1.78.

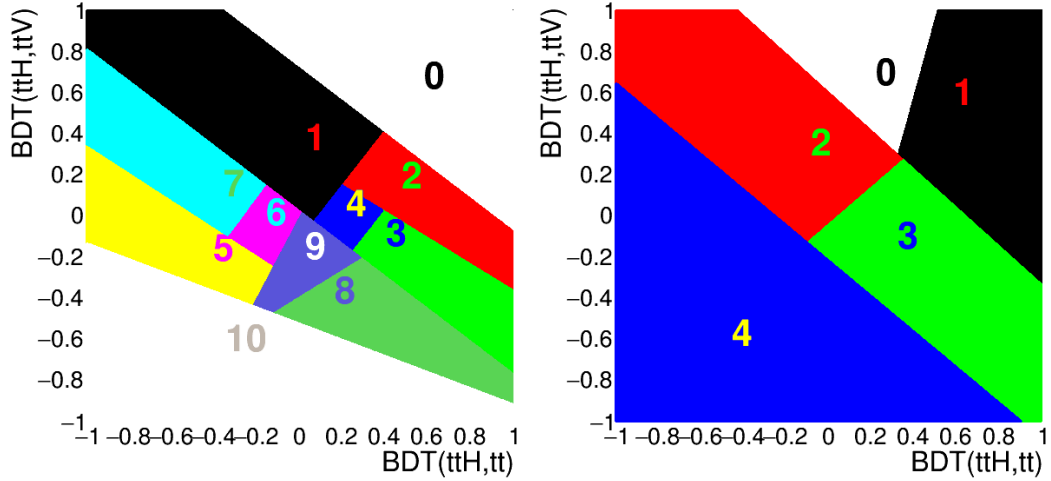


Figure C.3: Binning into geometric regions using a k -means algorithm for $2lss$ (left) and $3l$ (right).

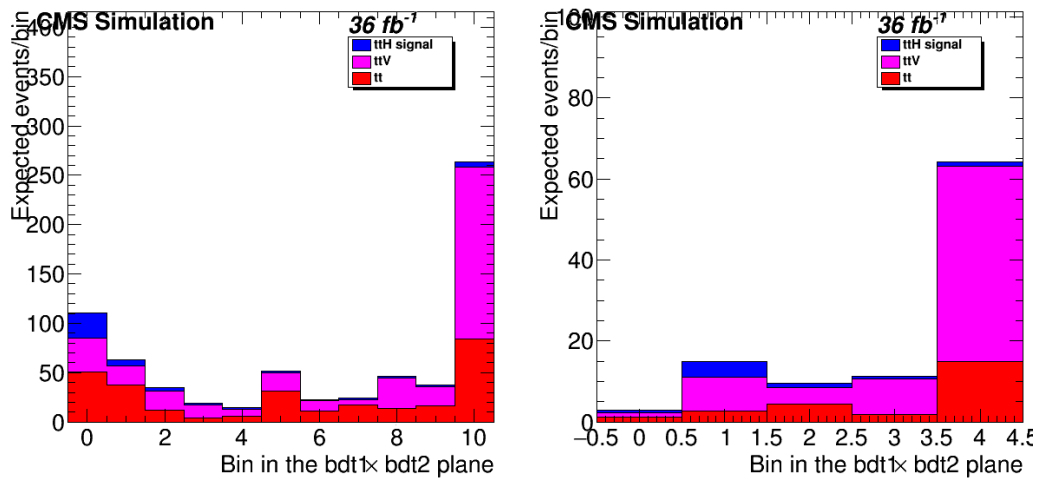


Figure C.4: Final bins using a k -means algorithm for $2lss$ (left) and $3l$ (right). Note that the bin numbering here is such that signal-like bins are lower.

³⁹⁸⁶ **Appendix D**

³⁹⁸⁷ **BDTG output variation with κ_V/κ_t**

³⁹⁸⁸ The BDTG classifier output was described in Section in the $\kappa_t = -1, \kappa_V = 1$ scenario; the
³⁹⁸⁹ change of BDTG classifiers output shape when varying the κ_V/κ_t coupling scenario
³⁹⁹⁰ is shown in Figure D.1 in the $3l$ channel for five different values of κ_t , with κ_V fixed
at 1.0.

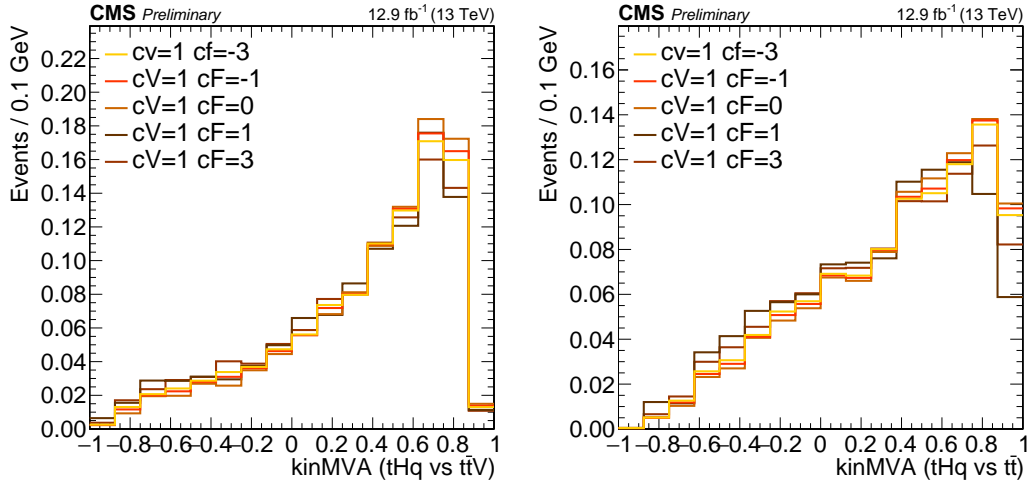


Figure D.1: Change of the BDTG classifiers output when varying κ_t coupling (κ_V is fixed at 1.0). Training vs. $t\bar{t}V$ (right) and vs. $t\bar{t}$ (left).

³⁹⁹¹

³⁹⁹² Given that the BDT classifier output shape does not change, it is enough to train
³⁹⁹³ the BDTG in one of the κ_t/κ_V points. It was chosen the SM point.

3994 **Appendix E**

3995 **tHq - $t\bar{t}H$ overlap**

3996 This section provides a quick overview of the differences and commonalities in event
3997 selections between this analysis and the $t\bar{t}H$ multilepton search [149]. The object
3998 selections of the two analysis are perfectly synchronized due to shared frameworks
3999 and samples. The only exception is the usage of forward jets ($|\eta| > 2.4, p_T > 40$ GeV)
4000 in this analysis. Such jets are not considered in the $t\bar{t}H$ analysis.

4001 Table E.1 gives an overview of the main differences in the event selections. Here,
4002 $E_T^{miss}_{LD}$ is defined as $E_T^{miss} \times 0.00397 + H_T^{miss} \times 0.00265$. Untagged jets in the tHq
4003 analysis are jets that do not pass the CSV loose working point and are either central
4004 ($|\eta| < 2.4, p_T > 25$ GeV) or forward ($|\eta| < 2.4, p_T > 40$ GeV). All jets in the $t\bar{t}H$ analysis
4005 are selected with $p_T > 25$ GeV. Lepton p_T cuts and the trigger selections are identical.

Channel	tHq	$t\bar{t}H$
3l	Z veto, 15bGeV $N_{jets}^{b, med.} \geq 1$ ≥ 1 un-tagged jet	Z veto, 10 GeV $N_{jets}^{b, med.} \geq 1$ OR $N_{jets}^{b, loose} \geq 2$ $E_T^{miss}_{LD} > 0.2$ OR $N_{jets}^{centr.} \geq 4$
2lss	$N_{jets}^{b, med.} \geq 1$ ≥ 1 un-tagged jet	$N_{jets}^{b, med.} \geq 1$ OR $N_{jets}^{b, loose} \geq 2$ $N_{jets}^{central} \geq 4$

Table E.1: Differences in event selection between this analysis and the $t\bar{t}H$ multilepton analysis.

4006 Table E.2 shows the total events yields in the individual channels, and the yield
 4007 of shared events between each channel, for the tHq signal sample, the $t\bar{t}H$ signal
 4008 sample, and the data. In the data, for the $3l$ channel, about 80% of events passing
 4009 the tHq selection also pass the $t\bar{t}H$ selection, constituting about 70% of that channel.
 4010 In the $2lss$ channel, about 50% of data events passing the tHq selection also pass the
 4011 $t\bar{t}H$ selection, but these events constitute almost 90% of the $t\bar{t}H$ selection in those
 4012 channels. Similar overlaps are also seen in the tHq and $t\bar{t}H$ signal samples.

4013 There is no migration between different channels and different selections, i.e., no
 4014 events passing the selection of a given tHq channel pass the selection of any other
 4015 channels of $t\bar{t}H$ and vice versa.

tHq sample	tHq	$t\bar{t}H$	Common	(% tHq)	(% $t\bar{t}H$)
$\mu^\pm\mu^\pm$	7400	2353	2166	29.3	92.1
$e^\pm\mu^\pm$	11158	3600	3321	29.8	92.2
$e^\pm e^\pm$	3550	1106	1025	28.9	92.7
$\ell\ell\ell$	3115	2923	2347	75.3	80.3

$t\bar{t}H$ sample	tHq	$t\bar{t}H$	Common	(% tHq)	(% $t\bar{t}H$)
$\mu^\pm\mu^\pm$	32612	28703	26547	81.4	92.5
$e^\pm\mu^\pm$	48088	42521	39164	81.4	92.1
$e^\pm e^\pm$	15476	12869	11896	76.9	92.4
$\ell\ell\ell$	26627	30598	25288	95.0	82.6

Data	tHq	$t\bar{t}H$	Common	(% tHq)	(% $t\bar{t}H$)
$\mu^\pm\mu^\pm$	280	160	140	50.0	87.5
$e^\pm\mu^\pm$	525	280	242	46.1	86.4
$e^\pm e^\pm$	208	90	79	38.0	87.8
$\ell\ell\ell$	126	154	104	82.5	67.5

Table E.2: Individual and shared event yields between this analysis (tHq) and $t\bar{t}H$ multilepton selections.

⁴⁰¹⁶ **Appendix F**

⁴⁰¹⁷ **Forward jet impact plots**

⁴⁰¹⁸ The impact of the data/MC disagreement for forward jet η is observed to reduce with
⁴⁰¹⁹ higher p_T cuts; Figures F.1, F.2 and F.3 show this reduction in the impact of the
⁴⁰²⁰ forward jet η nuisance in the fit.

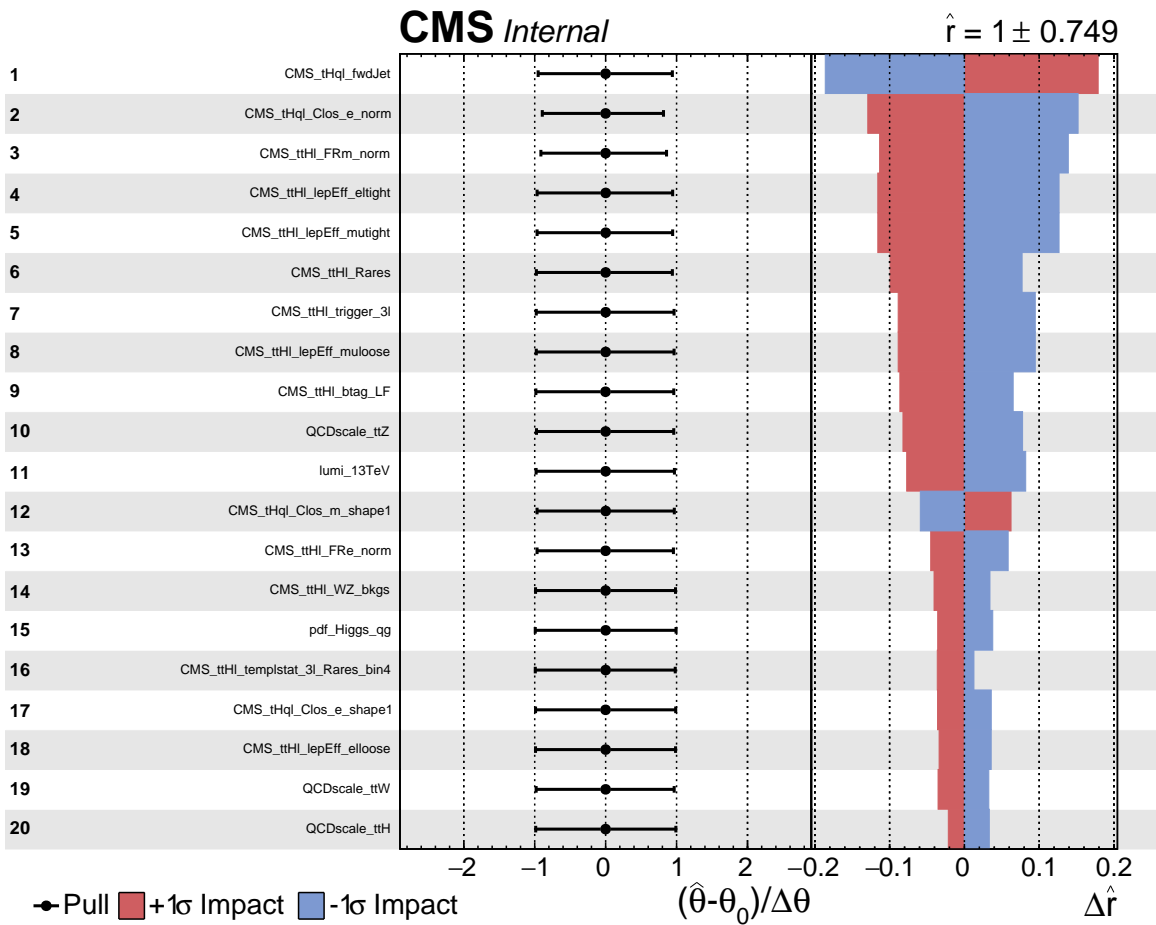


Figure F.1: Post-fit pulls and impacts of the 20 nuisance parameters with p_T cut 25 GeV for the forward jet.

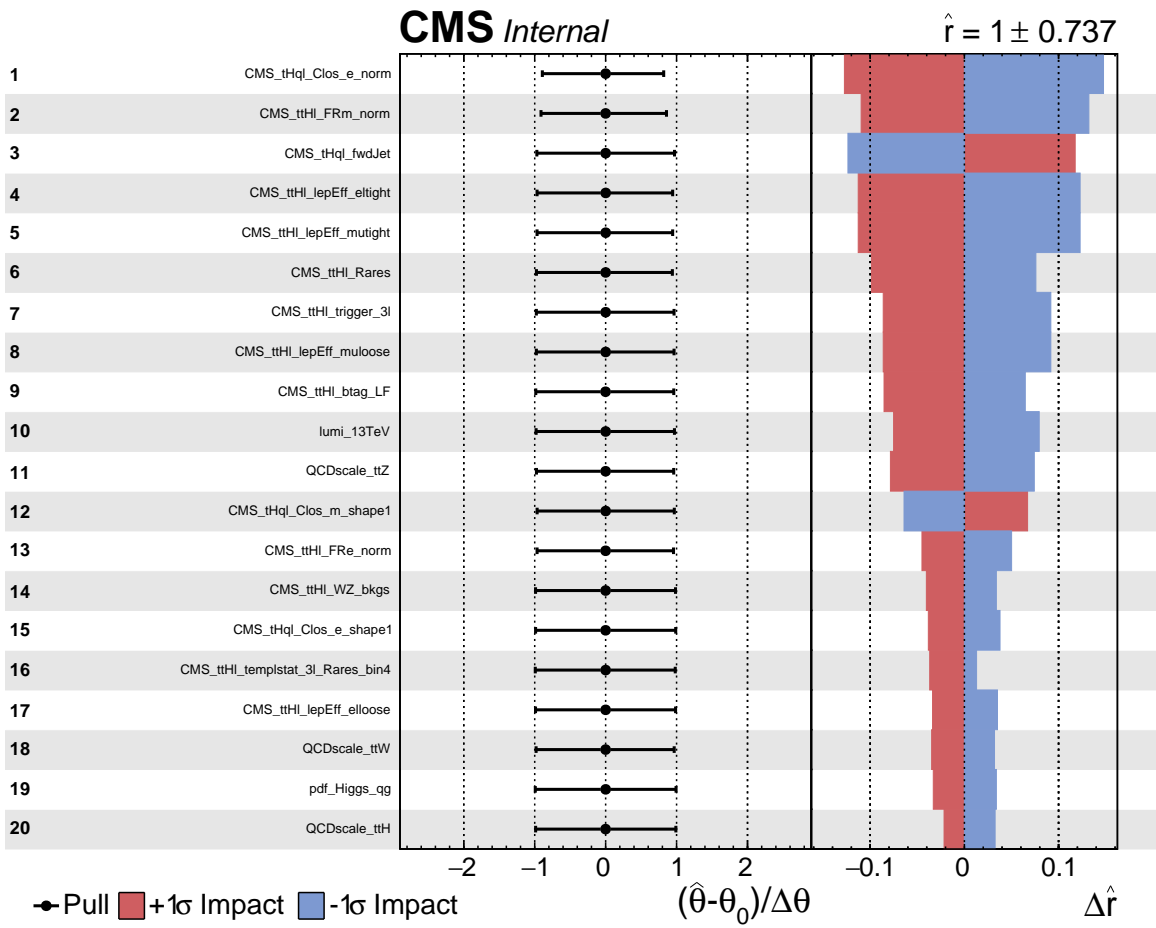


Figure F.2: Post-fit pulls and impacts of the 20 nuisance parameters with p_T cut 30 GeV for the forward jet.

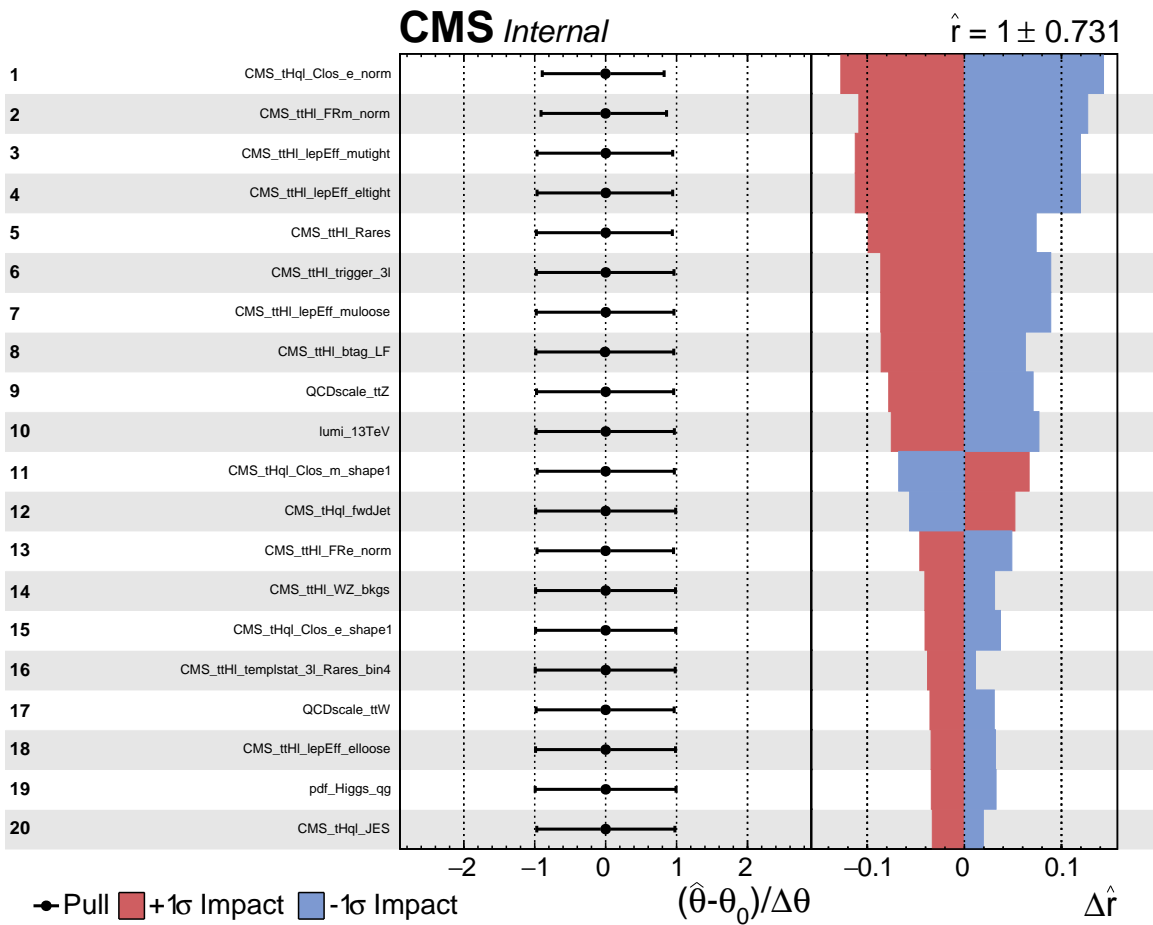


Figure F.3: Post-fit pulls and impacts of the 20 nuisance parameters with p_T cut 40 GeV for the forward jet.

⁴⁰²¹ **Appendix G**

⁴⁰²² **Cross sections and Branching**

⁴⁰²³ **ratios scalings**

κ_V	κ_t	HWW	HZZ	H $\tau\tau$	H $\mu\mu$	Hbb	Hcc	H $\gamma\gamma$	HZ γ	Hgg
0.5	-6.0	0.0827	0.0827	11.9098	11.9098	0.3308	0.3308	0.3308	0.3308	0.3308
0.5	-4.0	0.1417	0.1417	9.0699	9.0699	0.5669	0.5669	0.5669	0.5669	0.5669
0.5	-3.0	0.1889	0.1889	6.7999	6.7999	0.7555	0.7555	0.7555	0.7555	0.7555
0.5	-2.5	0.2173	0.2173	5.4325	5.4325	0.8692	0.8692	0.8692	0.8692	0.8692
0.5	-2.0	0.2478	0.2478	3.9647	3.9647	0.9912	0.9912	0.9912	0.9912	0.9912
0.5	-1.5	0.2782	0.2782	2.5034	2.5034	1.1126	1.1126	1.1126	1.1126	1.1126
0.5	-1.333	0.2877	0.2877	2.0448	2.0448	1.1508	1.1508	1.1508	1.1508	1.1508
0.5	-1.25	0.2922	0.2922	1.8264	1.8264	1.1689	1.1689	1.1689	1.1689	1.1689
0.5	-1.0	0.3048	0.3048	1.2194	1.2194	1.2194	1.2194	1.2194	1.2194	1.2194
0.5	-0.833	0.3122	0.3122	0.8665	0.8665	1.2487	1.2487	1.2487	1.2487	1.2487
0.5	-0.75	0.3154	0.3154	0.7097	0.7097	1.2617	1.2617	1.2617	1.2617	1.2617
0.5	-0.667	0.3184	0.3184	0.5666	0.5666	1.2736	1.2736	1.2736	1.2736	1.2736
0.5	-0.5	0.3235	0.3235	0.3235	0.3235	1.2938	1.2938	1.2938	1.2938	1.2938
0.5	-0.333	0.3272	0.3272	0.1451	0.1451	1.3087	1.3087	1.3087	1.3087	1.3087
0.5	-0.25	0.3285	0.3285	0.0821	0.0821	1.3139	1.3139	1.3139	1.3139	1.3139
0.5	-0.167	0.3294	0.3294	0.0367	0.0367	1.3177	1.3177	1.3177	1.3177	1.3177
0.5	0.0	0.3302	0.3302	0.0000	0.0000	1.3207	1.3207	1.3207	1.3207	1.3207
0.5	0.167	0.3294	0.3294	0.0367	0.0367	1.3177	1.3177	1.3177	1.3177	1.3177
0.5	0.25	0.3285	0.3285	0.0821	0.0821	1.3139	1.3139	1.3139	1.3139	1.3139
0.5	0.333	0.3272	0.3272	0.1451	0.1451	1.3087	1.3087	1.3087	1.3087	1.3087
0.5	0.5	0.3235	0.3235	0.3235	0.3235	1.2938	1.2938	1.2938	1.2938	1.2938
0.5	0.667	0.3184	0.3184	0.5666	0.5666	1.2736	1.2736	1.2736	1.2736	1.2736
0.5	0.75	0.3154	0.3154	0.7097	0.7097	1.2617	1.2617	1.2617	1.2617	1.2617
0.5	0.833	0.3122	0.3122	0.8665	0.8665	1.2487	1.2487	1.2487	1.2487	1.2487
0.5	1.0	0.3048	0.3048	1.2194	1.2194	1.2194	1.2194	1.2194	1.2194	1.2194
0.5	1.25	0.2922	0.2922	1.8264	1.8264	1.1689	1.1689	1.1689	1.1689	1.1689
0.5	1.333	0.2877	0.2877	2.0448	2.0448	1.1508	1.1508	1.1508	1.1508	1.1508
0.5	1.5	0.2782	0.2782	2.5034	2.5034	1.1126	1.1126	1.1126	1.1126	1.1126
0.5	2.0	0.2478	0.2478	3.9647	3.9647	0.9912	0.9912	0.9912	0.9912	0.9912
0.5	2.5	0.2173	0.2173	5.4325	5.4325	0.8692	0.8692	0.8692	0.8692	0.8692
0.5	3.0	0.1889	0.1889	6.7999	6.7999	0.7555	0.7555	0.7555	0.7555	0.7555
0.5	4.0	0.1417	0.1417	9.0699	9.0699	0.5669	0.5669	0.5669	0.5669	0.5669
0.5	6.0	0.0827	0.0827	11.9098	11.9098	0.3308	0.3308	0.3308	0.3308	0.3308

Table G.1: Scalings of Higgs decay branching ratios vs. κ_t and $\kappa_V = 0.5$ for the non-resolved model.

κ_V	κ_t	HWW	HZZ	H $\tau\tau$	H $\mu\mu$	Hbb	Hcc	H $\gamma\gamma$	HZ γ	Hgg
1.0	-6.0	0.3122	0.3122	11.2408	11.2408	0.3122	0.3122	0.3122	0.3122	0.3122
1.0	-4.0	0.5144	0.5144	8.2305	8.2305	0.5144	0.5144	0.5144	0.5144	0.5144
1.0	-3.0	0.6651	0.6651	5.9862	5.9862	0.6651	0.6651	0.6651	0.6651	0.6651
1.0	-2.5	0.7517	0.7517	4.6979	4.6979	0.7517	0.7517	0.7517	0.7517	0.7517
1.0	-2.0	0.8412	0.8412	3.3647	3.3647	0.8412	0.8412	0.8412	0.8412	0.8412
1.0	-1.5	0.9271	0.9271	2.0859	2.0859	0.9271	0.9271	0.9271	0.9271	0.9271
1.0	-1.333	0.9534	0.9534	1.6941	1.6941	0.9534	0.9534	0.9534	0.9534	0.9534
1.0	-1.25	0.9658	0.9658	1.5091	1.5091	0.9658	0.9658	0.9658	0.9658	0.9658
1.0	-1.0	1.0000	1.0000	1.0000	1.0000	1.0000	1.0000	1.0000	1.0000	1.0000
1.0	-0.833	1.0196	1.0196	0.7075	0.7075	1.0196	1.0196	1.0196	1.0196	1.0196
1.0	-0.75	1.0283	1.0283	0.5784	0.5784	1.0283	1.0283	1.0283	1.0283	1.0283
1.0	-0.667	1.0362	1.0362	0.4610	0.4610	1.0362	1.0362	1.0362	1.0362	1.0362
1.0	-0.5	1.0495	1.0495	0.2624	0.2624	1.0495	1.0495	1.0495	1.0495	1.0495
1.0	-0.333	1.0593	1.0593	0.1175	0.1175	1.0593	1.0593	1.0593	1.0593	1.0593
1.0	-0.25	1.0627	1.0627	0.0664	0.0664	1.0627	1.0627	1.0627	1.0627	1.0627
1.0	-0.167	1.0652	1.0652	0.0297	0.0297	1.0652	1.0652	1.0652	1.0652	1.0652
1.0	0.0	1.0672	1.0672	0.0000	0.0000	1.0672	1.0672	1.0672	1.0672	1.0672
1.0	0.167	1.0652	1.0652	0.0297	0.0297	1.0652	1.0652	1.0652	1.0652	1.0652
1.0	0.25	1.0627	1.0627	0.0664	0.0664	1.0627	1.0627	1.0627	1.0627	1.0627
1.0	0.333	1.0593	1.0593	0.1175	0.1175	1.0593	1.0593	1.0593	1.0593	1.0593
1.0	0.5	1.0495	1.0495	0.2624	0.2624	1.0495	1.0495	1.0495	1.0495	1.0495
1.0	0.667	1.0362	1.0362	0.4610	0.4610	1.0362	1.0362	1.0362	1.0362	1.0362
1.0	0.75	1.0283	1.0283	0.5784	0.5784	1.0283	1.0283	1.0283	1.0283	1.0283
1.0	0.833	1.0196	1.0196	0.7075	0.7075	1.0196	1.0196	1.0196	1.0196	1.0196
1.0	1.0	1.0000	1.0000	1.0000	1.0000	1.0000	1.0000	1.0000	1.0000	1.0000
1.0	1.25	0.9658	0.9658	1.5091	1.5091	0.9658	0.9658	0.9658	0.9658	0.9658
1.0	1.333	0.9534	0.9534	1.6941	1.6941	0.9534	0.9534	0.9534	0.9534	0.9534
1.0	1.5	0.9271	0.9271	2.0859	2.0859	0.9271	0.9271	0.9271	0.9271	0.9271
1.0	2.0	0.8412	0.8412	3.3647	3.3647	0.8412	0.8412	0.8412	0.8412	0.8412
1.0	2.5	0.7517	0.7517	4.6979	4.6979	0.7517	0.7517	0.7517	0.7517	0.7517
1.0	3.0	0.6651	0.6651	5.9862	5.9862	0.6651	0.6651	0.6651	0.6651	0.6651
1.0	4.0	0.5144	0.5144	8.2305	8.2305	0.5144	0.5144	0.5144	0.5144	0.5144
1.0	6.0	0.3122	0.3122	11.2408	11.2408	0.3122	0.3122	0.3122	0.3122	0.3122

Table G.2: Scalings of Higgs decay branching ratios vs. κ_t and $\kappa_V = 1.0$ for the non-resolved model.

κ_V	κ_t	HWW	HZZ	H $\tau\tau$	H $\mu\mu$	Hbb	Hcc	H $\gamma\gamma$	HZ γ	Hgg
1.5	-6.0	0.6424	0.6424	10.2785	10.2785	0.2855	0.2855	0.2855	0.2855	0.2855
1.5	-4.0	1.0028	1.0028	7.1307	7.1307	0.4457	0.4457	0.4457	0.4457	0.4457
1.5	-3.0	1.2477	1.2477	4.9909	4.9909	0.5545	0.5545	0.5545	0.5545	0.5545
1.5	-2.5	1.3802	1.3802	3.8338	3.8338	0.6134	0.6134	0.6134	0.6134	0.6134
1.5	-2.0	1.5115	1.5115	2.6870	2.6870	0.6718	0.6718	0.6718	0.6718	0.6718
1.5	-1.5	1.6322	1.6322	1.6322	1.6322	0.7254	0.7254	0.7254	0.7254	0.7254
1.5	-1.333	1.6682	1.6682	1.3175	1.3175	0.7414	0.7414	0.7414	0.7414	0.7414
1.5	-1.25	1.6851	1.6851	1.1702	1.1702	0.7489	0.7489	0.7489	0.7489	0.7489
1.5	-1.0	1.7310	1.7310	0.7693	0.7693	0.7693	0.7693	0.7693	0.7693	0.7693
1.5	-0.833	1.7570	1.7570	0.5419	0.5419	0.7809	0.7809	0.7809	0.7809	0.7809
1.5	-0.75	1.7684	1.7684	0.4421	0.4421	0.7860	0.7860	0.7860	0.7860	0.7860
1.5	-0.667	1.7788	1.7788	0.3517	0.3517	0.7906	0.7906	0.7906	0.7906	0.7906
1.5	-0.5	1.7962	1.7962	0.1996	0.1996	0.7983	0.7983	0.7983	0.7983	0.7983
1.5	-0.333	1.8089	1.8089	0.0891	0.0891	0.8039	0.8039	0.8039	0.8039	0.8039
1.5	-0.25	1.8133	1.8133	0.0504	0.0504	0.8059	0.8059	0.8059	0.8059	0.8059
1.5	-0.167	1.8165	1.8165	0.0225	0.0225	0.8073	0.8073	0.8073	0.8073	0.8073
1.5	0.0	1.8191	1.8191	0.0000	0.0000	0.8085	0.8085	0.8085	0.8085	0.8085
1.5	0.167	1.8165	1.8165	0.0225	0.0225	0.8073	0.8073	0.8073	0.8073	0.8073
1.5	0.25	1.8133	1.8133	0.0504	0.0504	0.8059	0.8059	0.8059	0.8059	0.8059
1.5	0.333	1.8089	1.8089	0.0891	0.0891	0.8039	0.8039	0.8039	0.8039	0.8039
1.5	0.5	1.7962	1.7962	0.1996	0.1996	0.7983	0.7983	0.7983	0.7983	0.7983
1.5	0.667	1.7788	1.7788	0.3517	0.3517	0.7906	0.7906	0.7906	0.7906	0.7906
1.5	0.75	1.7684	1.7684	0.4421	0.4421	0.7860	0.7860	0.7860	0.7860	0.7860
1.5	0.833	1.7570	1.7570	0.5419	0.5419	0.7809	0.7809	0.7809	0.7809	0.7809
1.5	1.0	1.7310	1.7310	0.7693	0.7693	0.7693	0.7693	0.7693	0.7693	0.7693
1.5	1.25	1.6851	1.6851	1.1702	1.1702	0.7489	0.7489	0.7489	0.7489	0.7489
1.5	1.333	1.6682	1.6682	1.3175	1.3175	0.7414	0.7414	0.7414	0.7414	0.7414
1.5	1.5	1.6322	1.6322	1.6322	1.6322	0.7254	0.7254	0.7254	0.7254	0.7254
1.5	2.0	1.5115	1.5115	2.6870	2.6870	0.6718	0.6718	0.6718	0.6718	0.6718
1.5	2.5	1.3802	1.3802	3.8338	3.8338	0.6134	0.6134	0.6134	0.6134	0.6134
1.5	3.0	1.2477	1.2477	4.9909	4.9909	0.5545	0.5545	0.5545	0.5545	0.5545
1.5	4.0	1.0028	1.0028	7.1307	7.1307	0.4457	0.4457	0.4457	0.4457	0.4457
1.5	6.0	0.6424	0.6424	10.2785	10.2785	0.2855	0.2855	0.2855	0.2855	0.2855

Table G.3: Scalings of Higgs decay branching ratios vs. κ_t and $\kappa_V = 1.5$ for the non-resolved model.

κ_V	κ_t	ttHWW	ttHZZ	ttH $\tau\tau$	tHqWW	tHqZZ	tHq $\tau\tau$	tHWWW	tHWZZ	tHW $\tau\tau$
0.5	-6.0	2.9775	2.9775	428.7530	9.2066	9.2066	1325.7460	9.7660	9.7660	1406.3049
0.5	-4.0	2.2675	2.2675	145.1182	7.5740	7.5740	484.7357	7.8819	7.8819	504.4411
0.5	-3.0	1.7000	1.7000	61.1988	6.1214	6.1214	220.3702	6.2562	6.2562	225.2227
0.5	-2.5	1.3581	1.3581	33.9529	5.1857	5.1857	129.6430	5.2277	5.2277	130.6931
0.5	-2.0	0.9912	0.9912	15.8589	4.1227	4.1227	65.9633	4.0762	4.0762	65.2197
0.5	-1.5	0.6259	0.6259	5.6327	2.9838	2.9838	26.8544	2.8645	2.8645	25.7805
0.5	-1.333	0.5112	0.5112	3.6333	2.6025	2.6025	18.4974	2.4648	2.4648	17.5190
0.5	-1.25	0.4566	0.4566	2.8538	2.4154	2.4154	15.0962	2.2700	2.2700	14.1878
0.5	-1.0	0.3048	0.3048	1.2194	1.8696	1.8696	7.4784	1.7078	1.7078	6.8310
0.5	-0.833	0.2166	0.2166	0.6012	1.5271	1.5271	4.2386	1.3605	1.3605	3.7760
0.5	-0.75	0.1774	0.1774	0.3992	1.3657	1.3657	3.0729	1.1987	1.1987	2.6970
0.5	-0.667	0.1417	0.1417	0.2521	1.2111	1.2111	2.1553	1.0451	1.0451	1.8598
0.5	-0.5	0.0809	0.0809	0.0809	0.9236	0.9236	0.9236	0.7640	0.7640	0.7640
0.5	-0.333	0.0363	0.0363	0.0161	0.6720	0.6720	0.2981	0.5249	0.5249	0.2328
0.5	-0.25	0.0205	0.0205	0.0051	0.5618	0.5618	0.1405	0.4231	0.4231	0.1058
0.5	-0.167	0.0092	0.0092	0.0010	0.4622	0.4622	0.0516	0.3334	0.3334	0.0372
0.5	0.0	0.0000	0.0000	0.0000	0.2953	0.2953	0.0000	0.1909	0.1909	0.0000
0.5	0.167	0.0092	0.0092	0.0010	0.1755	0.1755	0.0196	0.1010	0.1010	0.0113
0.5	0.25	0.0205	0.0205	0.0051	0.1339	0.1339	0.0335	0.0762	0.0762	0.0191
0.5	0.333	0.0363	0.0363	0.0161	0.1043	0.1043	0.0463	0.0647	0.0647	0.0287
0.5	0.5	0.0809	0.0809	0.0809	0.0809	0.0809	0.0809	0.0809	0.0809	0.0809
0.5	0.667	0.1417	0.1417	0.2521	0.1044	0.1044	0.1859	0.1480	0.1480	0.2634
0.5	0.75	0.1774	0.1774	0.3992	0.1329	0.1329	0.2991	0.1993	0.1993	0.4485
0.5	0.833	0.2166	0.2166	0.6012	0.1720	0.1720	0.4775	0.2620	0.2620	0.7272
0.5	1.0	0.3048	0.3048	1.2194	0.2811	0.2811	1.1243	0.4200	0.4200	1.6801
0.5	1.25	0.4566	0.4566	2.8538	0.5119	0.5119	3.1993	0.7270	0.7270	4.5438
0.5	1.333	0.5112	0.5112	3.6333	0.6041	0.6041	4.2939	0.8449	0.8449	6.0051
0.5	1.5	0.6259	0.6259	5.6327	0.8096	0.8096	7.2863	1.1020	1.1020	9.9179
0.5	2.0	0.9912	0.9912	15.8589	1.5402	1.5402	24.6428	1.9827	1.9827	31.7238
0.5	2.5	1.3581	1.3581	33.9529	2.3549	2.3549	58.8716	2.9329	2.9329	73.3233
0.5	3.0	1.7000	1.7000	61.1988	3.1686	3.1686	114.0678	3.8625	3.8625	139.0502
0.5	4.0	2.2675	2.2675	145.1182	4.6200	4.6200	295.6829	5.4873	5.4873	351.1881
0.5	6.0	2.9775	2.9775	428.7530	6.6207	6.6207	953.3740	7.6698	7.6698	1104.4467

Table G.4: Scalings of cross section times BR for the non-resolved model, for the different $t\bar{t}H$, tHq , tHW signal components and $\kappa_V = 0.5$.

κ_V	κ_t	ttHWW	ttHZZ	ttH $\tau\tau$	tHqWW	tHqZZ	tHq $\tau\tau$	tHWWW	tHWZZ	tHW $\tau\tau$
1.0	-6.0	11.2408	11.2408	404.6686	40.4768	40.4768	1457.1666	41.3681	41.3681	1489.2533
1.0	-4.0	8.2305	8.2305	131.6886	34.2339	34.2339	547.7422	33.8480	33.8480	541.5676
1.0	-3.0	5.9862	5.9862	53.8759	28.5396	28.5396	256.8562	27.3983	27.3983	246.5850
1.0	-2.5	4.6979	4.6979	29.3616	24.8511	24.8511	155.3195	23.3557	23.3557	145.9734
1.0	-2.0	3.3647	3.3647	13.4590	20.6360	20.6360	82.5440	18.8497	18.8497	75.3987
1.0	-1.5	2.0859	2.0859	4.6933	16.0557	16.0557	36.1254	14.0919	14.0919	31.7068
1.0	-1.333	1.6941	1.6941	3.0102	14.4942	14.4942	25.7545	12.5059	12.5059	22.2216
1.0	-1.25	1.5091	1.5091	2.3579	13.7201	13.7201	21.4377	11.7273	11.7273	18.3239
1.0	-1.0	1.0000	1.0000	1.0000	11.4220	11.4220	11.4220	9.4484	9.4484	9.4484
1.0	-0.833	0.7075	0.7075	0.4909	9.9372	9.9372	6.8953	8.0059	8.0059	5.5552
1.0	-0.75	0.5784	0.5784	0.3254	9.2212	9.2212	5.1869	7.3200	7.3200	4.1175
1.0	-0.667	0.4610	0.4610	0.2051	8.5229	8.5229	3.7917	6.6579	6.6579	2.9620
1.0	-0.5	0.2624	0.2624	0.0656	7.1807	7.1807	1.7952	5.4076	5.4076	1.3519
1.0	-0.333	0.1175	0.1175	0.0130	5.9375	5.9375	0.6584	4.2814	4.2814	0.4748
1.0	-0.25	0.0664	0.0664	0.0042	5.3616	5.3616	0.3351	3.7730	3.7730	0.2358
1.0	-0.167	0.0297	0.0297	0.0008	4.8163	4.8163	0.1343	3.3009	3.3009	0.0921
1.0	0.0	0.0000	0.0000	0.0000	3.8183	3.8183	0.0000	2.4676	2.4676	0.0000
1.0	0.167	0.0297	0.0297	0.0008	2.9624	2.9624	0.0826	1.7981	1.7981	0.0501
1.0	0.25	0.0664	0.0664	0.0042	2.5928	2.5928	0.1620	1.5284	1.5284	0.0955
1.0	0.333	0.1175	0.1175	0.0130	2.2612	2.2612	0.2507	1.3014	1.3014	0.1443
1.0	0.5	0.2624	0.2624	0.0656	1.7115	1.7115	0.4279	0.9742	0.9742	0.2435
1.0	0.667	0.4610	0.4610	0.2051	1.3198	1.3198	0.5871	0.8188	0.8188	0.3643
1.0	0.75	0.5784	0.5784	0.3254	1.1834	1.1834	0.6657	0.8042	0.8042	0.4524
1.0	0.833	0.7075	0.7075	0.4909	1.0852	1.0852	0.7530	0.8301	0.8301	0.5760
1.0	1.0	1.0000	1.0000	1.0000	1.0000	1.0000	1.0000	1.0000	1.0000	1.0000
1.0	1.25	1.5091	1.5091	2.3579	1.1380	1.1380	1.7782	1.5278	1.5278	2.3872
1.0	1.333	1.6941	1.6941	3.0102	1.2492	1.2492	2.2197	1.7691	1.7691	3.1434
1.0	1.5	2.0859	2.0859	4.6933	1.5628	1.5628	3.5163	2.3434	2.3434	5.2727
1.0	2.0	3.3647	3.3647	13.4590	3.1023	3.1023	12.4092	4.6362	4.6362	18.5449
1.0	2.5	4.6979	4.6979	29.3616	5.2667	5.2667	32.9167	7.4799	7.4799	46.7493
1.0	3.0	5.9862	5.9862	53.8759	7.7435	7.7435	69.6914	10.5403	10.5403	94.8625
1.0	4.0	8.2305	8.2305	131.6886	12.7892	12.7892	204.6276	16.4642	16.4642	263.4266
1.0	6.0	11.2408	11.2408	404.6686	20.9516	20.9516	754.2573	25.5403	25.5403	919.4497

Table G.5: Scalings of cross section times BR for the non-resolved model, for the different $t\bar{t}H$, tHq , tHW signal components and $\kappa_V = 1.0$.

κ_V	κ_t	ttHWW	ttHZZ	ttH $\tau\tau$	tHqWW	tHqZZ	tHq $\tau\tau$	tHWWW	tHWZZ	tHW $\tau\tau$
1.5	-6.0	23.1266	23.1266	370.0260	96.1923	96.1923	1539.0768	95.1080	95.1080	1521.7272
1.5	-4.0	16.0441	16.0441	114.0913	81.6690	81.6690	580.7570	77.3512	77.3512	550.0531
1.5	-3.0	11.2295	11.2295	44.9178	68.8703	68.8703	275.4812	62.9086	62.9086	251.6344
1.5	-2.5	8.6261	8.6261	23.9614	60.7939	60.7939	168.8720	54.1622	54.1622	150.4505
1.5	-2.0	6.0458	6.0458	10.7481	51.7152	51.7152	91.9381	44.6227	44.6227	79.3293
1.5	-1.5	3.6725	3.6725	3.6725	41.9469	41.9469	41.9469	34.6991	34.6991	34.6991
1.5	-1.333	2.9643	2.9643	2.3410	38.6171	38.6171	30.4971	31.4016	31.4016	24.7987
1.5	-1.25	2.6330	2.6330	1.8284	36.9629	36.9629	25.6687	29.7807	29.7807	20.6810
1.5	-1.0	1.7310	1.7310	0.7693	32.0233	32.0233	14.2326	25.0144	25.0144	11.1175
1.5	-0.833	1.2192	1.2192	0.3760	28.7953	28.7953	8.8803	21.9653	21.9653	6.7740
1.5	-0.75	0.9948	0.9948	0.2487	27.2234	27.2234	6.8058	20.5014	20.5014	5.1254
1.5	-0.667	0.7914	0.7914	0.1565	25.6778	25.6778	5.0772	19.0767	19.0767	3.7720
1.5	-0.5	0.4491	0.4491	0.0499	22.6628	22.6628	2.5181	16.3435	16.3435	1.8159
1.5	-0.333	0.2006	0.2006	0.0099	19.7986	19.7986	0.9758	13.8117	13.8117	0.6807
1.5	-0.25	0.1133	0.1133	0.0031	18.4397	18.4397	0.5122	12.6364	12.6364	0.3510
1.5	-0.167	0.0507	0.0507	0.0006	17.1281	17.1281	0.2123	11.5203	11.5203	0.1428
1.5	0.0	0.0000	0.0000	0.0000	14.6443	14.6443	0.0000	9.4640	9.4640	0.0000
1.5	0.167	0.0507	0.0507	0.0006	12.3858	12.3858	0.1535	7.6760	7.6760	0.0951
1.5	0.25	0.1133	0.1133	0.0031	11.3529	11.3529	0.3154	6.8916	6.8916	0.1914
1.5	0.333	0.2006	0.2006	0.0099	10.3820	10.3820	0.5117	6.1783	6.1783	0.3045
1.5	0.5	0.4491	0.4491	0.0499	8.6227	8.6227	0.9581	4.9621	4.9621	0.5513
1.5	0.667	0.7914	0.7914	0.1565	7.1299	7.1299	1.4098	4.0411	4.0411	0.7990
1.5	0.75	0.9948	0.9948	0.2487	6.4888	6.4888	1.6222	3.6932	3.6932	0.9233
1.5	0.833	1.2192	1.2192	0.3760	5.9148	5.9148	1.8241	3.4176	3.4176	1.0540
1.5	1.0	1.7310	1.7310	0.7693	4.9627	4.9627	2.2057	3.0782	3.0782	1.3681
1.5	1.25	2.6330	2.6330	1.8284	4.0340	4.0340	2.8014	3.0873	3.0873	2.1440
1.5	1.333	2.9643	2.9643	2.3410	3.8531	3.8531	3.0429	3.2206	3.2206	2.5434
1.5	1.5	3.6725	3.6725	3.6725	3.6725	3.6725	3.6725	3.6725	3.6725	3.6725
1.5	2.0	6.0458	6.0458	10.7481	4.4580	4.4580	7.9254	6.3144	6.3144	11.2255
1.5	2.5	8.6261	8.6261	23.9614	6.8533	6.8533	19.0368	10.4359	10.4359	28.9887
1.5	3.0	11.2295	11.2295	44.9178	10.3536	10.3536	41.4143	15.4728	15.4728	61.8913
1.5	4.0	16.0441	16.0441	114.0913	18.9646	18.9646	134.8595	26.5208	26.5208	188.5926
1.5	6.0	23.1266	23.1266	370.0260	35.9359	35.9359	574.9741	46.2619	46.2619	740.1909

Table G.6: Scalings of cross section times BR for the non-resolved model, for the different $t\bar{t}H$, tHq , tHW signal components and $\kappa_V = 1.5$.

$\cos(\alpha_{CP})$	Exp.	SM exp.	Obs.	Best fit $\sigma[pb]$.	Best fit r
-1.0	0.299 ^{0.130} _{-0.088}	0.396 ^{0.190} _{-0.135}	0.594	0.284 ^{0.183} _{-0.171}	0.650 ^{0.418} _{-0.391}
-0.9	0.297 ^{0.130} _{-0.088}	0.388 ^{0.184} _{-0.132}	0.578	0.268 ^{0.182} _{-0.171}	0.686 ^{0.466} _{-0.438}
-0.8	0.294 ^{0.129} _{-0.088}	0.377 ^{0.179} _{-0.127}	0.562	0.251 ^{0.181} _{-0.171}	0.725 ^{0.522} _{-0.493}
-0.7	0.292 ^{0.129} _{-0.087}	0.377 ^{0.165} _{-0.132}	0.545	0.235 ^{0.179} _{-0.170}	0.768 ^{0.587} _{-0.556}
-0.6	0.288 ^{0.128} _{-0.086}	0.368 ^{0.155} _{-0.128}	0.523	0.215 ^{0.177} _{-0.169}	0.798 ^{0.638} _{-0.627}
-0.5	0.285 ^{0.127} _{-0.086}	0.365 ^{0.166} _{-0.132}	0.500	0.194 ^{0.176} _{-0.167}	0.813 ^{0.739} _{-0.701}
-0.4	0.281 ^{0.126} _{-0.085}	0.357 ^{0.150} _{-0.128}	0.479	0.175 ^{0.174} _{-0.165}	0.840 ^{0.833} _{-0.792}
-0.3	0.279 ^{0.125} _{-0.084}	0.350 ^{0.150} _{-0.125}	0.463	0.162 ^{0.173} _{-0.162}	0.884 ^{0.943} _{-0.884}
-0.2	0.277 ^{0.124} _{-0.084}	0.346 ^{0.153} _{-0.117}	0.453	0.153 ^{0.172} _{-0.153}	0.954 ^{0.968} _{-0.954}
-0.1	0.277 ^{0.124} _{-0.084}	0.345 ^{0.155} _{-0.123}	0.454	0.154 ^{0.171} _{-0.154}	1.075 ^{1.197} _{-1.075}
0.0	0.279 ^{0.125} _{-0.084}	0.353 ^{0.161} _{-0.130}	0.469	0.167 ^{0.173} _{-0.164}	1.304 ^{1.356} _{-1.282}
0.1	0.285 ^{0.127} _{-0.086}	0.371 ^{0.160} _{-0.137}	0.504	0.197 ^{0.177} _{-0.167}	1.683 ^{1.508} _{-1.427}
0.2	0.293 ^{0.129} _{-0.087}	0.390 ^{0.159} _{-0.143}	0.556	0.246 ^{0.180} _{-0.171}	2.234 ^{1.639} _{-1.552}
0.3	0.300 ^{0.130} _{-0.089}	0.416 ^{0.178} _{-0.152}	0.610	0.303 ^{0.182} _{-0.171}	2.860 ^{1.723} _{-1.612}
0.4	0.302 ^{0.129} _{-0.088}	0.422 ^{0.193} _{-0.143}	0.644	0.349 ^{0.177} _{-0.166}	3.331 ^{1.693} _{-1.587}
0.5	0.296 ^{0.125} _{-0.086}	0.434 ^{0.157} _{-0.145}	0.651	0.374 ^{0.165} _{-0.159}	3.452 ^{1.527} _{-1.467}
0.6	0.284 ^{0.120} _{-0.082}	0.425 ^{0.136} _{-0.141}	0.639	0.377 ^{0.155} _{-0.150}	3.261 ^{1.339} _{-1.298}
0.7	0.270 ^{0.114} _{-0.078}	0.408 ^{0.118} _{-0.133}	0.616	0.366 ^{0.147} _{-0.140}	2.910 ^{1.167} _{-1.111}
0.8	0.258 ^{0.109} _{-0.074}	0.386 ^{0.120} _{-0.120}	0.594	0.354 ^{0.141} _{-0.132}	2.530 ^{1.006} _{-0.945}
0.9	0.246 ^{0.104} _{-0.071}	0.358 ^{0.128} _{-0.105}	0.570	0.341 ^{0.135} _{-0.126}	2.161 ^{0.857} _{-0.798}
1.0	0.238 ^{0.101} _{-0.069}	0.351 ^{0.125} _{-0.101}	0.555	0.331 ^{0.132} _{-0.121}	1.851 ^{0.736} _{-0.679}

Table G.7: Expected (for background only, and for a SM-like Higgs signal) and observed 95% C.L. upper limits (in pb), and best fit signal strength r and corresponding best fit cross section for the combined $tH + t\bar{t}H$ cross section times branching ratio for the combination of all three channels, for different values of $\cos(\alpha_{CP})$.

4024 **References**

- 4025 [1] J. Schwinger. "Quantum Electrodynamics. I. A Covariant Formulation". Phys-
4026 ical Review. 74 (10): 1439-61, (1948). <https://doi.org/10.1103/PhysRev.74.1439>
- 4028 [2] R. P. Feynman. "Space-Time Approach to Quantum Electrodynamics". Physical
4029 Review. 76 (6): 769-89, (1949). <https://doi.org/10.1103/PhysRev.76.769>
- 4030 [3] S. Tomonaga. "On a Relativistically Invariant Formulation of the Quantum
4031 Theory of Wave Fields". Progress of Theoretical Physics. 1 (2): 27-42, (1946).
4032 <https://doi.org/10.1143/PTP.1.27>
- 4033 [4] D.J. Griffiths, "Introduction to electrodynamics". 4th ed. Pearson, (2013).
- 4034 [5] F. Mandl, G. Shaw. "Quantum field theory." Chichester, Wiley (2009).
- 4035 [6] F. Halzen, and A.D. Martin, "Quarks and leptons: An introductory course in
4036 modern particle physics". New York: Wiley, (1984) .
- 4037 [7] File: Standard_Model_of_Elementary_Particle_dark.svg. (2017, June 12)
4038 Wikimedia Commons, the free media repository. Retrieved November 27, 2017
4039 from <https://www.collegiate-advanced-electricity.com/single-post/2017/04/10/The-Standard-Model-of-Particle-Physics>.

- 4041 [8] E. Noether, "Invariante Variationsprobleme", Nachrichten von der Gesellschaft
4042 der Wissenschaften zu Göttingen, mathematisch-physikalische Klasse, vol. 1918,
4043 pp. 235-257, (1918).
- 4044 [9] C. Patrignani et al. (Particle Data Group), Chin. Phys. C, 40, 100001 (2016)
4045 and 2017 update.
- 4046 [10] M. Goldhaber, L. Grodzins, A.W. Sunyar "Helicity of Neutrinos", Phys. Rev.
4047 109, 1015 (1958).
- 4048 [11] Palanque-Delabrouille N et al. "Neutrino masses and cosmology with Lyman-
4049 alpha forest power spectrum", JCAP 11 011 (2015).
- 4050 [12] M. Gell-Mann. "A Schematic Model of Baryons and Mesons". Physics Letters.
4051 8 (3): 214-215 (1964).
- 4052 [13] G. Zweig. "An SU(3) Model for Strong Interaction Symmetry and its Breaking"
4053 (PDF). CERN Report No.8182/TH.401 (1964).
- 4054 [14] G. Zweig. "An SU(3) Model for Strong Interaction Symmetry and its Breaking:
4055 II" (PDF). CERN Report No.8419/TH.412(1964).
- 4056 [15] M. Gell-Mann. "The Interpretation of the New Particles as Displaced Charged
4057 Multiplets". Il Nuovo Cimento 4: 848. (1956).
- 4058 [16] T. Nakano, K. Nishijima. "Charge Independence for V-particles". Progress of
4059 Theoretical Physics 10 (5): 581-582. (1953).
- 4060 [17] N. Cabibbo, "Unitary symmetry and leptonic decays" Physical Review Letters,
4061 vol. 10, no. 12, p. 531, (1963).

- 4062 [18] M.Kobayashi, T.Maskawa, “CP-violation in the renormalizable theory of weak
4063 interaction,” Progress of Theoretical Physics, vol. 49, no. 2, pp. 652-657, (1973).
- 4064 [19] File: Weak Decay (flipped).svg. (2017, June 12). Wikimedia Com-
4065 mons, the free media repository. Retrieved November 27, 2017
4066 from [https://commons.wikimedia.org/w/index.php?title=File:
4067 Weak_Decay_\(flipped\)\.svg&oldid=247498592](https://commons.wikimedia.org/w/index.php?title=File:Weak_Decay_(flipped)\.svg&oldid=247498592).
- 4068 [20] Georgia Tech University. Coupling Constants for the Fundamental Forces(2005).
4069 Retrieved January 10, 2018, from [http://hyperphysics.phy-astr.gsu.edu/
4070 hbase/Forces/couple.html#c2](http://hyperphysics.phy-astr.gsu.edu/hbase/Forces/couple.html#c2)
- 4071 [21] M. Strassler. (May 31, 2013).The Strengths of the Known Forces. Retrieved Jan-
4072 uary 10, 2018, from [https://profmattstrassler.com/articles-and-posts/
4073 particle-physics-basics/the-known-forces-of-nature/
4074 the-strength-of-the-known-forces/](https://profmattstrassler.com/articles-and-posts/particle-physics-basics/the-known-forces-of-nature/the-strength-of-the-known-forces/)
- 4075 [22] S.L. Glashow. “Partial symmetries of weak interactions”, Nucl. Phys. 22 579-
4076 588, (1961).
- 4077 [23] A. Salam, J.C. Ward. “Electromagnetic and weak interactions”, Physics Letters
4078 13 168-171, (1964).
- 4079 [24] S. Weinberg, “A model of leptons”, Physical Review Letters, vol. 19, no. 21, p.
4080 1264, (1967).
- 4081 [25] M. Peskin, D. Schroeder, “An introduction to quantum field theory”. Perseus
4082 Books Publishing L.L.C., (1995).
- 4083 [26] A. Pich. “The Standard Model of Electroweak Interactions” <https://arxiv.org/abs/1201.0537>
- 4084

- 4085 [27] G. Arnison et al. (UA1 Collaboration), Phys. Lett. B 122, 103 (1983).
- 4086 [28] M. Banner et al. (UA2 Collaboration), Phys. Lett. B 122, 476 (1983).
- 4087 [29] G. Arnison et al. (UA1 Collaboration), Phys. Lett. B 126, 398 (1983).
- 4088 [30] P. Bagnaia et al. (UA2 Collaboration), Phys. Lett. B 129, 130 (1983).
- 4089 [31] F.Bellaiche. (2012, 2 September). “What’s this Higgs boson anyway?”. Retrieved
4090 from: <https://www.quantum-bits.org/?p=233>
- 4091 [32] M. Endres et al. Nature 487, 454-458 (2012) doi:10.1038/nature11255
- 4092 [33] F. Englert, R. Brout. “Broken Symmetry and the Mass of Gauge
4093 Vector Mesons”. Physical Review Letters. 13 (9): 321-23.(1964)
4094 doi:10.1103/PhysRevLett.13.321
- 4095 [34] P.Higgs. “Broken Symmetries and the Masses of Gauge Bosons”. Physical Re-
4096 view Letters. 13 (16): 508-509,(1964). doi:10.1103/PhysRevLett.13.508.
- 4097 [35] G.Guralnik, C.R. Hagen and T.W.B. Kibble. “Global Conservation Laws
4098 and Massless Particles”. Physical Review Letters. 13 (20): 585-587, (1964).
4099 doi:10.1103/PhysRevLett.13.585.
- 4100 [36] CMS collaboration. “Observation of a new boson at a mass of 125 GeV with
4101 the CMS experiment at the LHC”. Physics Letters B. 716 (1): 30-61 (2012).
4102 arXiv:1207.7235. doi:10.1016/j.physletb.2012.08.021
- 4103 [37] ATLAS collaboration. “Observation of a New Particle in the Search for the Stan-
4104 dard Model Higgs Boson with the ATLAS Detector at the LHC”. Physics Letters
4105 B. 716 (1): 1-29 (2012). arXiv:1207.7214. doi:10.1016/j.physletb.2012.08.020.

- 4106 [38] ATLAS collaboration; CMS collaboration (26 March 2015). “Combined Mea-
 4107 surement of the Higgs Boson Mass in pp Collisions at $\sqrt{s} = 7$ and 8 TeV with
 4108 the ATLAS and CMS Experiments”. Physical Review Letters. 114 (19): 191803.
 4109 arXiv:1503.07589. doi:10.1103/PhysRevLett.114.191803.
- 4110 [39] LHC InternationalMasterclasses“When protons collide”. Retrieved from http://atlas.physicsmasterclasses.org/en/zpath_protoncollisions.htm
- 4111
- 4112 [40] CMS Collaboration, “SM Higgs Branching Ratios and Total Decay Widths (up-
 4113 date in CERN Report4 2016)”. <https://twiki.cern.ch/twiki/bin/view/LHCPhysics/CERNYellowReportPageBR> , last accessed on 17.12.2017.
- 4114
- 4115 [41] R.Grant V. “Determination of Higgs branching ratios in $H \rightarrow W^+W^- \rightarrow l\nu jj$
 4116 and $H \rightarrow ZZ \rightarrow l^+l^-jj$ channels”. Physics Department, University of Ten-
 4117 nessee (Dated: October 31, 2012). Retrieved from <http://aesop.phys.utk.edu/ph611/2012/projects/Riley.pdf>
- 4118
- 4119 [42] LHC Higgs Cross Section Working Group, Denner, A., Heinemeyer, S. et al.
 4120 “Standard model Higgs-boson branching ratios with uncertainties”. Eur. Phys.
 4121 J. C (2011) 71: 1753. <https://doi.org/10.1140/epjc/s10052-011-1753-8>
- 4122
- 4123 [43] D. de Florian et al., LHC Higgs Cross Section Working Group, CERN-2017-
 002-M, arXiv:1610.07922[hep-ph] (2016).
- 4124
- 4125 [44] ATLAS and CMS Collaborations, “Measurements of the Higgs boson produc-
 4126 tion and decay rates and constraints on its couplings from a combined ATLAS
 4127 and CMS analysis of the LHC pp collision data at $\sqrt{s} = 7$ and 8 TeV,” (2016).
 CERN-EP-2016-100, ATLAS-HIGG-2015-07, CMS-HIG-15-002.

- 4128 [45] J. A. Aguilar-Saavedra, R. Benbrik, S. Heinemeyer, and M. Perez-Victoria,
 4129 “Handbook of vector-like quarks: Mixing and single production”, Phys. Rev. D
 4130 88 (2013) 094010, doi:10.1103/PhysRevD.88.094010, arXiv:1306.0572.
- 4131 [46] A. Greljo, J. F. Kamenik, and J. Kopp, “Disentangling flavor vio-
 4132 lation in the top-Higgs sector at the LHC”, JHEP 07 (2014) 046,
 4133 doi:10.1007/JHEP07(2014)046, arXiv:1404.1278.
- 4134 [47] F. Demartin, F. Maltoni, K. Mawatari, and M. Zaro, “Higgs production in
 4135 association with a single top quark at the LHC,” European Physical Journal C,
 4136 vol. 75, p. 267, (2015). doi:10.1140/epjc/s10052-015-3475-9, arXiv:1504.00611.
- 4137 [48] F. Demartin, B. Maier, F. Maltoni, K. Mawatari, and M. Zaro, “tWH associated
 4138 production at the LHC”, European Physical Journal C, vol. 77, p. 34, (2017).
 4139 arXiv:1607.05862
- 4140 [49] F. Maltoni, K. Paul, T. Stelzer, and S. Willenbrock, “Associated production
 4141 of Higgs and single top at hadron colliders”, Phys.Rev. D64 (2001) 094023,
 4142 [hep-ph/0106293].
- 4143 [50] S. Biswas, E. Gabrielli, F. Margaroli, and B. Mele, “Direct constraints on the
 4144 top-Higgs coupling from the 8 TeV LHC data,” Journal of High Energy Physics,
 4145 vol. 07, p. 073, (2013).
- 4146 [51] M. Farina, C. Grojean, F. Maltoni, E. Salvioni, and A. Thamm, “Lifting de-
 4147 generacies in Higgs couplings using single top production in association with a
 4148 Higgs boson,” Journal of High Energy Physics, vol. 05, p. 022, (2013).
- 4149 [52] T.M. Tait and C.-P. Yuan, “Single top quark production as a window to physics
 4150 beyond the standard model”, Phys. Rev. D 63 (2000) 014018 [hep-ph/0007298].

- 4151 [53] CMS Collaboration, “Modelling of the single top-quark production in associa-
 4152 tion with the Higgs boson at 13 TeV.” <https://twiki.cern.ch/twiki/bin/viewauth/CMS/SingleTopHiggsGeneration13TeV>, last accessed on 16.01.2018.
- 4154 [54] CMS Collaboration, “SM Higgs production cross sections at $\sqrt{s} =$
 4155 13 TeV.” <https://twiki.cern.ch/twiki/bin/view/LHCPhysics/CERNYellowReportPageAt13TeV>, last accessed on 16.01.2018.
- 4157 [55] S. Dawson, The effective W approximation, Nucl. Phys. B 249 (1985) 42.
- 4158 [56] S. Biswas, E. Gabrielli and B. Mele, JHEP 1301 (2013) 088 [arXiv:1211.0499
 4159 [hep-ph]].
- 4160 [57] LHC Higgs Cross Section Working Group, “Handbook of LHC Higgs Cross
 4161 Sections: 4.Deciphering the Nature of the Higgs Sector”, arXiv:1610.07922.
- 4162 [58] J. Ellis, D. S. Hwang, K. Sakurai, and M. Takeuchi.“Disentangling Higgs-Top
 4163 Couplings in Associated Production”, JHEP 1404 (2014) 004, [arXiv:1312.5736].
- 4164 [59] CMS Collaboration, V. Khachatryan et al., “Precise determination of the mass
 4165 of the Higgs boson and tests of compatibility of its couplings with the standard
 4166 model predictions using proton collisions at 7 and 8 TeV,” arXiv:1412.8662.
- 4167 [60] ATLAS Collaboration, G. Aad et al., “Updated coupling measurements of the
 4168 Higgs boson with the ATLAS detector using up to 25 fb^{-1} of proton-proton
 4169 collision data”, ATLAS-CONF-2014-009.
- 4170 [61] File:Cern-accelerator-complex.svg. Wikimedia Commons, the free media repos-
 4171 itory. Retrieved January, 2018 from <https://commons.wikimedia.org/wiki/File:Cern-accelerator-complex.svg>

- 4173 [62] J.L. Caron , “Layout of the LEP tunnel including future LHC infrastructures.”,
4174 (Nov, 1993). A C Collection. Legacy of AC. Pictures from 1992 to 2002. Re-
4175 trieved from <https://cds.cern.ch/record/841542>
- 4176 [63] M. Vretenar, “The radio-frequency quadrupole”. CERN Yellow Report CERN-
4177 2013-001, pp.207-223 DOI:10.5170/CERN-2013-001.207. arXiv:1303.6762
- 4178 [64] L.Evans. P. Bryant (editors). “LHC Machine”. JINST 3 S08001 (2008).
- 4179 [65] CERN Photographic Service.“Radio-frequency quadrupole, RFQ-1”, March
4180 1983, CERN-AC-8303511. Retrieved from <https://cds.cern.ch/record/615852>.
- 4182 [66] CERN Photographic Service “Animation of CERN’s accelerator network”, 14
4183 October 2013. DOI: 10.17181/cds.1610170 Retrieved from <https://videos.cern.ch/record/1610170>
- 4185 [67] C.Sutton. “Particle accelerator”.Encyclopedia Britannica. July 17,
4186 2013. Retrieved from <https://www.britannica.com/technology/particle-accelerator>.
- 4188 [68] L.Guiraud. “Installation of LHC cavity in vacuum tank.”. July 27 2000. CERN-
4189 AC-0007016. Retrieved from <https://cds.cern.ch/record/41567>.
- 4190 [69] J.L. Caron, “Magnetic field induced by the LHC dipole’s superconducting coils”.
4191 March 1998. AC Collection. Legacy of AC. Pictures from 1992 to 2002. LHC-
4192 PHO-1998-325. Retrieved from <https://cds.cern.ch/record/841511>.
- 4193 [70] AC Team. “Diagram of an LHC dipole magnet”. June 1999. CERN-DI-9906025
4194 retrieved from <https://cds.cern.ch/record/40524>.

- 4195 [71] CMS Collaboration “Public CMS Luminosity Information”. https://twiki.cern.ch/twiki/bin/view/CMSPublic/LumiPublicResults#2016__proton_proton_13_TeV_collis, last accessed 24.01.2018
- 4196
- 4197
- 4198 [72] J.L Caron. “LHC Layout” AC Collection. Legacy of AC. Pictures from 1992
4199 to 2002. September 1997, LHC-PHO-1997-060. Retrieved from <https://cds.cern.ch/record/841573>.
- 4200
- 4201 [73] J.A. Coarasa. “The CMS Online Cluster:Setup, Operation and Maintenance
4202 of an Evolving Cluster”. ISGC 2012, 26 February - 2 March 2012, Academia
4203 Sinica, Taipei, Taiwan.
- 4204 [74] CMS Collaboration. “The CMS experiment at the CERN LHC” JINST 3 S08004
4205 (2008).
- 4206 [75] CMS Collaboration. “CMS detector drawings 2012” CMS-PHO-GEN-2012-002.
4207 Retrieved from <http://cds.cern.ch/record/1433717>.
- 4208 [76] Davis, Siona Ruth. “Interactive Slice of the CMS detector”, Aug. 2016,
4209 CMS-OUTREACH-2016-027, retrieved from <https://cds.cern.ch/record/2205172>
- 4210
- 4211 [77] R. Breedon. “View through the CMS detector during the cooldown of the
4212 solenoid on February 2006. CMS Collection”, February 2006, CMS-PHO-
4213 OREACH-2005-004, Retrieved from <https://cds.cern.ch/record/930094>.
- 4214 [78] Halyo, V. and LeGresley, P. and Lujan, P. “Massively Parallel Computing and
4215 the Search for Jets and Black Holes at the LHC”, Nucl.Instrum.Meth. A744
4216 (2014) 54-60, DOI: 10.1016/j.nima.2014.01.038”

- 4217 [79] A. Dominguez et. al. “CMS Technical Design Report for the Pixel Detector
4218 Upgrade”, CERN-LHCC-2012-016. CMS-TDR-11.
- 4219 [80] CMS Collaboration. “Description and performance of track and primary-vertex
4220 reconstruction with the CMS tracker,” Journal of Instrumentation, vol. 9, no.
4221 10, p. P10009,(2014).
- 4222 [81] CMS Collaboration and M. Brice. “Images of the CMS Tracker Inner Bar-
4223 rel”, November 2008, CMS-PHO-TRACKER-2008-002. Retrieved from <https://cds.cern.ch/record/1431467>.
- 4225 [82] M. Weber. “The CMS tracker”. 6th international conference on hyperons, charm
4226 and beauty hadrons Chicago, June 28-July 3 2004.
- 4227 [83] CMS Collaboration. “Projected Performance of an Upgraded CMS Detector at
4228 the LHC and HL-LHC: Contribution to the Snowmass Process”. Jul 26, 2013.
4229 arXiv:1307.7135
- 4230 [84] L. Veillet. “End assembly of HB with EB rails and rotation inside SX ”,Jan-
4231 uary 2002. CMS-PHO-HCAL-2002-002. Retrieved from <https://cds.cern.ch/record/42594>.
- 4233 [85] J. Puerta-Pelayo.“First DT+RPC chambers installation round in the UX5 cav-
4234 ern.”. January 2007, CMS-PHO-OREACH-2007-001. Retrieved from <https://cds.cern.ch/record/1019185>
- 4236 [86] X. Cid Vidal and R. Cid Manzano. “CMS Global Muon Trigger” web site:
4237 Taking a closer look at LHC. Retrieved from https://www.lhc-closer.es/taking_a_closer_look_at_lhc/0.lhc_trigger

- 4239 [87] WLCG Project Office, “Documents & Reference - Tiers - Structure,”
 4240 (2014). <http://wlcg.web.cern.ch/documents-reference> , last accessed on
 4241 30.01.2018.
- 4242 [88] CMS Collaboration. “CMSSW Application Framework”, <https://twiki.cern.ch/twiki/bin/view/CMSPublic/WorkBookCMSSWFramework>,
 4243 last accesses 06.02.2018
- 4245 [89] A. Buckleya, J. Butterworthb, S. Giesekec, et. al. “General-purpose event gen-
 4246 erators for LHC physics”. arXiv:1101.2599v1 [hep-ph] 13 Jan 2011
- 4247 [90] A. Quadt. “Top Quark Physics at Hadron Colliders”. Advances in the Physics
 4248 of Particles and Nuclei. Springer-Verlag Berlin Heidelberg. DOI: 10.1007/978-
 4249 3-540-71060-8 (2007)
- 4250 [91] DurhamHep Data Project, “The Durham HepData Project - PDF Plotter.”
 4251 <http://hepdata.cedar.ac.uk/pdf/pdf3.html> , last accessed on 02.02.2018.
- 4252 [92] G. Altarelli and G. Parisi. “ASYMPTOTIC FREEDOM IN PARTON LAN-
 4253 GUAGE”, Nucl.Phys. B126:298 (1977).
- 4254 [93] Yu.L. Dokshitzer. Sov.Phys. JETP 46:641 (1977)
- 4255 [94] V.N. Gribov, L.N. Lipatov. “Deep inelastic e p scattering in perturbation the-
 4256 ory”, Sov.J.Nucl.Phys. 15:438 (1972)
- 4257 [95] F. Maltoni, G. Ridolfi, and M. Ubiali, “b-initiated processes at the LHC: a
 4258 reappraisal,” Journal of High Energy Physics, vol. 07, p. 022, (2012).
- 4259 [96] B. Andersson, G. Gustafson, G.Ingelman and T. Sjostrand, “Parton fragmen-
 4260 tation and string dynamics”, Physics Reports, Vol. 97, No. 2-3, pp. 31-145,
 4261 1983.

- 4262 [97] CMS Collaboration, “Event generator tunes obtained from underlying event
4263 and multiparton scattering measurements;” European Physical Journal C, vol.
4264 76, no. 3, p. 155, (2016).
- 4265 [98] J. Alwall et. al., “The automated computation of tree-level and next-to-leading
4266 order differential cross sections, and their matching to parton shower simula-
4267 tions,” Journal of High Energy Physics, vol. 07, p. 079, (2014).
- 4268 [99] T. Sjöstrand and P. Z. Skands, “Transverse-momentum-ordered showers and
4269 interleaved multiple interactions,” European Physical Journal C, vol. 39, pp.
4270 129–154, (2005).
- 4271 [100] S. Frixione, P. Nason, and C. Oleari, “Matching NLO QCD computations with
4272 Parton Shower simulations: the POWHEG method,” Journal of High Energy
4273 Physics, vol. 11, p. 070, (2007).
- 4274 [101] S. Agostinelli et al., “GEANT4: A Simulation toolkit,” Nuclear Instruments
4275 and Methods in Physics, vol. A506, pp. 250–303, (2003).
- 4276 [102] J.Allison et.al.,“Recent developments in Geant4”, Nuclear Instruments and
4277 Methods in Physics Research A 835 (2016) 186-225.
- 4278 [103] CMS Collaboration “Full Simulation Offline Guide”, <https://twiki.cern.ch/twiki/bin/view/CMSPublic/SWGuideSimulation>, last accessed 04.02.2018
- 4280 [104] A. Giammanco. “The Fast Simulation of the CMS Experiment” J. Phys.: Conf.
4281 Ser. 513 022012 (2014)
- 4282 [105] A.M. Sirunyan et. al. “Particle-flow reconstruction and global event description
4283 with the CMS detector”, JINST 12 P10003 (2017) <https://doi.org/10.1088/1748-0221/12/10/P10003>.

- 4285 [106] The CMS Collaboration. “ Description and performance of track and pri-
4286 mary vertex reconstruction with the CMS tracker”. JINST 9 P10009 (2014).
4287 doi:10.1088/1748-0221/9/10/P10009
- 4288 [107] J. Incandela. “Status of the CMS SM Higgs Search” July 4, 2012. Pdf slides.
4289 Retrieved from [https://indico.cern.ch/event/197461/contributions/](https://indico.cern.ch/event/197461/contributions/1478917/attachments/290954/406673/CMS_4July2012_Final.pdf)
4290 [1478917/attachments/290954/406673/CMS_4July2012_Final.pdf](https://indico.cern.ch/event/197461/contributions/1478917/attachments/290954/406673/CMS_4July2012_Final.pdf)
- 4291 [108] P. Billoir and S. Qian, “Simultaneous pattern recognition and track fitting by
4292 the Kalman filtering method”, Nucl. Instrum. Meth. A 294 219. (1990).
- 4293 [109] W. Adam, R. Fruhwirth, A. Strandlie and T. Todorov, “Reconstruction of
4294 electrons with the Gaussian sum filter in the CMS tracker at LHC”, eConf
4295 C 0303241 (2003) TULT009 [physics/0306087].
- 4296 [110] K. Rose, “Deterministic Annealing for Clustering, Compression, Classification,
4297 Regression and related Optimisation Problems”, Proc. IEEE 86 (1998) 2210.
- 4298 [111] R. Fruhwirth, W. Waltenberger and P. Vanlaer, “ Adaptive Vertex Fitting”,
4299 CMS Note 2007-008 (2007).
- 4300 [112] CMS collaboration, “Performance of CMS muon reconstruction in pp collision
4301 events at $\sqrt{s} = 7 \text{ TeV}$ ”, JINST 7 P10002 2012, [arXiv:1206.4071].
- 4302 [113] Coco, Victor and Delsart, Pierre-Antoine and Rojo-Chacon, Juan and Soyez,
4303 Gregory and Sander, Christian, “Jets and jet algorithms”, Proceedings,
4304 HERA and the LHC Workshop Series on the implications of HERA for LHC
4305 physics: 2006-2008, pag. 182-204. <http://inspirehep.net/record/866539/files/access.pdf>, (2009), doi:10.3204/DESY-PROC-2009-02/54

- 4307 [114] M. Cacciari, G. P. Salam, and G. Soyez, “The anti- k_t jet clustering algorithm,”
 4308 Journal of High Energy Physics, vol. 04, p. 063, (2008).
- 4309 [115] S. Catani, Y. L. Dokshitzer, M. H. Seymour, and B. R. Webber, “Longitudi-
 4310 nally invariant K_t clustering algorithms for hadron hadron collisions”, Nuclear
 4311 Physics B, vol. 406, pp. 187–224, (1993).
- 4312 [116] Y.L. Dokshitzer, G.D. Leder, S.Moretti, and B.R. Webber, “Better jet clustering
 4313 algorithms,” Journal of High Energy Physics, vol. 08, p. 001, (1997).
- 4314 [117] B. Dorney. “Anatomy of a Jet in CMS”. Quantum Diaries. June
 4315 1st, 2011. Retrieved from [https://www.quantumdiaries.org/2011/06/01/
 4316 anatomy-of-a-jet-in-cms/](https://www.quantumdiaries.org/2011/06/01/anatomy-of-a-jet-in-cms/)
- 4317 [118] The CMS Collaboration.“Event Displays from the high-energy collisions at 7
 4318 TeV”, May 2010, CMS-PHO-EVENTS-2010-007, Retrieved from [https://cds.
 4319 cern.ch/record/1429614.](https://cds.cern.ch/record/1429614)
- 4320 [119] The CMS collaboration. “Determination of jet energy calibration and transverse
 4321 momentum resolution in CMS”. JINST 6 P11002 (2011). [http://dx.doi.org/
 4322 10.1088/1748-0221/6/11/P11002](http://dx.doi.org/10.1088/1748-0221/6/11/P11002)
- 4323 [120] The CMS Collaboration, “Introduction to Jet Energy Corrections at
 4324 CMS.”. <https://twiki.cern.ch/twiki/bin/view/CMS/IntroToJEC>, last ac-
 4325 cessed 10.02.2018.
- 4326 [121] CMS Collaboration Collaboration. “Identification of b quark jets at the CMS
 4327 Experiment in the LHC Run 2”. Tech. rep. CMS-PAS-BTV-15-001. Geneva:
 4328 CERN, (2016). <https://cds.cern.ch/record/2138504>.

- 4329 [122] CMS Collaboration Collaboration. “Performance of missing energy reconstruction
4330 in 13 TeV pp collision data using the CMS detector”. Tech. rep. CMS-PAS-
4331 JME16-004. Geneva: CERN, 2016. <https://cds.cern.ch/record/2205284>.
- 4332 [123] CMS Collaboration, “New CMS results at Moriond (Electroweak) 2013”,
4333 Retrieved from http://cms.web.cern.ch/sites/cms.web.cern.ch/files/styles/large/public/field/image/HIG13004_Event01_0.png?itok=LAWZzPHR
- 4336 [124] CMS Collaboration, “New CMS results at Moriond (Electroweak) 2013”,
4337 Retrieved from http://cms.web.cern.ch/sites/cms.web.cern.ch/files/styles/large/public/field/image/TOP12035_Event01.png?itok=uMdnSqzC
- 4340 [125] K. Skovpen. “Event displays highlighting the main properties of heavy flavour
4341 jets in the CMS Experiment”, Aug 2017, CMS-PHO-EVENTS-2017-006. Re-
4342 trieval from <https://cds.cern.ch/record/2280025>.
- 4343 [126] G. Cowan. “Topics in statistical data analysis for high-energy physics”.
4344 arXiv:1012.3589v1
- 4345 [127] A. Hoecker et al., “TMVA-Toolkit for multivariate data analysis”
4346 arXiv:physics/0703039v5 (2009)
- 4347 [128] L. Lista. “Statistical Methods for Data Analysis in Particle Physics”, 2nd
4348 ed. Springer International Publishing. (2017) <https://dx.doi.org/10.1007/978-3-319-62840-0>

- 4350 [129] I. Antcheva et al., “ROOT-A C++ framework for petabyte data storage, sta-
 4351 tistical analysis and visualization ,” Computer Physics Communications, vol.
 4352 182, no. 6, pp. 1384â€¢1385, (2011).
- 4353 [130] Y. Coadou. “Boosted decision trees”, ESIPAP, Archamps, 9 Febru-
 4354 ary 2016. Lecture. Retrieved from https://indico.cern.ch/event/472305/contributions/1982360/attachments/1224979/1792797/ESIPAP_MVA160208-BDT.pdf
- 4357 [131] J.H. Friedman. “Greedy function approximation: A gradient boosting ma-
 4358 chine”. Ann. Statist. Volume 29, Number 5 (2001), 1189-1232. https://projecteuclid.org/download/pdf_1/euclid-aos/1013203451.
- 4360 [132] W. Verkerke and D. Kirkby, “The RooFit toolkit for data modeling,” arXiv
 4361 preprint physics, (2003).
- 4362 [133] CMS Collaboration, “Documentation of the RooStats-based statistics
 4363 tools for Higgs PAG”. <https://twiki.cern.ch/twiki/bin/view/CMS/SWGuideHiggsAnalysisCombinedLimit>, last accessed on 08.04.2018.
- 4365 [134] F. James, M. Roos, “MINUIT: Function minimization and error analysis”. Cern
 4366 Computer Centre Program Library, Geneve Long Write-up No. D506, 1989
- 4367 [135] J. Neyman and E. S. Pearson, “On the problem of the most efficient tests of
 4368 statistical hypotheses”. Springer-Verlag, (1992).
- 4369 [136] A.L. Read. “Modified frequentist analysis of search results (the CL_s method),”
 4370 (2000). CERN-OPEN-2000-205.
- 4371 [137] C. Palmer. “Searches for a Light Higgs with CMS”, CMS-CR-2012-215. <https://cds.cern.ch/record/1560435>.

- 4373 [138] A. Wald, “Tests of statistical hypotheses concerning several parameters when
 4374 the number of observations is large”, Transactions of the American Mathematical
 4375 society, vol. 54, no. 3, pp. 426–482, (1943).
- 4376 [139] G. Cowan, K. Cranmer, E. Gross, and O. Vitells, “Asymptotic formulae for
 4377 likelihood-based tests of new physics”, European Physical Journal C, vol. 71,
 4378 p. 1554, (2011).
- 4379 [140] S. S. Wilks, “The Large-Sample Distribution of the Likelihood Ratio for Testing
 4380 Composite Hypotheses”, Annals of Mathematical Statistics, vol. 9, pp. 60–62,
 4381 (03, 1938).
- 4382 [141] B. Hespel, F. Maltoni, and E. Vryonidou, “Higgs and Z boson associated pro-
 4383 duction via gluon fusion in the SM and the 2HDM”, JHEP 06 (2015) 065,
 4384 [https://dx.doi.org/10.1007/JHEP06\(2015\)065](https://dx.doi.org/10.1007/JHEP06(2015)065), arXiv:1503.01656.
- 4385 [142] ATLAS Collaboration, “Measurements of Higgs boson pro-
 4386 duction and couplings in diboson final states with the AT-
 4387 LAS detector at the LHC”, Phys. Lett. B726 (2013) 88–119,
 4388 doi:10.1016/j.physletb.2014.05.011, 10.1016/j.physletb.2013.08.010,
 4389 arXiv:1307.1427. [Erratum: Phys. Lett.B734,406(2014)].
- 4390 [143] CMS Collaboration, “Search for the associated production of a Higgs boson
 4391 with a single top quark in proton-proton collisions at $\sqrt{s} = 8$ TeV”, JHEP 06
 4392 (2016) 177, doi:10.1007/JHEP06(2016)177, arXiv:1509.08159.
- 4393 [144] B. Stieger, C. Jorda Lope et al., “Search for Associated Production of a Single
 4394 Top Quark and a Higgs Boson in Leptonic Channels”, CMS Analysis Note CMS
 4395 AN-14-140, 2014.

- 4396 [145] M. Peruzzi, C. Mueller, B. Stieger et al., “Search for ttH in multilepton final
4397 states at $\sqrt{s} = 13$ TeV”, CMS Analysis Note CMS AN-16-211, 2016.
- 4398 [146] CMS Collaboration, “Search for H to bbar in association with a single top quark
4399 as a test of Higgs boson couplings at $\sqrt{s} = 13$ TeV”, CMS Physics Analysis
4400 Summary CMS-PAS-HIG-16-019, 2016.
- 4401 [147] CMS Collaboration, “Search for production of a Higgs boson and a single top
4402 quark in multilepton final states in proton collisions at $\sqrt{s} = 13$ TeV”, CMS
4403 Physics Analysis Summary CMS-PAS-HIG-17-005, 2016.
- 4404 [148] CMS Collaboration, “PdmV2016Analysis,” (2016). <https://twiki.cern.ch/twiki/bin/viewauth/CMS/PdmV2016Analysis#DATA>, last accessed 11.04.2016.
- 4406 [149] M. Peruzzi, F. Romeo, B. Stieger et al., “Search for ttH in multilepton final1
4407 states at $\sqrt{s} = 13$ TeV”, CMS Analysis Note CMS AN-17-029, 2017.
- 4408 [150] B. Maier, “SingleTopHiggProduction13TeV”, February, 2016. <https://twiki.cern.ch/twiki/bin/viewauth/CMS/SingleTopHiggsGeneration13TeV>.
- 4410 [151] B. WG, “BtagRecommendation80XReReco”, February, 2017. <https://twiki.cern.ch/twiki/bin/view/CMS/BtagRecommendation80XReReco>.
- 4412 [152] CMS Collaboration, “Identification of b quark jets at the CMS Experiment
4413 in the LHC Run 2”, CMS Physics Analysis Summary CMS-PAS-BTV-15-001,
4414 2016.
- 4415 [153] CMS Collaboration, “Baseline muon selections for Run-II.” <https://twiki.cern.ch/twiki/bin/view/CMSPublic/SWGuideMuonIdRun2>, last accessed on
4416 24.02.2018.

- 4418 [154] G. Petrucciani and C. Botta, “Two step prompt muon identification”, January,
4419 2015. [https://indico.cern.ch/event/368007/contribution/2/material/
4420 slides/0.pdf](https://indico.cern.ch/event/368007/contribution/2/material/slides/0.pdf).
- 4421 [155] H. Brun and C. Ochando, “Updated Results on MVA eID with 13 TeV samples”,
4422 October, 2014. [https://indico.cern.ch/event/298249/contribution/3/
4423 material/slides/0.pdf](https://indico.cern.ch/event/298249/contribution/3/material/slides/0.pdf).
- 4424 [156] K. Rehermann and B. Tweedie, “Efficient Identification of Boosted Semileptonic
4425 Top Quarks at the LHC”, JHEP 03 (2011) 059, [https://dx.doi:10.1007/
4426 JHEP03\(2011\)059](https://dx.doi.org/10.1007/JHEP03(2011)059), arXiv:1007.2221.
- 4427 [157] CMS Collaboration. “Tag and Probe”, [https://twiki.cern.ch/twiki/bin/
4428 view/CMS/TagAndProbe](https://twiki.cern.ch/twiki/bin/view/CMS/TagAndProbe), last accessed on 02.03.2018.
- 4429 [158] CMS Collaboration. “ \hat{t}_z coupling modifiers”, [https://twiki.cern.ch/
4430 twiki/bin/view/LHCPhysics/LHCHXSWG2KAPPA#t_ch_qbtHq](https://twiki.cern.ch/twiki/bin/view/LHCPhysics/LHCHXSWG2KAPPA#t_ch_qbtHq), last accessed on
4431 27.04.2018.
- 4432 [159] CMS Tracker Group. “The Performance plots for Phase 1 Pixel De-
4433 tector 2017” [https://twiki.cern.ch/twiki/bin/view/CMSPublic/
4434 PixelOfflinePlotsAugust2017#Alignment_of_the_forward_pixels](https://twiki.cern.ch/twiki/bin/view/CMS/PixelOfflinePlotsAugust2017#Alignment_of_the_forward_pixels), last
4435 accessed on 01.05.2018
- 4436 [160] UNL Silicon pixel group “Pixel Phase-I activities at University of
4437 Nebraska-Lincoln (UNL)” [https://twiki.cern.ch/twiki/bin/view/CMS/
4438 UNLPixelPhaseI](https://twiki.cern.ch/twiki/bin/view/CMS/UNLPixelPhaseI), last accessed on 01.05.2018.

- 4439 [161] Aerotech (n.d). “AGS15000 Series”, retrieved from <https://www.aerotech.com/product-catalog/gantry-system/ags15000.aspx?p=%2fproduct-catalog%2fgantry-system.aspx%3f>
- 4442 [162] C. Fangmeier. “Fiducial recognition”, 2016. Github repository,https://github.com/cfangmeier/Small/blob/master/JupyterNotebooks/Fiducial_Recognition.ipynb
- 4445 [163] F. Meier and J. Monroy “ SOP 103 - Module assembly: Gluing of HDI to BBM”, retrieved from <https://twiki.cern.ch/twiki/pub/CMS/UNLPixelPhaseI/UNL-PxPhI-SOP-103-v0.pdf>, last accessed on 05.30.2018.
- 4448 [164] F. Meier “ Forward Pixel Module Glueing at UNL” YouTube, Sep. 15, 2014, retrieved from <https://www.youtube.com/watch?v=ofdntTIwKY4>.
- 4450 [165] J. Monroy (n.d). Home [YouTube Channel]. Retrieved from <https://www.youtube.com/channel/UCi7S7vhYpieL0y2KJ0SS0eg>.
- 4452 [166] F. Meier and J. Monroy “ SOP 105 - Module assembly: Encapsulation of wirebonds”, retrieved from <https://twiki.cern.ch/twiki/pub/CMS/UNLPixelPhaseI/UNL-PxPhI-SOP-103-v0.pdf>, last accessed on 05.30.2018.